

Strength and fracture of silicon second-phase particles in aluminium casting alloys

THÈSE N° 7892 (2017)

PRÉSENTÉE LE 22 AOÛT 2017

À LA FACULTÉ DES SCIENCES ET TECHNIQUES DE L'INGÉNIEUR
LABORATOIRE DE MÉTALLURGIE MÉCANIQUE
PROGRAMME DOCTORAL EN SCIENCE ET GÉNIE DES MATÉRIAUX

ÉCOLE POLYTECHNIQUE FÉDÉRALE DE LAUSANNE

POUR L'OBTENTION DU GRADE DE DOCTEUR ÈS SCIENCES

PAR

Martin Guillermo MUELLER

acceptée sur proposition du jury:

Prof. P. Murali, président du jury
Prof. A. Mortensen, directeur de thèse
Prof. C. Eberl, rapporteur
Prof. R. Spolenak, rapporteur
Prof. J. Botsis, rapporteur



ÉCOLE POLYTECHNIQUE
FÉDÉRALE DE LAUSANNE

Suisse
2017

Acknowledgements

This thesis could not have been possible without the invaluable support of institutions, colleagues, friends, and family. The following lines are dedicated to them.

In the first place, I deeply thank my thesis director Prof. Andreas Mortensen for the trust that he put in me since the beginning, the thorough scientific advice he gave me during these years, and for his very friendly and caring approach at a personal level. Working with Andreas has been an immense honour and a great pleasure.

I kindly acknowledge the funding agent of this thesis: the European Research Council (ERC) under the European Union's Seventh Framework Programme (FP/2007-2013) / ERC Advanced Grant Agreement No. 291085.

I also sincerely thank the thesis jury Prof. John Botsis, Prof. Chris Eberl, Prof. Ralph Spolenak and Prof. Paul Muralt for the careful examination and the interesting discussions on the work presented here.

I am very much thankful to the EPFL, to the personnel at the Doctoral School and at the EDMX, to the Microscopy Centre CIME-EPFL (particularly to Dr. Marco Cantoni and to Fabienne Bobard for their valuable help), and to the workshop ATMX (to Pierre-André Despont and his team). I also thank Prof. Elida Hermida, Dr. Ramgopal Thodla and Dr. Philippe Spätig for their support at the time I was applying for the PhD candidate position at EPFL. At different stages of my PhD, I also received the support from Prof. Gerhard Dehm, Prof. Bhaskar Majumdar and Prof. Nina Orlovskaya, to whom I am grateful.

I wish to transmit a gigantic “thank you” to the current staff of the Laboratory of Mechanical Metallurgy (LMM-EPFL) for their limitless kindness and efficiency: Fabienne Ubezio, Raphaël Charvet, Cyril Dénéréaz and Ludger Weber.

It has been a real pleasure to work within the “ERC-team” at the LMM with Goran Žagar, Vaclav Pejchal, Marta Fornabaio and Lionel Michelet. They contributed substantially to the work presented here. We shared hundreds of meetings, worked hard, and had a lot of fun together; thank you!

I also sincerely thank my current or past colleagues at the LMM: Gabriella Tarantino, Ana Fernandez, Maïté Blank, Suzanne Verheyden, Marie-Thérèse Zanetta, Hamed Kazemi, Cyrill Cattin, Alain Leger, Alex Athanasiou-Ioannou, Gionata Schneider, Roberto Arpón, José Miguel Molina, Arda Cetin, Amaël Cohades, Andreas Rossoll, Willy Dufour, Aparna Singh, Christian Monachon, Florian Gallien and my dear office mates Léa Deillon and Jérôme Krebs. Sharing these years with them has been very gratifying.

Thank you also to the students whose projects I supervised: Hammam Elaïan, Gloria Young, Florian Cottier, Matia Bulloni, Tom Powell, Pauline Treboz, Emily Smith, Damien Tailens and Joonatan Laulainen.

Besides the work at LMM-EPFL, the time during which this thesis was produced was full of great experiences shared with my wife and my friends in Lausanne: Paola, Luciano, Ogi, Ceci, Damian, Alexia, Car-

los, Maria Nydia, Saúl, Sandra, Fernando, Adrián, Sofía, Pablo, Erica, Luciano. On vacations, I got my batteries refilled by sharing great times with my family and friends in Salta, in Buenos Aires and in Bariloche (Argentina). Thank you to all of them!

Completing this PhD would have not been possible without the loving support that I have received during all my life from my mom Silvia, my dad Joaquin, my sister Mariana, my brothers Pablo and Tomas and the rest of my family. Thank you all!

Finally, and above all, a huge “thank you” full of love to Ursula for her support and patience in this journey, as well as to our lovely baby Felix.

Abstract

The mechanical behaviour of metallic materials that have a microstructure composed of a brittle phase embedded in a ductile matrix is dictated by a complex interplay of factors such as local phase properties, cohesive properties, geometrical characteristics, and specific damage mechanisms. An important example of such two-phase materials are Al-Si casting alloys, which are widely used in automotive applications. In the micromechanics of these alloys, fracture of the particulate brittle phase plays a dominant role. Namely, when the alloy is deformed, the brittle silicon particles within the aluminium matrix start fracturing, leading ultimately to fracture of the alloy.

In this thesis, micromechanical methods to measure local fracture toughness or strength of individual brittle microscopic particles within alloys and metal matrix composites (MMCs) are developed. The methods are based on coupling experimental techniques such as Scanning Electron Microscopy (SEM), Focused Ion Beam (FIB) milling and nanoindentation with finite element modelling (FEM). Special attention is put in probing portions of the particles that are left unaffected by the FIB micromachining process, and are thus representative of the particles' intrinsic properties. These novel methods are also used to study the fracture of silicon particles within Al-Si casting alloys.

To measure fracture toughness at a small scale, a microscopic chevron notch test is developed and demonstrated on benchmark materials. The main advantage of this method with respect to most existing small-scale fracture toughness test methods is that in chevron-notched samples the crack growth resistance is measured on a real crack instead of a pre-notch. The main difficulty, on the other hand, is achieving crack initiation at applied loads low enough to allow for subsequent stable crack growth. This was found to be particularly challenging in silicon.

Local strength measurements on individual microscopic silicon particles within Al-Si alloys were achieved through two different, novel, methods. The first is a microscopic 3-point bending test by which the large facets of plate-like particles extracted from an Al-Si alloy can be probed. In the second approach, particles that are only partially exposed by deep-etching from an Al-Si sample are carved by FIB milling into such a shape that by compressing its top, bending is produced on a well-defined portion of the particle.

The main finding of the local strength measurements is that silicon particles within Al-Si alloys can achieve extremely high strength values, yet fracture early when an Al-Si alloy is deformed because most of them feature stress-concentrating defects on their surfaces. The most important stress-limiting defects are found to be grooved interfaces between contacting silicon crystals, followed by surface *pinholes*, this being a defect identified here. Using FIB cross-sectioning and EDX examination it was revealed that these pinholes originate from alloy impurities.

The insights gained on the intrinsic strength of silicon particles unveil the great potential of silicon as a reinforcing phase in Al-Si alloys. This, together with the acknowledgement of particle strength-limiting defects, may be used to devise strategies that, through the avoidance of those defects, should lead to improved alloy mechanical properties.

Keywords: Aluminium alloys ; Silicon ; Fracture ; Micromechanical testing ; Strength ; Fracture toughness ; Defects

Résumé

Le comportement mécanique des matériaux métalliques ayant une microstructure formée par une phase fragile intégrée dans une matrice ductile est déterminé par l'interaction complexe de facteurs tel que les propriétés locales des phases, les propriétés de cohésion, les caractéristiques géométriques et des mécanismes d'endommagement spécifiques. Les alliages Al-Si, notamment utilisés dans l'industrie des transports, sont un exemple important de tels matériaux biphasés. Dans ceux-ci la fracture des particules fragiles de Si gouverne la résistance mécanique de l'alliage.

Cette thèse présente le développement de méthodes micromécaniques permettant de mesurer la ténacité ou la résistance mécanique locales de particules microscopiques fragiles dans des alliages et des matériaux métalliques. Les méthodes sont basées sur l'association de techniques expérimentales comme la microscopie électronique de balayage (MEB), la sonde ionique focalisée (FIB), et la nanoindentation avec la modélisation par éléments finis. Les méthodes sont soigneusement conçues pour sonder des secteurs sur les particules qui ne sont pas affectés par la procédure de microusinage avec le FIB, et qui sont donc représentatifs des propriétés intrinsèques des particules. Ces méthodes sont ensuite utilisées pour étudier la fracture de particules de silicium dans des alliages Al-Si.

Pour mesurer la ténacité à petite échelle, une méthode basée sur des échantillons microscopiques contenant une entaille en forme de chevron est développée et mise en œuvre sur des matériaux de référence. L'avantage principal par rapport aux essais de ténacité à petite échelle existants est que la résistance à la propagation la fissure est mesurée sur une vraie fissure au lieu d'une entaille. Par contre, la méthode présente une difficulté, qui est de réussir à initier une fissure à une force suffisamment basse pour permettre ensuite la propagation stable de la fissure, étape qui s'est avérée difficile dans le silicium.

Des mesures locales de la résistance de particules microscopiques de silicium dans des alliages Al-Si ont été réalisées par le biais de deux méthodes nouvelles. Une est un essai de flexion en 3 points, utilisé pour solliciter les grandes facettes plates des particules en forme de plaquette extraits d'un alliage Al-Si. L'autre approche est utilisée sur des particules partiellement exposées depuis la surface d'un échantillon d'alliage Al-Si attaqué chimiquement et taillées de manière à ce que, en exerçant une force de compression sur le haut de la particule, une contrainte de flexion est produite le bord de la particule.

Ce travail montre que les particules de silicium dans les alliages Al-Si peuvent être extrêmement résistantes, mais se fracturent prématurément dans les alliages Al-Si car elles présentent des défauts superficiels concentrateurs de contrainte. Les défauts les plus importants sont aux lignes triples formées là où deux cristaux de silicium se rejoignent. Un autre défaut est formé par des microcavités; on montre ici que celles-ci sont causées par la présence d'impuretés dans l'alliage.

L'issue de cette thèse dévoile le potentiel considérable des particules de silicium comme phase de renfort pour l'aluminium. Cela, ajouté à la reconnaissance des défauts spécifiques limitant la résistance de ces particules, pourra peut-être mener à trouver des stratégies qui, en empêchant la formation de ces défauts, devraient conduire à des alliages Al-Si plus résistants et plus ductiles.

Mots-clés: Alliages d'aluminium ; Silicium ; Fracture ; Essais micromécaniques ; Résistance ; Ténacité ; Défauts.

Contents

Acknowledgements.....	i
Abstract.....	iii
Résumé.....	v
Contents.....	vii
List of Figures.....	xi
List of Tables.....	xxv
List of Equations.....	xxvii
Chapter 1 Introduction.....	29
1.1 Background and motivation	29
1.2 Statement of objectives.....	34
1.3 Thesis's framework and funding	34
Chapter 2 Literature Review	37
2.1 Microstructure of Al-Si alloys.....	37
2.2 Micromechanics of Al-Si alloys and particle strength.....	54
2.3 Small-scale fracture toughness testing.....	60
2.4 Small-scale strength testing.....	69
2.5 Fracture properties of single crystalline silicon.....	76
2.6 Concluding remarks	80
Chapter 3 Fracture toughness	81
3.1 Microscopic Chevron notch test.....	81
3.1.1 Test development using test-bench materials.....	81
3.1.1.1 Methodology	82
3.1.1.2 Sample preparation	83
3.1.1.3 Testing procedure	86
3.1.1.4 Results	88
3.1.1.5 Discussion	90
3.1.1.6 Conclusions	94
3.1.2 Extension of the chevron notch test to triangular microcantilevers.....	95
3.1.2.1 Materials and methods	95
3.1.2.2 Results and discussion	97
3.1.2.3 Conclusion	101

3.2	Chevron-notch tests on silicon particles.....	101
3.3	Chevron and straight-through notch tests on silicon wafer.....	103
3.3.1	Materials and Methods.....	103
3.3.2	Results.....	107
3.3.3	Discussion.....	113
3.3.3.1	Straight-through notched samples	113
3.3.3.2	Crack initiation in microscopic Chevron-notched specimens	114
3.3.3.3	Crack growth and fracture toughness	115
3.3.3.4	Influence of Mode II in the interpretation of CN and STN tests	118
3.3.4	Conclusion.....	120
Chapter 4	Strength.....	123
4.1	Microscopic 3-point bending test of silicon particles.....	123
4.1.1	Method.....	124
4.1.1.1	Principle of the test	124
4.1.1.2	Material	125
4.1.1.3	Test specimen preparation	126
4.1.1.4	Testing procedure	128
4.1.2	Results.....	129
4.1.2.1	General response	129
4.1.2.2	Stress analysis and sensitivity analysis	130
4.1.2.3	Measurements and test results	133
4.1.3	Discussion.....	133
4.1.3.1	Flexural strength of the silicon plate-like particles	133
4.1.3.2	Re-evaluation using Simple Beam Theory	137
4.1.3.3	Influence of the etching procedure	138
4.1.4	Conclusion.....	139
4.2	In-situ strength measurements of individual silicon particles.....	140
4.2.1	Materials and Methods.....	140
4.2.1.1	Material	140
4.2.1.2	Generalities of the method	141
4.2.1.3	Sample preparation and testing	142
4.2.1.4	Test interpretation	144
4.2.2	Results.....	147
4.2.3	Discussion.....	153
4.2.3.1	The method and its precision	153

4.2.3.2	Silicon deformation and particle strength	155
4.2.4	Conclusion.....	157
4.3	Investigation on the origin of particle defects.....	157
4.3.1	Introduction and examination of fractured particles	157
4.3.2	Materials and methods	160
4.3.3	Results	162
4.3.3.1	FIB-tomography	162
4.3.3.2	Control experiment	163
4.3.4	Discussion	165
4.3.5	Conclusions.....	166
Chapter 5	Summary and conclusions.....	169
5.1	Summary.....	169
5.2	General conclusions.....	171
Chapter 6	Outlook	173
References.....		175
Curriculum Vitae.....		201

List of Figures

Figure 1.1 Left: Evolution in time (years) of the average aluminium content in cars produced in Europe, revealing a steadily increasing tendency. The data are from 2012; projections are shown until 2020. Right: Distribution of aluminium in European cars. Products marked with an asterisk (*) are largely made of cast aluminium. (Adapted from Ref. [1])..... 32

Figure 1.2 Greenhouse-gas emission targets for passenger vehicles across the world. The declining tendency motivates the need for enhanced fuel efficiency, which is partly achieved through substituting high- for low-density materials such as aluminium alloys. Data and figure from Ref. [71], updated in September 2015. 33

Figure 1.3 Cast aluminium products: (a) an engine block, (b) a wheel, (c) pistons and (d) a transmission case. (Images from Refs. [72–75]) 33

Figure 1.4 Metallographic examination of the fracture surfaces of different Al-Si alloys tested in tension or by impact. As seen, fracture paths follow fractured Si particles (in darker grey). (Images from Refs. [17,76] reproduced with permission of ASM International and Springer) 34

Figure 2.1 (a) Al-Si equilibrium phase diagram. Coloured arrows in the phase diagram indicate compositions of each of the representative microstructure of (b) hypoeutectic, (c) eutectic and (d) hypereutectic Al-Si alloys shown along (Adapted from Refs. [17,84] with permission of ASM International and Elsevier). In the micrographs, silicon particles are dark and aluminium is bright..... 38

Figure 2.2 SEM images of the microstructure of a near-eutectic, binary, Al-Si alloy (a) non-modified and (b) Sr-modified. Silicon particles are bright, while the aluminium phase is dark. (Reproduced from Ref. [93] with permission of Elsevier)..... 39

Figure 2.3 Silicon particles within the microstructure of a Al-11Si-0.6Mg alloy exposed by deep-etching the aluminium matrix using a two-step etching procedure consisting in first immersing the sample in a mixture of HCl and HF, and then in HNO₃ solution. Eutectic particles in non-modified alloys are typically plate-like (a1-a2). (Figure adapted from Ref. [76] with permission of Springer)..... 39

Figure 2.4 Twins in a silicon plate-like particle parallel to the large {111} facets observed in the SEM using Back Scattered Electrons. (Adapted from Ref. [94] with permission of Elsevier) 40

Figure 2.5 (a) Octahedron crystal bounded by {111} facets. (b) Spinel-type crystal bounded by {111} facets resulting from twinning the octahedron along the (111) plane labelled bbb. The twin plane is shaded in (b). (Figure from Ref. [96] with permission of Springer) 40

Figure 2.6 SEM micrographs of a deep-etched Al-20Si alloy, showing the morphology of primary silicon particles. The area indicated with a white square in (a) is magnified in (b). (Adapted from Ref. [98] with permission of Elsevier) 41

Figure 2.7 Primary silicon particles extracted from an Al-20Si alloy. In the left image, the top particle has a spinel-type morphology, while the bottom particle is a perfect octahedron. The

image in the right shows an imperfect, hopper-like (i.e., with centrally hollowed facets), octahedral silicon particle. (Figure adapted from Ref. [99] with permission of Elsevier)41

Figure 2.8 Observation of a AlP as the possible nucleant of a Si particle; figure adapted from Ref. [108] with permission of Oxford University Press. The EDS results of a line scan on the particle in (a) are shown in (b). Note that the presence of O in the EDS results is an artefact introduced upon metallographic sample preparation. A TEM image of a lamella prepared using FIB out of a silicon particle attached to a potential nucleant is shown in (c)..... 42

Figure 2.9 The top image shows the part of the cooling curves upon solidification associated with the formation of Al-Si eutectic in alloys having different P concentrations, ranging from 0.5 to 20 ppm. The obtained microstructures are shown below in images (a)-(e), corresponding to alloys having 0.5, 2, 3, 5 and 20 ppm of P, respectively. (Figure adapted from Ref. [107] with permission of Springer)..... 43

Figure 2.10 A proposed eutectic nucleation mechanism; figure from Ref. [108] with permission of Oxford University Press. (a) Aluminium phosphide segregates to the melt at the interface with a growing dendrite. (b) Segregated AlP particles act as heterogeneous sites onto which eutectic silicon nucleates, starting the formation of eutectic grains..... 43

Figure 2.11 Elemental map and bright field TEM images of eutectic Si particles within the Al matrix, where a (Al,Si,Fe) phase is shown in association with Si particles, suggesting, according to Shankar et al. [112], that the Fe-rich phase nucleated the Si particles. (Reproduced from Ref. [112] with permission of Elsevier) 44

Figure 2.12 A proposed eutectic Si nucleation mechanism; figure reproduced from Ref. [112] with permission of Elsevier. Primary Al dendrites are growing in (a). In (b), β -(Al-Si-Fe) phase nucleates at the solid-melt interface. Then, in (c), eutectic Si nucleates on the Fe-rich phase, followed by nucleation of eutectic Al on the eutectic Si. In (d), eutectic Si can further nucleate within the growing eutectic Al. Eventually, the growth of the solid phases is completed.45

Figure 2.13 Phase fraction as a function of temperature as computed from solidification simulations of a hypoeutectic Al-Si alloy with Fe and P impurities; figure reproduced from Ref. [117] with permission of Springer. In (a), all phases can grow (standard Scheil simulation), while in (b) the formation of (Si) is suspended (constrained Scheil simulation). In either case, AlP is observed to form before the β -(Al-Si-Fe) phase, which, moreover, appears at a significant undercooling if Si does not nucleate earlier elsewhere (as seen in (b)). These results were claimed to disprove the hypothesis that the β -(Al-Si-Fe) phase in the form of tiny particles nucleates eutectic Si. 45

Figure 2.14 (a) Representation of turbulence at the surface of molten metal causing the entrainment of oxide bifilms and bubbles during manipulation and pouring into the mould. (b) Long central cracks in elongated β -(Al-Si-Fe) and Si particles, claimed to be consistent with the hypothesis that those particles have nucleated on entrained bifilms. (Adapted from Ref. [48] with permission of Taylor & Francis)..... 46

Figure 2.15 Polished cross section of a spinel-like primary Si particle observed under light microscope (left) and a simplified scheme (right) indicating the crystal growth traces, which were exposed using a hot etching technique; figure reproduced from Ref. [96] with permission of Springer..... 47

Figure 2.16 Primary plate-like Si particles extracted from a Al-Si alloy (a), and a magnified view showing in detail the edge of a plate-like primary Si particle (indicated with an arrow), where grooves resulting from twins are readily visible; from Refs. [95,100] with permission of Taylor & Francis and Springer.	47
Figure 2.17 Coalescence of two primary Si crystals forming one particle. The octahedron crystal features a further deviation from perfection, including a non- $\{111\}$ facet (see scheme on the right). (Reproduced from Ref. [96] with permission of Springer)	47
Figure 2.18 Twin Plane Re-Entrant (TPRE) growth mechanism of plate-like silicon particles; figure adapted from Ref. [127] with permission of AIP Publishing LLC. In (a1-a2), the crystal only has one twin, which prevents its perpetual growth. In (b1-b3), the crystal has two twins and growth by the TPRE mechanism can self-perpetuate. See main text for a step-by-step description.	48
Figure 2.19 Modified TPRE mechanism to account for the fact that plate-like Si particles in Al-Si alloys are found to be elongated in a $\langle 110 \rangle$ direction. In this case, growth at the atomic scale is in $\langle 112 \rangle$ directions (as in the traditional TPRE mechanism) but in zigzag, which leads to an overall $\langle 110 \rangle$ microscopic growth direction. (Reproduced from Ref. [94] with permission of Elsevier)	49
Figure 2.20 “Broom-like” appearance of eutectic Si plate-like particles (scale not indicated in the original document); figure from Ref. [129] with permission of Springer.....	49
Figure 2.21 Reconstructed 3D microtomography images of a non-modified Al-Si alloy. (a-b) are for the as-cast condition. Interconnected particles share a common level of grey; as seen, particles mostly form an interconnected network in the as-cast condition. On the other hand, (c-d) are images after heat treatment: particles with different colours are disconnected from each other. As seen, the heat treatment defragmented the silicon phase. (Adapted from Ref. [93] with permission of Elsevier)	51
Figure 2.22 Same as the previous Figure, but in this case the alloy is a Sr-modified Al-Si alloy. In this case, heat treatment not only defragmented but also spheroidized the silicon phase. (Adapted from Ref. [93] with permission of Elsevier)	51
Figure 2.23 (left) TEM image of a Si particle from an Al-Si alloy, in which Al precipitates roughly 10 nm in size (HR-TEM image on the right) are observed in a sector of the particle marked with a red rectangle; figure adapted from Ref. [143] with permission of Springer. These Al precipitates inside Si particles have been observed in many Al-Si alloys and are insensitive to heat treatments.....	53
Figure 2.24 SEM and light microscopy images of the microstructure of a Al-Si-Cu-Mg-Ni alloy showing the presence of many different intermetallic phases within the Al matrix; figure from Ref. [149] with permission of Elsevier.....	54
Figure 2.25 Micrographs of Al-Si alloys under Nomarski phase contrast to expose slip bands in the aluminium matrix; figure adapted from Ref. [12] with permission of Elsevier. The left image corresponds to an alloy with a large dendrite arm spacing (DAS). Here, slip bands are observed in dendrite cells and interact with the silicon particles at cell boundaries. The right image corresponds to an alloy with a small DAS. The density of silicon particles is in this case lower, and hence cell boundaries interact less with dislocations. Slip bands are, in contrast, observed to strongly interact with a grain boundary (indicated with black arrows).	57

Figure 2.26 A Si particle cracked at three locations and slip bands in the surrounding Al matrix. The particle is at the surface of a tensile sample tested in-situ in a SEM. (Reproduced from Ref. [19] with permission of Springer)	58
Figure 2.27 (a) SEM image showing fractured particles and the trace left by a scratching indenter on the surface of an Al-Si alloy. (b) Side view (left) and top view (right) of the geometry of the idealized contact between the indenter and the particle used to estimate the fracture strength of the particles based on average dimensions, vertical force and estimated friction coefficient. (Adapted from Ref. [45] with permission of Elsevier).....	59
Figure 2.28 Idealized crack morphologies produced by indentation; figure adapted from Ref. [174] with permission of John Wiley & Sons.	61
Figure 2.29 Indentation fracture toughness values computed using different published equations (labelled “Niihara”, “Miyoshi” and “Anstis”) compared to the certified value of a material of calibrated fracture toughness (dashed line); reproduced from Ref. [204] with permission of John Wiley & Sons. As seen, the equations fail to give the true value and their results are significantly different from each other.....	62
Figure 2.30 Vickers indentations on a (110) plane of single crystalline silicon. The indents are misaligned by 15°, 30° and 45° from the [001] direction in (a), (b) and (c), respectively. Complex crack systems including extensive surface spalling and secondary cracks are observed. (Reproduced from Ref. [197] with permission of Elsevier).....	63
Figure 2.31 Vickers indentation on a silicon particle from an Al-Si alloy; figure reproduced from Ref. [212] with permission of Elsevier. In (c), a complex crack pattern and a plastic core underneath the indent are observed on a FIB-milled cross section of the indent.	64
Figure 2.32 A micropillar produced into TiN and subsequently indented with a Berkovich tip. This is an example of the pillar splitting method for fracture toughness measurement. (Reproduced from Ref. [215] with permission of Elsevier)	65
Figure 2.33 Notched microcantilever beam produced by FIB milling into a Ni-P film, tested to fracture using a nanoindenter. (Reproduced from Ref. [235] with permission of Elsevier)	66
Figure 2.34 FIB-produced straight-through notched microcantilever beams of NiAl to probe fracture toughness; figure from Ref. [242] with permission of Cambridge University Press.	66
Figure 2.35 Microscopic double cantilever beam produced using FIB-milling into SiC to measure fracture toughness; figure from Ref. [251] with permission of AIP Publishing LLC.	66
Figure 2.36 Microscopic clamped bending beam in single crystalline silicon to probe fracture toughness; figure from Ref. [253] with permission of Springer.	67
Figure 2.37 Approach to produce a precrack in a microcantilever beam for fracture toughness testing; figure adapted from Refs. [237,239] with permission of Elsevier. A pre-notch is milled with the FIB leaving pristine bridges at the sides. These will initiate a crack when the cantilever is bent.....	68
Figure 2.38 (a-d) Fracture toughness testing of a pre-cracked thin film specimen. The precrack is introduced by a Vickers indentation on the substrate, which is subsequently etched away before the mechanical test (Reproduced from Ref. [233] with permission of Elsevier). (e) An	

SEM image of the Vickers indentation and the crack running into the specimen (Reproduced from Ref. [280] with permission of ASME).....	68
Figure 2.39 Silicon whisker roughly 20 μm in diameter bent using a small quartz hook; reproduced from Ref. [296] with permission of Elsevier.....	69
Figure 2.40 Microcantilever beams of a SiO_2 thin film extending over a deep trench in a silicon wafer, produced by photolithography followed by wet etching; reproduced from Ref. [298] with permission of Cambridge University Press.....	70
Figure 2.41 Set-up for tensile testing of whiskers reported by Eisner in 1955; reproduced from Ref. [317] with permission of Elsevier.....	71
Figure 2.42 (a) Tensile specimen (in the centre of the picture) produced within a frame using semiconductor fabrication techniques; reproduced from Ref. [332] with permission of IEEE. (b-c) A frame (in this case made of cardboard) can be also used to probe small fibres, which are glued at the centre [335,336]. In this way, handling and alignment issues are largely avoided. The sides of the frame are cut with a small diamond saw in (a), or with scissors in (b), just before starting the tensile test.....	72
Figure 2.43 (a) Silicon nanowires synthesized using a vapor-liquid-solid approach. (b) Tensile testing of one of the nanowires in (a). (Adapted from Ref. [292] with permission of American Chemical Society).....	72
Figure 2.44 “Theta” silicon specimen produced using lithographic methods for indirect tensile testing; figure reproduced from Ref. [306] with permission of IEEE. Upon de application of the load P, the beam in the centre undergoes tensile stress.....	73
Figure 2.45 (D) “Push-to-pull” device for indirect tensile testing. Load is applied using a nanoindenter as shown in (G). The close-ups in E and F show the tensile specimen, while the load-displacement response is shown in (H). (Reproduced from Ref. [294] with permission of AAAS)	73
Figure 2.46 (a) Intermediate stage during fabrication using FIB milling of a micropillar. (b-c) Two micropillars of different size prepared using FIB-milling ready to be tested in compression. (Adapted from Ref. [302] with permission of Elsevier)	74
Figure 2.47 Stress-strain response of micropillars of Mo-alloy produced with and without FIB. The effect of FIB milling on the mechanical response of micropillars is shown to be very strong. (Reproduced from Ref. [340] with permission of Elsevier)	74
Figure 2.48 Stress-strain response of silicon nanopillars (scale bar is 100 nm) shown to be different in the as-FIB-produced and in the heat-treated conditions. FIB-milling produces a layer of amorphous Si with implanted Ga on the pillar surface (this is further shown in Figure 2.50), which enhances plasticity. This layer is recrystallized upon heat-treatment. (Reproduced from Ref. [342] with permission of AIP Publishing LLC).....	75
Figure 2.49 (a) Silicon nitride pebbles featuring a large notch that was machined to produced so-called “C-sphere” specimens. (b) Schematics of the test: upon the application of an increasing compressive force, the material at the external surface of the ligament is subject to tensile stress. (c) Maximum principal stress field on a quarter model of a C-sphere specimen, showing the region of high tensile stress. (Figure adapted from Ref. [348] with permission of John Wiley & Sons)	76

Figure 2.50 Deformation-induced crystalline-to-amorphous transformation during the TEM in-situ compression test of a silicon nanopillar prepared by FIB-milling; figure reproduced from Ref. [343] under Open Access licence CC-BY. Stress-strain response is shown in (a). Bright field TEM images as a function of strain are shown in (b), where slip bands along $\{111\}$ planes are visible. Note that in the inset images in (a) and (b), amorphous silicon, which initially coats the pillar surfaces, is grey. Crystalline silicon is black in the inset images in (a) and white in (b). Selected area diffraction patterns in (c) show the transition from diamond cubic Si into amorphous Si. 77

Figure 2.51 Observation of dislocations emitted from cracks in silicon (from the work of Langer et al. [375], reproduced with permission of Springer) (a) Geometry of the silicon specimen fabricated by etching and ion milling, tested in bending at room temperature in a TEM. (b) TEM image in $[1\ 10]$ projection after fracture. Failure was preceded by the propagation of two cracks in $\{111\}$ planes (dashed planes in (c)), one along $[1\ 1\ 2]$ and the other one along $[1\ 1\ 2]$, which emitted dislocations. 78

Figure 2.52 Original (a) and filtered (b) high resolution TEM image (HRTEM) of a crack tip in single crystalline silicon produced by Vickers indentation at room temperature. Dislocations are observed near the crack tip. The strain field calculated using geometric phase analysis based on the HRTEM image indicates crack tip shielding. (Reproduced from Ref. [376] under Open Access licence CC-BY) 78

Figure 2.53 Clamped beams produced by lithographic methods and tested in bending by Namazu et al. [65] (Reproduced with permission of IEEE). Specimens of sizes in the nano- (a), micro- (b) and macro-scales (c) where probed in that work to study size effects on single crystalline electronic grade silicon. Some results are shown in (d), where letters A-F indicate groups of specimens of given dimensions. 79

Figure 2.54 Compiled data in the literature of fracture strength as a function of probed surface area for single crystalline silicon. (Reproduced from Ref. [164] with permission of AIP Publishing LLC) 80

Figure 3.1 Sketch of the chevron-notched samples used to measure fracture toughness. (a) Overcut notch. (b) Undercut notch. (Reproduced from Mueller et al. [380]) 83

Figure 3.2 Chevron-notched cantilever beams (indicated with red arrows) produced by FIB milling along the edge of a fused quartz sample. 85

Figure 3.3 Chevron-notched cantilever beam prepared in fused quartz. (a) Overview of a beam after testing, indicating the size of the beam support. (b) View of the beam and the notch after testing, indicating the point of load application and relevant beam dimensions. (Reproduced from Mueller et al. [380]) 85

Figure 3.4 (a) SEM image of alumina fibres (Nextel 610™) exposed by deep etching the Al matrix of a composite wire polished along two planes with a $\sim 90^\circ$ edge passing roughly through the wire diameter. (b) Close-up of a random sector at the edge, showing the polished fibres protruding from the Al matrix. 86

Figure 3.5 Chevron-notched cantilever beam prepared in a Nextel™ 610 alumina fibre, with relevant dimensions indicated. (a) Overview of a fibre from which a beam was machined. Note that the fibre is accessible from both its side and its top. (b) The same cantilever beam at higher magnification. (c) View of the triangular ligament (fracture surface) after testing. (d) Beam

after testing, with an inset showing the trace of the point of load application. The bigger imprint corresponds to post-failure impact of the nanoindenter tip. (Reproduced from Mueller et al. [380])..... 86

Figure 3.6 Indentation-corrected load—displacement responses of (a) fused quartz and (b) alumina chevron-notched cantilever beam samples. The progressive increase in compliance, a signature of stable crack growth, is smooth in (a) and stepped in (b). Colours represent different samples. (Reproduced from Mueller et al. [380])..... 90

Figure 3.7 Fracture surface of (a) fused quartz and (b) alumina chevron-notched samples. (Reproduced from Mueller et al. [380])..... 90

Figure 3.8 3-D FE model for (a) fused quartz and (b) alumina cantilever beams. The uncracked region of the chevron notch is highlighted in red. For clarity, deformation of the models is magnified by a factor 100. (Reproduced from Mueller et al. [380]) 92

Figure 3.9 Dimensionless compliance C_v and geometrical function F_v as a function of normalized crack length \tilde{a} for (a, c) fused quartz and (b, d) alumina samples with dimensions given in Table 3-1 and Table 3-2. (Reproduced from Mueller et al. [380]) 92

Figure 3.10 (a) Triangular micro-cantilever beam with the chevron notch, as prepared on a flat fused quartz surface by FIB milling. (b) Sketch of chevron notch geometry with characteristic ligament dimensions. The fractured surface of a chevron ligament is assumed to be triangular. Shaded region (in red) represents the unfractured portion of the ligament. (c) Fracture surface of a chevron-notch ligament. (Reproduced from Zagar et al. [381]) 96

Figure 3.11 (a) Force–displacement response of tested triangular chevron-notched cantilevers corrected for the indentation. The critical (peak) load of each test is indicated with open symbols. (b) Example of the FE mesh (deformation is enhanced by the factor of 100) used for compliance calibration. Shaded region (in red) in half of the cross-sectional view represents the unfractured portion of the ligament. (c) Compliance calibration data for cantilevers tested in (a). Dimensionless compliance, $C_v = CBE'$, as a function of normalized crack length, $\tilde{a} = a/W$, is shown with open symbols (FE calculations) and solid lines (fits). Minimum values, $F_v(\tilde{a}_c)$, of corresponding specimen geometrical functions F_v (dashed lines) are indicated with solid symbols. (Reproduced from Zagar et al. [381])..... 99

Figure 3.12 (a) Linear elastic compliance as a function of the applied load, up to critical load P_c , as obtained from force—displacement responses in Figure 3.11a (symbols are the same); compliance—load signals after smoothing are indicated with lines. (b) Crack velocity as a function of the load obtained from smooth compliance—load curves in (a). (c) Stress intensity factor at the crack tip versus applied load as calculated from experimental data (Figure 3.11 and Figure 3.12a) using compliance calibration curves. (Reproduced from Zagar et al. [381])100

Figure 3.13 Eutectic silicon particles (indicated with white arrows) lying on a polished steel substrate. The particles were extracted from a heat-treated Al-12.6Si alloy by selectively etching the aluminium matrix.....102

Figure 3.14 Chevron-notch fracture toughness test on a eutectic silicon particle extracted from an Al-12.6Si alloy. (a) Silicon particle lying of a steel substrate. (b) The same particle after FIB-micromachining to produce a cantilever beam of triangular cross section with a chevron notch. To prevent the particle from moving upon testing, it was welded to the substrate using carbon

deposition. (c) Front view of the particle ready to be tested. (d) Force—displacement response: no sign of stable crack initiation and growth is observed. (e) Fractured cantilever after the micromechanical testing. (d) Fractography of the notch.102

Figure 3.15 (a) General geometry of triangular micro-cantilevers prepared by FIB milling single crystal silicon (110) wafer. (b) Straight-through notch (sample S4, Table 3-6) and (c) chevron notch (sample C2, Table 3-6) fracture surfaces of tested cantilevers (shaded in grey on the right-hand sketches). Straight-through notches are FIB milled perpendicular to the $(\bar{1}10)$ plane, which preferentially removes material near the edges of the notch front. To account for that, the geometry of these samples is approximated in calculations as being chevron-like with static crack length $a = a_p$ (see sketch). (Reproduced from Mueller et al. [382]).....105

Figure 3.16 Sample C1 during the “small chevron notch pre-fatigue” preparation step to ease crack initiation at the subsequent testing stage. (a) The micromanipulator is approached to the FIB-produced cantilever beam. (b) The micromanipulator is carbon-welded to the beam. The dashed white line is for reference. In (c) and (d) the beam is slightly bent downwards and upwards, respectively. (e) The micromanipulator is detached by FIB milling its tip. (f) The free-end of the cantilever beam is cut by FIB milling, leaving the sample ready for micromechanical testing. (Reproduced from the Supplementary Material of Mueller et al. [382]).....106

Figure 3.17 (a) SEM image of Sample C2 from a tilted point of view. Close-up views of the notch (dashed square in (a)) before and after the small cyclic pre-deformation step are shown in (b) and (c), respectively, where the view is straight down from the top. Signs of a small crack may be distinguished in (c) at the tip of the triangular ligament. (Reproduced from the Supplementary Material of Mueller et al. [382]).....107

Figure 3.18 Force—displacement response of micro-cantilevers with straight-through notches (STN Samples S1—S4, Table 3-6). All data are corrected for additional displacement caused by tip indentation into the cantilevers. (Reproduced from Mueller et al. [382])108

Figure 3.19 Force—displacement response of micro-cantilevers with chevron notch (CN Samples C1—C3, Table 3-6). All data are corrected for displacements due to relative tip indentation into the cantilevers. Region of the response of chevron-notched cantilevers where the crack is growing is indicated with bold lines. (Reproduced from Mueller et al. [382])108

Figure 3.20 Calculated compliance calibration curves of the three chevron-notched cantilever samples: compliance C (a) and geometrical function g_F (b) vs. crack length a for chevron-notched micro-cantilevers samples: C1 (red), C2 (green) and C3 (blue). Square symbol in Panel (b) indicates minimum of g_F . (Reproduced from the Supplementary Material of Mueller et al. [382]).....109

Figure 3.21 (Top row) Linear elastic compliance $C = u/P$ vs. displacement u obtained from CN cantilever responses shown in Figure 3 (only data indicated with a bold line are considered). (Bottom row) Calculated elastic strain energy release rate G versus measured displacement u . For convenience, right-hand scale corresponding to the stress intensity is indicated according to, $K_I = \sqrt{GM_{(111)}}$, where the elastic fracture factor of SC Si for (111) plane $M_{(111)} = 178$ GPa [164]. The dotted line indicates the critical compliance that corresponds to the critical crack length of the chevron-notched geometry. (Reproduced from Mueller et al. [382]).....110

Figure 3.22 Fractured surfaces, all along (111) planes, of the four tested single crystal silicon micro-cantilevers with a straight-through notch (STN). Scale bar in all images represents 1 μm .

Columns of images (a) to (d) correspond to different images of the fracture surface of Specimen S1 to S4, respectively. Images on the top and middle rows are taken from different perspectives. Notch geometries used for calculations are superimposed and indicated with a white dashed line in the top-row images. The brightness and contrast of the bottom-row images have been manipulated to enhance the visibility of marks on the fracture surfaces. (Reproduced from the Supplementary Material of Mueller et al. [382])..... 111

Figure 3.23 Fractured surfaces, (111) planes, of the three tested single crystal silicon micro-cantilevers with a chevron notch (CN). Scale bar in all images represents 0.5 μm . Columns of images (a) to (c) correspond to different images of the fracture surface of Specimens C1 to C3, respectively. Images on the top and middle rows are taken from different perspectives. The brightness and contrast of the bottom-row images have been manipulated to enhance the visibility of marks on the fracture surfaces. (Reproduced from the Supplementary Material of Mueller et al. [382])..... 112

Figure 3.24 Post-test SEM examination of the chevron-notched specimens. The location of the load-application point, identified as a shallow indent, is indicated with black arrows in the lower images, which are close-ups of the area marked with a black, dashed, rectangle in the top images. 113

Figure 3.25 CN Sample C2 before (a) and after (b) cyclic elastic deformation. Cyclic deformation of the micro-cantilever resulted in the formation of spherical drops at the notch end. The drop was removed prior to the mechanical test by additional FIB milling under a current of 10 pA. (Reproduced from the Supplementary Material of Mueller et al. [382])..... 115

Figure 3.26 SEM images (b) and (c) are close-ups of the chevron-notch of the specimen in (a) before and after subjecting the sample to 500 $^{\circ}\text{C}$ in vacuum, respectively. The arrow in (c) points to a droplet, likely of Ga, that appeared after the heat treatment. This specimen was at a later stage dismissed because a stable crack could not be initiated upon mechanical testing. (Reproduced from the Supplementary Material of Mueller et al. [382])..... 115

Figure 3.27 Von Mises stress distribution in the chevron ligament of Sample C1 at (a) the maximal displacement recorded during the pre-fatigue preparation step and (b) immediately before the crack initiation pop-in during the micromechanical test. The results are obtained for isotropic, elastic-perfectly plastic silicon (see the main text for material parameters). Plastic yielding (von Mises stress exceeding 7.6 GPa) is found in a very narrow region near the edges at the top part of the chevron notch. (Reproduced from the Supplementary Material of Mueller et al. [382])..... 118

Figure 3.28 (a) Linear and (b) logarithmic plot of the normal (σ_{33}) and the shear (σ_{32}) stress as a function of the distance from the crack, y , along the line of symmetry in the chevron notch plane of the cantilever specimen C1 at several relative crack lengths, $\hat{a} = (a - a_0)/(a_1 - a_0)$. Stress distributions obtained by FEM at $\hat{a} = 0.05, 0.26, 0.48, 0.69$ and 0.90 are shown with filled (σ_{33}) and open (σ_{32}) circles. Fitted near-field crack singularity expressions are indicated with solid (σ_{33}) and dashed (σ_{32}) lines. (c) Ratio of the stress intensity factors, K_I/K_{II} , as a function of the relative crack length \hat{a} for chevron-notched specimens C1 (circle) C2 (square) and C3 (triangle). (Reproduced from the Supplementary Material of Mueller et al. [382]) 120

Figure 4.1 Fractured half-beam and fracture surface of a rectangular cross-section specimen produced in early phases of the work described in this Section. The fracture origin is at a FIB-damaged edge of the beam (indicated with a white arrow). Throughout the rest of the present

body of work a tapered cross-section design was used instead, to prevent fracture from starting from the edges as shown here. (Reproduced from the Supplementary Material of Mueller et al. [412]).....125

Figure 4.2 Illustration of the difference in the maximum principal stress distribution between a rectangular (left) and a trapezoidal (right) cross-section three-point bending specimen (cut view through mid-span plane). The design with a trapezoidal cross-section was thus used here to keep the higher maximum stresses away from the edges of the beam, which are affected by ion milling. (Reproduced from Mueller et al. [412]).....125

Figure 4.3 Optical micrograph of the heat-treated near-eutectic Al-Si alloy used in this work. Inset: SEM image of a few eutectic silicon particles such as the ones probed in this work after selectively etching the aluminium phase to expose them. (Reproduced from Mueller et al. [412])126

Figure 4.4 Scheme of the preparation of a microscopic three-point bending specimen from a silicon particle extracted from the Al-Si alloy. (Reproduced from Mueller et al. [412])127

Figure 4.5 (a) Eutectic silicon plate-like particle extracted from the Al-Si alloy, lying on a steel substrate. (b) Microscopic three-point bending specimen (S8 in Table 4-1) ready to be tested prepared from the particle in (a). FIB milling, transportation with a micromanipulator and carbon FIB induced depositing were used for the preparation; however, the bottom surface of the specimen is unaffected by these. Relevant geometrical dimensions are indicated on the image and on the inset. Bottom-view (c) and side-view (d) of the nanoindenter diamond tip used for the microscopic three-point bending tests. (Reproduced from Mueller et al. [412])128

Figure 4.6 (a-d) Eutectic silicon particles extracted from the Al-Si alloy featuring distinctive surface defects: a small pore in (a), a larger pore in (b), a deep trench-like interface in (c) and a shallow stepped interface in (d). These particles were turned over before producing a three-point bending specimen out of each, to probe the strength of their defect-containing surface. One such specimen (S11 in Table 4-1) is shown in (e); it was prepared from the particle in (c). Image (f) is the fractured half-beam and fracture surface after the three-point bending test of the specimen in (e). The fracture origin in (f) is indicated with a white arrow. (Reproduced from Mueller et al. [412]).....128

Figure 4.7 Typical measured load—displacement response of a microscopic three-point bending test of the silicon specimen shown in the inset (specimen S1 in Table 4-1). Responses calculated by finite element modelling with rigid supports (long-dashed line) and with elastic supports (short-dashed line) are also shown (corresponding to the models in Figure 4.8a and Figure 4.8b respectively). (Reproduced from Mueller et al. [412])130

Figure 4.8 Finite element models of the microscopic three-point bending test on silicon particles (Specimen S1 in Table 4-1). The model in (a), where the supports are rigid surfaces, was used to obtain the maximum first principal stress of each tested specimen. The model in (b), where the supports are elastic, was used to analyse the influence of various possible misalignments. The stress field shown in (a) is the first (tensile) principal stress in GPa. The values are largest at the centre of the bottom surface and decrease towards the edges in the X-direction as a consequence of the tapered cross-section. (Reproduced from Mueller et al. [412])132

Figure 4.9 Finite element models of different misaligned testing configurations that were considered to evaluate uncertainty sources of the microscopic 3-point bending test..132

Figure 4.10 Flexural strength (evaluated as the maximum first principal stress calculated from finite element model of each specimen) versus the specimen effective probed area for "regular" three-point bending specimens (black dots) and for specimens produced with a visible defect along the lower beam surface (hollow squares; their indications with letters a—f refers to the corresponding images in Figure 4.6). The error bars are +10% and -15%, which is an estimate of the pooled uncertainty arising from the sensitivity analysis (see main text). Strength of electronic grade silicon as reported by Namazu et al. [65] is shown with lines indicating 10%, 63% and 90% of failure probability. Inset: Weibull fit of regular specimens. (Adapted from Mueller et al. [412]).....136

Figure 4.11 Occurrence of different types of surface defects and necks on eutectic silicon plate-like particles extracted from heat-treated Al-12.6Si.137

Figure 4.12 (a) Eutectic silicon particle extracted from the Al-12.6Si alloy. (b) Image during the process of producing a TEM lamella out of the particle using FIB. Note that a protective layer of carbon was deposited on top of the particle. (c) SEM image of the prepared TEM lamella. The red rectangle indicates the area at the particle-carbon layer interface that is imaged in Figure 4.13.....139

Figure 4.13 Bright field TEM image and EDS element maps of the area in the red rectangle in Figure 4.12c. The thickness of the oxygen-containing layer is found to be about 30 nm.139

Figure 4.14 Microstructure of the alloy A356 heat-treated 6 hours at 540 °C used in this work. (a) Optical micrograph of a polished section. (b-c) SEM images showing silicon particles exposed after a deep-etching procedure. (Reproduced from Mueller et al. [413])141

Figure 4.15 C-shape test of a nanocrystalline alumina fibre exposed by deep-etching from a composite wire, itself shown in lower magnification in Figure 3.4. The fibre ready to be tested is shown in (a). Mechanical testing is conducted within a nanoindentation apparatus (in air), by loading the fibre tip up to fracture with a diamond flat punch. The interpretation scheme uses the load—displacement measurement and bespoke finite element model of the tested fibre section to compute the stress field at fracture, shown in (b), from which a measurement of local strength within the ligament material can be extracted. (Figure adapted from Ref. [411])142

Figure 4.16 Sample fabrication procedure (Specimen #10 in Figure 4.24). (a) Original silicon particle. (b) Sketch of the FIB milling process used to produce a C-shaped specimen out of the silicon particle (side and perspective views). (c) Resulting C-shaped particle ready to be tested. A surface pinhole defect is indicated with red arrows; note that it is located along a surface that is unaffected by the FIB and that it is stressed in tension upon the subsequent micromechanical test. (Reproduced from Mueller et al. [413])143

Figure 4.17 Testing procedure (Specimen #10 in Figure 4.24). (a) Sketch of the in-situ micromechanical test (side and perspective views). (b) The C-shaped particle of Figure 4.16 and the instrumented tungsten tip before testing. (c) Last frame before fracture during testing. (d) Fractured particle after testing. (e) Fractography of the particle showing the surface defect that originated fracture (red arrow). (Reproduced from Mueller et al. [413]).....144

Figure 4.18 A step-by-step example of the methodology used in this work to probe the strength of individual silicon particles of the alloy (Specimen #7 in Figure 4.24). (a) The original silicon particle from a perspective view. (b) Same particle after shaping using FIB milling, ready to be tested. (c) Last frame of the video recorded upon mechanical testing, immediately before particle fracture. (d) Fractography of the sample. (e) Linear elastic finite element modelling results of the deformed particle. (f) Superimposed SEM images and results of the FE model of the particle before the test (undeformed) and at the critical moment (deformed). (Reproduced from Mueller et al. [413]).....146

Figure 4.19 A second step-by-step example of the methodology used in this work (Specimen #1 in Figure 4.24). (a) The original silicon particle from a perspective view (and from a top view in the inset). (b) The particle ready to be tested. (c) Last frame before particle fracture. (d) Fractured particle. (e-f) Finite element modelling results of the deformed particle. (g) Superimposed SEM images and the shapes resulting from the FE model. (Reproduced from Mueller et al. [413]).....146

Figure 4.20 (a) A particle (Specimen #14 in Figure 4.24) featuring an interface that could be readily probed (no FIB-milling was required to prepare this sample). (b) The particle right after fracture. (c) Close-up, from a tilted angle, of the point of fracture, situated at a grooved silicon-silicon interface.....147

Figure 4.21 A representative selection of the particles tested in this work (each specimen is identified with a number, #nn, which is used correspondingly in Figure 4.24). In each subfigure (a-i), the undeformed and the deformed (just before fracture) images of each particle are superimposed. The corresponding shapes extracted from the finite element model (FEM) are also superimposed in blue and red, respectively –except for specimen (h), as this was only analysed using simple beam theory–. The fracture surface of each particle is shown as an inset in a white frame. The scale bar is 1 μm . Particles in (c-i) feature various surface defects that naturally occur in silicon particles within the alloy. On the other hand, no defect could be distinguished on the tensile surface of particle (a). The specimen in (b) was prepared deliberately such as to probe the strength of a surface milled with the FIB. (Reproduced from Mueller et al. [413]).....148

Figure 4.22 An alternative, simple, way to estimate the specimen fracture stress is based on curvature measurements (Equation 4-4), here exemplified with Specimen #1 (a1—a2) and with Specimen #2 (b1—b4). The location of maximum stress in Specimen #2 is indicated in green (b1—b2); to account for the initial curvature (of the stress-free particle), first a stress was computed using Equation 4-4 with ρ being the initial curvature (measured in b1), which was then subtracted from the stress computed with ρ being the critical curvature (measured in b2). Nevertheless, as seen in b3—b4, the specimen fractured in a location of lower stress (a critical defect could not be identified, though): the critical stress at that location was estimated from the curvature measurement indicated in purple. The radii of curvature indicated in the images are in nm. Results are tabulated in.....149

Figure 4.23 Test on a particle (Specimen #4 in Figure 4.24) featuring a FIB-milled tensile surface (the particle before and after preparation is shown in (a) and (b), respectively). Image (g) is the moment before catastrophic failure. The fractured particle is shown in (h). Note that the load application point and the deflection of the ligament change substantially throughout the test (c)—(g). The interpretation approach based on FEM used in this Section nevertheless captures well the particle deformation; this is shown in (i), where the initial and critical shapes

extracted from the FEM calculations are superimposed to the experimental SEM images.	150
Figure 4.24 Measured strength of individual silicon particles (Specimens #1—#15), which are classified according to the type of feature on their probed surface (see examples in Figure 4.21 and data in.....	151
Figure 4.25 (a)—(f) A sample that twisted before catastrophic failure, rendering the test invalid. Note the slight shift of the tungsten needle towards the back between (c) and (d).	153
Figure 4.26 SEM images of silicon particles from an Al-12.6 %Si alloy (a1–a2) and from alloy A356 (b1–b2) exposed by selectively dissolving the aluminium matrix of the alloys in either the as-cast or heat-treated conditions. Several defects on the particles are observable (see main text); among them pinholes are indicated with white arrows. (Reproduced from Mueller et al. [414]).....	159
Figure 4.27 Fractured silicon particles from Al-12.6 %Si and alloy A356, in the as-cast and heat-treated conditions. The alloy samples were deformed in tension, followed by aluminium selective etching to expose the silicon particles for subsequent examination in the SEM. Surface pinholes (or similar surface defects) and internal cavities along fracture surfaces are indicated with white arrows. In the insets, a lower magnification image of the fractured particle is shown. In most particles, the fracture origin can be identified and is found to be a stress-concentrating defect on the silicon particles: pinholes in (a), (b), (c), (d) and (h), a shallow-groove linked to a twin boundary in (e) and deep grooved interfaces in (f) and (i). (Reproduced from Mueller et al. [414]).....	160
Figure 4.28 SEM images obtained from cross sections of silicon particles embedded within the primary aluminium phase, produced by FIB milling. The alloy is Al-12.6 %Si. Images (a2) and (b2) are close-ups of the area indicated in (a1) and (b1), respectively, which correspond to pinholes on the surface of the silicon particles. EDX spectra (a3) and (b3) correspond to the intermetallic particles indicated with an arrow on images (a2) and (b2), respectively. In images (b1) and (b2), a burr-like ridge on the silicon surface can also be observed. (Reproduced from Mueller et al. [414]).....	164
Figure 4.29 (a)–(c) SEM images of silicon particles within the aluminium–silicon alloys obtained from cross sections produced by FIB milling. (a1) and (b1) show an intermetallic particle inside silicon and in a surface feature, respectively, in a A356 heat-treated alloy. (a2) and (b2) are the EDX spectra corresponding the intermetallic particles indicated with an arrow in (a1) and (b1), respectively. (c) Cross section of a silicon particle within aluminium showing the presence of irregular (eutectic) Fe-rich intermetallic phase in the as-cast Al-12.6 %Si alloy. (d) SEM image of a silicon particle extracted by deep-etching from the as-cast A356 alloy showing irregular (eutectic) Fe-rich intermetallic phase on its surface and in a shallow pinhole defect. (Reproduced from Mueller et al. [414]).....	164
Figure 4.30 (a)–(f) Successive cross sections produced by FIB milling of a silicon particle within aluminium, imaged using the SEM. The white arrows indicate a groove-/step-like interface; here, no intermetallic particle became apparent. (Reproduced from Mueller et al. [414]).....	165

List of Tables

Table 3-1 Experimental conditions (the FIB current used to machine the notch i_{FIB}^{notch} and the loading rate \dot{P}), sample dimensions (W to S_S , as defined in Figure 3.1 and Figure 3.3), indentation-corrected test stiffness (ICTS), stiffness calculated from the model (FEM), parameters obtained via compliance calibration (\tilde{a}_c and $F_V(\tilde{a}_c)$), measured critical load P_C and calculated fracture toughness K_{Ivb} (Equation 3-4) for fused quartz chevron-notched microscopic samples. (Reproduced from Mueller et al. [380]).....	87
Table 3-2 Experimental conditions (the FIB current used to machine the notch i_{FIB}^{notch} and the loading rate \dot{P}), sample dimensions (W to W_S , as defined in Figure 3.1 and Figure 3.5), parameters obtained via compliance calibration (S_S to $F_V(\tilde{a}_c)$), measured critical load P_C and calculated fracture toughness K_{Ivb} (Equation 3-4) for nanocrystalline alumina chevron-notched microscopic samples. (Reproduced from Mueller et al. [380]).....	88
Table 3-3 Fracture toughness values of vitreous SiO ₂ (fused quartz and fused silica) reported in the literature. Quoted references are Refs. [185,396–401]. (Reproduced from Mueller et al. [380]).....	93
Table 3-4 Sensitivity of the fracture toughness values on sample dimensional parameters investigated for fused quartz sample Q3. (Reproduced from Mueller et al. [380]).....	94
Table 3-5 Geometrical dimensions (as defined in Figure 3.10), experimental loading rates \dot{P} , critical (peak) loads P_C , minimum of the geometrical function $F_V(\tilde{a}_c)$ at normalized critical crack length \tilde{a}_c and calculated fracture toughness K_{Ivb} for triangular chevron-notched micro-cantilevers prepared from fused quartz. (Reproduced from Zagar et al. [381])	97
Table 3-6 Geometrical parameters of straight-through (S1—S4) and chevron (C1—C3) notched cantilevers, as defined in Figure 3.15. (Reproduced from Mueller et al. [382])	106
Table 3-7 Experimentally measured fracture load P_C and compliance C_e , and calculated model compliance C_m , geometrical function g_F , critical released elastic energy rate G_C and fracture toughness K_{Ic} for micro-cantilevers having straight-through notch. (Reproduced from Mueller et al. [382]).....	110
Table 4-1 Dimensions (S to α), experimentally measured force at fracture (F_{max}) and calculated flexural strength by Simple Beam Theory (σ_{SBT}) and by Finite Element analysis (σ_{FE}) of microscopic three-point bending tests of plate-like eutectic silicon particles extracted from the Al-Si alloy. Specimens marked with (*) are ones that probe particles containing visible flaws. (Reproduced from Mueller et al. [412]).....	136
Table 4-2 Data from the eutectic silicon particles probed in this work. Columns 1 and 2 indicate the specimen ID# and the characteristics of the surface probed in tension. Dimensions of the particle sections subjected to the highest deformations (i.e. the ligaments) are indicated in columns 3 through 5. Column 6 indicates if the surface probed in tension (i.e. the outermost surface of the ligament) was considered flat or curved in the bespoke 3D finite element models	

(FEM). Columns 7 and 8 indicate results from the FEM and columns 9 and 10 indicate results from curvature measurements (Equation 4-4 in the main text).....	152
Table 4-3 Chemical composition in wt.% of the alloys used in this work for FIB-tomography and EDX examination. (Reproduced from Mueller et al. [414])	162
Table 4-4 Chemical composition in ppm of the 5N6 aluminium used, together with high-purity silicon, to produce the high-purity Al-12.6 %Si alloy. (Reproduced from Mueller et al. [414])	162

List of Equations

Equation 2-1	55
Equation 2-2	55
Equation 2-3	61
Equation 2-4	64
Equation 3-1	82
Equation 3-2	82
Equation 3-3	82
Equation 3-4	83
Equation 3-5	97
Equation 3-6	104
Equation 3-7	105
Equation 4-1	133
Equation 4-2	134
Equation 4-3	134
Equation 4-4	145

Chapter 1 Introduction

The basic paradigm of materials science is the study of the relations between composition, processing, microstructure and property of materials. Namely, the composition and processing of a material dictate its microstructure, which, in turn, governs its properties and performance. Broadly, the focus of this thesis is on the mechanical properties of heterogeneous materials that have a microstructure composed of a hard, brittle, phase (also called “second phase” or “reinforcing phase” throughout this work) embedded in a relatively soft and ductile metallic matrix. Aluminium casting alloys, many steels and metal matrix composites are important examples of such multiphase materials. The link between the local (microscopic) properties of the individual phases together with their interaction, and the bulk (macroscopic) properties of the material constitute a classic micromechanics problem of which this work tackles one particular aspect, namely the detailed characterization of the brittle phase. Contrary to the vast majority of research efforts in the past, here the challenge is taken up from a local perspective: micromechanical testing methods are here developed and applied to probe individual reinforcing particles. Specifically, the object of study in this thesis are the silicon particles that constitute the main second phase in a very important class of alloys: the Al-Si-based casting alloys.

1.1 Background and motivation

On average, a modern European car is composed of 140 kg of several aluminium alloys [1]. In some high-end models, the value reaches 550 kg. The use of aluminium in the automotive industry, typically to replace more dense materials such as cast iron and steel, has been steadily increasing since the 1970's and at a significant rate since the 1990's [1–3] (Figure 1.1 left). This trend is expected to persist, largely motivated by the need to enhance fuel efficiency and therefore reduce the weight of vehicles to comply with greenhouse-gas emission standards established by different countries in the world (see Figure 1.2). According to different estimations, a 100 kg savings in the weight of a car spares the production of 3 to 13 g/km of CO₂ [1]. In turn, more than half of the aluminium used in modern cars corresponds to aluminium castings (items marked with an asterisk in Figure 1.1 right), while the rest are wrought aluminium products. Important examples of parts that are increasingly being made of aluminium casting alloys are engine blocks, wheels, pistons, cylinder heads, transmission cases, other various housings and heat exchangers (Figure 1.3 shows some examples). Furthermore, aluminium castings are not exclusively consumed by the automotive industry, but also by the aerospace industry, shipbuilding, railroad, defense, electronics, electrical and nuclear industries. Altogether, aluminium shaped castings account for roughly 25% of the aluminium produced in the world [4–7].

In turn, more than 90% of aluminium castings are made of alloys having silicon as the main alloying element, typically in the range 4 – 22 wt.% [4]. Note, incidentally, that silicon and aluminium are, respectively, the second and third most abundant elements in the Earth's crust [8]. The reason why silicon is so popular among aluminium castings is because of its great positive effects on alloy castability, i.e. a technological property that can be defined as the material's ability to produce sound, quality shape castings. Good castability encompasses properties such as high liquid fluidity (or mould-filling capability),

resistance to hot cracking or tearing (cracks that appear above the solidus temperature due to solidification shrinkage and thermally-induced deformation), resistance to the formation of shrinkage porosity and to macrosegregation [9,4,10]. Silicon also reduces the thermal expansion coefficient and lowers slightly the density of aluminium alloys. Moreover, of the greatest interest to the present work, silicon plays a key role in the solidification and microstructural development of Al-Si-based alloys, which have direct consequences on the alloys' mechanical properties.

Because of its very low solubility in α -aluminium, Si in these alloys is mostly present as a (brittle) second phase within the α -aluminium matrix. Under certain conditions, the silicon phase is in the form of a network of interconnected crystals within the eutectic, whereas under other conditions –notably after a heat treatment–, it takes the form of isolated particles. There is a particular feature about the silicon particles that motivates this thesis: in most Al-Si-based alloys, the fracture of silicon particles plays a key role among the various factors that determine the alloy's deformation and fracture properties [11–26]. Silicon particles, which are stiffer than the plastically deformable aluminium matrix, take a disproportionate portion of the applied stress when these alloys are deformed, in both elastic and elastoplastic deformation regimes. It is then observed that the particles start fracturing gradually, essentially as soon as the alloy starts to deform plastically (note that interfacial decohesion particle-matrix is generally much less relevant because the interfaces are strong in these alloys [27], except in particular cases [11,28,19,29,30]). As the number of fractured particles increases, nucleated microcracks start to grow, and then link by tearing the aluminium matrix that connects fractured silicon particles. The coalescence of such microcracks produces macrocracks that can drive final fracture of the material, see Figure 1.4. As seen, early stages of damage are typically found to be dominated by the fracture of silicon particles. Yet, little is known of the intrinsic fracture properties of Si particles within aluminium. For example, the fundamental question of what the (local) strength of the silicon particles is does not have yet a firm answer. Also, barely anything is known about their fracture toughness. This thesis aims to tackle those questions.

In part, the problem received little attention for many years because the optimization of casting aluminium alloys has traditionally been driven by the need to enhance castability. The reason is that, due to highly imperfect casting processes and practices, key mechanical properties such as fatigue resistance and ductility were dominated by the extensive casting defects present in the cast parts (shrinkage and gas porosity, hot cracks and other entraining defects) rather than by intrinsic aspects of the microstructure [31–34]. Eventually, with the progressive development of new and improved production techniques the quality of cast parts increased significantly and, hence, it became more relevant to consider the influence of microstructural features such as the eutectic microconstituent characteristics, silicon particle properties or the matrix hardening condition on global mechanical properties of Al-Si casting alloys.

The main reason why the strength and toughness of the silicon phase in Al-Si alloys remains largely unexplored is that silicon particles in Al-Si alloys are both microscopic and irregular in shape, which have long been major impediments to probing them mechanically. By far, thus, the main approach to characterize their property has been based on estimating their strength (or strength distribution) indirectly from measured macroscopic alloy properties. A classical methodology consists in relating the estimated (average) stress in the silicon phase to the fraction of broken particles, itself measured along polished sections of the probed material, at varying levels of macroscopic strain. To estimate the stress in the silicon particles different strategies have been implemented, such as micromechanical modelling, which rests on idealizations of the microstructure (in particular the particle's shape, size and distribution) and of the load transfer mechanics [35–38], or neutron and X-ray synchrotron diffraction [39,40],

which sample the average second phase strain in a finite volume of material containing a large number of particles.

Such studies have driven significant progress in the understanding of microstructure-property relations of several of these alloys; however, because they are indirect assessments of averaged property of the silicon phase, those methods prevent gaining a deep insight into the actual fracture mechanism of individual particles, which is essential to shed light on, for example, the reasons why silicon particles are found in those studies to exhibit strength values in the wide and low range of 0.1 – 3.5 GPa [13,29,39–45], which is well below the theoretical strength of Si, at 17 – 27 GPa [46]. Such a question has indeed been formulated (either explicitly or implicitly) repeatedly in the literature on Al-Si alloys [28,39,40,43,47–51]. This work also aims at identifying underlying reasons why the silicon particles are as weak – or strong – as they are found to be.

The problem presented in the above paragraphs is actually a general one in the field of micromechanics of materials: whereas the ductile phase has received much more attention [36,52–54], little quantitative data exist on the strength or toughness of particulate reinforcements in two-phase ductile-brittle materials in general. Yet, except when interfaces are weak, the properties of the brittle second phase generally control local fracture events, which in turn cause the materials to accumulate internal damage and hence limit both their ductility and their strength. In fact, when second phases (and interfaces) are strong and tough, the material that contains them can be very strong, ductile, and tough (e.g. [35,55]). Approaches (mentioned above) that have been used to study Al-Si alloys have been also applied to other two-phase materials, and so were too other internal damage detection methods, such as synchrotron X-ray microtomography or acoustic emission [56,57]. The alternative approach consisting of testing the microscopic brittle second phases directly is, on the other hand, practically virgin territory.

More broadly, interest in measuring fracture properties of brittle materials at a small scale is found in several areas. For example, in comminution processes, which are widely used in the chemical, material, food, cement and pharmaceutical industries [58], it is known that the weaker the particles are, the easier it is to reduce them into smaller fragments. The opposite, namely stronger particles, are, on the other hand, sought in the case of beads used in catalysts in the oil&gas sector, which are subjected to stresses during their lifetime due to handling and vibrations [59–61]. In those areas, particle crushing between hard platens and particle impact tests are typically used to probe the strength of the particles [59,62,58,63,64]. Conversely, microscopic samples of materials can be probed using microfabrication or micromachining techniques to produce specimens such as bending microbeams or tensile microbars. An area from which many of these techniques have been developed is the Microelectromechanical Systems (MEMS) community. The motivation is that in MEMS, which are typically made of silicon, strength and fracture toughness at small scale are critical factors controlling their reliability [65,66]. The micromechanical testing methods are also of great relevance to the thin films and coatings communities, which are very interested in improving, for example, the fracture toughness of single and multi-layered films to avoid their degradation or debonding [67–69]. Finally, small scale testing is also crucial in the study of heavily irradiated materials used for nuclear applications; in particular for future fusion reactors [70]. In this case, the embrittlement of materials is a major concern; it is investigated using small samples given that, unfortunately, irradiation doses mimicking future in-service conditions can only be achieved in small volumes of material.

In view of the general picture presented above, the research work in this thesis intends to make smart use of technologies that have become increasingly available over the last years (particularly nanoindenters and dual-beam microscopes) to devise, develop and implement micromechanical methods that can

be used to probe the strength and the fracture toughness of the silicon particles that constitute the main second phase of Al-Si-based alloys and play a key role in the mechanical behaviour of these alloys.

As a starting point, a literature review on relevant topics is presented in Chapter 2. Previous work in the field of micromechanics of two-phase brittle-ductile materials, with emphasis on the work done on aluminium casting alloys, is reviewed. Also, micromechanical testing methods that have been applied on small particles or on small volume of materials to measure fracture properties are critically discussed. Then, the two properties on which this research is focused, i.e. fracture toughness and strength, are the subjects of Chapter 3 and Chapter 4, respectively. In Chapter 3, a methodology for measuring the fracture toughness of micron-sized specimens that avoids the main drawbacks of existing testing methods is developed and demonstrated using test-bench materials. The microscopic chevron notch test is then used to study silicon particles and silicon wafers, where unexpected challenges specific to silicon are revealed. In Chapter 4, two novel approaches for probing the local strength of individual reinforcing particles within a metallic matrix are developed and used to measure the strength of the silicon particles in Al-Si-based casting alloys. The particles are shown to be capable of locally sustaining considerably higher stress than what was previously expected. Also, factors that weaken the particles are identified and investigated. Then, to wrap up, Chapter 5 states the general conclusions extracted from the work done in this thesis. Perspectives for future research on the topic are finally discussed in Chapter 6.

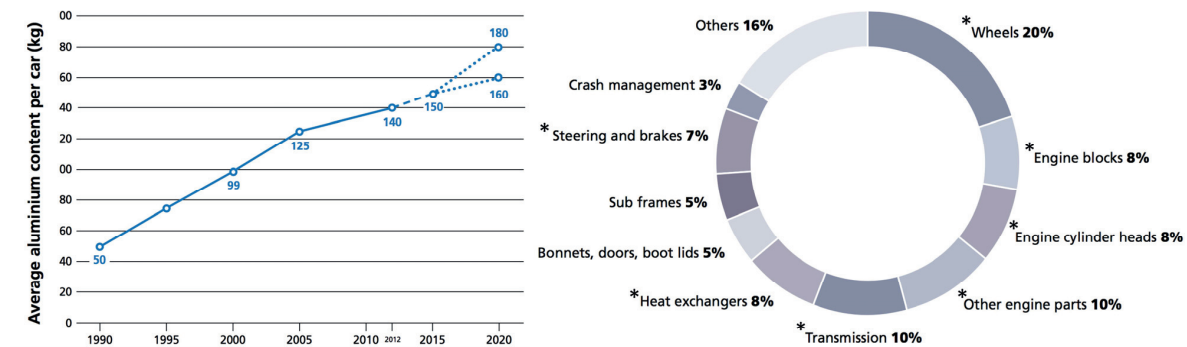


Figure 1.1 Left: Evolution in time (years) of the average aluminium content in cars produced in Europe, revealing a steadily increasing tendency. The data are from 2012; projections are shown until 2020. Right: Distribution of aluminium in European cars. Products marked with an asterisk (*) are largely made of cast aluminium. (Adapted from Ref. [1])

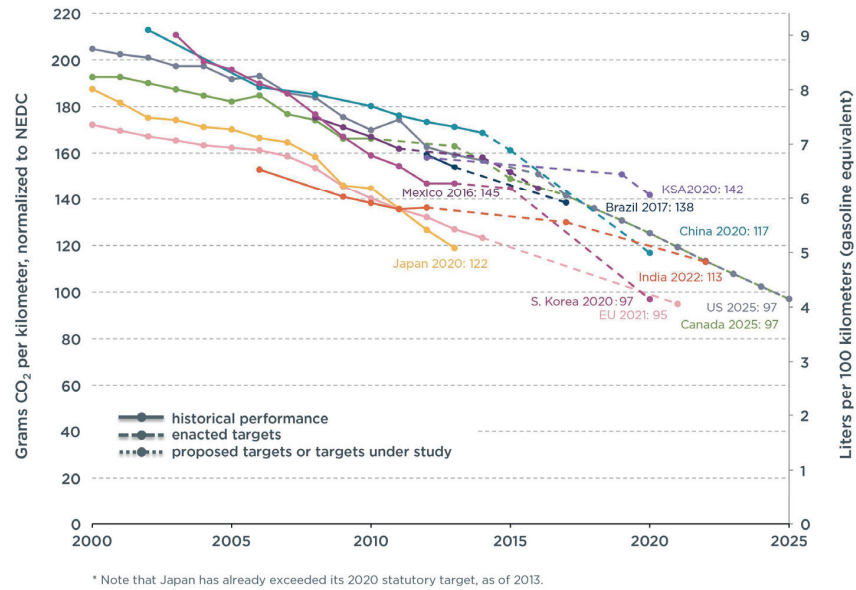


Figure 1.2 Greenhouse-gas emission targets for passenger vehicles across the world. The declining tendency motivates the need for enhanced fuel efficiency, which is partly achieved through substituting high- for low-density materials such as aluminium alloys. Data and figure from Ref. [71], updated in September 2015.

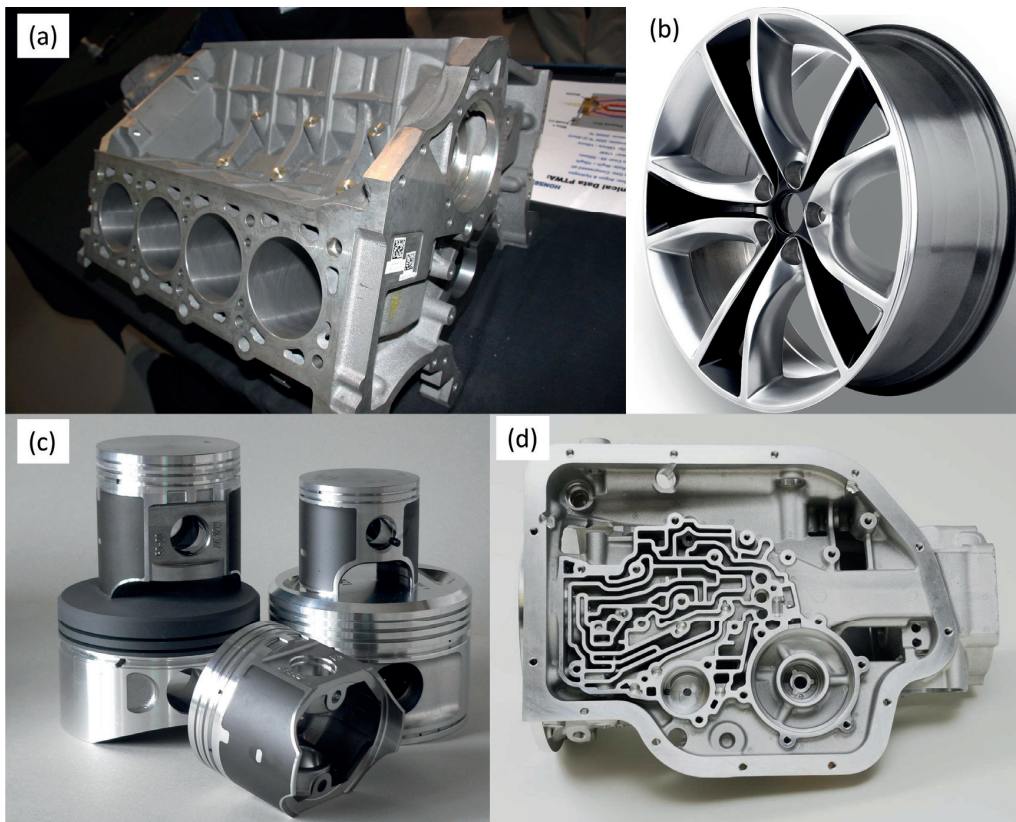


Figure 1.3 Cast aluminium products: (a) an engine block, (b) a wheel, (c) pistons and (d) a transmission case. (Images from Refs. [72–75])

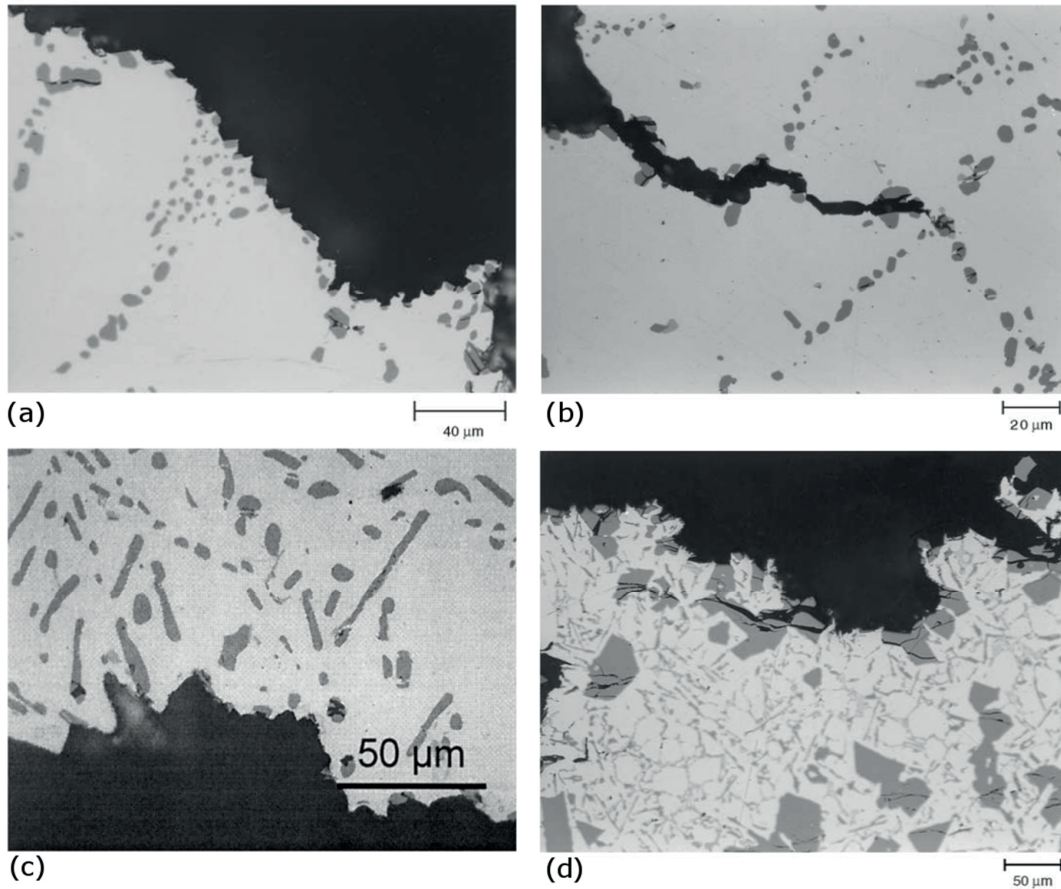


Figure 1.4 Metallographic examination of the fracture surfaces of different Al-Si alloys tested in tension or by impact. As seen, fracture paths follow fractured Si particles (in darker grey). (Images from Refs. [17,76] reproduced with permission of ASM International and Springer)

1.2 Statement of objectives

The objective of this work is two-fold:

- First, to develop micromechanical testing methodologies by which the strength and the fracture toughness of particulate, microscopic, hard reinforcing phases in alloys and metal matrix composites can be directly measured. The methodologies to be developed must be suitable to comply with the second part of the objective, which is
- to investigate the local fracture properties of the main second phase in Al-Si casting alloys, i.e. the microscopic silicon particles within the α -aluminium matrix.

1.3 Thesis's framework and funding

The work in this thesis was done in the framework of a European Research Council project short-labelled “NanoPhaseCrack” awarded to this thesis’s advisor Prof. Andreas Mortensen at EPFL as the Principal Investigator (PI) under the European Union’s Seventh Framework Programme (FP/2007-2013) / ERC Advanced Grant Agreement No. 291085 between May 1 2012 and April 30 2017. Broadly, the project’s objective is to develop micromechanical testing methods and use them to probe the mechanical

properties of hard second phases in alloys and metal matrix composites. The project has been run by a team of five (three PhD students and two post-docs) plus the PI. Accordingly, three PhD theses were or will be produced within this project: (i) the present thesis, focused on silicon in Al-Si alloys, (ii) a thesis by V. Pejchal, focused on alumina reinforcements, and (iii) a thesis by L. Michelet, focused on carbides in steel. The two post-docs in the project were Dr. G. Zagar (involved from the launching of the project) and Dr. M. Fornabaio (who joined at later stages). The two laboratory technicians, R. Charvet and C. Dénéreaz, provided many valuable contributions. Also, briefly involved in the project were Dr. A. Rossoll and Dr. A. Singh.

Chapter 2 Literature Review

This chapter is a review of previous work published in the literature on subjects relevant to the objectives and the context of this thesis. The review starts with an introduction to Al-Si alloys with focus on their microstructure and how silicon particles are formed (Section 2.1). This is followed by Section 2.2, which deals with the core matter of this thesis: fracture properties of silicon particles within Al-Si alloys. Next, the challenge of measuring fracture toughness and strength at small scale is treated in Sections 2.3 and 2.4, respectively. Finally, the state of the art on fracture properties (toughness and strength) of electronic-grade single crystalline silicon is reviewed because this is the obvious reference material to be compared with silicon particles in Al-Si alloys (Section 2.5).

2.1 Microstructure of Al-Si alloys

Due to the extensive importance of Al-Si-based alloys in today's society (see Chapter 1), the literature on engineering/metallurgical aspects of Al-Si alloys is vast and comprises different topics such as mechanical and physical properties, applications, recycling, alloy selection, the effect of alloying elements, casting processes, melt treatments, heat treatments, etc. Examples of general reviews and text books that deal with many of those topics are Refs. [4,9,17,77–81]. The scope of this Section is limited to the most important aspects related to these alloys' microstructures, which will hopefully provide an adequate background to the following Section 2.2, where micromechanics and silicon particle strength of Al-Si-based alloys are described.

Al and Si form a simple eutectic system, with the eutectic point situated at 577 °C and 12.6 wt.% Si in the equilibrium phase diagram (Figure 2.1) [82]. This gives rise to the subdivision of these alloys into three groups according to their Si content: hypoeutectic (roughly 4 - 12 wt.% Si), eutectic (about 12.6 wt.% Si) and hypereutectic alloys (roughly 13 – 30 wt.% Si). The microstructure of hypoeutectic Al-Si alloys consists in rounded primary α -Al dendrites and the eutectic microconstituent in between dendrite arms, which is formed by eutectic α -Al and faceted eutectic Si particles (Figure 2.1b). Hypoeutectic alloys are typically used when a good compromise between castability, alloy ductility and tensile strength is sought. With increasing Si content in the alloy, the proportion of eutectic increases. The closer to the eutectic the composition is, the better is the castability at the expense of alloy ductility. At the eutectic composition, the microstructure is mostly composed of the eutectic, although primary Si and primary α -Al may also be present (Figure 2.1c). In fact, primary Si particles can be found even in hypoeutectic alloys under certain conditions, a feature that has been attributed to conditions of local enrichment beyond the eutectic composition of Si expelled into the melt from the growing Al dendrites [83]. Finally, hypereutectic compositions are used when the key requirement is wear resistance. The reason is that these compositions have high hardness because of the large volume fraction of large primary silicon particles within the microstructure (Figure 2.1d).

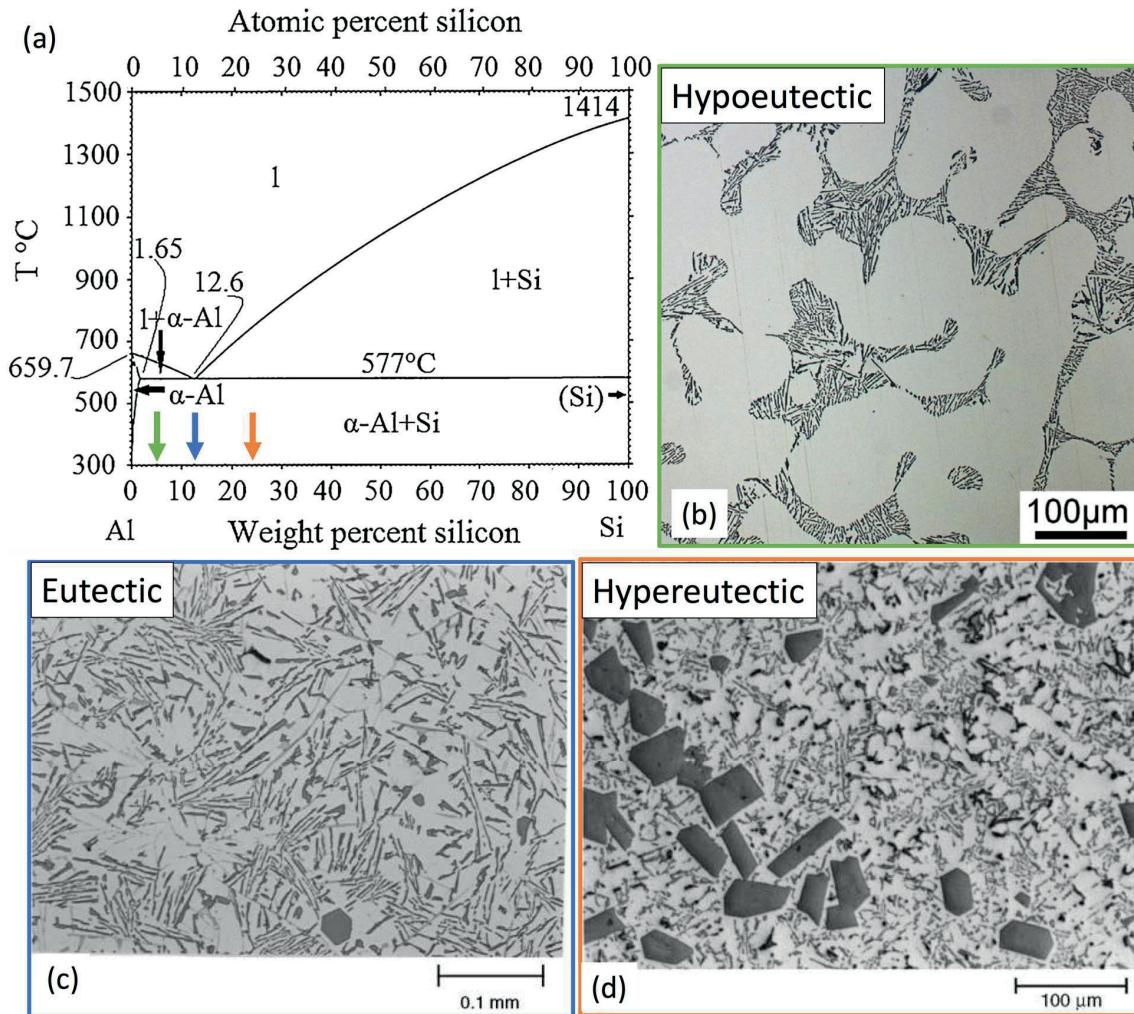


Figure 2.1 (a) Al-Si equilibrium phase diagram. Coloured arrows in the phase diagram indicate compositions of each of the representative microstructure of (b) hypoeutectic, (c) eutectic and (d) hypereutectic Al-Si alloys shown along (Adapted from Refs. [17,84] with permission of ASM International and Elsevier). In the micrographs, silicon particles are dark and aluminium is bright.

As seen, the great majority of silicon in these alloys forms a second phase within the α -Al matrix in the form of particles, whose dimensions, morphologies and degree of interconnectivity can be substantially varied with alloy composition, and with casting, alloying and heat treatment procedures [11,15,18,21,23,42,76,79,85–89]. Day and Hellaway [90], in the late 1960's, carried out a seminal investigation on the microstructures of Al-Si cast alloys. Different forms of silicon in a binary, eutectic, Al-Si alloy were identified as a function of solidification rate and thermal gradient using directional solidification. The region where typical industrial and laboratory practice conditions fall was associated with a dispersion of eutectic silicon particles forming interconnected networks of faceted *plate-like* particles (sometimes called *flakes*) (Figure 2.3a1), which look like faceted rods on a 2D micrograph of a polished sample (Figure 2.2a and Figure 2.1b-c). Salient features noted on the silicon plates were the presence of multiple $\{1\ 1\ 1\}$ twins (Figure 2.4) and that the largest facets are $\{111\}$ planes.

With increasing solidification rate, the Si phase was observed to become finer, ultimately forming an interconnected structure of irregular branched fibres [90] (Figure 2.2b and Figure 2.3b1). This is the

morphology of a *modified* eutectic. Such *modification* of the eutectic silicon morphology comprises altering the regular plate-like morphology into a fine, fibrous, coral-like (also described as "woolly" or "seaweed"), network of silicon crystals. Modification may be induced not only by a high cooling rate (this is called *chill* or *quench* modification), but also by the addition of certain elements (*chemical* modification), notably Sr or Na in very low concentrations. These fibrous silicon crystals have also been shown to be (heavily) twinned [91]. Modification is of considerable technological interest because it has a positive impact on alloy ductility. Namely, non-modified Al-Si alloys featuring plate-like silicon particles typically show elongations of no more than a few percent together with primarily brittle fracture surfaces (fracture progresses through the silicon particles, as discussed in the next Section), whereas modified alloys present significantly increased elongation and more ductile fracture surfaces featuring dimples [92].

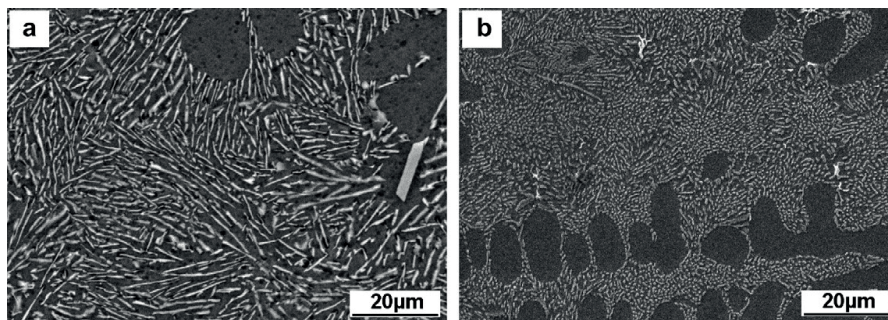


Figure 2.2 SEM images of the microstructure of a near-eutectic, binary, Al-Si alloy (a) non-modified and (b) Sr-modified. Silicon particles are bright, while the aluminium phase is dark. (Reproduced from Ref. [93] with permission of Elsevier)

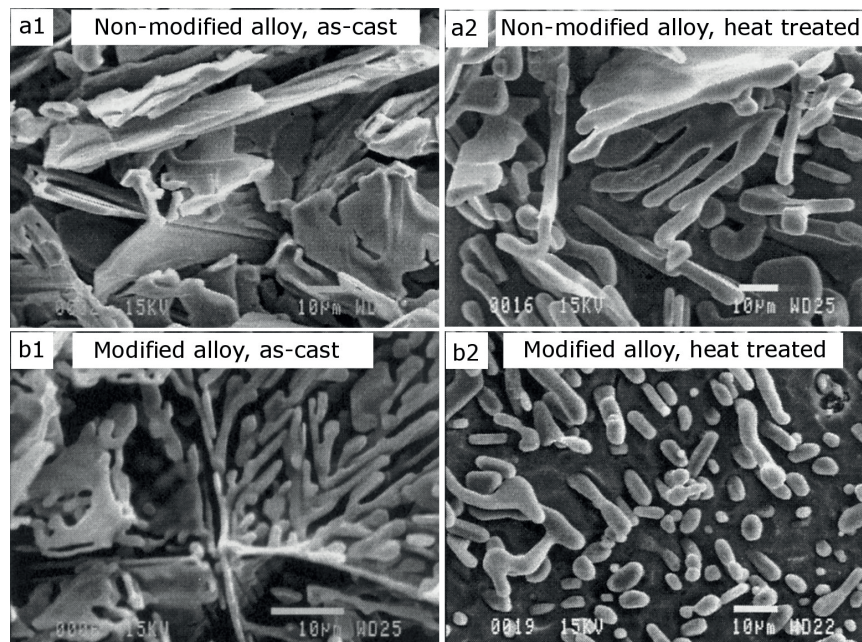


Figure 2.3 Silicon particles within the microstructure of a Al-11Si-0.6Mg alloy exposed by deep-etching the aluminium matrix using a two-step etching procedure consisting in first immersing the sample in a mixture of HCl and HF, and then in HNO_3 solution. Eutectic particles in non-modified alloys are typically plate-like (a1-a2). (Figure adapted from Ref. [76] with permission of Springer)

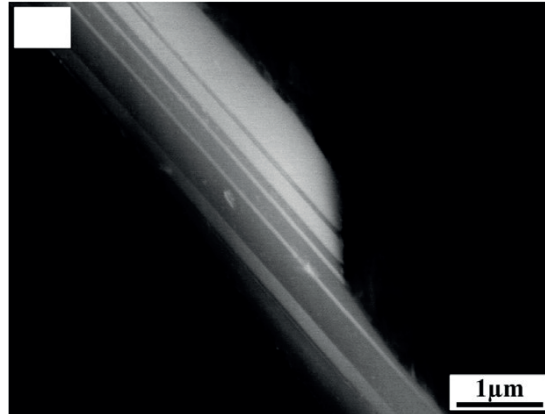


Figure 2.4 Twins in a silicon plate-like particle parallel to the large $\{111\}$ facets observed in the SEM using Back Scattered Electrons. (Adapted from Ref. [94] with permission of Elsevier)

Primary Si particles can take many different shapes depending on conditions such as composition and cooling rate. In studies of the growth of primary Si in Al-Si alloys, Wang et al. [95,96] conclude that the most frequent morphologies of primary Si are $\{111\}$ faceted octahedral crystals and related spinel-type variants (Figure 2.5, Figure 2.6 and Figure 2.7). These have also received other names in the literature, such as "massive", "polyhedral", "polygonal", "geometric", "faceted globular", "angular" or "blocky". Other, less common, primary Si shapes are star-like, dendritic-like, plate-like or skeletal-complex crystals [95–97].

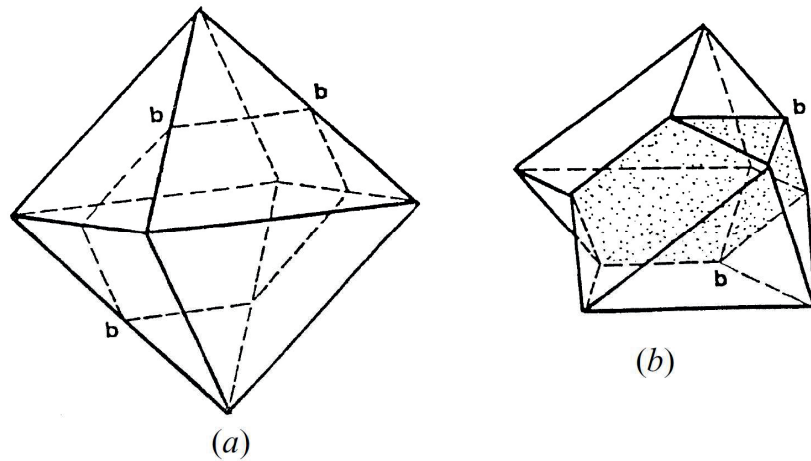


Figure 2.5 (a) Octahedron crystal bounded by $\{111\}$ facets. (b) Spinel-type crystal bounded by $\{111\}$ facets resulting from twinning the octahedron along the (111) plane labelled bbb . The twin plane is shaded in (b). (Figure from Ref. [96] with permission of Springer)

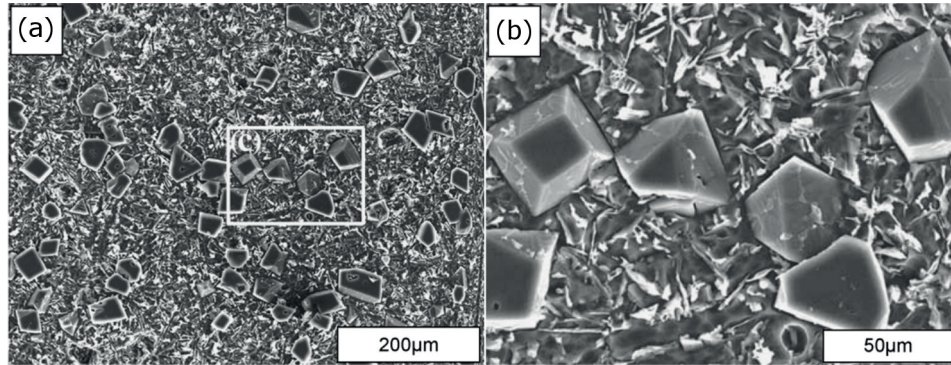


Figure 2.6 SEM micrographs of a deep-etched Al-20Si alloy, showing the morphology of primary silicon particles. The area indicated with a white square in (a) is magnified in (b). (Adapted from Ref. [98] with permission of Elsevier)

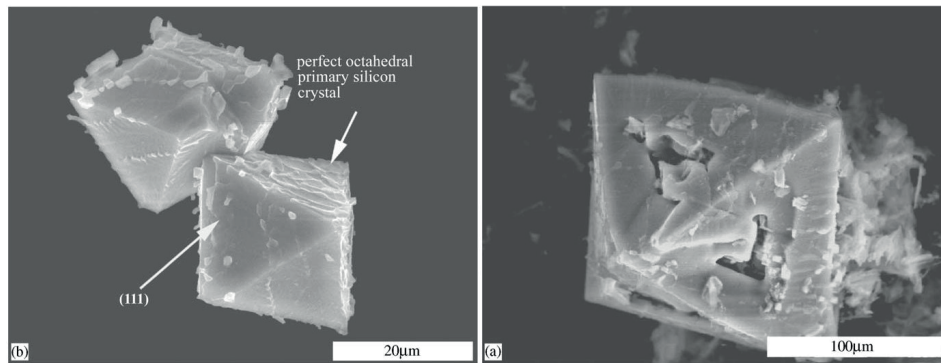


Figure 2.7 Primary silicon particles extracted from an Al-20Si alloy. In the left image, the top particle has a spinel-type morphology, while the bottom particle is a perfect octahedron. The image in the right shows an imperfect, *hopper*-like (*i.e.*, with centrally hollowed facets), octahedral silicon particle. (Figure adapted from Ref. [99] with permission of Elsevier)

Silicon particles in Al-Si alloys originate and take their shapes by mechanisms of nucleation, growth, and coarsening. Before introducing those mechanisms, some general observations are worth recalling. The crystalline structure of silicon is diamond-cubic, where the closest-packed and lowest surface energy planes are the $\{111\}$ planes. It is well-known that silicon particles have a strong tendency to be highly faceted, bounded by $\{111\}$ planes [90,94,95,97,100–103]. A straightforward example of this are the plate-like silicon particles, whose large flat facets are $\{111\}$ planes [94,100,104–106]. Another example are the octahedral primary silicon particles [83,98,99]. It is also well-established that plate-like particles feature several $\{111\}$ twins parallel to their large facets [94,105]; these, as will be seen, play a key role in their growth. Nucleation and growth mechanisms of silicon particles are subjects that have received significant attention over many years (coarsening mechanisms, on the other hand, have been less investigated). Yet, as will be seen next, there is still considerable debate about the specific mechanisms involved.

It is often considered that the most potent nucleant of Si in Al-Si alloys is aluminium phosphide (AlP). The two have the same arrangement of atoms: Si has a diamond cubic structure whereas AlP has a zincblende structure, which is like a diamond cubic structure but with alternating atom types along $\{111\}$ planes. They also have similar lattice parameters: 5.421 Å and 5.431 Å in the case of AlP and Si,

respectively [107]. Thus, Si can easily nucleate heterogeneously with a cube-cube orientation relationship on AlP. Evidence of AlP particles within primary and eutectic Si particles has been extracted based on techniques such as X-ray Energy Dispersive Spectroscopy (EDS), or TEM with lamellas produced into particles with the FIB [107,108], e.g., Figure 2.8.

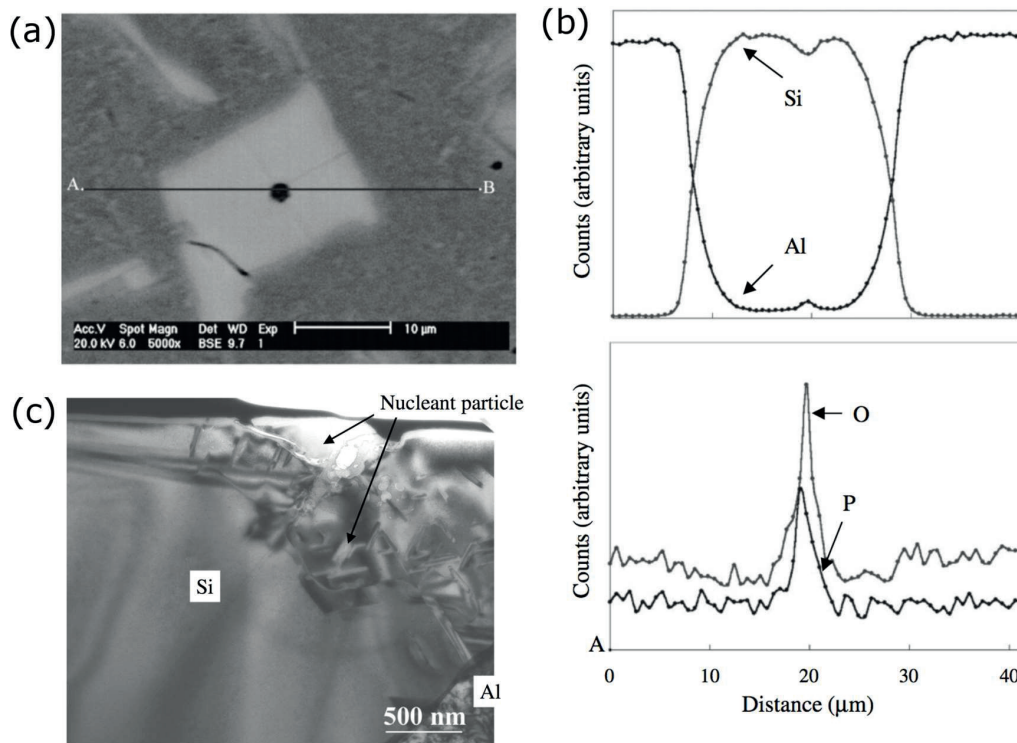


Figure 2.8 Observation of a AlP as the possible nucleant of a Si particle; figure adapted from Ref. [108] with permission of Oxford University Press. The EDS results of a line scan on the particle in (a) are shown in (b). Note that the presence of O in the EDS results is an artefact introduced upon metallographic sample preparation. A TEM image of a lamella prepared using FIB out of a silicon particle attached to a potential nucleant is shown in (c).

Ho and Cantor [109] (and later others [107,108,110,111]) studied the nucleation of Si using non-modified hypoeutectic Al-Si alloys of varying concentrations of P, present as an impurity. It was observed that the higher the alloy purity, (i) the higher the necessary undercooling to nucleate eutectic silicon particles (Figure 2.9), (ii) the larger the proportion of fine vs. coarse particles, and (iii) the higher the frequency of Si particles with a cube-cube orientation relationship with primary Al. These observations were attributed to the effect of P on AlP and hence Si particle nucleation, as follows. When the concentration of P is high, most P is in the form of solid AlP particles at temperatures above the liquidus, while only a small proportion of P remains in (saturated) solution. When the temperature goes below the liquidus, primary Al dendrites start forming, rejecting P into the interdendritic liquid, while also the solubility of P in the melt decreases. The resulting extra P attaches to the pre-existent AlP particles. Note that in this scenario primary Al and AlP are formed independently and hence without an orientation relationship between the two. Finally, with further decrease of temperature below the eutectic, the AlP particles become sites where Si nucleates at low undercooling (Figure 2.10). Conversely, when the alloy contains little P, there are only few pre-existent AlP particles in the melt that can nucleate Si particles at low undercooling because most of the P is dissolved in the liquid. When the temperature decreases below the liquidus, the primary Al dendrites start to grow and expel the excess of P. In this case, however, in

the absence of AIP particles the P will attach as a layer of P on {111} planes of the Al dendrites that are exposed to the melt. Alternating {111} layers of Al and P result in a small AIP precipitate, which eventually, at a larger undercooling, will act as a heterogeneous nucleation site for Si. Since the Si particle nucleates with a cubic-cubic orientation relationship with AIP, it will, in this case, also be in cubic-cubic orientation with the Al dendrite [109].

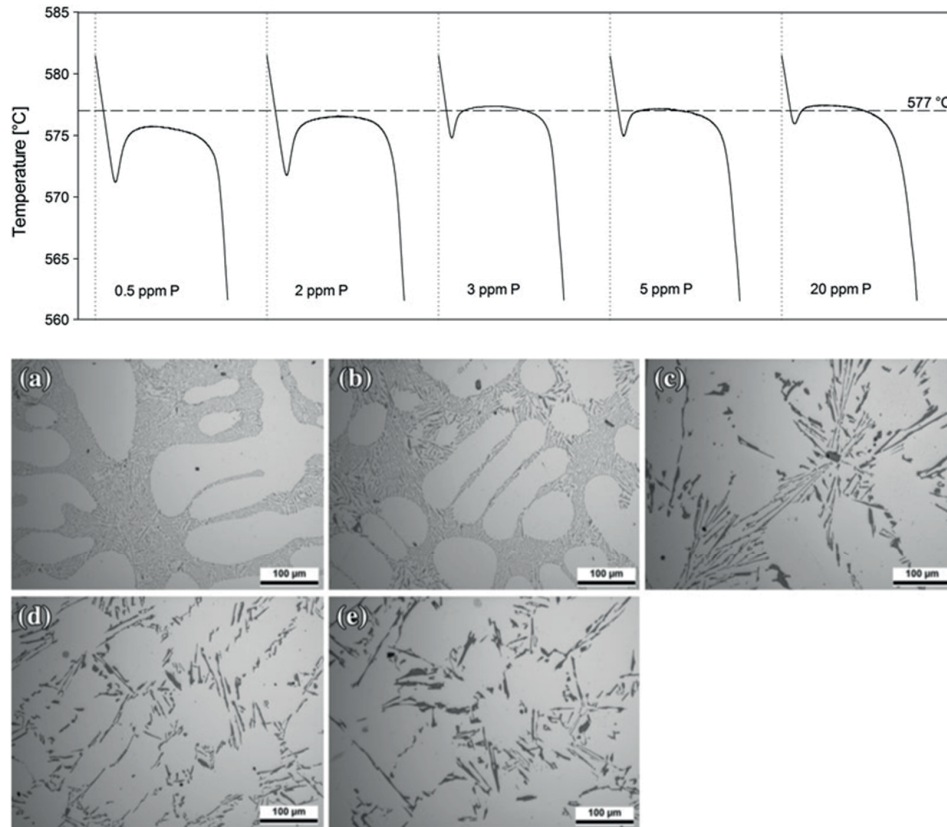


Figure 2.9 The top image shows the part of the cooling curves upon solidification associated with the formation of Al-Si eutectic in alloys having different P concentrations, ranging from 0.5 to 20 ppm. The obtained microstructures are shown below in images (a)-(e), corresponding to alloys having 0.5, 2, 3, 5 and 20 ppm of P, respectively. (Figure adapted from Ref. [107] with permission of Springer)

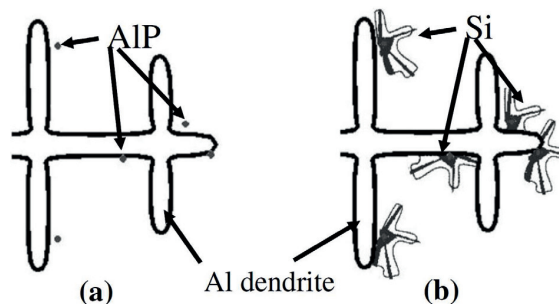


Figure 2.10 A proposed eutectic nucleation mechanism; figure from Ref. [108] with permission of Oxford University Press. (a) Aluminium phosphide segregates to the melt at the interface with a growing dendrite. (b) Segregated AIP particles act as heterogeneous sites onto which eutectic silicon nucleates, starting the formation of eutectic grains.

Besides AlP, other particles have been claimed to nucleate eutectic silicon in non-modified alloys. There is a body of work that sustains that tiny β -(Al-Si-Fe) particles play the most important role. In this sense, Shankar et al. [112] have shown using TEM and elemental mapping that tiny β -(Al-Si-Fe) particles are found attached to many eutectic Si particles (Figure 2.11). Also, a finer microstructure is obtained when the level of Fe as impurity is diminished while keeping the P content constant. The hypothesis of Shankar et al. [112] is that these β -(Al-Si-Fe) particles are produced in front of growing primary Al dendrites where the melt is enriched with expelled Si and Fe. Some eutectic Si then nucleates on those particles, which marks the onset of the eutectic colony growth (Figure 2.12). This work has prompted a heated debate between researchers in the field, particularly with Dahle and Hillert [113–116]. An argument against this hypothesis is that thermodynamic calculations of the solidification sequence in the Al-Si-P-Fe system by Liang and Schmid-Fetzer [117] show that β -(Al-Si-Fe) forms last in the solidification sequence compared to AlP and Si at relevant alloy compositions (e.g. Figure 2.13). Potential kinematic effects are, on the other hand, not discussed in that work. These could be important: Khalifa et al. [118] showed that the β -(Al-Si-Fe) phase can form before Si for kinematic reasons.

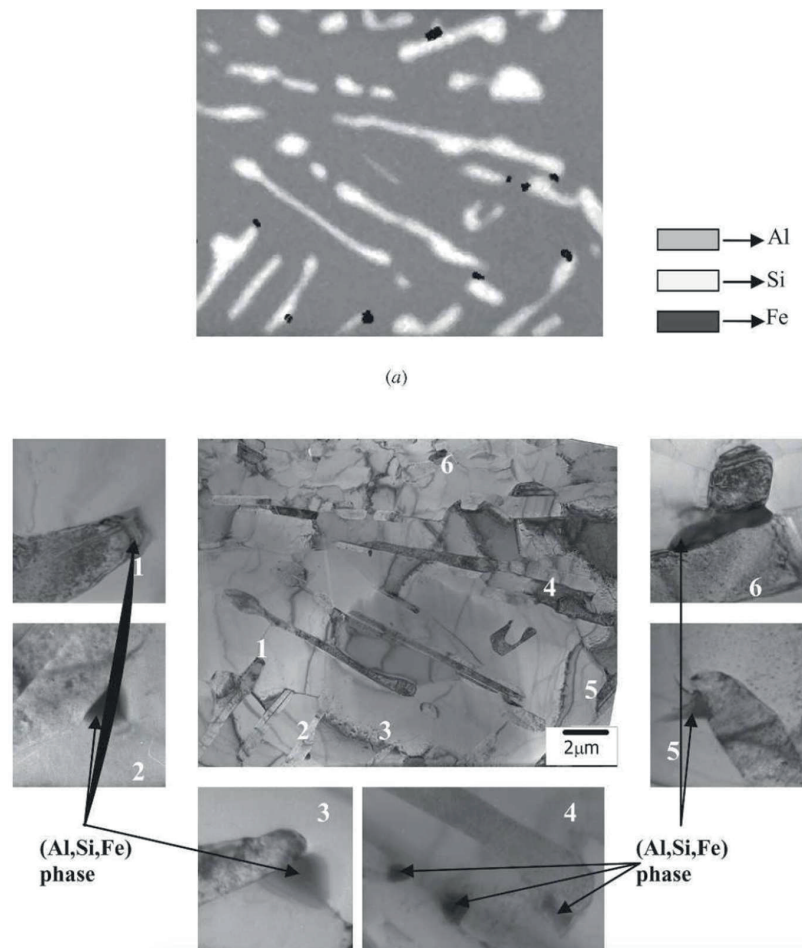


Figure 2.11 Elemental map and bright field TEM images of eutectic Si particles within the Al matrix, where a (Al,Si,Fe) phase is shown in association with Si particles, suggesting, according to Shankar et al. [112], that the Fe-rich phase nucleated the Si particles. (Reproduced from Ref. [112] with permission of Elsevier)

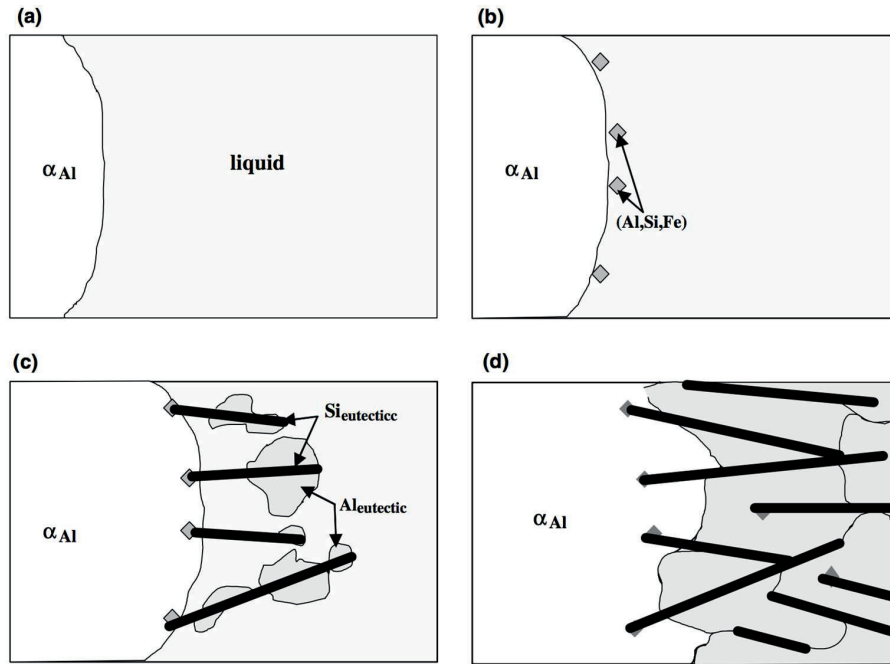


Figure 2.12 A proposed eutectic Si nucleation mechanism; figure reproduced from Ref. [112] with permission of Elsevier. Primary Al dendrites are growing in (a). In (b), β -(Al-Si-Fe) phase nucleates at the solid-melt interface. Then, in (c), eutectic Si nucleates on the Fe-rich phase, followed by nucleation of eutectic Al on the eutectic Si. In (d), eutectic Si can further nucleate within the growing eutectic Al. Eventually, the growth of the solid phases is completed.

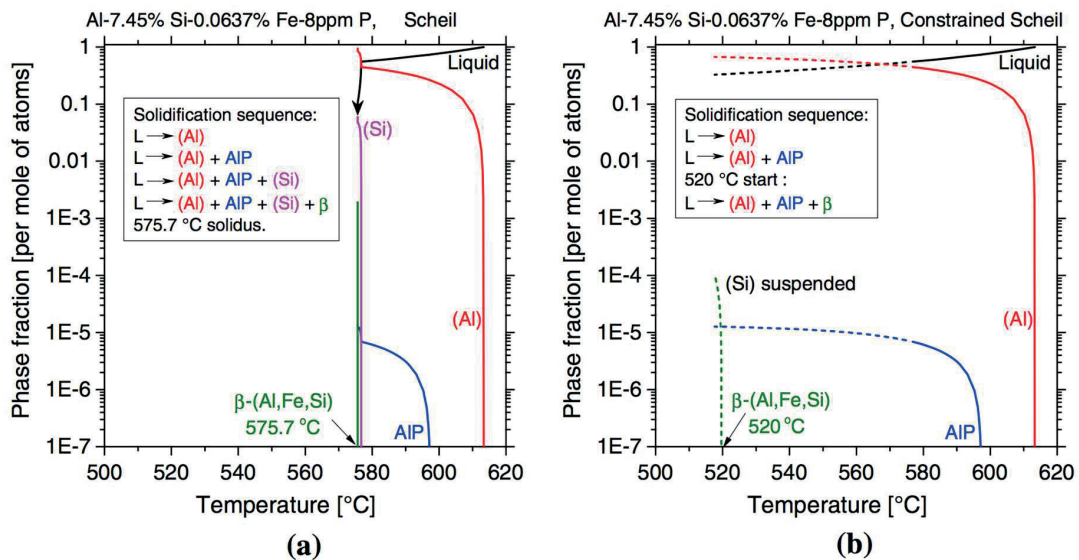


Figure 2.13 Phase fraction as a function of temperature as computed from solidification simulations of a hypoeutectic Al-Si alloy with Fe and P impurities; figure reproduced from Ref. [117] with permission of Springer. In (a), all phases can grow (standard Scheil simulation), while in (b) the formation of (Si) is suspended (constrained Scheil simulation). In either case, AlP is observed to form before the β -(Al-Si-Fe) phase, which, moreover, appears at a significant undercooling if Si does not nucleate earlier elsewhere (as seen in (b)). These results were claimed to disprove the hypothesis that the β -(Al-Si-Fe) phase in the form of tiny particles nucleates eutectic Si.

Moreover, Nafisi et al. [119] proposed that, in addition to the heterogeneous nucleation on impurity particles, the eutectic Si nucleates as dome- or doughnut-shaped Si nuclei. In this view, eutectic Al first nucleates at primary Al dendrites (as was also suggested in Refs. [120,121] for non-modified alloys but contradicts publications where eutectic Si is claimed to nucleate before eutectic Al [101,112]). This then gives rise to local enrichment of Si in the melt in front of growing Al crystals, which, in turn, produces the Si nuclei.

Finally, Campbell [48,122,123] believes that entrained oxide bifilms, which enter into the microstructure during handling and pouring of the melt into the mould (Figure 2.14 left), are the second best nucleants (after AlP) for both primary and eutectic Si. This would explain the observation of long central cracks along large and elongated Si and β -(Al-Si-Fe) particles (Figure 2.14 right). Sigworth [124], however, notes that supporting evidence of bifilms being the substrate for Si nucleation is limited to few observations of bifilms inside particles in non-modified Al-Si alloys.

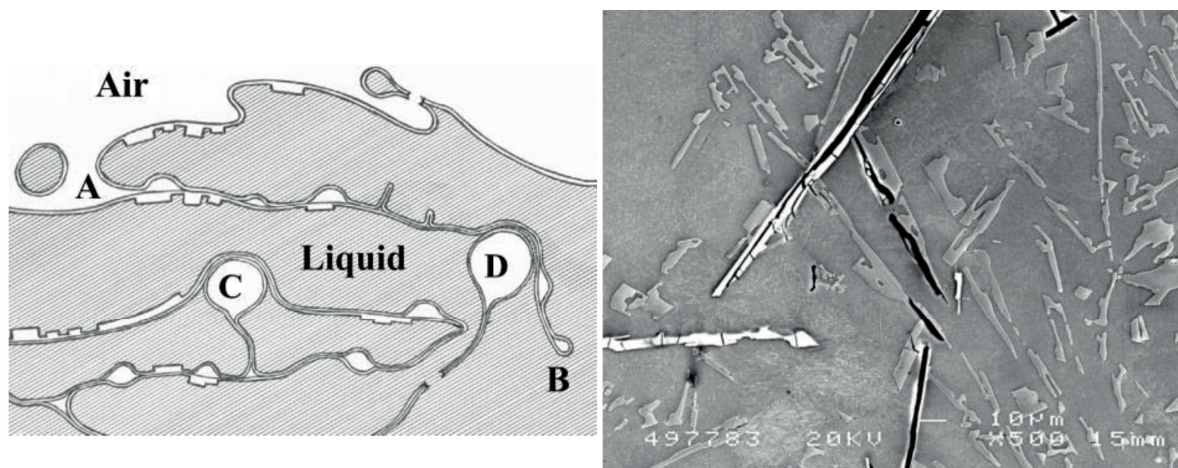


Figure 2.14 (a) Representation of turbulence at the surface of molten metal causing the entrainment of oxide bifilms and bubbles during manipulation and pouring into the mould. (b) Long central cracks in elongated β -(Al-Si-Fe) and Si particles, claimed to be consistent with the hypothesis that those particles have nucleated on entrained bifilms. (Adapted from Ref. [48] with permission of Taylor & Francis)

Once nucleated, silicon particles grow. In studies on the growth of primary Si in hypereutectic alloys, Wang et al. [95,96] used an etching technique to reveal growth traces of primary Si particles on polished sections of a hypereutectic Al-Si alloy. Growth traces are marks left by the effect of the etchant on impurity-rich layers within the crystals, which are believed to be a consequence of the ejection of impurities during crystal growth. Hence, these marks reveal the outer shape the crystal had at different stages during its growth and their spacing can be used to estimate the relative growth rates in different directions. An example of the growth traces of a spinel-type primary Si is shown in Figure 2.15. In Ref. [96], it is proposed that, if the nucleus has no twins, a simple octahedron bounded by $\{111\}$ facets will develop (Figure 2.5a and Figure 2.7), whereas if the nucleus has one twin, the particle will develop into a spinel-type crystal (Figure 2.5b and Figure 2.15). If there are more than one twin and they are parallel, the result is a plate-like particle grown by the Twin Plane Re-entrant Edge (TPRE) mechanism (described below) (Figure 2.16). Finally, a five-branched star-like crystal can develop from a cluster of five octahedrons in twin relationship, with each branch growing as faceted octahedra [95,96]. Deviations of those shapes are attributed to mechanisms of accelerated corner growth, retention of facets other than $\{111\}$, and/or coalescence of growing crystals (Figure 2.17).

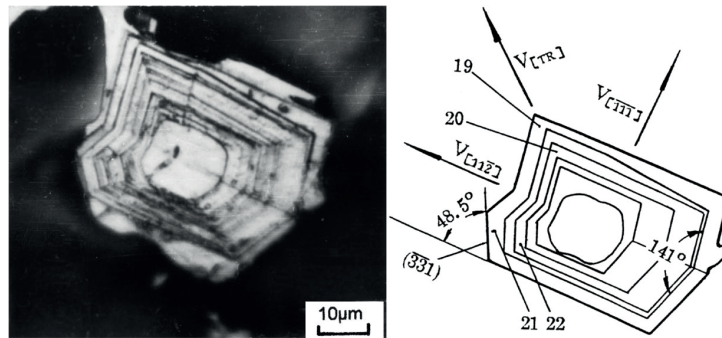


Figure 2.15 Polished cross section of a spinel-like primary Si particle observed under light microscope (left) and a simplified scheme (right) indicating the crystal growth traces, which were exposed using a hot etching technique; figure reproduced from Ref. [96] with permission of Springer.

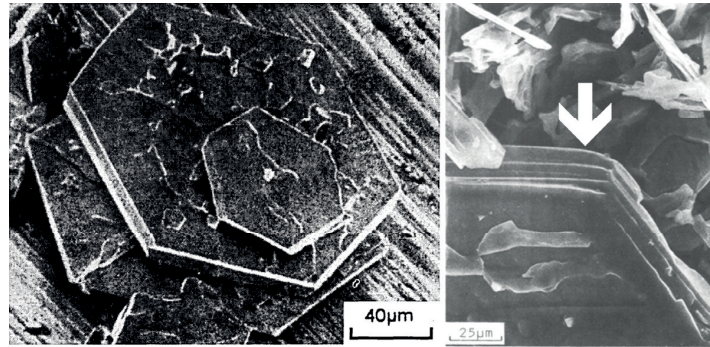


Figure 2.16 Primary plate-like Si particles extracted from a Al-Si alloy (a), and a magnified view showing in detail the edge of a plate-like primary Si particle (indicated with an arrow), where grooves resulting from twins are readily visible; from Refs. [95,100] with permission of Taylor & Francis and Springer.

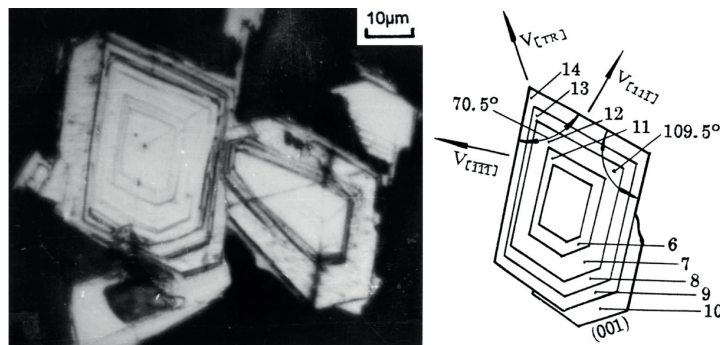


Figure 2.17 Coalescence of two primary Si crystals forming one particle. The octahedron crystal features a further deviation from perfection, including a non- $\{111\}$ facet (see scheme on the right). (Reproduced from Ref. [96] with permission of Springer)

Octahedral crystals and variations thereof with $\{111\}$ facets, which are the most common primary Si particles in Al-Si alloys, grow by a layer growth mechanism [95–98,125]. Layer growth postulates the presence of flat terraces and raised partial layers (steps) that define kinks, which is where incoming atoms attach preferentially. Wang et al. [96] suggest that an important source of layer growth steps are emerging screw dislocations on $\{111\}$ facets. Alternatively, corners and edges are favoured sites in layer growth because those are locations where Si in the adjacent melt is depleted to a lesser extent than at

the centre of the facets. Evidence of the latter is provided by the observation of hollow (“hopper-like”) crystals (Figure 2.7 right), which are formed under certain conditions as a result of the deposition of Si on edges and corners of an octahedron, while the central part of facets is not readily filled due to local silicon depletion in the adjacent melt [96,98].

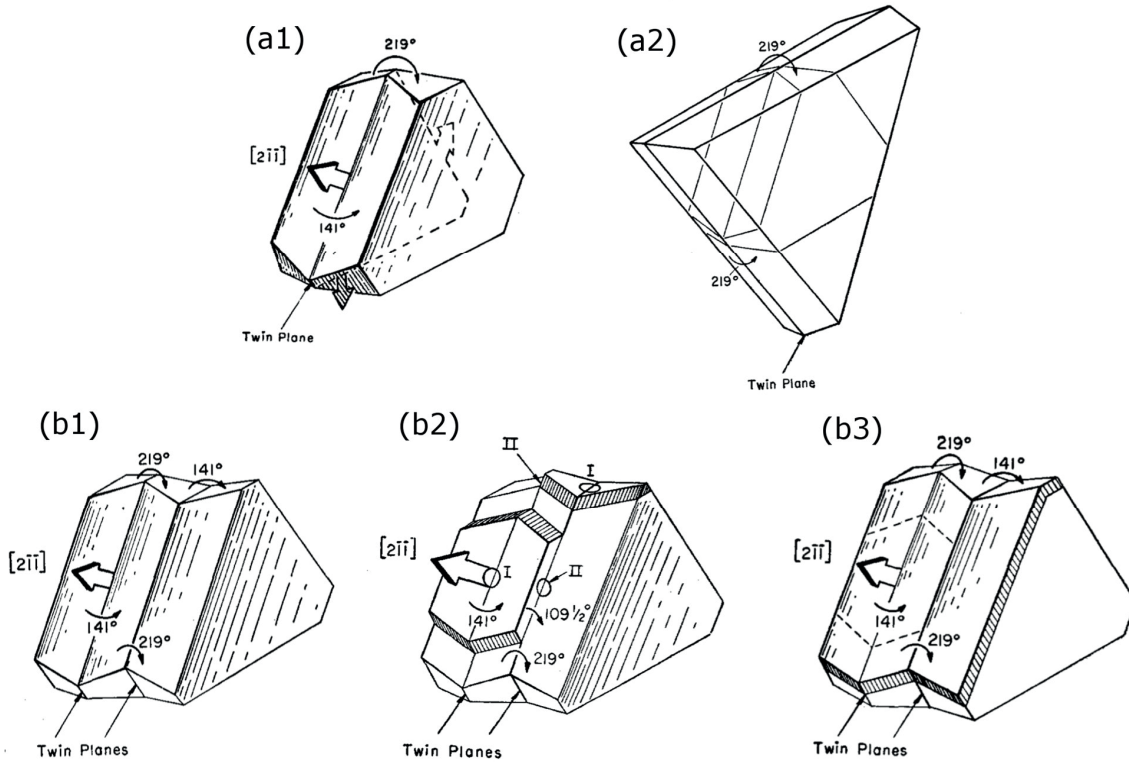


Figure 2.18 Twin Plane Re-entrant (TPRE) growth mechanism of plate-like silicon particles; figure adapted from Ref. [126] with permission of AIP Publishing LLC. In (a1-a2), the crystal only has one twin, which prevents its perpetual growth. In (b1-b3), the crystal has two twins and growth by the TPRE mechanism can self-perpetuate. See main text for a step-by-step description.

As mentioned above, the typical shape of eutectic silicon particles in non-modified alloys is the plate-like morphology (e.g., Figure 2.3a). Its growth is typically attributed to a mechanism known as Twin Plane Re-entrant Edge (TPRE). The TPRE mechanism was originally proposed in two publications by different authors almost simultaneously in 1960 as a means to explain previously reported experimental results on the growth of Ge dendrites [126,127]. The mechanism explains how a crystal needs at least two parallel $\{1\ 1\ 1\}$ twins to self-perpetuate growth perpendicular to $\langle 1\ 1\ 1 \rangle$, which is more favourable than layer growth on $\{1\ 1\ 1\}$ facets, hence generating a plate-like crystal. The reasoning is as follows. The equilibrium habit of Ge (and also of Si) is an octahedron bounded by eight $\{111\}$ facets (Figure 2.5a). A related favourable shape is a crystal twinned along bbb in Figure 2.5a, which gives Figure 2.5b. The outline of this crystal is composed six central edges at the intersection of pairs of $\{111\}$ planes, producing three 141° and three 219° boundaries (indicated in Figure 2.18a1). The 141° edges form re-entrant edges, which are -according to this theory- sites where nucleation is favoured. Thus, the re-entrant edge readily undergoes rapid crystal growth in a $\langle 112 \rangle$ direction (at a much higher rate than layer growth in $\{111\}$ facets), which is, however stopped soon after because of the disappearance of the re-entrant groove, leading to its replacement with a ridge (Figure 2.18a2). In contrast, if the initial crystal has two (or more) parallel twins instead of one, the formation of a ridge due to the growth from a re-

entrant edge will in turn produce a 109.5° re-entrant edge (Figure 2.18b1), which will readily nucleate and propagate the growth further. As shown in Figure 2.18b3, after one “step” of growth, the crystal keeps its shape but it has increased in size. Most importantly, the crystal still has six re-entrant edges to keep it growing steadily in the same manner and form a plate.

Liu et al. [94] recently revised the validity of the TPRES mechanism on plate-like eutectic silicon particles in Al-Si alloys and made the observation using EBSD that plates are typically elongated along $\langle 110 \rangle$ directions rather than along $\langle 112 \rangle$ directions. They proposed thus a modification to the TPRES growth of silicon in which growth at the atomic scale still takes place along $\langle 112 \rangle$ directions, but consecutive growth steps follow a zigzag pattern, such that at the microscopic scale, the overall growth direction is $\langle 110 \rangle$ (Figure 2.19). Modifications to the TPRES mechanism have also been made by Fujiwara et al [102,128] in studies where an in-situ observation technique was used to follow the growth of Si dendrites from pure Si melts in real time.

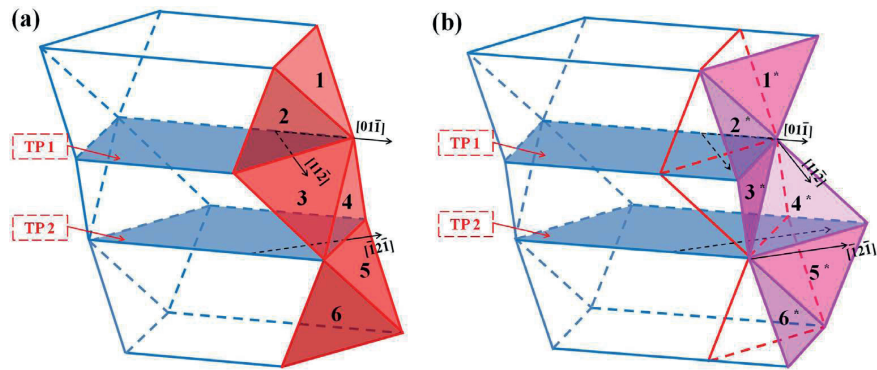


Figure 2.19 Modified TPRES mechanism to account for the fact that plate-like Si particles in Al-Si alloys are found to be elongated in a $\langle 110 \rangle$ direction. In this case, growth at the atomic scale is in $\langle 112 \rangle$ directions (as in the traditional TPRES mechanism) but in zigzag, which leads to an overall $\langle 110 \rangle$ microscopic growth direction. (Reproduced from Ref. [94] with permission of Elsevier)

Whereas individual eutectic silicon plates grow by a TPRES mechanism (or a variation thereof), when a colony of eutectic silicon plates of a non-modified Al-Si alloy is observed in a metallographic cross section, it frequently has a “broom-like” or “wheat-sheaf” appearance (Figure 2.20). To explain this, it has been proposed that, during the growth of eutectic Si particles, fragments break off, slightly rotate in the melt, and then give rise to new plates [129]. Alternatively, slightly misoriented particles can be side-branches formed by a displacement twinning mechanism of a silicon plate [101].

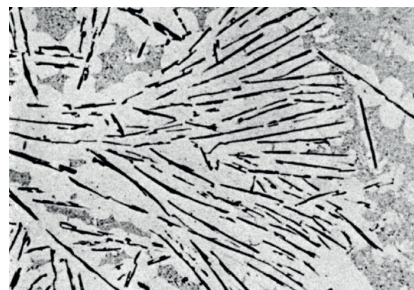


Figure 2.20 “Broom-like” appearance of eutectic Si plate-like particles (scale not indicated in the original document); figure from Ref. [129] with permission of Springer.

The mechanisms of eutectic modification in Al-Si alloys have also been extensively studied and remain subject to controversy [92,123,124,130]. It is generally accepted that chemical modification has an influence on both Si nucleation and Si growth [94,111]. In modification with Sr, it has been shown that Sr readily forms Sr_3P preventing the formation of AlP nuclei [111]. Alternatively, $\text{Al}_2\text{Si}_2\text{Sr}$ intermetallic phase can form around pre-existing AlP particles, deactivating those nuclei and forcing silicon to nucleate on less favourable nuclei at larger undercooling [131]. Indeed, a high undercooling is normally associated with Sr modification, and the measurement of this undercooling is the most used Non-Destructive Testing (NDT) approach to assess the degree of modification of Al-Si alloys [92] - even though there are studies that argue that its applicability is unfounded [110].

Eutectic chemical modification is also a result of changes in particle growth mechanisms [94,111]. In this regard, two mechanisms are usually accepted: impurity induce twinning (IIT) [104] and restricted TPPE growth. IIT proposes that modifying atoms (e.g., Sr or Na) are adsorbed onto kinks at steps on $\{111\}$ facets exposed to the melt, preventing growth by further attachment of silicon atoms to the facet, and hence forcing the crystal to alter the stacking sequence, twin, and activate other growth directions. In the restricted TPPE mechanism, on the other hand, modifiers elements poison re-entrant grooves rendering them less favourable for growth, and hence deactivate the anisotropic TPPE growth, forcing the particle to twin further and branch. These modification mechanisms account for the very high density of twins and branching observed in chemically modified silicon fibres. On the other hand, those mechanisms do not apply to chill-modified fibres, which present much less twinning [111]. Chill-modified silicon particles are believed to be finer counterparts of unmodified plate-like particles grown by the TPPE mechanism [111,132].

Al-Si cast parts are sometimes subjected to heat treatments. A typical example is the age hardening of Al-Si alloys containing Mg and/or Cu, which comprises a solubilisation step at a temperature in the range 500-550 °C, followed by quenching and an aging step at intermediate temperature. The main objective of this treatment is to produce strengthening of the aluminium matrix driven by β'' (Mg_2Si), θ' (Al_2Cu) and/or Q' ($\text{Al}_5\text{Cu}_2\text{Mg}_8\text{Si}_6$) precipitates [21,23,133]. The presence of other nanometric precipitates has also been reported [11,134]. Heat treatment introduces changes to the Si phase. Plate-like silicon particles undergo morphological changes, which are typically described by the following sequence: (i) fragmentation, (ii) spheroidization of the fragments, and finally (iii) coarsening. The loss of particle interconnectivity and the decrease of particle aspect ratio significantly improve alloy ductility and fatigue resistance [4,133]; however, they can be detrimental to alloy strength [135].

The effect of heat treatment on the morphology of silicon particles has been characterized in 3D by Lasagni et al. [93] using high-resolution FIB-tomography on both non-modified and Sr-modified Al-12Si alloys. As shown in Figure 2.21 and Figure 2.22, the initially interconnected network of silicon (coarse plate-like in one case and coral-like fibrous in the other) defragmented into isolated particles after only 20 minutes at 540 °C. As expected, it was also found that spheroidization and coarsening occur predominantly for smaller particles. Also, plate-like particles did not readily take a spherical shape. In fact, as will be seen in the work of this thesis and also in Figure 2.3 from the work of Pedersen et al. [76], even after long heat treatments plate-like particles tend to retain their plate-like morphology (they do, nevertheless, become somewhat more regular and tend to round off their edges).

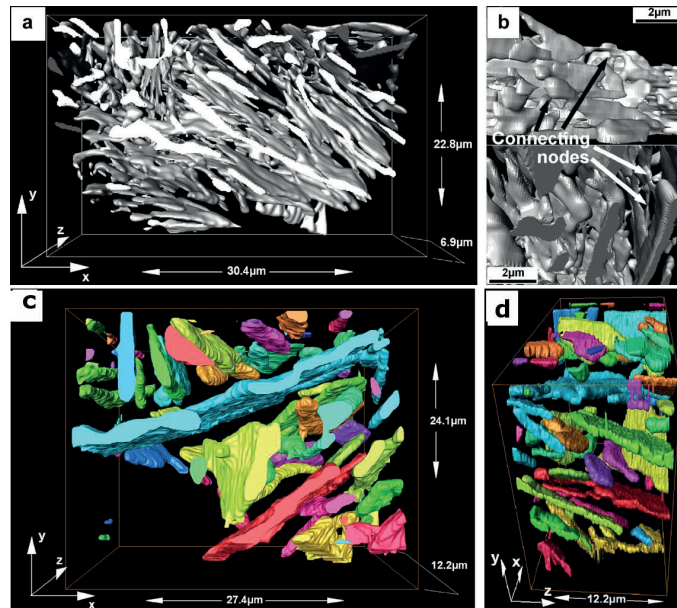


Figure 2.21 Reconstructed 3D microtomography images of a non-modified Al-Si alloy. (a-b) are for the as-cast condition. Interconnected particles share a common level of grey; as seen, particles mostly form an interconnected network in the as-cast condition. On the other hand, (c-d) are images after heat treatment: particles with different colours are disconnected from each other. As seen, the heat treatment defragmented the silicon phase. (Adapted from Ref. [93] with permission of Elsevier)

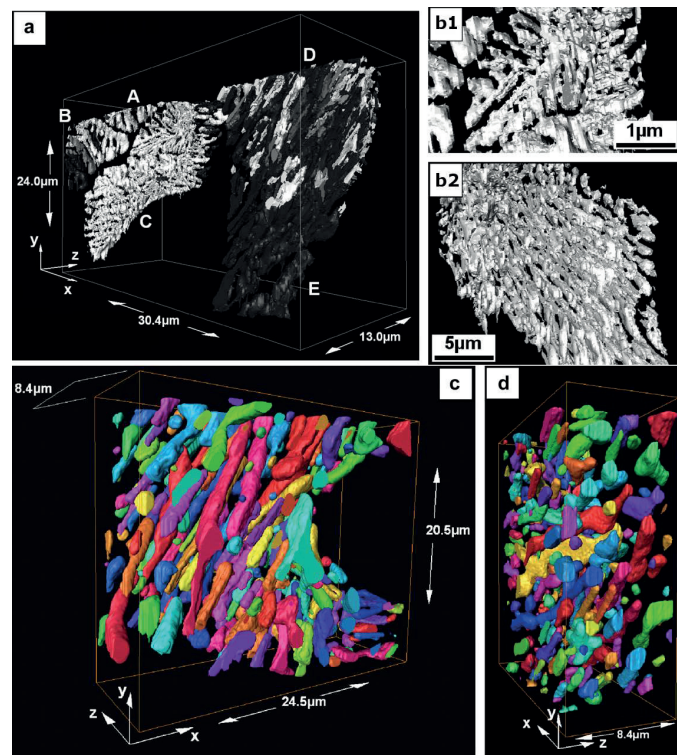


Figure 2.22 Same as the previous Figure, but in this case the alloy is a Sr-modified Al-Si alloy. In this case, heat treatment not only defragmented but also spheroidized the silicon phase. (Adapted from Ref. [93] with permission of Elsevier)

The time that it takes for silicon particles to undergo changes upon heat treatment depends strongly on the size and morphology of the starting particles (i.e. on the initial, as-cast condition), as typical times employed in the literature vary widely with this parameter, ranging from a few minutes for modified (fine) structures [87,136] to several hours for coarser initial morphologies [137–139]. The effect of heat treatment depends as well on the chemical composition of the alloy. For example, Ni is added to certain grades of piston alloys that are subjected to elevated in-service temperatures. In those alloys, Ni-aluminides enhance microstructure thermal stability, which maintains alloy strength at intermediate temperatures. Specifically, Al_3Ni and Al_9FeNi prevent the fragmentation of the network of second phases, as shown by Asghar et al. [140] using synchrotron tomography.

The driving force of thermally-induced particle fragmentation, spheroidization and coarsening is the tendency to minimize the Gibbs free energy of the system. Volumetric, surface (interfacial) and elastic contributions all come into play [4]. Note also, that the problem is complex due to the high surface energy anisotropy of silicon. From a kinetic point of view, the process is expected to begin at local crystal disturbances (or morphological faults) like terminations, kinks, striations, holes and microcracks, and to then progress by migration of Si atoms by solid-state diffusion [141,87]. Detailed, quantitative, modelling of the process that considers both thermodynamic and kinetic effects is, however, not available in the literature to the best of the author's knowledge.

Up to here, only structural aspects (e.g., twins, facets, surface grooves and steps, interconnectivity) of the silicon particles in Al-Si have been discussed. The chemical composition of silicon particles, on the other hand, has been very rarely examined in the literature. The general assumption that silicon particles are fully made of Si is good enough for the scope of most studies on Al-Si alloys; however, HR-TEM studies of silicon particles indicate that the particles are not simply pure Si [142–145]. This was first shown in 1992 by Andersen et al. [142], who found equiaxed aluminium precipitates roughly 10 nm in size in the interior of silicon particles in a Al-Si-Ni-Mn alloy. Later, Hogg et al. [146] found similar precipitates within Si particles of a spray-formed hypereutectic Al-Si alloy. Also Donlon [143] looked in detail at silicon particles of as-cast and heat treated A356 (Al-Si-Mg) and A319 (Al-Si-Mg-Cu) hypoeutectic alloys under a HR-TEM and found tiny Al precipitates contained in silicon particles of both alloys (Figure 2.23). Large quantities of precipitates were observed along specific bands within the particles, while other locations within the particles were shown to be free of such precipitates [143]. No strain contrast was found in the surrounding silicon, indicating that strains are largely accommodated by the precipitate. EDX spectra of the precipitates also revealed the presence of small amounts of O and Cu (the latter in the case of alloy A319). Subsequent heat treatment was shown not to affect their morphology nor their distribution, a fact confirmed also by Jia et al. [145]. Donlon [143] suggests that the stability of the precipitates may be related to the presence of O within the precipitate, or to slow diffusion of Al in solid Si. The occurrence of Al precipitates in silicon particles is proposed to be a consequence of supersaturation of Al in solid Si during Si particle growth, followed by precipitation of Al phase within the Si crystal. Note that the maximum solubilities of Al and Cu in Si are small, namely 0.016 and 0.002 at.%, respectively [143].

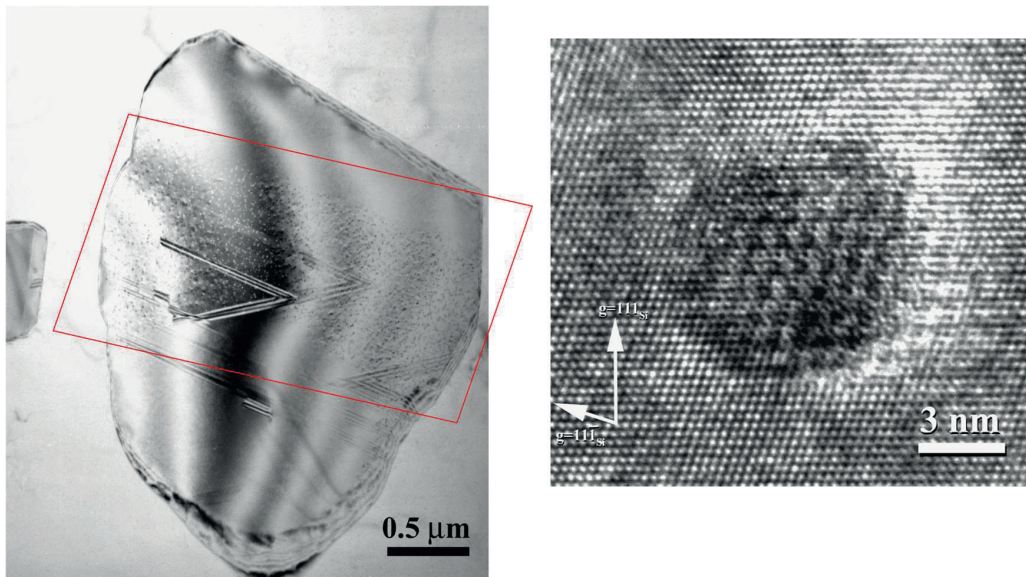


Figure 2.23 (left) TEM image of a Si particle from an Al-Si alloy, in which Al precipitates roughly 10 nm in size (HR-TEM image on the right) are observed in a sector of the particle marked with a red rectangle; figure adapted from Ref. [143] with permission of Springer. These Al precipitates inside Si particles have been observed in many Al-Si alloys and are insensitive to heat treatments.

In the previous paragraphs, only silicon has been discussed as a second phase; however, impurity-rich and alloying element-rich precipitates are also more or less normally present in commercial Al-Si cast alloys. Even though they are usually in much lower volume fraction than Si, they may, in some cases, also have a strong influence on the alloy's mechanical properties. The basic example is iron, which is the main impurity in these alloys (although in certain grades it is added as an alloying element). As an impurity, it forms elongated, thin, β -phase (Al_5FeSi) precipitates, which are highly detrimental to tensile properties and fatigue resistance [4,86,147]. Other Fe-rich phases can also be found in Al-Si alloys, such as the α - $\text{Al}(\text{Fe},\text{Mn})\text{Si}$ or the π - $\text{Al}_9\text{FeMg}_3\text{Si}_5$ phases [148]; the latter limits alloy ductility in certain Al-Si-Mg alloys [86].

Moreover, (highly) alloyed compositions can feature several other second phases. An illustrative example can be found in Chen et al. [149]. In that work, the intermetallic phases present in a eutectic Al-Si-Cu-Mg-Ni alloy were analysed by EBSD, EDX and DSC analysis. Besides elemental silicon particles, the authors identified the following phases in the form of particles: $\text{Al}_5\text{Cu}_2\text{Mg}_8\text{Si}_6$, Mg_2Si , AlFeCuSiMn , Al_3Ni_2 , AlCuFeNi , Al_9FeNi , AlCuFeNi (Figure 2.24). As seen, the range of second phase particles in Al-Si alloys can be extremely large.

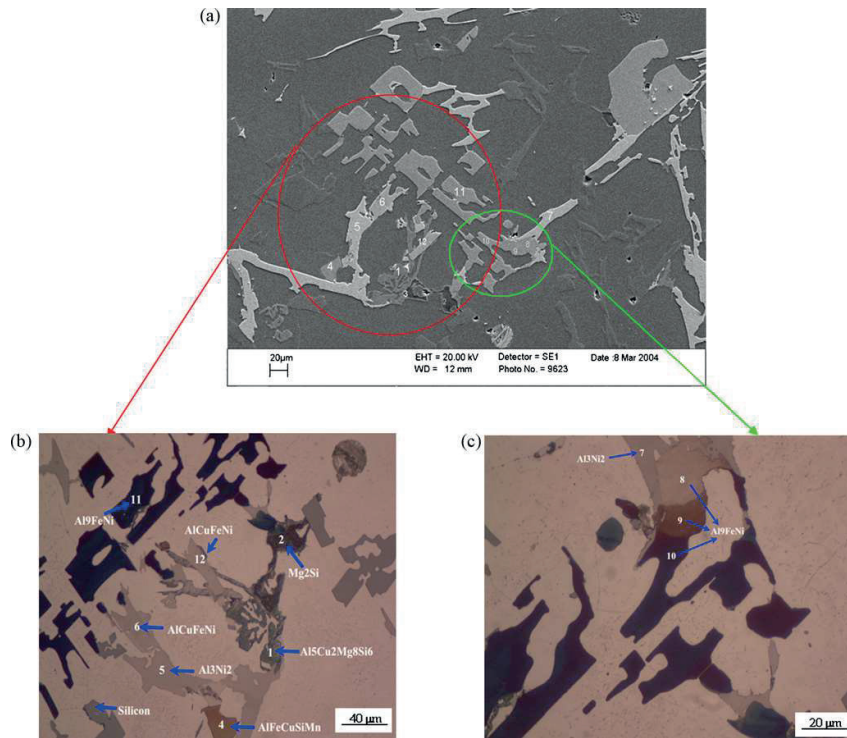


Figure 2.24 SEM and light microscopy images of the microstructure of a Al-Si-Cu-Mg-Ni alloy showing the presence of many different intermetallic phases within the Al matrix; figure from Ref. [149] with permission of Elsevier.

2.2 Micromechanics of Al-Si alloys and particle strength

Micromechanics serves in understanding the relations between the bulk properties of a material and the local properties of its microstructure. This encompasses considering how mechanical load is borne across the phases and microconstituents, and resulting consequences such as the onset and evolution of specific damage mechanisms that depend on the properties of those phases and on the cohesive properties of the interfaces (e.g., [55,150–155]). Work on the micromechanics of Al-Si alloys has been typically prompted by two kinds of motivation. The first, more obvious, is the desire to understand the mechanical properties of this very important class of engineering alloys. The second, is that Al-Si alloys can be used as model materials towards understanding and modelling the damage accumulation and fracture process of many other heterogeneous materials where a ductile matrix is reinforced with hard second phases, notably Metal Matrix Composites (MMCs) and some other alloys [156,14,41,139,157,158]. The reason is that intervening factors such as particle size, shape, aspect ratio, volume fraction and morphology as well as hardness of the matrix can be relatively easily adjusted in Al-Si-based alloys through composition, solidification conditions and heat treatment, therefore providing versatility to the studies. In the following paragraphs, relevant literature on this subject is reviewed with emphasis in the importance of the fracture properties of silicon in the micromechanics of unmodified Al-Si alloys. Also, existing approaches in the literature to determine fracture properties of the silicon particles (even though generally indirectly) are here described.

The first studies in this sense done on Al-Si alloys date from the mid 1990's (except for the earlier work of Coade et al. [39] in 1981, discussed later in this Section). Mocellin et al. [14] identified the sequence of events in the damage process of an hypereutectic Al-15Si-3Fe during tensile testing (which applies in general to most Al-Si alloys [19,22,44,47,159]) as: (i) the onset of silicon particle cracking, (ii) the increase in the volume fraction of cracked particles, and (iii) the linkage through the aluminium phase of the microcracks producing a macrocrack. Interfacial decohesion particle-matrix was not observed. To explain step (i), a purely energetic argument was used: a particle (considered spherical) fractures when the stored elastic energy in the particle

$$W = w \frac{4}{3} \pi R^3 \quad \text{Equation 2-1}$$

exceeds the energy of the newly created surfaces

$$2\pi R^2 \gamma_s \quad \text{Equation 2-2}$$

where w is the elastic energy density in the particles, γ_s is the surface energy of silicon, and R the particle radius. This leads to a particle fracture criterion given by $w > (3/2)(\gamma_s/R)$, which, according to this model, explains the observation that larger particles fracture preferentially over smaller ones.

Such a size effect in the strength of silicon particles is also seen in the work by Slámová et al. [156], where the mechanical properties and the evolution of damage under tensile loading of an Al-1%Si alloy subjected to different heat treatments was studied. The Si content of this alloy was significantly lower than in typical Al-Si casting alloys. Differences in the results among the differently heat-treated samples were explained in terms of the size distribution and morphology of the silicon particles. Via acoustic emission it was observed that, for two materials with the same average particle size but different size distributions, damage initiated at lower strains in the material with the widest distribution. This was adjudicated to the fact that bigger particles fail at lower stresses, just as ceramic materials typically do: the larger the specimen is, the higher the probability of it containing a larger critical flaw, thus the lower the critical remotely applied stress. This is, in fact, the most usual argument used to explain the apparent particle strength size effect [47,159].

Caceres and Griffiths [13] developed for a heat-treated Al-7Si-0.4Mg (A356) alloy a model to express the ductility as a function of dendrite cell size and average size and aspect ratio of the brittle silicon particles. The analysis, also used by Wang et al. [42] on an alloy with slightly more Mg content (alloy A357) and by Joseph et al. [29] on a eutectic Al-Si-Cu-Mg alloy, is based on damage by fracturing of the silicon particles. The experiments consisted in tensile and 4-point bending tests, which were carried out using square cross-section specimens. After every plastic strain increment of roughly 1%, tests were stopped and the fraction of fractured particles along the surface of the sample was measured under an optical microscope. This was done, in the case of the tensile sample, on one of its faces, which was repolished to remove a depth of roughly 100 μm after each strain increment; the exposed surface was assumed to represent the "bulk" state. Measurements of fractured particles in the bending sample were done on its tensile surface, which was polished only once, prior to testing (i.e. it was not repolished after each strain increment). Measured in this way, the fraction of cracked particles at varying levels of macroscopic strain was found to be fairly consistent across both tests and was used to compute the particle failure probability. The method is unfortunately prone to artefacts: in particular, polishing produces scratches that can weaken or fracture particles at the surface. The stress in the particles as a function of applied strain was approximated using a dispersion hardening approach proposed by Bréchet et al. [151] and further developed by Caceres et al. [160]; this considers a Weibull distributed particle strength and

takes into account local work hardening of the surrounding matrix. A failure criterion was then defined based on the critical level of damage observed in fractured samples, which occurred roughly when a level of 45% volume fraction (20% number fraction) of fractured particles was attained. Caceres and Griffiths [13], Wang et al. [42] and Joseph et al. [29] estimated in this way the strength of the silicon particles to be in the range 0.5 – 3.5 GPa, albeit widely distributed (calculated Weibull modulus values were roughly in the range 1 to 4), with a reference strength of 3 GPa for eutectic silicon particles having a 4 μm representative diameter in heat-treated A356 and A357 alloys.

A similar approach involving counting fractured particles as a function of strain was used in investigations by Kiser et al. [41] and by Nishido et al. [43]. The former calculated the stress in the particles from a constitutive law derived from a finite element analysis [161], while the latter used an expression from an equivalent Eshelby inclusion method. Kiser et al. [41] reported a Weibull modulus of 6.1 for silicon particles in a hypereutectic (20 %Si) alloy, which started to fracture at estimated stress of 150 MPa. Nishido et al. [43], on the other hand, discriminated primary from eutectic silicon particles, reporting a strength of 200-300 MPa for the former and 500-900 MPa for the latter. Furthermore, Wang [159] estimated the average tensile stress on the silicon particles as a function of the alloy plastic strain using the model to derive the stress in the particles by Caceres and Griffiths [13]. Damage was in this case quantified by monitoring the Young's modulus loss. Their results show a change in the shape of the curve at a particle stress level in the range of 600 - 800 MPa (depending on the particle aspect ratio). This was associated with the onset of particle cracking and matrix plastic relaxation.

Another important question is that of how the silicon particles are loaded within the microstructure. Yeh and Liu [162], in their investigation on particle cracking in alloy A357, argue that silicon particles fracture because of the strong stress concentration at their surface resulting from dislocation pile up in the surrounding aluminium matrix. This seems to be supported by the observations of Wang and Caceres [12], where fracture surfaces were examined after an electro etching process designed to clearly distinguish between transgranular and intergranular fracture. Transgranular, in the context of hypoeutectic Al-Si alloys, means *through cell walls* (cells are the regions between two secondary dendrite arms; hence, cells contain α -aluminium in their interior and the eutectic at their walls). Conversely, intergranular means *between dendrites*, which is also a region with the eutectic microconstituent and also segregation. When the secondary dendrite arm spacing (SDAS) is large, the fracture is transgranular and this is rationalized by the fact that the eutectic at cell walls is highly concentrated in silicon particles, which are an effective obstacle to slip bands, leading to the formation of dislocation pile ups, which produce particle cracking. Conversely, a microstructure of small SDAS leads to intergranular fracture given that the particles in cell walls are, in this case, more isolated and do not provide a strong enough obstacle to dislocations as grain boundaries do. Figure 2.25 shows the interaction of slip bands with cell walls and with dendrite boundaries in materials of large and small SDAS, respectively. Note that in all cases, fracture progresses through the fracturing of silicon particles.

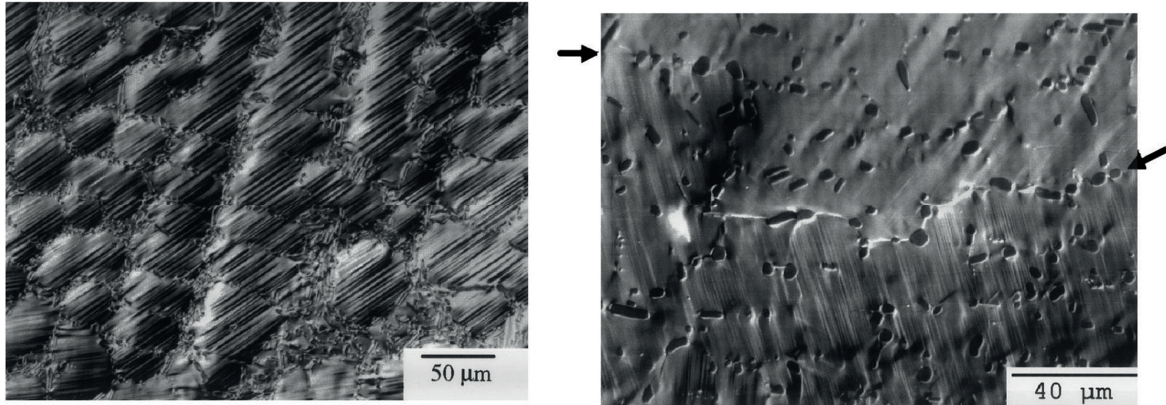


Figure 2.25 Micrographs of Al-Si alloys under Nomarski phase contrast to expose slip bands in the aluminum matrix; figure adapted from Ref. [12] with permission of Elsevier. The left image corresponds to an alloy with a large dendrite arm spacing (DAS). Here, slip bands are observed in dendrite cells and interact with the silicon particles at cell boundaries. The right image corresponds to an alloy with a small DAS. The density of silicon particles is in this case lower, and hence cell boundaries interact less with dislocations. Slip bands are, in contrast, observed to strongly interact with a grain boundary (indicated with black arrows).

Other studies suggest that the stress that leads to particle fracture is mostly a result of a fibre loading mechanism. In fibre loading, the load is transferred to the particles by a shearing mechanism at the interface between the yielding matrix and the stiff particle [29,150]. Berdin et al. [163] followed the evolution of damage on a polished surface of an Al-9Si-3Cu-0.8Fe alloy sample during tensile testing of the polished sample in a SEM. Cracks were observed to be perpendicular to the tensile axis (thus governed by the maximum principal stress) as opposed to randomly oriented, as would be expected, according to the authors [163], if particles fractured due to the local stress concentration of dislocation pile-ups (an argument also raised by Joseph et al. [29]). In Ref. [163] a FE model was applied to estimate the strength of a particle in the observed surface, which resulted in a minimum strength of 600 MPa (but note that such a particle is not representative of particles within the bulk material because its surface was damaged by polishing). In a later contribution from the same group, Doglione [19] presented results of a similar *in-situ* tensile test on an Na-modified alloy A357 where slip bands in the matrix are claimed to lead to particle cracking, see Figure 2.26 [19]. It must be noted, however, that the observed slip band traces adjacent to particle fracture locations may potentially have been produced *after* particle fracture. The evidence provided in the paper is thus unfortunately not conclusive in this regard. Incidentally, one can note in the same Figure 2.26 that the cracks are located at what seem to be stress concentration sites in the particle, as judged from the 2D image of the surface. Finally, according to Joseph et al. [29], fracture via dislocation pile-up applies when the dislocations mean free path is shorter than the particle size (e.g., in the case of the small, spheroidized, particles in a modified alloy); otherwise, particles fracture due to a stress that can be accounted for by the fibre loading mechanism (in unmodified alloys, where particles are larger in size and in aspect ratio).

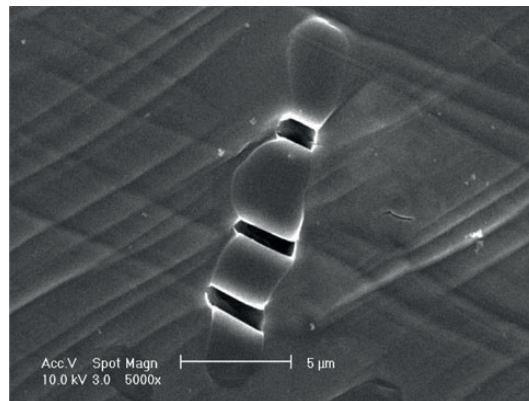


Figure 2.26 A Si particle cracked at three locations and slip bands in the surrounding Al matrix. The particle is at the surface of a tensile sample tested *in-situ* in a SEM. (Reproduced from Ref. [19] with permission of Springer)

Another indirect estimation of the average silicon particle strength can be found in the work by Huber et al. [44], who developed a void (microcrack) nucleation and growth model using a near-eutectic, Sr-modified, Al-11Si alloy with silicon particles of shape near that of a spheroid. In the model, microcracking was attributed to fracture of the silicon particles. The critical stress value for particle fracture was the free parameter used to fit the model to the experiments, which resulted in a value of 550 MPa. The authors deemed this value reasonable based on two arguments. The first is an energy balance in the sense of Griffith fracture criterion as in Ref. [14] and Equation 2-1 and Equation 2-2 (note that there are errors, however, in this computation in Ref. [44]: notably, the critical strain energy release rate G_c is considered numerically equal to γ_s , while it should be $2\gamma_s$; also, the value of Young's modulus used is too low for silicon: 110 GPa versus 130-187 GPa [164]). The second is a fracture mechanics argument: considering a reasonable value for the fracture toughness of silicon, a solution for a crack in a sphere in Mode I loading and the estimated critical stress of 550 MPa, critical crack-like defects shall be roughly 100 nm in length. Note that both approaches need an estimation of the silicon particle fracture toughness (or strain energy release rate or surface energy), yet actual values have not been measured (as discussed below in Subsection 2.3).

There is also an interesting body of work based on techniques that can sample finite volumes of the multiphase material under stress by means of neutron or X-ray diffraction [39,40] or synchrotron X-ray microtomography [153,165–168,140,24]. In an early work in 1981, Coade et al. [39] used X-ray diffraction to measure the average strain of the silicon particles in a Na-modified A356 alloy submitted to bending. The strain of the silicon phase was used to estimate the average stress in the particles and the fracture stress of the particles was estimated to be 230 MPa. It is noteworthy that, as the authors state in the paper, such a fracture stress would imply surface cracks 2 - 4 μm deep on the particles, which is admittedly inconsistent given that the particles size was also on that order. Along the same line, in a more recent work, Finlayson et al. [40] used a neutron diffraction technique during tensile testing to measure the average strain in the silicon particles of Sr-modified A356 alloys heat treated to T4 and T6 conditions. To evaluate the strength of the silicon particles, a macroscopic applied plastic strain of only 0.01 was considered (strains larger than that were claimed to yield too large uncertainties), which resulted in average particle stress values of 220 - 330 MPa. At that level of applied plastic strain only 1 to 2% of the particles would be fractured, which makes this assessment a strength estimate of only the weakest particles in the alloy [40]. Finally, microtomography work by Asghar and Requena [24,140]

provided evidence of the damage sequence of Al-Si alloys with additions of Ni, which forms Ni aluminides that prevent the loss of interconnectivity and spheroidization of the silicon phase upon heat treatment; however, no quantitative data on particle strength were extracted.

A very different approach to estimate the strength of particles in Al-Si alloys was proposed in the context of wear resistance, which is important in certain applications such as cylinder liners for car engines [9,169,170]. Riahi et al. [169] performed scratching tests with a Vickers diamond indenter on Al-12Si modified alloy with Fe, Cu, Mg, Mn, Zn and different percentages of Ni as alloying elements. The samples were slightly etched in 10% NaOH to expose the second phase particles, as is applied in some commercial sleeveless cylinders to enhance their wear resistance [171]. It was found that the debris of fractured particles act as abrasives and promote the onset of scuffing. This debris could however be of different sizes and thus be differently effective. In fact, two types of particle fracture were observed: some particles would break at the root (i.e. where anchored to the matrix) whereas other particles would break at their edges (i.e. at the contact with the indenter). The first type of fracture would generate larger debris and lower wear resistance. Motivated by these observations, Riahi and Alpas [45] performed a scratching test on a deep-etched surface with protruding particles (Figure 2.27a) and reported that the tensile stress at the root of the particles reached 2.5 GPa based on an expression that relates (using a number of assumptions) the average bending strength at the root of the particles with the friction coefficient, the alloy hardness, the particle average height and the vertical load upon sliding (Figure 2.27b).

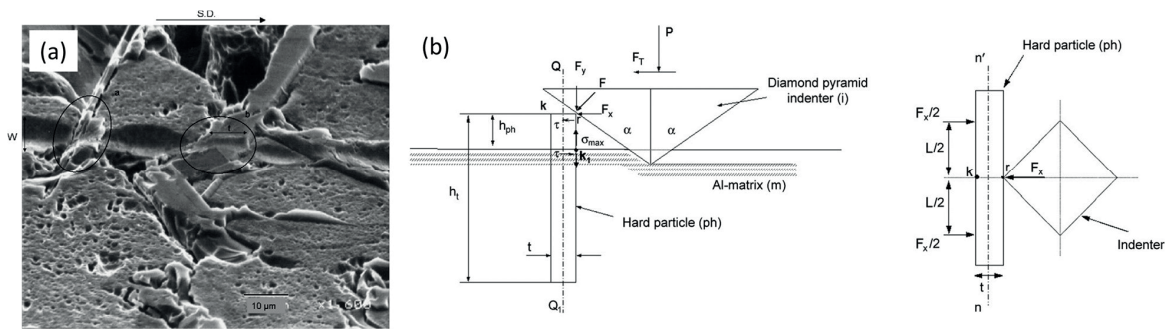


Figure 2.27 (a) SEM image showing fractured particles and the trace left by a scratching indenter on the surface of an Al-Si alloy. (b) Side view (left) and top view (right) of the geometry of the idealized contact between the indenter and the particle used to estimate the fracture strength of the particles based on average dimensions, vertical force and estimated friction coefficient. (Adapted from Ref. [45] with permission of Elsevier)

The methods discussed so far have produced rich and relevant results; yet to obtain the stress of a single particle knowing the composite or the average phase stress requires micromechanical modelling, which in turn rests on idealizations of the material microstructure and/or load transfer mechanics. This in turn raises two issues, namely (i) the validity of approximations made in constructing the micromechanical models, and (ii) the fact that such models give a value for the average stress exerted on the particles, which may differ significantly from the stress exerted on those particles that fracture at a given point of the composite's deformation history. As a result, precisely when and why silicon particles in Al-Si alloys fracture is at present still poorly understood. Measuring locally the strength of individual silicon particles can provide direct insights into the matter; however, this kind of strength measurements are extremely rare and constitute a significant challenge, which this thesis aims to tackle.

The only approach that has been proposed to measure the strength of individual silicon particles is based on the micro-Raman technique [50,25], specifically a method developed by Narayanan et al. [172],

which allows to relate the shift of the silicon peak in the Raman spectrum with the in-plane stresses of a (111) silicon wafer. Applying this on silicon particles in an Al-Si alloy thus requires a well-polished surface of bending [50] or compression [25] test samples of the alloy, along which a silicon particle identified as having a (111) orientation can be spotted. With this technique, Joseph et al. [25] found that eutectic silicon particle fracture occurred at stresses in the range 500–1000 MPa, whereas Harris et al. [50] reported a value of 600 MPa. The significance of the resulting particle strength is, however, questionable because the particles were polished, which introduces defects (scratches) on the particle, as mentioned above.

In summary, it can be concluded that, to date, the strength of silicon particles within Al-Si has almost exclusively been assessed by indirect methods that estimate averaged property of the silicon phase. Those investigations thus have limitations, both in terms of quantitative data that they generate, and in terms of identification of the actual fracture mechanism of individual particles. The lack of understanding and of strong evidence can also lead to unfounded conclusions. For example, Wang, Caceres, Griffiths et al. [173], in discussing their much-used model developed roughly 15 years earlier (Caceres and Griffiths [13]), state that the partitioning of stress is not well represented by the model because it predicts an (average) particle stress that is higher than the (unreliable) results of measured particle strength values in the literature. Direct measurements on the particles themselves, of their strength or fracture toughness, would therefore be of interest. We next turn to methods that have been used to measure fracture properties at small scales on other materials.

2.3 Small-scale fracture toughness testing

The most common small-scale fracture toughness measurement approach is the indentation toughness technique. The method consists in indenting a polished sample of the material of interest using either a sharp indenter (Vickers indentation toughness) or, less commonly, a spherical indenter (Hertzian indentation toughness). The Vickers indentation typically forms *Palmqvist* (also called *surface radial*) cracks, *half-penny* (also called *median/radial*) cracks or a mixture thereof that, at the sample surface, look alike and emanate from the corners of the imprint. Also, *lateral* cracks may be produced, which lead to surface spalling (note that the crack type nomenclature used here is based on the comprehensive paper on indentation cracks by Cook and Pharr [174], Figure 2.28). Evans and Charles [175] set the bases for the Vickers indentation method in the mid 1970's in a short publication where they developed a theory based on stress analysis to relate the indentation load and the lengths of the cracks with the material's fracture toughness. In the case of Hertzian indentation, *ring* cracks are generated (from a pre-existing surface flaw) and can develop into *cone* cracks with increasing load. Its main interpretation schemes are based on the early work by Frank and Lawn [176] and the later contributions from Warren [177,178].

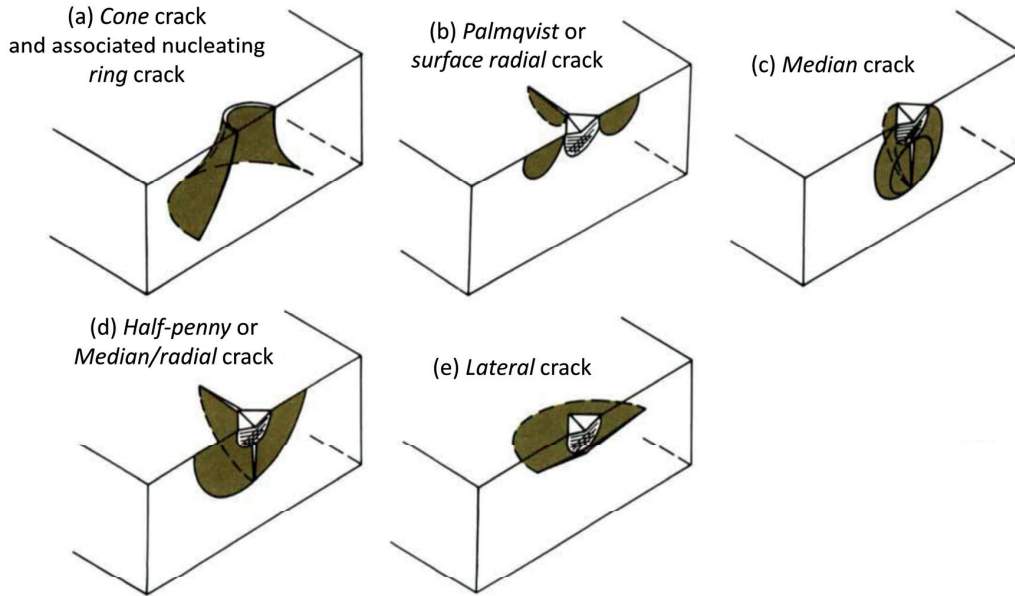


Figure 2.28 Idealized crack morphologies produced by indentation; figure adapted from Ref. [174] with permission of John Wiley & Sons.

Due to the great potential of indentation fracture toughness methods as a universal and experimentally convenient test, much work has been done on the subject during the following years including, particularly, the development of numerous interpretation schemes for different materials and for the different crack systems that can appear (e.g., [179–183]). Generally, equations that are used to interpret Vickers indentation toughness take the form

$$K_c = \chi P / c^{3/2} \quad \text{Equation 2-3}$$

where K_c is the fracture toughness, P is the indentation load, c is the crack length and χ is a factor that takes into account crack and indent geometry effects as well as the residual stress field. This factor is often a function of $\sqrt{E/H}$, where E is the Young modulus and H is the hardness. More recently, the up-coming of instrumented (nano)indentation has led to adaptations of the method for Berkovich and cube-corner indenters [184–186] and also to the development of energy-based models to extract fracture toughness from indentation load—displacement curves (e.g. [187,188]), these being particularly of interest for the testing of thin films [189,190].

The indentation method as a means of measuring fracture toughness has been used and is still being used extensively (e.g., Refs. [191–201,69,202]); however, it is also subject to strong criticism [164,203,204]. Quinn et al. [204] note that over 30 different formulas have been published in the literature to determine toughness from Vickers indentation, that none of them has a strong theoretical grounding, and that most of them rely on poorly-based calibration factors (entering typically into χ in Equation 2-3), which moreover are material- and crack system-dependent. In that work, the inaccuracy and inconsistency across the most used formulas is demonstrated on a material of well-established fracture toughness (Figure 2.29). Moreover, Morrell [203] states that the method does not meet fracture mechanics criteria. Quoting a definition of fracture toughness K_{Ic} from Munz and Fett [205] is here relevant: “If a component or a test specimen with a crack is loaded, K_I increases with increasing load until unstable

crack propagation occurs at a critical value of K_I . This critical value is the fracture toughness, K_{Ic} . In view of this, a problem of the indentation fracture method is fact that toughness is evaluated in an ill-defined crack-arrest condition instead of the onset of rapid crack propagation. Other fundamental arguments against the method include: the variability and poor knowledge of the complex 3D crack systems that are produced (because only their surface signature is considered in the analyses); the unknown effect on the cracks of the residual stress field; and the damage left from polishing as well as from indenting. Hertzian indentation is not free from those objections and is furthermore strongly influenced by indenter—sample friction conditions [206,207].

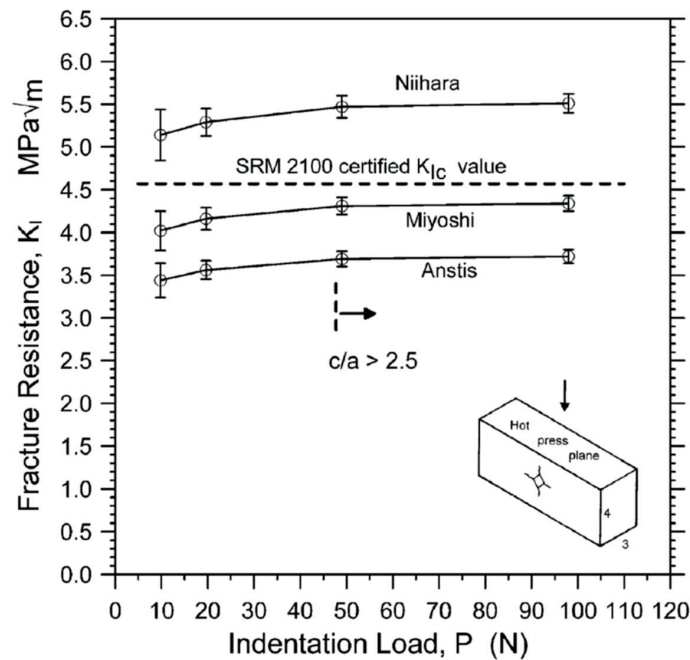


Figure 2.29 Indentation fracture toughness values computed using different published equations (labelled “Niihara”, “Miyoshi” and “Anstis”) compared to the certified value of a material of calibrated fracture toughness (dashed line); reproduced from Ref. [204] with permission of John Wiley & Sons. As seen, the equations fail to give the true value and their results are significantly different from each other.

In electronic grade single crystalline and polycrystalline silicon, several studies to measure fracture toughness based on (micro)indentation are found in the literature [195–199,201]. A critical, in-depth, review by Del Rio et al. [164] concludes that those measurements are invalid and that the fact that published values (in the range $0.7 - 1 \text{ MPa}\cdot\text{m}^{1/2}$) agree with other, more suitable, fracture toughness tests should be regarded as fortuitous. The reasons, here too, are related to the arguments brought to discussion in the previous paragraph [164]. Specifically, in silicon crack patterns are very often disrupted by lateral cracks even at moderate loads and are highly dependent on alignment (due to the anisotropy of single crystalline silicon). An example of the complex cracks in silicon is shown in Figure 2.30 from the contribution by Ebrahimi and Kalwani [197]. Also, calibration factors used in the expressions to evaluate toughness are incompatible with silicon due to the non-volume-conserving indentation response of this material, which itself is a consequence of hydrostatic-stress-induced phase transformations underneath the indenter [208–210].

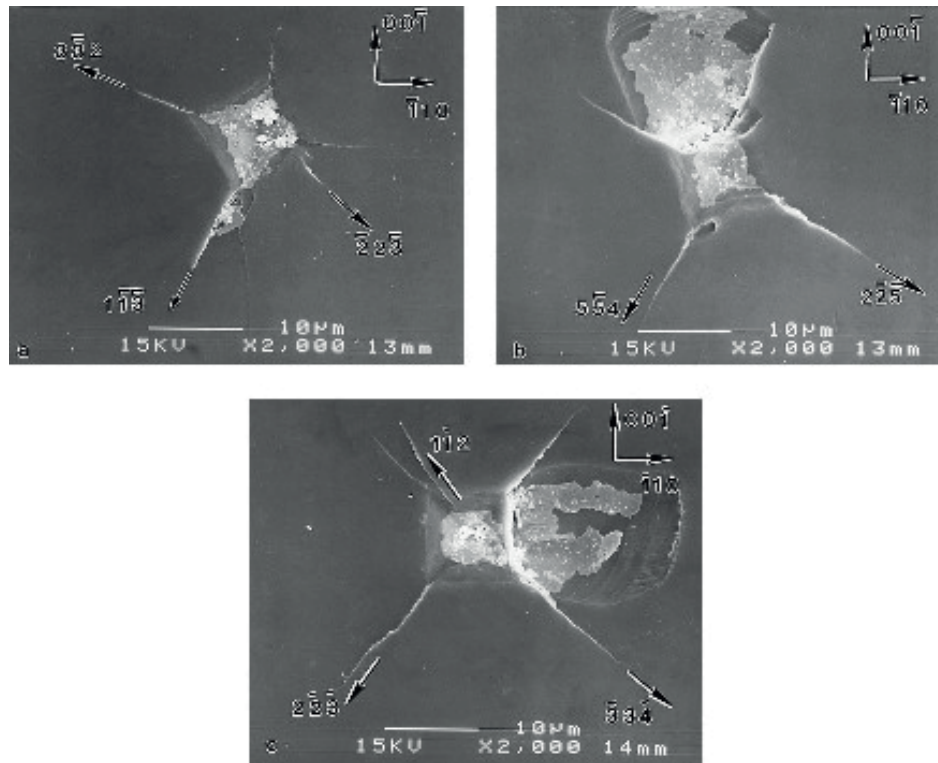


Figure 2.30 Vickers indentations on a (110) plane of single crystalline silicon. The indents are misaligned by 15°, 30° and 45° from the [001] direction in (a), (b) and (c), respectively. Complex crack systems including extensive surface spalling and secondary cracks are observed. (Reproduced from Ref. [197] with permission of Elsevier)

Besides those fundamental interpretation problems, also practical problems can arise when using the indentation toughness method to probe (very) small volumes of material. In work on hard coatings or thin films, due to the small thickness of the probed material, it is a challenge -and sometimes impossible- to produce appropriate indentation cracks [68,211]. This is also the case in tests on small particles embedded in a matrix, such as found in the work by Casellas et al. [194] on the indentation toughness of carbides within tool steel. Here too, cracking patterns are generally too irregular and only marginally smaller than the particles for interpretation, anisotropy is shown to be important (yet difficult to take into account), and results are shown to considerably depend on the expression used to calculate fracture toughness [194]. All these problems and those discussed in the previous paragraph also apply to the only attempt to measure fracture toughness of silicon particles within Al-Si found in the literature, which is the work by Bhattacharya et al. [212,213] where complex fracture systems including lateral cracking and surface chipping, phase transformations underneath the indenter and other complexities are clearly present (Figure 2.31) and results vary significantly depending on the equation used. In view of the drawbacks of the indentation toughness methods (both in general and in the specific case of silicon), in the present thesis no use is made of this technique.

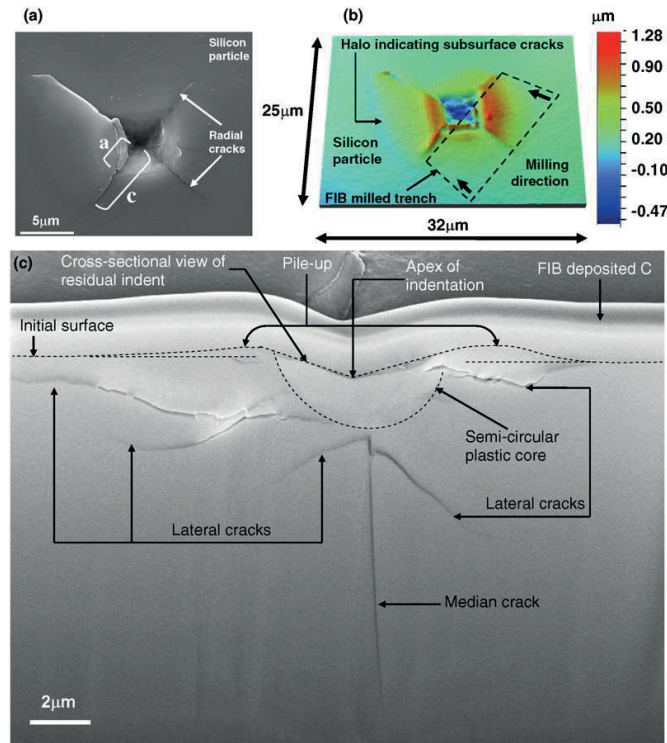


Figure 2.31 Vickers indentation on a silicon particle from an Al-Si alloy; figure reproduced from Ref. [212] with permission of Elsevier. In (c), a complex crack pattern and a plastic core underneath the indent are observed on a FIB-milled cross section of the indent.

A related method that avoids some of the problems encountered by indentation toughness is the recent microscopic pillar splitting test [214–217] developed by Sebastiani et al. [214,215] on ceramic coatings (CrN and others), where it was shown to yield values within 25% of those independently measured by other means. Here, Focused Ion Beam (FIB) milling is used to carve a small pillar into a sample of the material of interest. The pillar is subsequently indented with a Berkovich tip (or potentially another sharp indenter geometry [216]) until fracture (Figure 2.32). The load at which the pillar fractures P_c is finally related via a calibration parameter γ to the toughness of the material K_c using

$$K_c = \gamma P_c / R^{3/2} \quad \text{Equation 2-4}$$

where R is the pillar radius. The approach to estimate γ has been based on cohesive zone finite element techniques [214,215] under a number of assumptions (e.g., isotropic, elastic-ideally plastic material, a given cohesive law) and is a function of E/H . The method presents two important advantages with respect to traditional indentation approaches. First, the material within the pillar is relaxed from residual stresses [218], which can be very important in thin films and coatings. Second, there is no need to perform (often imprecise) post-test measurements such as determining crack lengths. On the other hand, the main drawback is the strong dependence of the results on the insufficiently defined calibration parameter γ .

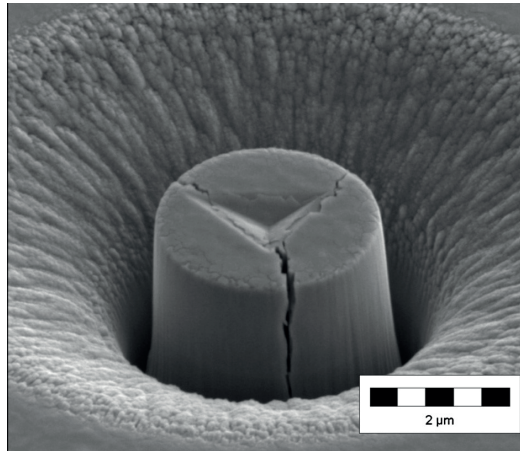


Figure 2.32 A micropillar produced into TiN and subsequently indented with a Berkovich tip. This is an example of the pillar splitting method for fracture toughness measurement. (Reproduced from Ref. [215] with permission of Elsevier)

Other approaches that use samples free of initial cracks or notches include experiments in which cracks appear in small samples of simple shape (spheres or cylinders) under uniaxial compression [219–221] or where through-thickness cracks are produced in stacked and bonded thin films subjected to in-plane tensile [222] or compressive (buckling) deformation [223]. None of these methods, however, can be applied on microscopic reinforcing particles such as Si in Al-Si alloys.

Micrometric toughness test samples have alternatively been produced using selective microetching, or Focused Ion Beam (FIB) micromilling techniques. Testing such samples comes much closer to conventional macroscopic fracture toughness testing practice: here, miniature precracked or prenotched beams are produced and loaded, often using a nanoindentation apparatus, and the fracture toughness is computed from a measurement of the applied load at the onset of rapid crack propagation. Miniature fracture toughness tests come in a variety of configurations; most often, small-scale cantilever beams or tensile samples are produced along a polished surface of the material to be tested. If the material to be tested is a coating or a thin film, photolithography-based selective (plasma or chemical) etching can be used to machine sidewalls of the beam, which is then freed from its substrate by etching the latter selectively [224–234]. Alternatively, toughness test samples can be carved out (also into bulk material samples) entirely by FIB milling, as shown by Li et al. [235] in 2003 (Figure 2.33). Di Maio and Roberts [236], in 2005, measured fracture toughness of silicon using smaller microcantilever beams (10 μm in length) with a straight-through FIB-milled notch. The approach was further developed by many other authors [216,217,237–248]. Microscopic FIB-notched cantilever [216,217,236–242,244–247,249,250] (Figure 2.33 and Figure 2.34), double cantilever beam samples [216,217,251] (Figure 2.35) or clamped bending beams [216,243,248,252] (Figure 2.36) have been produced in this way.

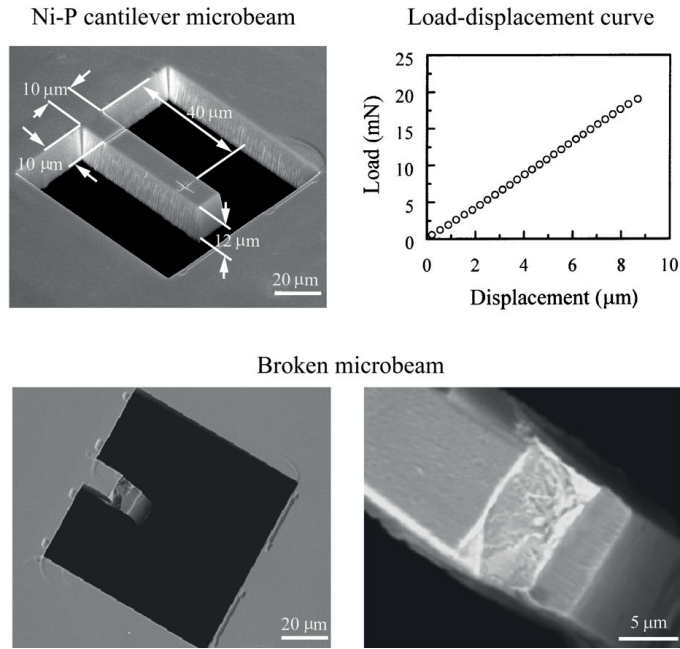


Figure 2.33 Notched microcantilever beam produced by FIB milling into a Ni-P film, tested to fracture using a nanoindenter. (Reproduced from Ref. [235] with permission of Elsevier)

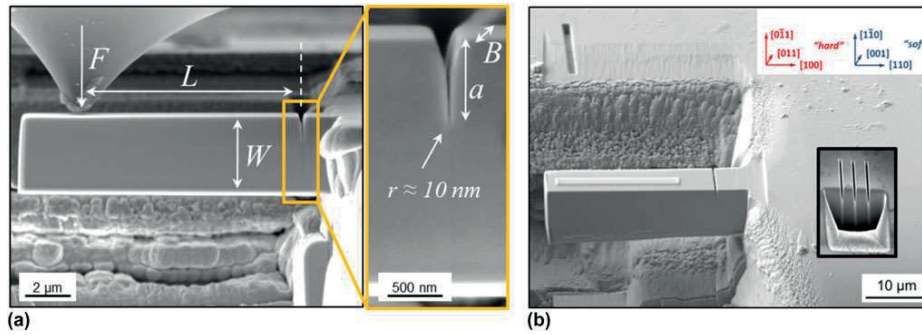


Figure 2.34 FIB-produced straight-through notched microcantilever beams of NiAl to probe fracture toughness; figure from Ref. [242] with permission of Cambridge University Press.

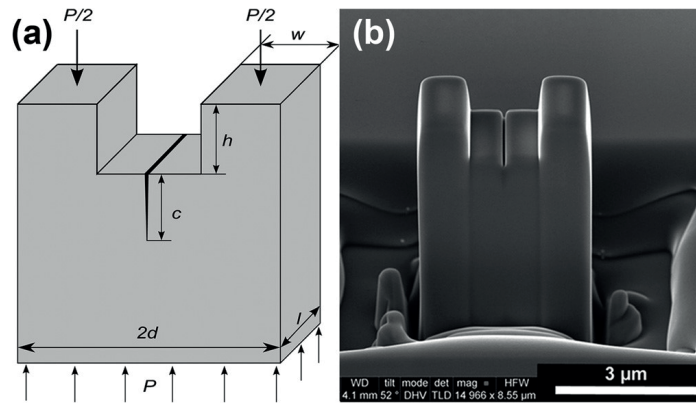


Figure 2.35 Microscopic double cantilever beam produced using FIB-milling into SiC to measure fracture toughness; figure from Ref. [251] with permission of AIP Publishing LLC.

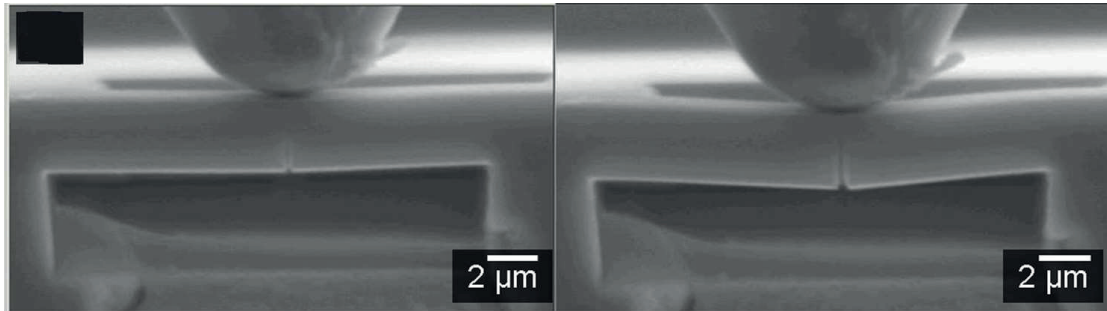


Figure 2.36 Microscopic clamped bending beam in single crystalline silicon to probe fracture toughness; figure from Ref. [253] with permission of Springer.

The greatest challenge is most often to create a precrack in such small-scale samples. Early attempts [224,254–256] used samples having relatively wide, straight-through, prenotches, roughly 1 μm or so wide, instead of precracks. This led to grossly exaggerated K_{Ic} values. In 1998, Kraft et al. [225] used FIB milling to produce a straight-through prenotch on microcantilever beams produced by lithography. Nowadays, prenotching is often done by FIB milling, using a low intensity beam in final stages of the process so that the tip radius of what is, in fact, a milled notch be made as small as possible. Resulting notch root radii range from a few tens to several hundreds of nanometres (e.g. [216,225,228,232,236,240,241,244,246,249,257–269]). Beyond the need to produce a notch of sufficient sharpness, another difficulty with ion-milling lies in producing a uniform notch depth and/or width.

Testing of small-scale beams containing FIB-premachined notches has been shown in several studies to give K_{Ic} values near those found for macroscopic samples [216,237,240,257,263,264]; however, in many other studies different results, ranging from values slightly to much higher [228,236,241,243,258,260–262,269–271], or in some cases lower [259,272] data than toughness data from tests on macroscopic specimens of the same material, were obtained with FIB-notched specimens. This betrays an obvious disadvantage of this method: failing a comparison of notched microsample test data with separate results from valid tests conducted on macrosamples, there is little way of knowing *a priori* that test data were not biased by the initial bluntness or other defects of the micromachined prenotch. This is problematic in view of this thesis' objective, because such a comparison is impossible to do in the case of reinforcing particles within alloys. Another important disadvantage, which is shared also with earlier etch-based notching methods [273], is that the nature and the morphology of the notch surface, which will often play an important role in fracture initiation, may be affected by the notch machining process. Focused ion beam milling is indeed well-known to cause significant implantation and irradiation damage, and also to redeposit removed material along the periphery of the beam trajectory and to induce residual stresses within that material and its surroundings [274–276].

These pitfalls of notched versus precracked toughness samples have motivated the development of workarounds. Matoy et al. [237,239], in their studies on thin film samples of silicon oxide, nitride or oxynitride, machined the prenotch straight-down in the central part of the sample only, leaving two side walls (Figure 2.37). This way, a sharp precrack is formed upon bend-testing following the fracture of the two thin side walls. In another example, the microsample precrack is made by a fracture process that produces, before the microsample is machined, a precrack of relatively well-controlled depth. In Ref. [238] such precracks were produced by machining microsamples into one fracture surface of a larger previously fractured specimen, using sidecracks as precracks. In Ref. [277] internal defects, the size of

which was deduced by post-test fractography, were used as precracks. Use has also been made at times of the presence of internal planes of lowered fracture energy (interfaces or embrittled grain boundaries) to nucleate and guide the crack [238]. A very elegant method in this vein is that demonstrated initially by Kahn *et al.* [273] and subsequently used by several other laboratories, in which thin films are precracked using a hardness indenter before being etched and separated from their underlying substrate, with a portion of the precrack remaining in the etched thin-film test specimen. In this way, tensile or bend specimens amenable to testing could be produced (Figure 2.38). Once the method was perfected, these often gave data consistent with data from macroscopic tests of the same material (Si notably) [68,270,273,278–281]. Finally, some authors have used fatigue of notched microspecimens to create precracks in metallic specimens (which are, however, prone to large scale yielding) [282–284] and also in polycrystalline silicon [285], in the latter case by an electrostatic resonance method.

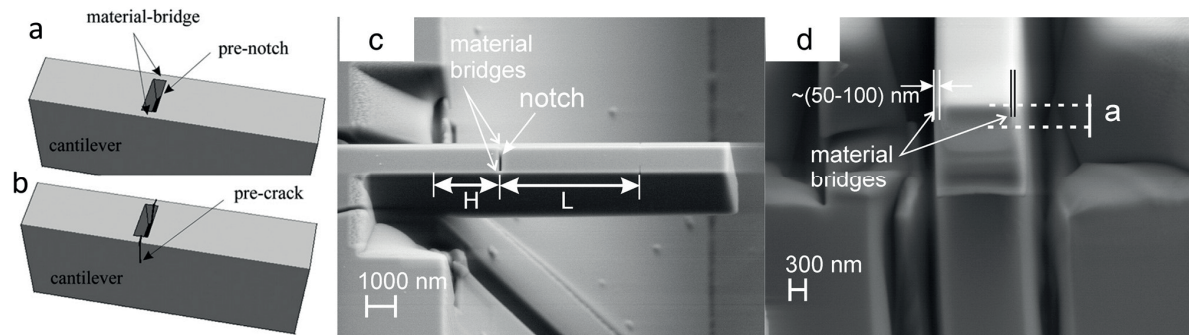


Figure 2.37 Approach to produce a precrack in a microcantilever beam for fracture toughness testing; figure adapted from Refs. [237,239] with permission of Elsevier. A pre-notch is milled with the FIB leaving pristine bridges at the sides. These will initiate a crack when the cantilever is bent.

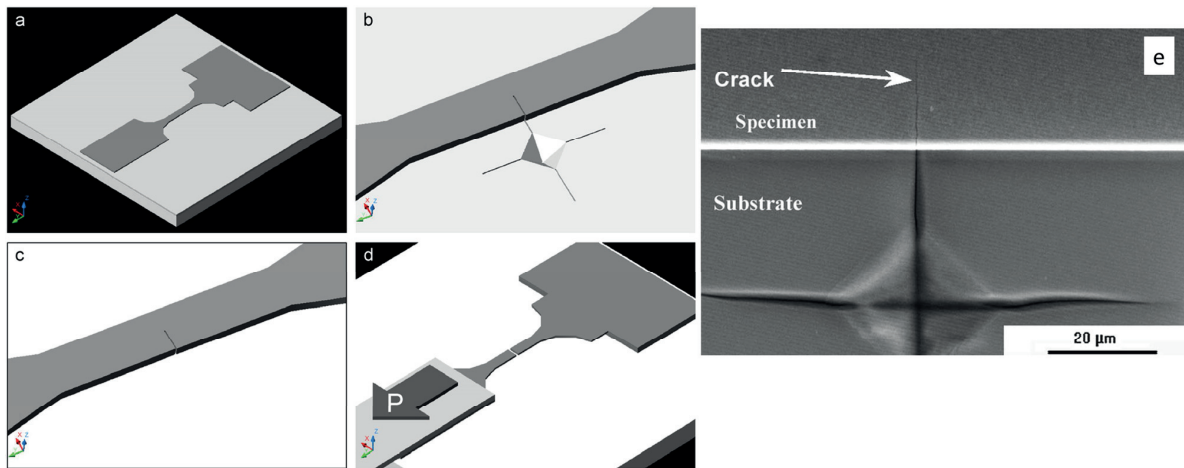


Figure 2.38 (a-d) Fracture toughness testing of a pre-cracked thin film specimen. The precrack is introduced by a Vickers indentation on the substrate, which is subsequently etched away before the mechanical test (Reproduced from Ref. [233] with permission of Elsevier). (e) An SEM image of the Vickers indentation and the crack running into the specimen (Reproduced from Ref. [280] with permission of ASME).

2.4 Small-scale strength testing

Measuring strength at mesoscopic scales presents a series of challenges with respect to conventional, macroscopic, testing. Issues related to specimen manipulation, positioning, gripping, alignment, sensitivity of the measuring devices and post-test sample recovery to examine fracture surfaces are exacerbated when probing miniature specimens. Yet, much progress has been achieved and many testing techniques have been developed including miniature tensile testing [286–294], bending of nano- or microwires [295–297], microbeam bending [65,225,298], nanoindentation [299,300], micropillar compression [301–303], indirect tensile testing (such as the theta specimen [304–306]) and biaxial flexure specimens [307–311,230]. As will be seen in the next paragraphs, the areas that have motivated small scale testing for mechanical properties are thin films and coatings [298,307–309,312], micro/nano-electromechanical systems (MEMS) [65,291,313–315] and research on plasticity at small scales [301,302].

Bending was the first approach used to probe micro samples (roughly at the same time as tensile testing of whiskers was developed [286,316,317], see below). In 1952, Herring and Galt [295] bent tin whiskers 2 μm in diameter and calculated the strains from the whiskers' radius of curvature upon bending. The method was then used in 1958 by Webb and Forgeng [318] in what constitutes a pioneering work on probing the strength of the second phase of two-phase alloys. In that work, microscopic iron carbide (Fe_3C), chromium nitride (Cr_2N), chromium oxide (Cr_2O_3), and chromium metal crystals were extracted from the alloys using chemical etching to dissolve the metallic matrix and were then tested in bending. Of interest in the present context is the fact that the authors also extracted silicon particles from an Al-Si alloy, but were not able to test them [318]. At about the same time, in 1957, Pearson et al. [296] used a similar but better controlled approach to probe single crystal silicon microwires of different cross-sections at several temperatures. The microwires were fixed at their ends and centrally bent using a small hook (Figure 2.39). The stress within the samples was estimated by measuring their deflection. Interestingly enough, nanowire bending is still done nowadays in a similar fashion. Stan et al. [297,319] bent silicon nanowires of diameters as small as 20 nm by manipulating the wires using an Atomic Force Microscope (AFM). The stress at failure was also estimated from their deflection resulting in measured values as high as 18 GPa [297].

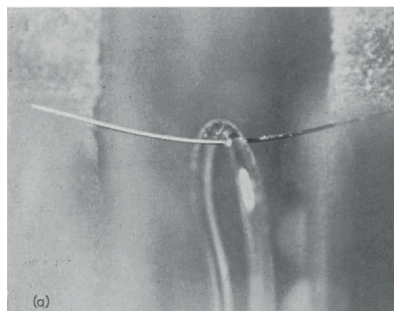


Figure 2.39 Silicon whisker roughly 20 μm in diameter bent using a small quartz hook; reproduced from Ref. [296] with permission of Elsevier.

In most cases, however, microscopic bending testing is done using microbeams shaped either as cantilevers or having fixed ends; typically, elastic, plastic and/or fracture properties can be extracted (in the latter case using notched or precracked specimens, as described above in Section 2.3). In the pioneering work of Weihs et al. [298], thin films were deposited on a silicon wafer, which was subsequently subjected to patterning using photolithography and wet etching, resulting in cantilever beams of the thin film material extending over a large silicon trench (Figure 2.40). Loading was done with a nanoindenter,

which records the load-displacement response, and simple beam theory was used for test interpretation. Already in this early work it was recognized that the spring constant of the nanoindenter must be taken into account in the measured displacement (because nanoindenters are typically highly compliant machines) as well as the extra displacement of the indent into the material at the load-application point. As was already mentioned in the previous Section, microbeams for bending can also be produced by micromilling using a Focused Ion Beam (FIB) [320], which provides versatility because specimens can be carved into any material including bulk materials along their surface. Furthermore, test interpretation is often done using finite element modelling when conditions are such that simple beam theory is no longer valid [65,312,321].

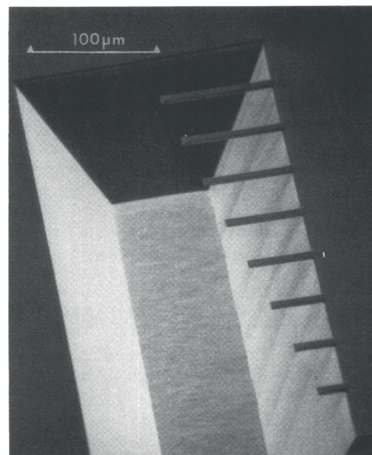


Figure 2.40 Microcantilever beams of a SiO_2 thin film extending over a deep trench in a silicon wafer, produced by photolithography followed by wet etching; reproduced from Ref. [298] with permission of Cambridge University Press.

Microbeam bending techniques have been used, for example, to characterize thin layers on stiff substrates using coated microbeams [322,225,313,312]. Moreover, closer to the scope of this thesis, microbeam bending has also extensively been used to measure the strength of brittle materials [70], notably silicon [323,65]. Ericson and Schweitz [323] tested silicon micro cantilever beams in a SEM and extracted fracture statistics out of the samples. A salient observation of their work -as well as of other works in the literature [65,306]- is that the strength distribution of silicon microbeams varied significantly depending on how the silicon wafer surface was prepared (e.g., the parameters of the polishing and the etching procedure). This betrays one of the main drawbacks of using microbeams to probe the strength of brittle materials: the surface subjected to the largest tensile stress, which is where fracture initiates, is typically either polished, etched or ion-milled and is hence subject to artefacts. This is not necessarily undesired when materials for MEMS applications are characterized because MEMS devices are produced using those kinds of procedures and therefore the microbeams may represent an in-service condition; however, surface artefacts need to be suppressed if an investigation aims to probe pristine material, as is the purpose of this thesis regarding silicon particles.

The problem of probing a polished surface also applies to the rarely used indentation methods to probe strength. As known, conventional microindentation is broadly used to measure hardness of all sorts of materials including individual phases within alloys, and more recent instrumented nanoindentation techniques have also been used to extract elastic and viscoelastic properties. Also, as discussed in the previous Section, fracture toughness techniques have been developed using indentation and, finally, indentation is frequently used to produce pre-cracks into specimens that are subsequently probed using

a more conventional test such as the 3- or 4-point bending test [324]. Direct strength measurements from indentation are, on the other hand, much less conventional. There is, nevertheless, an approach to measure local strength of brittle materials based on spherical indentation. Recalling the Hertzian fracture toughness test described in the previous Section, spherical indentation can produce ring-cone cracks that initiate at the sample surface around the indenter in a zone of high tensile stress [176,325,326]. Here, however, the objective and hence test interpretation are different. The idea is that the probability to initiate a crack depends on the probability of finding a critical defect within the stress field. Test interpretation is, however, difficult because of the complex indentation stress field. Also, note that, here too, it is the surface flaws (surface roughness) of polished samples which are probed. The method thus has seldom been used for the measurement of the strength of materials [327,328]. Furthermore, another reason why this approach is not useful for the purpose of this thesis is that indentation in silicon at small scales produces half-penny or median cracks rather than cone cracks, even when using a spherical tip [329].

In contrast to indentation, important mechanical properties such as elastic modulus, elongation to failure and strength values can readily be extracted from conventional tensile testing, which is hence a key test of materials at macroscopic scale. It seems thus natural that researchers devised miniaturized versions of the tensile test to measure those properties on small samples. Experimental challenges are related to specimen handling and mounting, sensing, and test actuation among other issues. The literature on micro- and nanotensile testing is vast; a detailed review was published by Gianola and Eberl [291]. One of the earliest microscopic tensile test was reported by Eisner [317] in 1955, in which a clever use of simple technologies available at the time was made. Silicon whiskers with diameters in the order of 1 μm were glued from their ends to wire loops, one of which was attached to the small 33 g bob of a 330 cm-long pendulum, while the other wire was attached to a mechanical micromanipulator used to actuate the test (Figure 2.41). The displacement of the pendulum bob from its equilibrium position was used to quantify the force: 0.1 mN of tensile force was applied on the whisker per each 1 mm displacement of the bob. The highest fracture strength of a silicon whisker that was measured in that work was 3.8 GPa [317]. Also pioneering works on microtensile testing are those of Gyulai [316] in 1954 on NaCl whiskers and Brenner [286] in 1956 on metal whiskers.

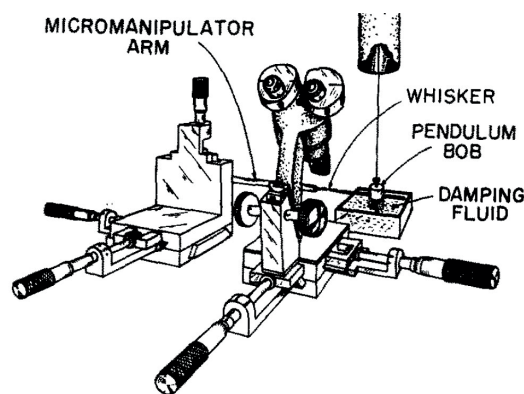


Figure 2.41 Set-up for tensile testing of whiskers reported by Eisner in 1955; reproduced from Ref. [317] with permission of Elsevier.

More recent and conventional micro tensile testing approaches have used miniaturized dog-bone specimens. These can be produced, for example, using evaporation techniques or electrodischarge machining [330,331]. Gripping and handling of such specimens, however, is quite inconvenient due to their

fragility related to their small size. Alternatively, microfabrication techniques including lithography and etching have been applied to co-fabricate tensile specimens as part of a MEMS [290], or attached to a frame [287,288,332] (Figure 2.42a). In this way, manipulation and alignment issues are largely overcome. Tensile samples within a frame have also been produced using FIB milling [293]. In most frame designs, the frame walls parallel to the specimen are cut with a small saw just before the tensile test, so that only the free-standing specimen will sustain the applied force upon testing [293,332,333]. Noteworthy is the fact that this concept has also been used to probe reinforcing fibres used to produce composite materials, including Metal Matrix Composites (MMCs); here, a paper or cardboard frame onto which the fibre is glued, transported, and placed in the testing apparatus. Examples are the work of Cantonwine [334,335] and work in our laboratory [336] (Figure 2.42b-c), where nanocrystalline alumina Nextel 610 fibres 12 μm in diameter were individually probed in tension. Other tensile testing methods use a micromanipulator needle inside the SEM to probe nanowires fixed using electron beam induced deposition [292] (Figure 2.43). Finally, approaches have been developed to produce uniaxial tension by applying compressive force via a nanoindenter. Examples are the theta specimen (Figure 2.44) [304–306] and the Push-to-Pull device by the micromechanical testing brand Hysitron® (Figure 2.45) [294,337]. In the former, the specimen is part of the structure produced by lithography, while in the latter, the specimen (a micro or nano wire) is glued to the testing device.

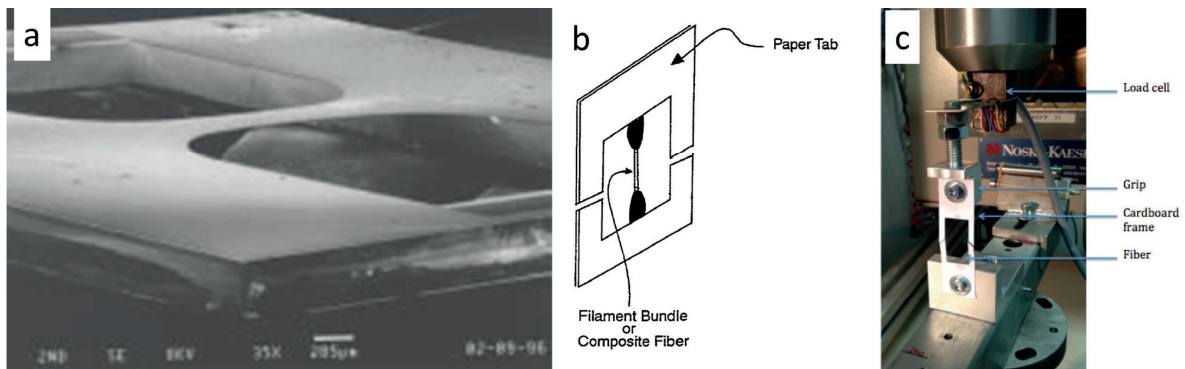


Figure 2.42 (a) Tensile specimen (in the centre of the picture) produced within a frame using semiconductor fabrication techniques; reproduced from Ref. [332] with permission of IEEE. **(b-c)** A frame (in this case made of cardboard) can be also used to probe small fibres, which are glued at the centre [335,336]. In this way, handling and alignment issues are largely avoided. The sides of the frame are cut with a small diamond saw in (a), or with scissors in (b), just before starting the tensile test.

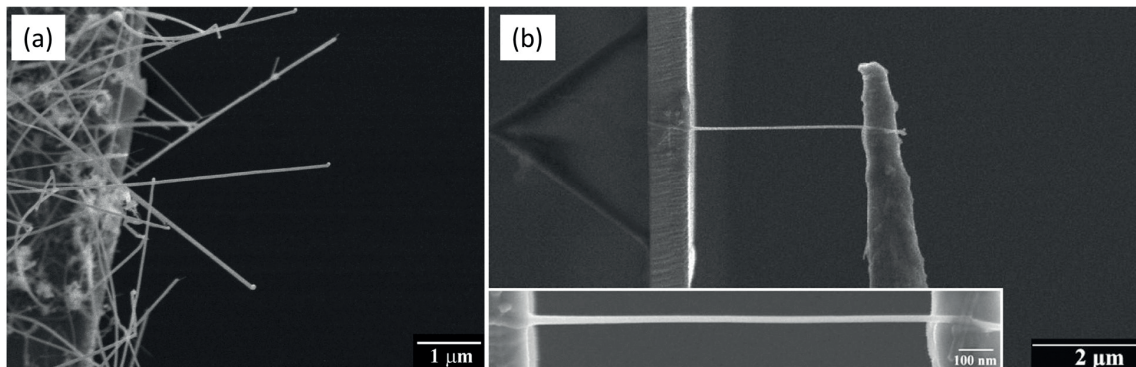


Figure 2.43 (a) Silicon nanowires synthesized using a vapor-liquid-solid approach. **(b)** Tensile testing of one of the nanowires in (a). (Adapted from Ref. [292] with permission of American Chemical Society)

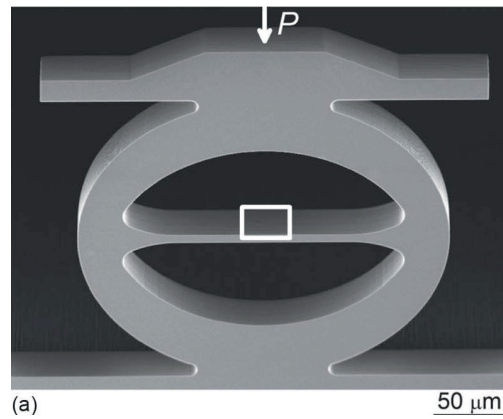


Figure 2.44 “Theta” silicon specimen produced using lithographic methods for indirect tensile testing; figure reproduced from Ref. [306] with permission of IEEE. Upon de application of the load P , the beam in the centre undergoes tensile stress.

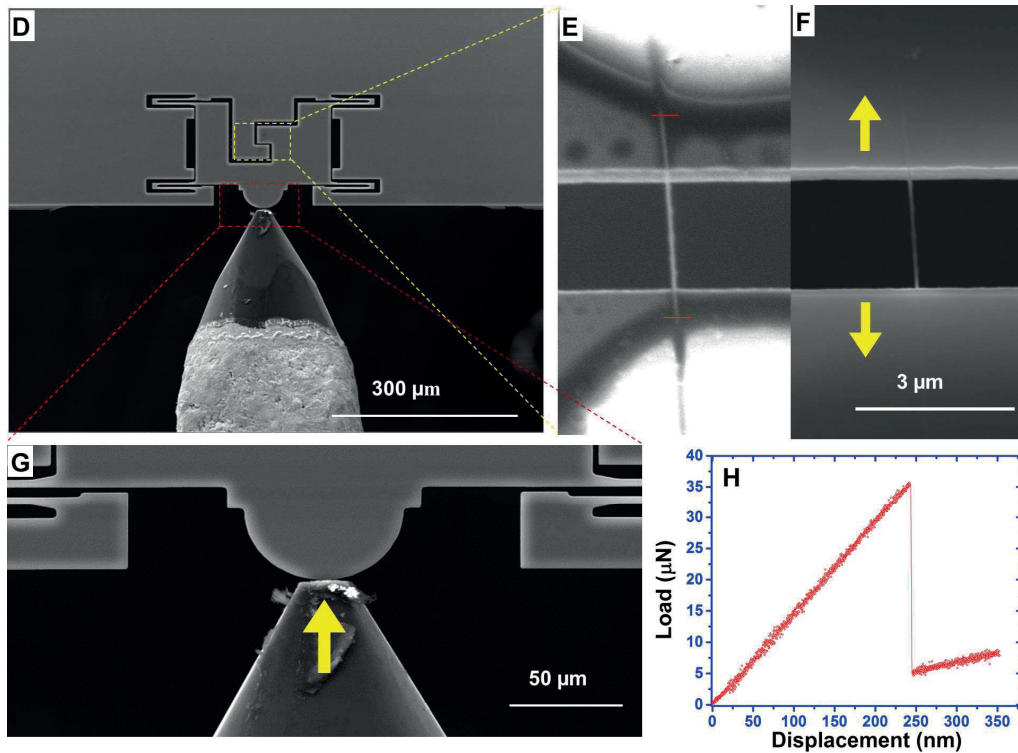


Figure 2.45 (D) “Push-to-pull” device for indirect tensile testing. Load is applied using a nanoindenter as shown in (G). The close-ups in E and F show the tensile specimen, while the load-displacement response is shown in (H). (Reproduced from Ref. [294] with permission of AAAS)

In the mid 2000’s, Uchic et al. [301,302] introduced the micropillar compression test. Typically, FIB milling is used to carve a pillar with a square or circular cross section of micro or nanometric dimensions into a sample of the material of interest (Figure 2.46). The pillar is subsequently compressed using a nanoindenter mounted with a flat punch and load and displacement are recorded. This method has mostly been used to study plasticity size effects in metals and alloys; nevertheless, some researchers

have also tested brittle materials and evaluated fracture strength as the engineering stress at the moment of pillar failure [221,338,339]. The main concern about this technique is linked with the artefacts introduced to the specimen (the micropillar) by FIB micromachining. The influence of FIB damage on the mechanical response is clearly shown in the work of Shim et al. [340]. In that work, a eutectic NiAl-Mo alloy was solidified directionally to produce a composite of regular, aligned, Mo-rich fibres within a NiAl matrix. The sample was then polished perpendicular to the fibres axis and the matrix was etched away, leaving the fibres ready to be tested in compression. Results showed that the mechanical response of those pillars was very different from that of micropillars of the same material produced by the more conventionally used FIB milling method [340] (Figure 2.47). FIB-artefacts on nanopillars and their influence on tests data vary with the material. For example, Dietiker et al. [341] compared gold pillars prepared by nanoimprinting with pillars prepared using FIB and found that the difference in mechanical behaviour was negligible. In silicon, however, artefacts in pillar response associated to FIB milling have been demonstrated: as shown in Figure 2.48, silicon nanopillars in the as-FIB-milled condition show a mechanical response very different than that of heat-treated nanopillars [342,343]; it has been shown that this is related to FIB-induced surface amorphization, which in turn enhances incipient plasticity in the neighbouring Si material (this is further discussed below in Section 2.5).

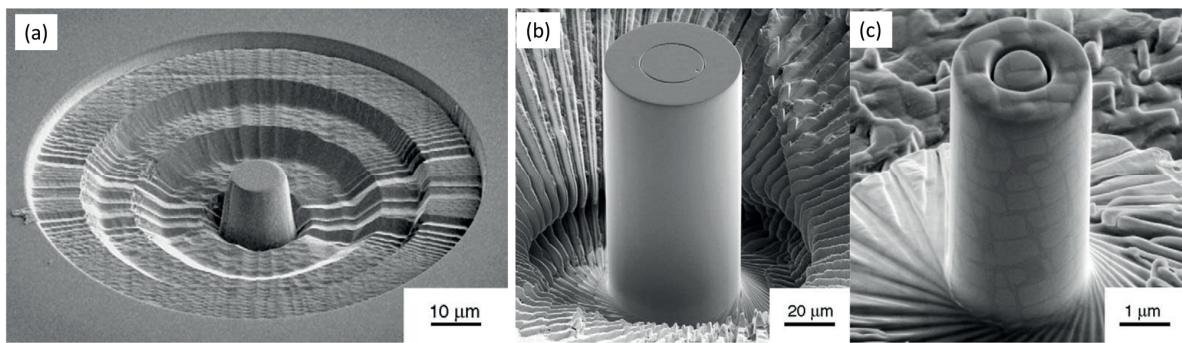


Figure 2.46 (a) Intermediate stage during fabrication using FIB milling of a micropillar. **(b-c)** Two micropillars of different size prepared using FIB-milling ready to be tested in compression. (Adapted from Ref. [302] with permission of Elsevier)

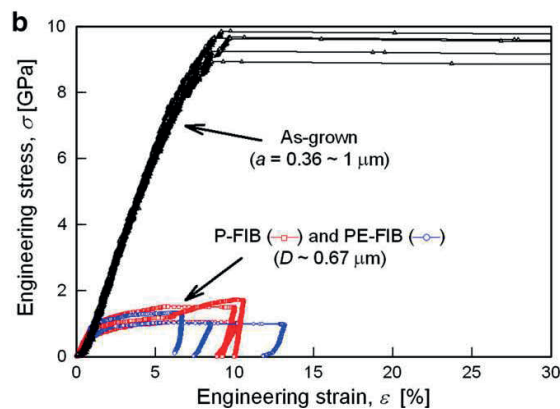


Figure 2.47 Stress-strain response of micropillars of Mo-alloy produced with and without FIB. The effect of FIB milling on the mechanical response of micropillars is shown to be very strong. (Reproduced from Ref. [340] with permission of Elsevier)

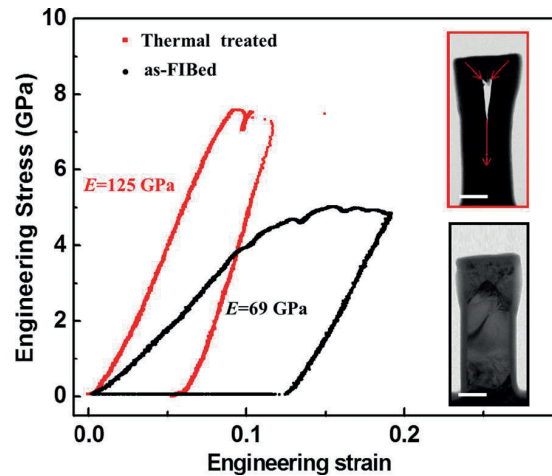


Figure 2.48 Stress-strain response of silicon nanopillars (scale bar is 100 nm) shown to be different in the as-FIB-produced and in the heat-treated conditions. FIB-milling produces a layer of amorphous Si with implanted Ga on the pillar surface (this is further shown in Figure 2.50), which enhances plasticity. This layer is recrystallized upon heat-treatment. (Reproduced from Ref. [342] with permission of AIP Publishing LLC)

It has been said in Chapter 1 that some of the most common tests that have been used to probe the strength of small particles are the particle compression test and the fracture-by-impact test [62,220,344,345]. With both tests, the fact that hard platens are used brings along a fundamental problem: the effects of intrinsic particle defects, which would in other conditions trigger particle fracture, are in those tests superseded by microcracking at the platen-particle contacts. The local damage at the contacts, which is a result of the very large contact stresses in those contact regions, drives fracture instead [346]. This problem has been recently tackled by means of a microscopic particle compression test that uses elastoplastic platens, which has been developed as part of the PhD thesis work of V. Pejchal (from the same EPFL laboratory as the author of this thesis) [347].

Alternatively, Wereszczak et al. [348] developed an interesting approach to measure strength of brittle bearing-grade silicon nitride (Si_3N_4) spheres 12 mm in diameter. This test uses the concept mentioned above, namely it produces tension via the application of a compressive force. Note that the work in Ref. [348] is on a larger scale than all the other approaches described in this Section; nevertheless, the approach inspired one of the micromechanical methods that were developed and used within this thesis (the “C-shape” test) and hence it is worth describing it here. In that work [348], a slot (a wide notch) is machined into the balls in such a way that upon uniaxial compression, tensile stress is produced along an outer surface of the ball. The so-called “C-sphere” specimen is shown in Figure 2.49. Fracture of the specimen into two pieces initiates at the outer surface of the remaining ligament opposite to the slot, in the area where tensile stress is the highest. To extract the particle strength, the stress field produced by the measured force at failure is calculated using finite element modelling. Test interpretation is thus relatively simple compared to traditional crushing tests.

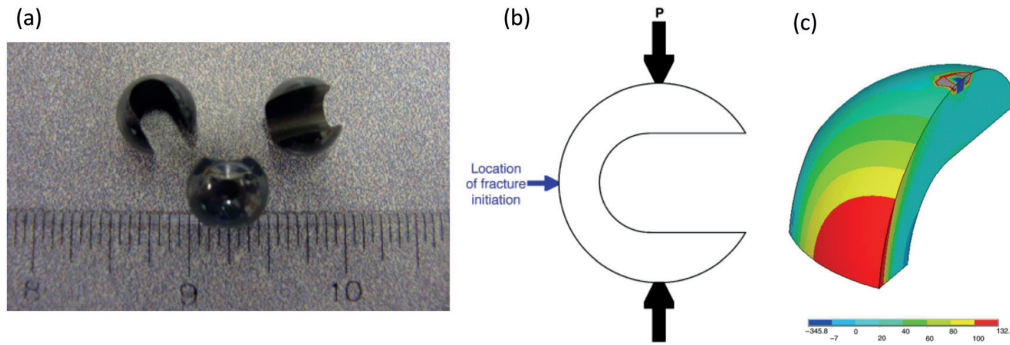


Figure 2.49 (a) Silicon nitride pebbles featuring a large notch that was machined to produced so-called “C-sphere” specimens. (b) Schematics of the test: upon the application of an increasing compressive force, the material at the external surface of the ligament is subject to tensile stress. (c) Maximum principal stress field on a quarter model of a C-sphere specimen, showing the region of high tensile stress. (Figure adapted from Ref. [348] with permission of John Wiley & Sons)

To summarize, micromechanical testing samples are typically produced either using semiconductor device fabrication processes such as lithographic patterning and etching, or using micromachining techniques, for which Focused Ion Beam (FIB) milling has become a fundamental tool over the last years. Such tests are now nearly routine; however, the data they yield are subject to artefacts because specimen surfaces produced by polishing, by etching or by ion-milling are generally damaged. This consideration shall thus be taken into account for the micromechanical tests to be developed in this thesis to probe reinforcing particles.

2.5 Fracture properties of single crystalline silicon

While fracture toughness measurement attempts of the silicon particles within Al-Si alloys are limited to the work of Bhattacharya et al. [212,213] (discussed above), much is found in the literature on the properties of electronic grade silicon. Silicon’s overwhelming technical importance has prompted numerous studies of its fracture behaviour, which is subject to several complexities, e.g. fracture anisotropy [197,260,349], a brittle-to-ductile transition (BDT) [350–353], initiation fracture toughness [354,355] and associated environmental effects [356], slow crack growth [357], dynamic fracture and instabilities [358,359], fractal fracture surface characteristics [360] or failure mechanisms specific to applications such as in lithium-ion batteries [361]. Moreover, its availability in virtually defect-free single-crystalline high-purity form has made silicon an oft-used model material for the general study of brittle fracture (even though its fracture characteristics are highly complex).

A bird’s eye view of the literature on the fracture of silicon reveals much scatter and inconsistency across the fracture toughness values reported. In their extensive review on silicon properties, Del Rio et al. [164] provide a critical survey of published measurements (at any scale) of silicon’s fracture toughness at room temperature. Focusing on silicon’s lowest energy planes, i.e. the (111) and the (110) planes, reported values cover the ranges $K_{Ic(111)} = 0.65 - 1.7 \text{ MPa}\sqrt{\text{m}}$ and $K_{Ic(110)} = 0.7 - 2.5 \text{ MPa}\sqrt{\text{m}}$. For comparison, values that have been predicted from bond energy and elastic moduli considerations are $K_{Ic(111)} = 0.72 \text{ MPa}\sqrt{\text{m}}$ and $K_{Ic(110)} = 0.73 - 0.82 \text{ MPa}\sqrt{\text{m}}$ [164]. Such a degree of scatter is impressive, particularly if one recalls that the surface energy is ultimately proportional to K_{Ic}^2 . In sections C6-C8 of Ref. [164], however, it is pointed out that a number of studies in the literature must be excluded due to their lack of accuracy and precision arising from basic flaws of methodology (notably data gleaned from nanoindentation cracking or from pre-notched specimens, as discussed in previous paragraphs). Also,

among the data, the lowest experimental values reported (i.e. $0.65 \text{ MPa}\sqrt{\text{m}}$ [164,362,363]) were later re-analysed yielding higher results [350]. Taking into account these considerations, the range of reliable experimental measurements on the (111) fracture plane (which is, as will be seen, the plane of most interest to this thesis) is narrowed to $K_{\text{Ic}(111)} = 0.83 - 1.0 \text{ MPa}\sqrt{\text{m}}$. This can be expressed in terms of the critical strain energy release rate G_{Ic} by using $K_{\text{I}} = \sqrt{G_{\text{I}}M_{(111)}}$ with $M_{(111)} = 178 \text{ GPa}$ the effective modulus accounting for anisotropy [164], which leads to $G_{\text{Ic}(111)} = 3.9 - 5.6 \text{ J/m}^2$ (to be compared with the predicted fracture energy $2\gamma_{(111)} = 2.94 \text{ J/m}^2$ [164]).

Adding to this complexity, the small-scale testing community has provided interesting data and observations on single crystalline silicon, particularly over the last 10 years. Nakao et al. [271] measured a BDT temperature as low as 65°C using single-edge notched tensile specimens $45 \mu\text{m}$ wide and $4 \mu\text{m}$ thick with a 1 to $2 \mu\text{m}$ notch introduced by Focused Ion Beam (FIB) milling; this value is in strong contrast with BDT temperatures documented for bulk silicon, which are around 600°C [210] (the exact value depends on the orientation and the strain rate [351,364]). Also, it has been acknowledged that dislocation motion is enabled at room temperature in nanometre-scale silicon samples [365–367]. This has been observed in compression tests of nanoparticles less than 100 nm in diameter [219,220,368], during *in-situ* TEM nanoindentation [369] or nanowire tension [370] tests, and in FIB-produced nanopillars of diameter below 400 nm [221]. In nanopillars, a strong influence of the FIB in promoting dislocation activity has later been proven [342,343] (Figure 2.48). Namely, it was shown that FIB-milling introduces an amorphous surface layer confining crystalline silicon, which first enhances incipient plasticity and then, as deformation progresses, leads to amorphization (followed by further deformation) of the crystalline silicon within the bulk of the pillars [343] (Figure 2.50). Another potential concern regarding some of the studies cited above is the possible influence of the high energy electron beams used for *in-situ* TEM tests on the mechanical response of silicon nano-sized samples, an effect that has been demonstrated in other materials [371,372] but found to be negligible in Si nanopillars by Wang et al. [343], who measured the same response on 150 nm nanopillars tested with the beam on or with the beam off.

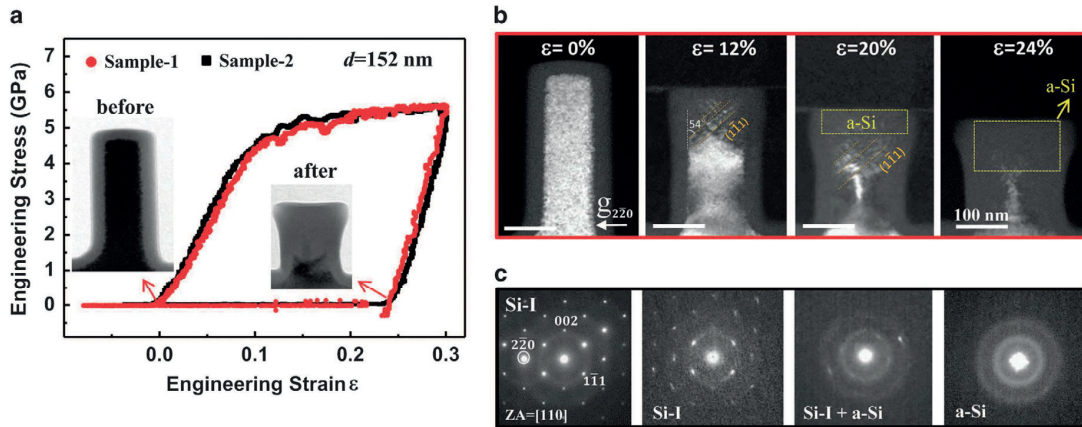


Figure 2.50 Deformation-induced crystalline-to-amorphous transformation during the TEM *in-situ* compression test of a silicon nanopillar prepared by FIB-milling; figure reproduced from Ref. [343] under Open Access licence CC-BY. Stress-strain response is shown in (a). Bright field TEM images as a function of strain are shown in (b), where slip bands along $\{111\}$ planes are visible. Note that in the inset images in (a) and (b), amorphous silicon, which initially coats the pillar surfaces, is grey. Crystalline silicon is black in the inset images in (a) and white in (b). Selected area diffraction patterns in (c) show the transition from diamond cubic Si into amorphous Si.

Early TEM examinations [373,374] have led to generally accept that silicon is an example of a perfectly brittle crystalline material at room temperature, i.e. featuring atomically sharp cracks and no dislocations around the crack tip. Later work in 1994 by Langer et al. [375] showed, however, the emission of dislocations from the tip of a growing crack during an *in-situ* bending test in the TEM at room temperature (Figure 2.51). While this observation might also have betrayed an influence of ion-milling (as mentioned above), the recent work by Adhika et al [376], on samples free of such potential artefacts, has shown dislocations at the tip of cracks in the $\{110\}$ fracture plane produced by Vickers indentation at room temperature and examined *post-mortem* in the TEM. These dislocations induce a compressive stress state at the crack tip, which will cause crack tip shielding (Figure 2.52). Limited but finite crack tip plasticity in silicon has thus been proposed to explain the fact that measured critical strain energy release rates are normally higher than surface energies in many brittle and semi-brittle materials, including silicon [377]. It is interesting to note, on the other hand, that there are also works that challenge the occurrence of plastic deformation in nanometre-sized silicon samples: fully elastic behaviour until fracture was observed on nanowires 100 nm in diameter tested in tension [294] and on nanowires down to 20 nm in diameter tested in bending [297]. Note, however, that none of those works used samples that were prepared by ion-milling or pre-cracked.

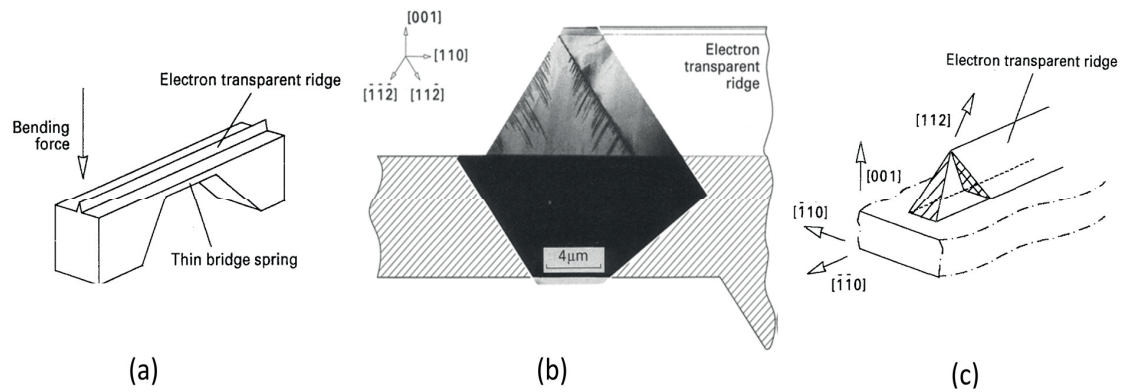


Figure 2.51 Observation of dislocations emitted from cracks in silicon (from the work of Langer et al. [375], reproduced with permission of Springer) (a) Geometry of the silicon specimen fabricated by etching and ion milling, tested in bending at room temperature in a TEM. (b) TEM image in $[1\ \bar{1}\ 0]$ projection after fracture. Failure was preceded by the propagation of two cracks in $\{111\}$ planes (dashed planes in (c)), one along $[\bar{1}\ \bar{1}\ \bar{2}]$ and the other one along $[1\ 1\ \bar{2}]$, which emitted dislocations.

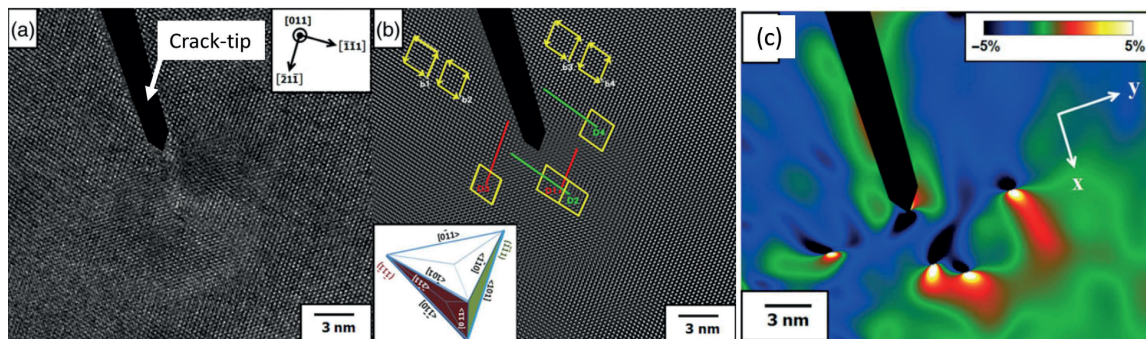


Figure 2.52 Original (a) and filtered (b) high resolution TEM image (HRTEM) of a crack tip in single crystalline silicon produced by Vickers indentation at room temperature. Dislocations are observed near the crack tip. The strain field calculated using geometric phase analysis based on the HRTEM image indicates crack tip shielding. (Reproduced from Ref. [376] under Open Access licence CC-BY)

Turning now to the fracture strength of single crystalline silicon, a key work in the literature is that of Namazu et al. [65]. In this work, a large number of clamped flexural specimens of dimensions in the nano-, micro- and millimetres scales were bent to fracture. All specimens, regardless of the length scale, were produced using semiconductor microfabrication techniques. For the smallest specimens, the load was applied using an AFM while for the largest specimens a nanoindenter was used. The resulting fracture strengths were analysed in terms of Weibull statistics (Figure 2.53) and a size effect in strength was determined: both the Weibull modulus as well as the representative strength were size-dependent. Measured strength values were in the range 11 – 18 GPa for the smallest samples, while larger samples were much weaker. Such values are not far from silicon's theoretical strength, which has been calculated *ab initio* or from stiffness tensor calculations to be in the range 17 – 27 GPa [46,378] depending on the crystal orientation. In the work of Namazu et al. [65] it was also determined that surface roughness was directly associated with strength (as was also discussed above in Section 2.4): indeed, measured surface peak-to-valley distances were consistent with the depth of critical cracks in a Griffiths fracture criterion framework. The authors thus concluded that the observed size-effect could be a consequence of the surface conditions resulting from different processing routes used across the different sized samples.

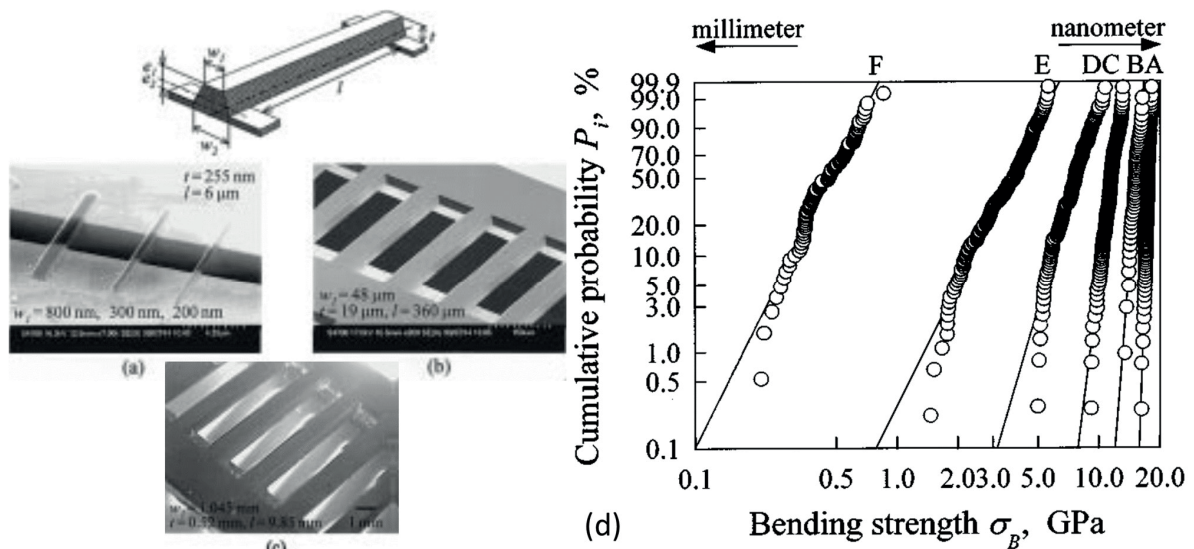


Figure 2.53 Clamped beams produced by lithographic methods and tested in bending by Namazu et al. [65] (Reproduced with permission of IEEE). Specimens of sizes in the nano- (a), micro- (b) and macro-scales (c) where probed in that work to study size effects on single crystalline electronic grade silicon. Some results are shown in (d), where letters A-F indicate groups of specimens of given dimensions.

A plot of fracture strength as a function of probed surface area showing a size effect of single crystalline silicon is shown in Figure 2.54, which is reproduced from the recent review paper of Del Rio et al. [164] and includes data from many studies published in the literature. The smallest samples in Figure 2.54 correspond to vapor-liquid-solid-grown silicon nanowires ~100 nm in diameter tested in bending [297,379] or in tension [292,294] (Figure 2.43 and Figure 2.45), and to nanometric bending beams ~250 nm thick prepared by photolithography and wet etching [65] (Figure 2.53a). Del Rio et al. [164] argue that the high strength values (approaching theoretical silicon strength) of those samples translate to critical flaw sizes of a few to tens of nanometres, which could be linked to planar defects in the lattice such as stacking faults or twin boundaries. These defects are considered *intrinsic* and are expected to govern fracture when other, larger, *extrinsic*, defects produced by processing or otherwise are absent.

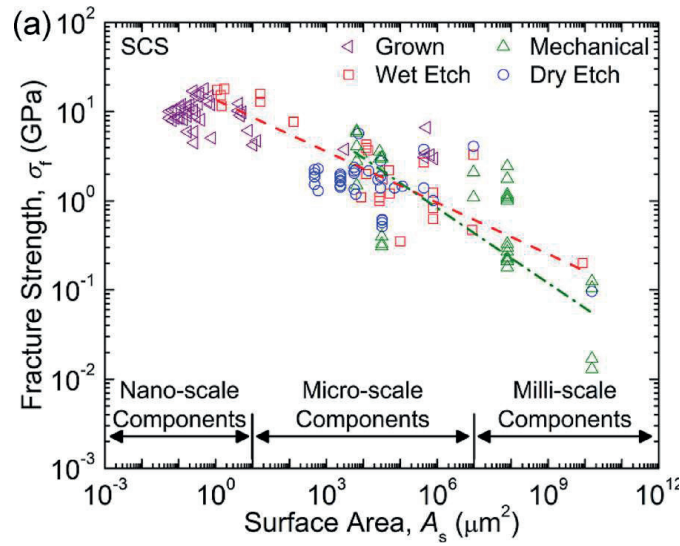


Figure 2.54 Compiled data in the literature of fracture strength as a function of probed surface area for single crystalline silicon. (Reproduced from Ref. [164] with permission of AIP Publishing LLC)

2.6 Concluding remarks

Recapitulating, the silicon particle strength values reported in the Al-Si literature are found to be much weaker than ideal silicon, i.e. 0.1 – 3.5 GPa [13,29,39–45] compared to 17 – 27 GPa [46], respectively. Such a difference is intriguing and has not yet been convincingly explained. Campbell [51] affirms that particles in Al-Si alloys “... should never crack because although they may have little ductility, they are in general extremely strong” and postulates that fracture of silicon particles can occur because of the presence of crack-like defects within the particles caused by entrained oxide bifilms [48]. On the other hand, Gall et al. [28] propose that “Although the silicon particles may not contain initial precracks *per se*, many of them have discontinuous shapes and local sharp corners. In single-crystal silicon deformed at room temperature, such sharp notches lead to failure stresses significantly lower than those in a pristine particle ...”.

Already in 1958 Webb and Forgeng [318] postulated that silicon particles in Al-Si alloys should be very strong and expressed interest in probing individual particles. As seen, almost 60 years later, the matter remains open. An illustrative recent quotation by an expert in the field serves as closing of this Chapter. In a letter [49], Griffiths comments on silicon particles: “... there are few calculations of the actual fracture stress, and even fewer direct measurements of it. Moreover, there are no fractographic observations of defects and other stress concentrators to explain crack initiation ...”. Then, he adds that “... I have to admit that I am not aware of existing evidence...” of weakening defects on silicon particles, and finally concludes with “There is a clear need to measure the fracture stresses of silicon particles ...”. The present work attempts to fill this gap; as will be seen, the intuition by Gall et al. expressed in the quote ending the previous paragraph will be proven to have been correct.

Chapter 3 Fracture toughness

This Chapter first describes in detail the development of a novel microscopic fracture toughness test based on the *chevron notch* approach using isotropic materials (fused quartz and nanocrystalline alumina fibres) as test-bench materials (Section 3.1). Then, early attempts to apply this test to silicon particles in Al-Si alloys are described together with the difficulties to obtain valid data that were encountered (Section 3.2). As a consequence, a step backwards is then taken in the following section (Section 3.3) to investigate the fracture toughness of silicon at microscopic scale using a simpler silicon sample, namely a silicon wafer. Among other outcomes, the latter study gives insights into the drawbacks of using the microscopic chevron notch test in the particular case of silicon.

Disclaimer: This Chapter contains extracts, including literal reproduction of full paragraphs and figures, of the following publications that the author has produced together with colleagues: Mueller et al. [380] (Section 3.1.1), Zagar et al. [381] (Section 3.1.2) and Mueller et al. [382] (Section 3.3). The text in each of those articles, which is extensively reproduced within this Chapter, was mainly in charge of its first author. The experimental work in Mueller et al. [380] (Section 3.1.1) and in Zagar et al. [381] (Section 3.1.2) was carried out, in equal parts, by the EPFL PhD candidates involved in each of the publications, i.e. the author and V. Pejchal in the former and the author, V. Pejchal and L. Michelet in the latter. The experimental work in Section 3.2 and in Mueller et al. [382] (Section 3.3) was entirely carried out by the author. The finite element modelling in these publications (and hence throughout this Chapter on fracture toughness) was done by Dr. G. Zagar.

3.1 Microscopic Chevron notch test

3.1.1 Test development using test-bench materials

(Adapted from Ref. [380]: M.G. Mueller, V. Pejchal, G. Žagar, A. Singh, M. Cantoni, A. Mortensen, *Fracture toughness testing of nanocrystalline alumina and fused quartz using chevron-notched microbeams*, *Acta Materialia*. 86 (2015) 385–395. doi:10.1016/j.actamat.2014.12.016)

In this Subsection, it is shown that chevron-notched samples offer an attractive approach to the measurement of fracture toughness in micron-scale samples of brittle materials. Focused ion beam (FIB) milling is used to carve bend bars of rectangular cross-section a few micrometres wide and containing a notch with a triangular ligament. Load-controlled testing is conducted using a nanoindentation apparatus. If the notch is appropriately machined, cracks nucleate and propagate in a stable fashion before becoming unstable. Sample dimensions are measured using a scanning electron microscope, and are used as input in finite element simulations of the bars' elastic deformation for various crack lengths. The calculated compliance calibration curve and the measured peak load then give the local fracture toughness of the material. Advantages of the method include a low sensitivity to environmental subcritical crack growth, and the fact that it measures toughness at the tip of a sharp crack situated in material unaffected by ion-milling. The approach is demonstrated on two materials, namely, monolithic fused quartz and nanocrystalline alumina Nextel™ 610 fibres; results for the latter give the intrinsic grain boundary toughness of alumina, free of grain bridging effects.

3.1.1.1 Methodology

The chevron-notched test bar of this study is a rectangular cantilever beam, of cross-section $W \times B$ and length L . It has a thin notch with a triangular ligament, the apex of which is nominally situated in the middle of the cross-section. Depending on the notch parameters a_1 and b_1 , the notch is overcut if $b_1 = B$ or undercut when $a_1 = W$, see Figure 3.1. In macroscopic samples, these geometrical differences are easily controlled; the standard for measuring the macroscopic fracture toughness of advanced ceramics (ASTM 1421-10) allows only overcut notch geometries, for which compliance calibration data are known [383,384]. When microscopic beams are prepared by FIB machining, however, it is generally difficult and time-consuming to produce notch geometries that comply with the standard. Because of this, here we calculate compliance parameters of each sample via computer modelling. We therefore also test samples with undercut notches.

When the beam is loaded in bending under force P , stress builds up normal to the notch. This promotes the development of a crack at the apex of the ligament and subsequent crack propagation across the triangular ligament. We define the instantaneous crack length a using the top surface of the beam as the origin (Figure 3.1). Assuming that the crack front is straight, its instantaneous width is $b = b_1 (a - a_0)/(a_1 - a_0)$. It is well known (e.g., page 36 of Ref. [385]) that the energy release rate G for any specimen depends on the load P , the width of the crack front b and the derivative of the sample compliance $C(a)$ with respect to crack length a according to:

$$G = \frac{P^2}{2b} \left(\frac{dC}{da} \right) \quad \text{Equation 3-1}$$

G is also related to the stress intensity factor K_I : $K_I^2 = E' G$, where E' is the effective elastic modulus, given in terms of the Young's modulus E and the Poisson ratio ν : $E' = E/(1 - \nu^2)$ for plane strain (which prevails over most of the crack front in chevron-notched samples). Considering the sample geometry shown in Figure 3.1, the average stress intensity factor along the straight crack front in a symmetric notch is:

$$K_I = \frac{P}{B\sqrt{W}} F_V(\tilde{a}) \quad \text{Equation 3-2}$$

with $F_V(\tilde{a})$ a dimensionless geometrical function given by:

$$F_V(\tilde{a}) = \sqrt{\frac{1}{2\tilde{b}_1} \left(\frac{\tilde{a}_1 - \tilde{a}_0}{\tilde{a} - \tilde{a}_0} \right) \frac{dC_V}{d\tilde{a}}} \quad \text{Equation 3-3}$$

where normalized lengths are $\tilde{a} = a/W$, $\tilde{a}_0 = a_0/W$, $\tilde{a}_1 = a_1/W$ and $\tilde{b}_1 = b_1/B$, and the dimensionless compliance is $C_V = CE'B$. Both b and C_V are monotonically increasing functions of \tilde{a} . As a result of the sample design, F_V in Equation 3-3 and hence both K_I in Equation 3-2 and G in Equation 3-1, exhibit simultaneously a minimum at a single critical crack length \tilde{a}_c .

If the material does not exhibit significant R -curve behavior (i.e. if its toughness is independent of crack length), then at $\tilde{a} = \tilde{a}_c$ there is a transition from stable to unstable cracking. Since both \tilde{a}_c and $F_V(\tilde{a})$ are functions only of the sample geometry, the fracture toughness K_{Ivb} as measured with the chevron-notched specimen is simply given as:

$$K_{Ivb} = \frac{P_c}{B\sqrt{W}} F_v(\tilde{a}_c) \quad \text{Equation 3-4}$$

in both displacement- or load-controlled testing, where P_c is the load at the onset of unstable crack propagation. Practically, P_c corresponds to the maximum load measured during the test. With the assumptions above, it is the only quantity (apart from geometrical dimensions) that needs to be measured to deduce the material's fracture toughness. This is because $F_v(\tilde{a}_c)$ and \tilde{a}_c depend only weakly on the Poisson's ratio of the material [386]; thus they can be determined separately via a compliance calibration procedure for the relevant test specimen geometry.

A major advantage of this method when dealing with brittle materials is that it generally does not require an initial precrack. The high stress concentration that exists at the apex of the ligament is (depending on the material) often sufficient to initiate a short crack there, at a load that is well below the critical load, P_c , at which crack instability sets in. In practice however, especially if the notch is insufficiently thin, the force needed to initiate a crack at the apex might exceed P_c . Then, unstable failure takes place as soon as the crack is initiated, rendering the test invalid. To guard against this, it is convenient to record both the load and the load point displacement during the test. Plotting the former vs. the latter will then provide a check for the necessary succession of events, namely: (i) crack nucleation followed by (ii) stable crack growth under increasing load before (iii) rapid unstable fracture at P_c . Typically, what is seen in a successful test on such a curve is a first linear portion (corresponding to deformation of the uncracked beam), followed by either a sudden load decrease if the test is run in displacement control or a displacement jump if it is run in load control (this is called crack “pop-in”), followed by a non-linear reloading region of monotonically decreasing slope. In this work, we transpose this method to samples having dimensions of the order of a few micrometres.

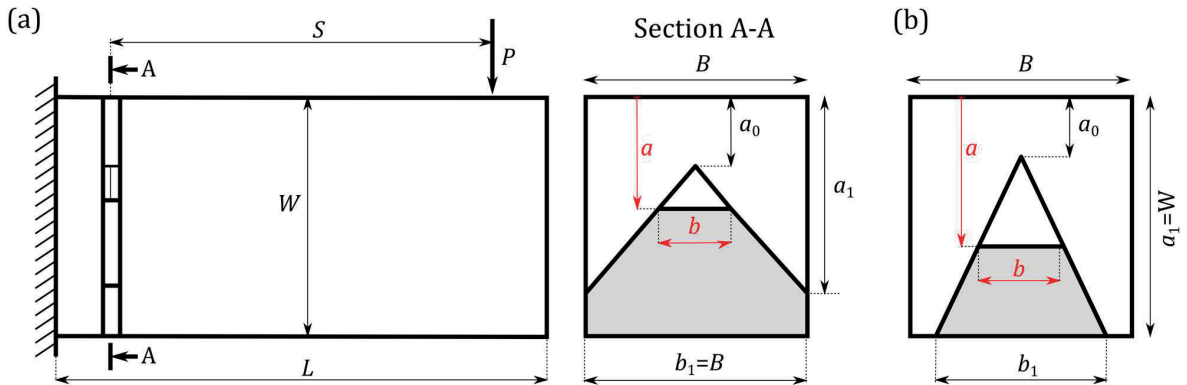


Figure 3.1 Sketch of the chevron-notched samples used to measure fracture toughness. (a) Overcut notch. (b) Undercut notch. (Reproduced from Mueller et al. [380])

3.1.1.2 Sample preparation

Two materials are tested: (i) amorphous fused quartz, provided by Hysitron® (Minneapolis, MN, USA) as a $\sim 10 \times 10 \times 2 \text{ mm}^3$ rectangular prism for use in nanoindenter calibration; and (ii) Nextel™ 610 $\sim 12 \text{ }\mu\text{m}$ -diameter alumina fibres produced by 3M (St. Paul, MN, USA), with a structure of equiaxed grains

about ~ 65 nm wide [387] and provided as the reinforcement of a continuous aluminium matrix wire ~ 2 mm in diameter, itself also produced by 3M.

Fused quartz bend bars were produced along the edge of the prism (Figure 3.2). Nano-crystalline alumina samples were prepared as follows. An ~ 1 cm long segment of the aluminium matrix composite wire 2 mm in diameter was first mounted in resin. The mounted sample was then ground and polished along two planes, one parallel and one perpendicular to the common axis of the wire and the fibres, thereby creating a sharp 90° edge passing roughly along the diameter of the wire. Fibres were then exposed by deep etching of the aluminium matrix by immersion in 20 wt.% NaOH solution for approximately 1 h at room temperature, followed by rinsing in distilled water. A general view of the prepared wire is shown in Figure 3.4. The length of exposed fibres after etching was typically between 30 and 40 μm . Loosely attached fibres, which remained after etching near the edge along the plane parallel to the fibres, were manually removed with tweezers under an optical microscope. By this procedure, fibres embedded in the aluminium and partly emerging from the matrix close to the sharp edge were readily accessible to the FIB. This, in turn, enabled us to machine the fibres both from the top (along their axis) and from the side (perpendicular to their axis); see Figure 3.5a. Fused quartz samples did not require any special preparation. Samples of both materials were covered with ~ 10 nm carbon coating using a CressingtonTM 208 Carbon Coater (Watford, England, UK) prior to FIB machining to avoid charging.

Chevron-notched cantilever beams of both materials (Figure 3.3 and Figure 3.5) were fabricated by FIB milling with 30 kV Ga^+ in a ZeissTM NVisionTM 40 (Oberkochen, Germany) dual beam (SEM/FIB) instrument. All cantilevers were initially machined by rough milling with a 6.5 nA beam current, followed by finer milling steps at lower currents. The last milling step of all cantilever faces was done with a beam current of 0.7 nA. In order to produce cantilever beams of neatly rectangular cross-section, the angle of incidence of the ion beam on each machined surface was compensated by a 2.5° additional tilt. Guiding lines on the top surface of the cantilever, which were added to help position the nanoindenter tip, were milled using a 10 pA ion probe current for a few seconds. The final and most crucial step in the micro-milling process was to machine the chevron notch. In most cases, a 10 pA ion probe was used; however, sometimes, e.g., for the larger samples or when substantial drift was experienced, a 40 pA ion probe was used.

The notch was shaped so as to place its apex roughly in the centre of the cantilever beam cross-section. In this way, the notch sides above the apex collimated the roughly Gaussian ion beam spot profile, enabling the notch width at the apex, where crack nucleation takes place, to be only a few tens of nanometres. This collimation effect has been demonstrated, for example, by Minoshima et al. [388], where it was shown that at constant ion beam current, the radius of curvature at the root of FIB-machined grooves decreases with increasing depth. Note that in this configuration, due to beam collimation, the V-shaped notch is always wider at its top than at greater depths, as can be seen in Figure 3.5b.

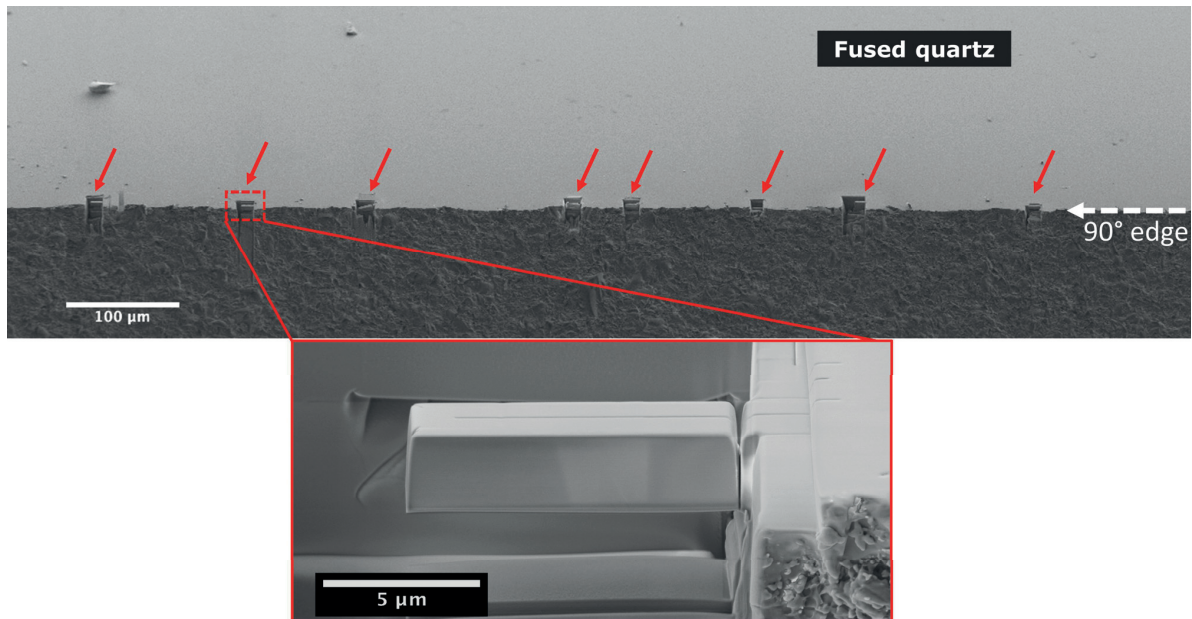


Figure 3.2 Chevron-notched cantilever beams (indicated with red arrows) produced by FIB milling along the edge of a fused quartz sample.

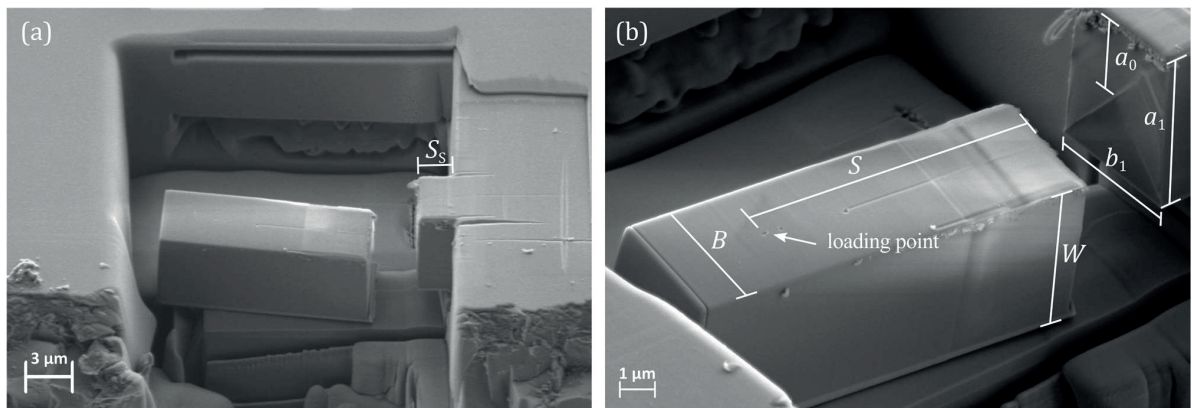


Figure 3.3 Chevron-notched cantilever beam prepared in fused quartz. (a) Overview of a beam after testing, indicating the size of the beam support. (b) View of the beam and the notch after testing, indicating the point of load application and relevant beam dimensions. (Reproduced from Mueller et al. [380])

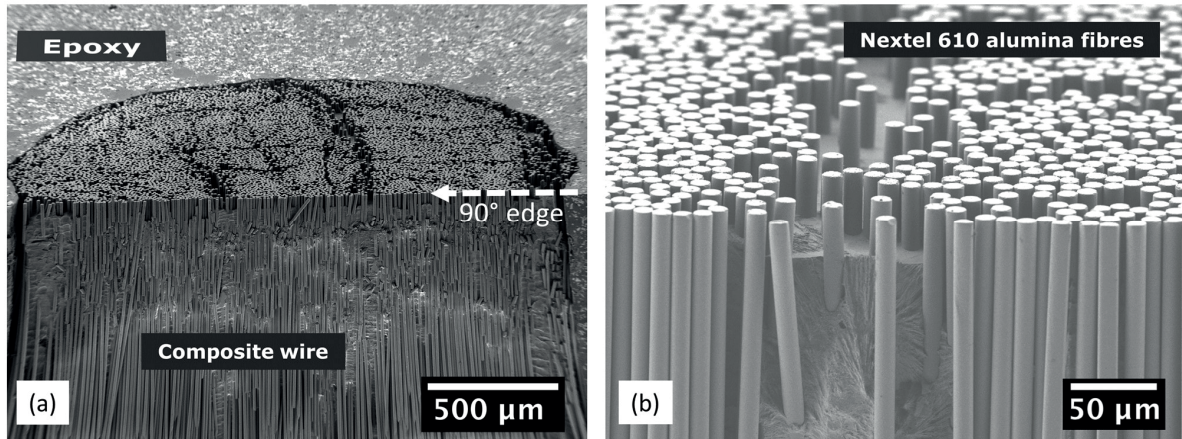


Figure 3.4 (a) SEM image of alumina fibres (Nextel 610™) exposed by deep etching the Al matrix of a composite wire polished along two planes with a $\sim 90^\circ$ edge passing roughly through the wire diameter. (b) Close-up of a random sector at the edge, showing the polished fibres protruding from the Al matrix.

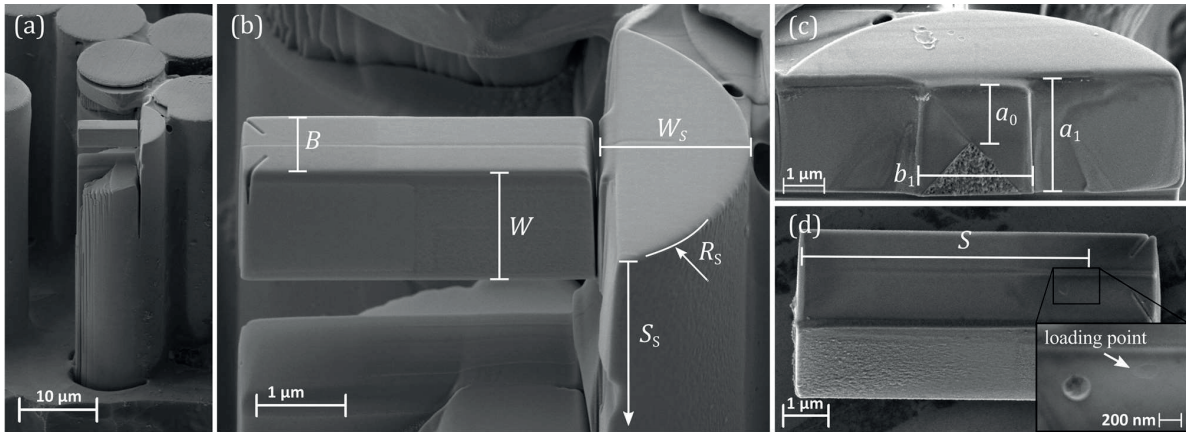


Figure 3.5 Chevron-notched cantilever beam prepared in a Nextel™ 610 alumina fibre, with relevant dimensions indicated. (a) Overview of a fibre from which a beam was machined. Note that the fibre is accessible from both its side and its top. (b) The same cantilever beam at higher magnification. (c) View of the triangular ligament (fracture surface) after testing. (d) Beam after testing, with an inset showing the trace of the point of load application. The bigger imprint corresponds to post-failure impact of the nanoindenter tip. (Reproduced from Mueller et al. [380])

3.1.1.3 Testing procedure

The micrometric chevron-notched cantilever beams were tested using a TI 950 TriboIndenter® (Hysitron® Corporation, Minneapolis, MN, USA) nanoindentation apparatus, equipped with a two-axis goniometric tilt stage (Newport Corp., Irvine, CA) fixed onto the nanoindenter positioning stage. Samples with FIB-machined cantilever beams were mounted on top of the tilt stage and aligned using the Scanning Probe Microscope (SPM) capability of the nanoindenter's transducer, to bring the loading axis to within $\pm 0.5^\circ$ of the normal to the cantilever top surface. The load was applied along the centreline of the beam, close to its free end, utilizing the SPM image and the guiding lines as references.

Alumina cantilevers were tested with a sphero-conical diamond probe of tip radius ~ 220 nm. It was found in early tests that, due to the low loads at failure, imprints left in fused quartz samples by this sphero-conical probe were too shallow to be imaged properly; for this reason, all fused quartz samples presented here were tested with a cube-corner diamond probe with a tip radius of ~ 100 nm. The point of load application was in all cases determined from SEM images of the fractured beam after test had been completed. It was observed that the actual point of load application, made visible by the imprint left along the beam surface, was often several tens of nanometres away from the point of application that was programmed on the SPM reference image. Thus, tests in which fractured cantilevers could not be found for subsequent SEM imaging were discarded.

Displacement measurements recorded during each fracture test were corrected for indentation by considering that they are the sum of the cantilever beam surface deflection and the displacement caused by the probe penetration into the material of the cantilever. The latter was measured by conducting several separate indentation tests (before and/or after the fracture test) into the support site to which each cantilever was attached, which was in the same FIB-polished condition as the cantilever beam surface. The net cantilever deflection is then obtained by subtracting indentation displacements for the current load level from the instantaneous nanoindenter tip displacement.

Given the low stiffness of the nanoindentation instrument, all tests were run in a closed-loop, quasi-static, load-control mode. The loading rates had to be sufficiently low to avoid introducing dynamic effects and achieve stable crack growth condition. They also had to be sufficiently high to minimize the effects of drift on the displacement data and to avoid the effects of environmentally assisted Sub-critical Crack Growth (SCG). Indeed, both silica and alumina are known to be susceptible to SCG [389] under the present testing conditions, i.e. air at room temperature and 20-50% relative humidity. The loading rate conditions for which the influence of SCG on the measured fracture toughness can be ignored (95% of confidence in K_{IC}) are analysed in Ref. [390]. For the materials at hand, the analysis indicates that the loading rates used in this work (between 1 and 3 $\mu\text{N/s}$) are in all cases high enough so that the SCG influence on test results is insignificant. An overview of the testing conditions for each sample of this work is given in Table 3-1 and Table 3-2.

Table 3-1 Experimental conditions (the FIB current used to machine the notch i_{FIB}^{notch} and the loading rate \dot{P}), sample dimensions (W to S_s , as defined in Figure 3.1 and Figure 3.3), indentation-corrected test stiffness (ICTS), stiffness calculated from the model (FEM), parameters obtained via compliance calibration (\tilde{a}_c and $F_v(\tilde{a}_c)$), measured critical load P_c and calculated fracture toughness K_{Ivb} (Equation 3-4) for fused quartz chevron-notched microscopic samples. (Reproduced from Mueller et al. [380])

#	i_{FIB}^{notch} pA	\dot{P} $\frac{\mu\text{N}}{\text{s}}$	W μm	B μm	S μm	b_1 μm	a_0 μm	a_1 μm	S_s μm	ICTS $\frac{\text{mN}}{\mu\text{m}}$	FEM $\frac{\text{mN}}{\mu\text{m}}$	\tilde{a}_c	$F_v(\tilde{a}_c)$	P_c μN	K_{Ivb} $\text{MPa } m^{1/2}$
Q1	10	1	4.47	2.42	7.46	2.42	2.52	4.18	0	1.09	1.02	0.66	41.7	77.5	0.63
Q2	10	2	3.22	2.33	8.07	1.73	1.85	3.22	0	0.24	0.23	0.67	96.7	26.6	0.62
Q3	10	2	2.96	2.32	6.54	2.32	1.45	2.67	0.35	0.48	0.46	0.58	56.2	44.2	0.62
Q4	10	2	3.12	2.58	8.84	2.58	2.05	2.83	0	0.23	0.22	0.73	90.7	35.1	0.70
Q5	40	3	5.11	4.20	10.16	4.20	2.59	4.96	2.22	0.73	0.67	0.61	67.7	92.2	0.66

Table 3-2 Experimental conditions (the FIB current used to machine the notch i_{FIB}^{notch} and the loading rate \dot{P}), sample dimensions (W to W_S , as defined in Figure 3.1 and Figure 3.5), parameters obtained via compliance calibration (S_S to $F_v(\tilde{a}_c)$), measured critical load P_c and calculated fracture toughness K_{Ivb} (Equation 3-4) for nanocrystalline alumina chevron-notched microscopic samples. (Reproduced from Mueller et al. [380])

#	i_{FIB}^{notch} pA	\dot{P} $\frac{\mu N}{s}$	W μm	B μm	S μm	b_1 μm	a_0 μm	a_1 μm	R_S μm	W_S μm	S_S μm	\tilde{a}_c	$F_v(\tilde{a}_c)$	P_c μN	K_{Ivb} $MPa m^{1/2}$
A1	10	3	2.98	2.54	7.25	2.54	1.49	2.95	5.81	3.69	4.51	0.59	74.3	148.1	2.51
A2	10	3	3.03	2.65	7.05	2.65	1.52	2.98	5.92	2.61	7.26	0.60	70.5	163.1	2.49
A3	40	3	2.96	2.48	6.54	2.38	1.53	2.96	5.87	2.92	12.60	0.61	74.6	127.8	2.23
A4	40	3	4.61	2.59	7.00	2.58	2.31	4.61	6.06	2.86	5.10	0.61	47.2	270.4	2.29
A5	40	3	2.70	2.70	7.22	2.60	1.22	2.70	6.42	3.30	3.31	0.54	73.9	132.0	2.20

3.1.1.4 Results

Chevron notches, by design, create a site of high stress concentration at the apex of their triangular ligament. This, in turn, promotes spontaneous crack initiation at that location – under a small load, if all goes well. In practice, this is not always achieved (regardless of the sample dimensions): with brittle materials, excessive pop-in at $P > P_c$, leading to immediate unstable fracture, is the greatest source of unsuccessful testing of chevron-notched samples. This often occurs because the notches are not sufficiently thin; indeed, producing sufficiently thin notches was indeed also found here to be a key factor in obtaining successful tests. In producing thin notches by FIB milling, we found two parameters to be important: (i) using, in the final notch machining stages, a low beam intensity; and (ii) machining a ligament the apex of which is situated well below the top surface of the beam ($a_0/W \geq 0.4$). This second feature helps produce a thin notch due to ion beam collimation effects along the notch walls [388].

Load-deflection curves from successful tests are shown in Figure 3.6 for both sample series. All curves are initially linear. The onset of nonlinear deflection, which is associated with crack nucleation, is visible as a small discontinuity in the slope of the curves. Thereafter, stable crack extension sets in. This manifests as a smooth continuous increase in compliance in the case of fused quartz, or a series of small stepwise displacements in nanocrystalline alumina. The peak load reached in the test, P_c , is immediately followed by unstable crack propagation and unloading (this portion of the curves is more lightly coloured in the plots in Figure 3.6). The greater separation of individual data points shows that, once the maximum load has been reached, the nanoindenter probe begins to move very rapidly. This is a dual result of (i) the release of elastic energy stored in the relatively soft load-train of the apparatus and (ii) the fact that the machine was programmed to produce a monotonically increasing prescribed load function. The test ends with a full or nearly full separation of the cantilever arm from the remainder of the tested material. Often the fractured cantilever arm was found in the vicinity of the test location (at times, it was still attached to its base by a thin ligament). In some cases, it remained electrostatically attached to the sides of the nanoindenter probe and was then recovered by indenting a few micrometres into aluminium. Generally, the detached beam was found; on one occasion, however, it was lost, causing the data from that test to be discarded (because the load application point can only be determined precisely by examining this arm in the SEM). In total, in addition to the 10 tests reported here, 16 other tests were conducted, data from which were discarded for one or another of the following reasons: (i) “pop-in” without stable crack growth, (ii) a geometrical defect in the notch shape, (iii) loss of the broken beam or (iv) an earlier ill-adapted setting on the testing apparatus.

Fractography shows that cracks grew within the thin ligament of the chevron notch, without substantial deviations other than those caused by grain boundary deflection in the nanocrystalline alumina fibre material. With amorphous fused quartz, the crack surface was almost perfectly flat (Figure 3.7a). Alumina samples showed characteristics typical of intergranular fracture, resulting in a relatively (nano-) rough fracture surface (Figure 3.7b). This, in turn, explains the stepped load–displacement response of this material (Figure 3.6b): displacement jumps most likely reflect the fracture of individual grain boundaries. Regions of stable or unstable crack growth could not be distinguished in the fractography of both materials.

Plane strain is always lost at free surfaces, i.e. at the sides of the triangular ligament of the present samples. Moreover, ligament edges are areas susceptible to alterations and residual stresses caused by FIB milling-induced damage. It is therefore possible that the crack front was curved and that the fracture processes were somewhat different in the proximity of its borders; however, other than a very thin band of material lining the triangular ligament (Figure 3.7) there are no signs of a difference in fracture mode near free surfaces in both materials, or of a curved crack front.

Knowing the point of load application is important in data analysis, since this is needed to measure distance S (Figure 3.1); this, in turn, is needed to calculate the bending moment across the triangular ligament. The point of load application was determined by examination of the top surface of fractured cantilevers. Along this surface, we found two indents on all tested specimens (e. g. Figure 3.3b and Figure 3.5d), one being deeper than the other. Comparison of the depths of the two indents with those of indents produced in conventional instrumented hardness tests on a fixed surface of the corresponding material under loads typical of that at which the samples fractured shows that the indent associated with the point where the load was applied during the test is the smaller of the two. The larger indent, which requires loads far higher than what was applied during the test, must therefore have been caused by post-fracture impact between the cantilever and the indenter (likely itself a result of the indenter following the beam once the crack became unstable, and then hitting it when the beam motion was stopped by the valley of solid material lying further down).

The dimensions of each sample tested in this work were measured individually using SEM images collected both before and after testing (the latter are needed to capture the ligament dimensions and the point of load application). The data are reported in Table 3-1 and Table 3-2. Uncertainty associated with the determination of dimensions has two main sources: imprecision inherent to the SEM, and a certain degree of subjectivity in defining the exact positions of limits. This second source of uncertainty, of relative magnitude not larger than 5%, was found to be the most important. It originates mostly from the rounding of machined edges, and from the limited level of symmetry that could be achieved in FIB machining. As can be seen in Table 3-1 and Table 3-2, the dimensions vary significantly from sample to sample. This is a consequence of FIB milling being inherently less precise (in relative terms) than macroscopic machining. For this reason, data interpretation leading to the fracture toughness values was conducted by coupling, for each sample, experimental data with a tailored numerical simulation, as detailed next.

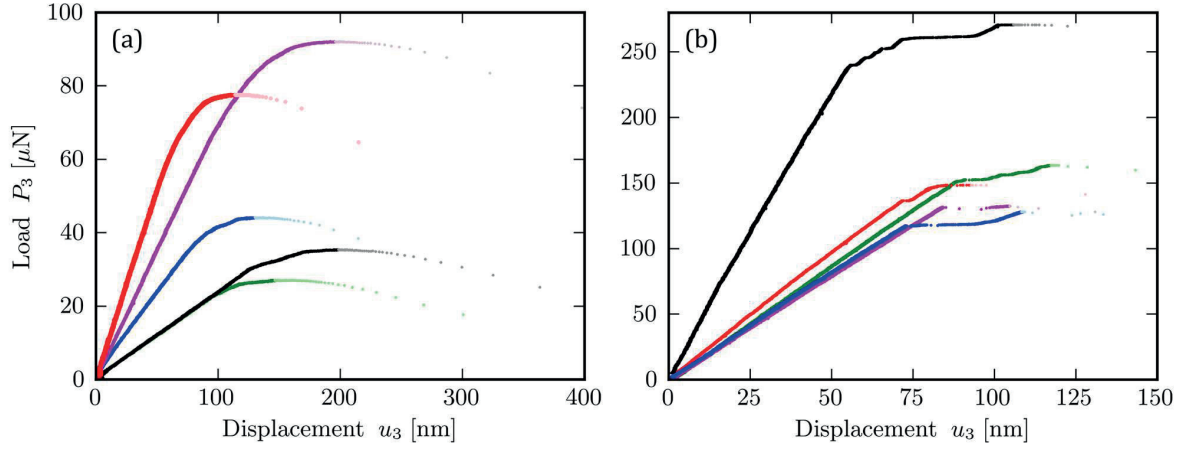


Figure 3.6 Indentation-corrected load—displacement responses of (a) fused quartz and (b) alumina chevron-notched cantilever beam samples. The progressive increase in compliance, a signature of stable crack growth, is smooth in (a) and stepped in (b). Colours represent different samples. (Reproduced from Mueller et al. [380])

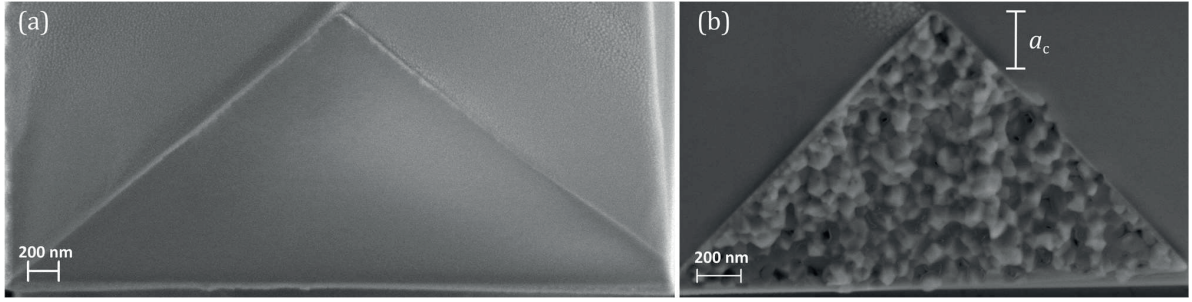


Figure 3.7 Fracture surface of (a) fused quartz and (b) alumina chevron-notched samples. (Reproduced from Mueller et al. [380])

3.1.1.5 Discussion

3.1.1.5.1 Compliance calibration

Because it is almost impossible to FIB mill a set of identical chevron-notched samples, we could not produce and use a single compliance calibration curve, together with its corresponding single value of $F_V(\tilde{a}_c)$, for interpretation of all test data. Each test was therefore coupled with a bespoke finite element (FE) simulation to deduce, based on measured values of its geometry and dimensions, its compliance calibration curve $C(a)$ and, from this, the relevant value of $F_V(\tilde{a}_c)$. To this end, SEM images were used to retrieve relevant dimensions of every sample (Figure 3.1, Figure 3.3, Figure 3.5, Table 3-1 and Table 3-2).

A parametric, linear elastic, 3-D FE model for each tested specimen of isotropic fused quartz or alumina was implemented in the commercial software Abaqus™ FEA 6.11 (Dassault Systèmes S.A., Vélizy-Villacoublay, France). The crack front in the model is taken to be straight and normal to the sample plane of symmetry. Since samples are symmetrical, despite small variations and imprecisions, it suffices to model only half of each specimen. In addition, since the load is commonly applied at a significant distance away from the free end of the cantilever, in the model only the “effective” cantilever length S is

considered (see Figure 3.1). Calculations use a general, quadratic brick (C8D20) finite element; however, middle nodes of elements associated with the crack front are shifted to a quarter-element size towards the crack front [391–393]. The mesh and element size are optimized to calculate converged values of system compliances for each simulation.

The modelled domain for fused quartz samples comprises only the cantilever or both the cantilever and the beam-like support situated on the other side of the chevron notch, as shown in Figure 3.8a, depending on whether the notch was machined at distance S_s away from the root of the cantilever or not (see Figure 3.3a and Table 3-1). In the former configuration, a fixed-displacement boundary condition is used for uncracked portions of the chevron face (highlighted in red in Figure 3.8). In the presence of a support, the uncracked chevron faces of the support and the cantilever are rigidly tied, while a fixed-displacement boundary condition is applied on the support face opposite the chevron notch. In modelling, the thickness of the chevron notch was implicitly assumed to be zero; thus, possible effects arising from a finite notch thickness [393] are not accounted for.

Fused quartz is treated as a homogeneous isotropic material with a Young's modulus of 72 GPa and a Poisson ratio of 0.17. With all relevant sample dimensions known, the model has no free parameters; hence, predicted and measured (indentation-corrected) beam compliances can be compared. This comparison is given in Table 3-1; as seen, the initial compliance calculated for each fused quartz sample agrees with the data to within ~5%.

The model for alumina cantilevers accounts for the fact that the cantilever is attached to a compliant circular-segment support, this being a consequence of FIB machining the cantilever from a small fibre (see Figure 3.8b) instead of a sample of bulk material. Since the height S_s of the compliant support is ill-defined in these samples (due to uneven FIB machining and because the cantilever is placed on top of an ~30 to ~40 μm long fibre segment), this parameter was considered as free. Its value was found by iteration until the initial compliance of the model matched the measured initial indentation-corrected compliance of the test to within 5%. All optimized values for the support length S_s were in accordance, to within a few microns, with expectations based on SEM images. As with fused quartz, the ligament is considered to have no thickness, such that possible effects of the chevron notch thickness are not taken into account. The material parameters for isotropic, nanocrystalline alumina cantilevers are a Young's modulus 373 GPa and a Poisson ratio 0.235 [394,395].

The general procedure that was used to calculate curves of the normalized compliance C_v versus the crack length \tilde{a} , for each tested specimen consists in first generating a set of 30 stress-free sub-models of the same cantilever geometry, in which the crack length inside the notch is progressively incremented. Each of the sub-models is then subjected to a small-strain quasi-static FE analysis to obtain the individual sub-model initial stiffness. Loading during quasi-static analysis is generally performed by prescribing a small vertical displacement of the central node (in the plane of symmetry) at the free end of a cantilever top face (Figure 3.8; we thus ignore any departure of the actual loading position during the test from the centreline of the beam). The compliance C for each sub-model (corresponding to a particular value of the crack length a) is then calculated from individual sub-model force–displacement responses. The data for the normalized sample compliance C_v vs. crack length \tilde{a} collected over all sub-models associated to a particular cantilever are then plotted and fitted by a fifth-order polynomial (Figure 3.9a,b). This polynomial representation of $C_v(\tilde{a})$ is then used to calculate the critical crack length, \tilde{a}_c , and the minimum of the geometrical function, $F_v(\tilde{a}_c)$, for each cantilever (Figure 3.9c,d). Then, knowing the measured peak load in the test, P_c , the material's fracture toughness, K_{Ivb} , can be deduced as

described in Section 3.1.1.1. Critical crack lengths, \tilde{a}_c , and corresponding minima, $F_v(\tilde{a}_c)$, are summarized in Table 3-1 and Table 3-2, together with the experimentally measured maximal loads and, finally, the calculated values of the fracture toughness K_{Ivb} according to Equation 3-4 for each sample.

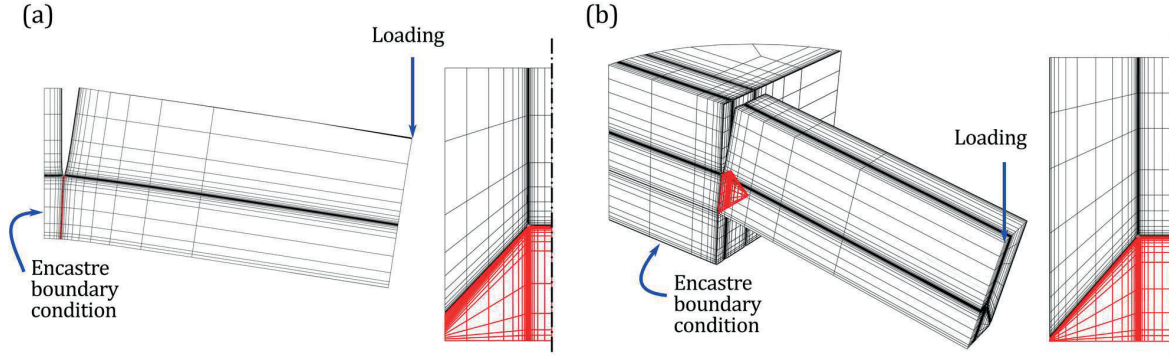


Figure 3.8 3-D FE model for (a) fused quartz and (b) alumina cantilever beams. The uncracked region of the chevron notch is highlighted in red. For clarity, deformation of the models is magnified by a factor 100. (Reproduced from Mueller et al. [380])

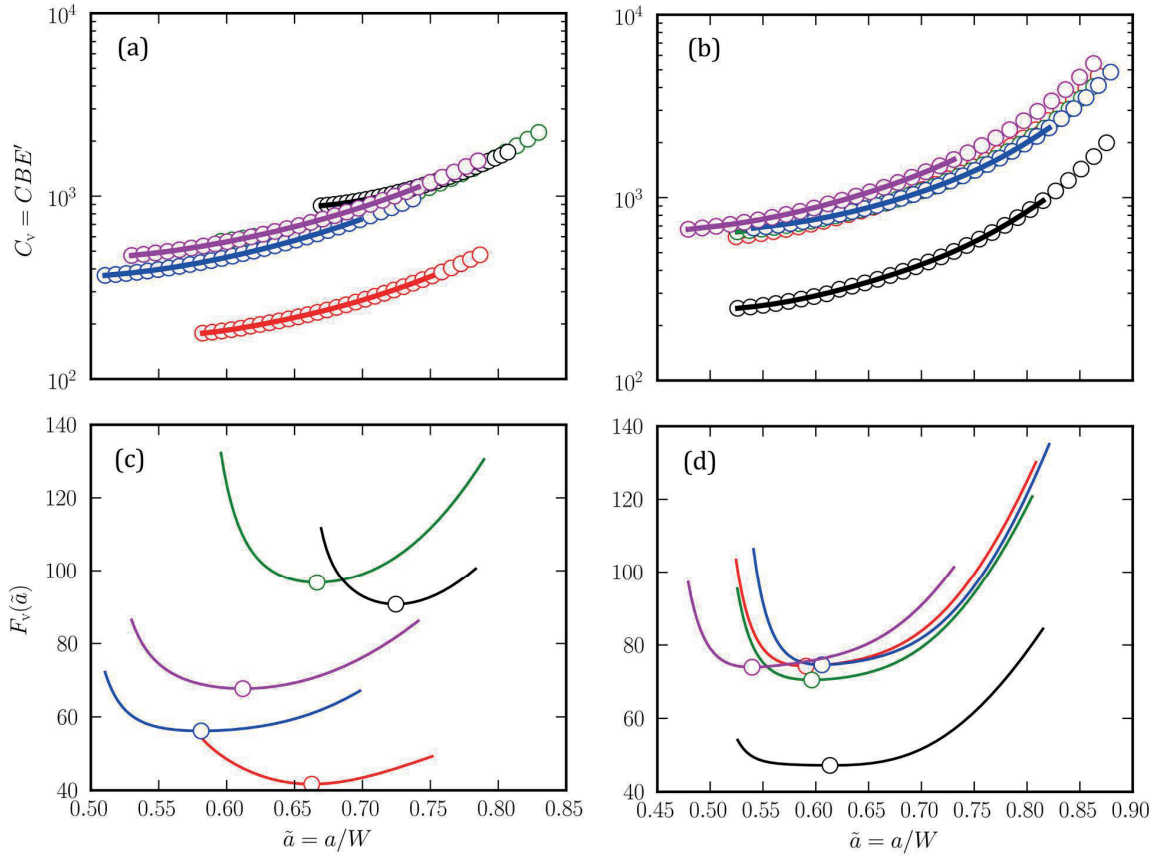


Figure 3.9 Dimensionless compliance C_v and geometrical function F_v as a function of normalized crack length \tilde{a} for (a, c) fused quartz and (b, d) alumina samples with dimensions given in Table 3-1 and Table 3-2. (Reproduced from Mueller et al. [380])

3.1.1.5.2 Measured fracture toughness values

The resulting measurement of fracture toughness for fused quartz, calculated as the mean and standard deviation over the five experiments given in Table 3-1, is $K_{Ivb} = 0.65 \pm 0.04 \text{ MPa}\sqrt{\text{m}}$. This result is in the middle of the range of values reported for fused quartz after testing macroscopic chevron-notched samples [185,396] or nanoindentation fracture testing [397] (see Table 3-3). Slightly higher values are reported by a few other authors for fused silica [398–401] (which is commonly referred to as vitreous SiO_2 produced from high-purity synthetic silica instead of naturally occurring quartz).

For alumina, the resulting fracture toughness (the mean and standard deviation over the five experiments given in Table 3-2) is $K_{Ivb} = 2.34 \pm 0.15 \text{ MPa}\sqrt{\text{m}}$. To the best of our knowledge, the toughness of such fine-grained alumina has not been reported to date. Insight into the validity of this result can be found in the work of Chantikul et al. [402]. In that work, fracture toughness measurements on alumina over a range of (equiaxed) grain sizes from 80 to $2.5 \mu\text{m}$ were performed, and a model for the toughness dependence on grain size and crack length was developed by considering grain-bridging effects. The extrapolation of that model into the grain-size range of this study yields a value of fracture toughness, $2.75 \text{ MPa}\sqrt{\text{m}}$, which is close to our result. Our measurements thus give experimental confirmation of Chantikul et al.'s model-derived estimation of the intrinsic fracture toughness of alumina, free of grain bridging contributions. The slight difference between the two values might be due to the fact that samples of Chantikul et al. displayed a significant fraction of transgranular fracture (up to $\sim 30\%$), whereas in the present alumina fibres, fracture was essentially all intergranular.

Table 3-3 Fracture toughness values of vitreous SiO_2 (fused quartz and fused silica) reported in the literature. Quoted references are Refs. [185,396–401]. (Reproduced from Mueller et al. [380])

Material, method(s), conditions	Fracture toughness ($\text{MPa}\sqrt{\text{m}}$)	Reference
Fused quartz. Macroscopic three-point bending chevron	0.58	Harding et al.
Fused quartz. Nanoindentation toughness, cube corner tip	0.6 ± 0.1	Scholz et al.
Fused quartz. Macroscopic chevron-notched short rod	0.735	Barker
Fused silica. Macroscopic double cantilever beam, precracked. In vacuum	0.73	Wiederhorn et al.
Fused silica. Macroscopic double cantilever beam, precracked	0.73	Mecholsky et al.
Fused silica. Macroscopic single-edged precracked beam and macroscopic chevron.	0.71–0.77	Salem
Material from a retired window of a space shuttle. Room and N_2 conditions		
Fused silica. Chevron-notched short rod	0.79	Lucas et al.

3.1.1.5.3 Precision of the method

The final toughness measurement is thus found to be quite reproducible across different chevron-notched samples of each material, despite the variations in their shape and dimensions (Table 3-1 and Table 3-2). The slightly higher variation for the alumina is likely related to the more complex and hence more variable crack surface that is developed in this nanocrystalline material as compared to the amorphous fused quartz (Figure 3.7).

The main source of error in calculating the fracture toughness via Equation 3-4 originates from the measurements of the sample dimensions taken from SEM images. It is therefore informative to examine the sensitivity and errors in the fracture toughness values arising from small perturbations in the sample dimensions.

We thus considered a single fused quartz sample (Q3, Table 3-1) and perturbed its dimensions by increasing each, one at a time, by 5%. The perturbed sample geometries were then compliance re-calibrated, first to obtain new values for \tilde{a}_c and $F_v(\tilde{a}_c)$ in the same way as explained above, and then to calculate deviations of the initial stiffness of the model and the fracture toughness values that would be

obtained for the same measured peak load. The relative difference in final stiffness and fracture toughness resulting from each of these perturbations is given in Table 3-4. As can be seen, $\sim 5\%$ error in dimension measurements causes up to $\sim 8\%$ error in fracture toughness for most of the dimensional parameters. This is of the same order as the observed sample-to-sample variations across data in Table 3-1. The exception to this is the cantilever beam height W , to which toughness calculation is the most sensitive. This large sensitivity to error in W is not surprising, since the bending stiffness at the notch, EI , via the cross-section moment of inertia, I , is generally expected to scale with the third power of the ligament height, which is linearly connected to W in this analysis. This, in turn, dramatically affects the sample compliance, C_v , and its derivative, $dC_v/d\tilde{a}$. Care must therefore be exerted in measuring this particular dimension. Interestingly, similarly large errors might be foreseen to be caused by errors in S . For a cantilever beam of length S with constant cross-section, the stiffness $P/u \propto 1/S^3$, where u is the deflection due to applied force P . However, this does not occur in chevron-notched cantilevers due to the localized rotation at the chevron notch, reflecting the hinge-like deformation of the sample.

It is also interesting to note that larger errors in the fracture toughness values correlate well with deviations of the initial sample stiffness. Thus, verification of the model against the measured initial sample stiffness or, when the beam is attached to a structure of finite compliance (as with the fibres in the present tests), comparing the predicted compliant structure dimensions with those of the actual structure surrounding the beam, provides a convenient test of consistency for the FE simulations. In other words, in the procedure there is a method by which the researcher may be warned against significant errors in the measurement of sample dimensional characteristics, or in the computations that were used to calibrate the relation between the measured peak load and the material's fracture toughness.

Table 3-4 Sensitivity of the fracture toughness values on sample dimensional parameters investigated for fused quartz sample Q3. (Reproduced from Mueller et al. [380])

Quantity increased by 5%	Resulting error in the initial model stiffness (%)	Resulting relative error produced on calculated fracture toughness (%)
W	30	-21
$(B/2)$	2	-4
S	-9	4
a_0	-10	7
a_1	-4	8
S_S	-1	<0.1

3.1.1.6 Conclusions

A micron-scale fracture toughness measurement method based on the chevron-notch approach is proposed and demonstrated on two brittle and isotropic materials, namely (i) a piece of fused quartz that is commercially available and is used as a standard for nanoindenter calibration and (ii) Nextel 610™ alumina fibres extracted from a commercially available wire of aluminium matrix composite. Data are interpreted using sample-specific finite element simulations, conducted assuming that the crack front is flat, that the material is isotropic and that there is no significant R -curve behavior.

The approach is shown to produce reproducible data consistent with what can be expected from the literature for both materials. Compared with other methods that have been proposed for the measurement of fracture toughness in samples of microscopic dimensions, chevron-notched bend bars have the following advantages:

- fracture toughness is measured using a real, atomically sharp crack;

- when K_{Ivb} is measured, the majority of the crack front is situated in pristine material, free of the various forms of internal damage (such as roughening, surface contamination, ion implantation, internal stresses, vacancies, and redeposited material) that are typically produced by micromachining processes such as ion milling or chemical etching; and
- if the material is susceptible to slow crack growth, lower loading rates are permissible than with straight-through, precracked or prenotched, sample geometries [390].

The method is conveniently implemented once procedures have been established for (i) for the production of triangular ligaments sufficiently thin to drive crack nucleation at low loads, and (ii) for parametric linear elastic finite element calculations that give the compliance calibration curve for each test. This latter step in the process is less limiting than it might at first glance appear to be: once procedures and computer routines have been established, FE calculations are typically far less time-consuming than micromilling procedures.

We also report the first (to our knowledge) measurement of the fracture toughness of nanocrystalline alumina; our result confirms estimations of the intrinsic grain boundary toughness of crystalline α -alumina predicted by a theoretical model for grain bridging toughening in alumina with micron-sized grains [402].

3.1.2 Extension of the chevron notch test to triangular microcantilevers

(Adapted from Ref. [381]: G. Žagar, V. Pejchal, M.G. Mueller, L. Michelet, A. Mortensen, *Fracture toughness measurement in fused quartz using triangular chevron-notched micro-cantilevers*, *Scripta Materialia*. 112 (2016) 132–135. doi:10.1016/j.scriptamat.2015.09.032)

In the previous Subsection (3.1.1), the microscopic chevron-notched sample method was demonstrated by measuring the fracture toughness of amorphous fused quartz and nanocrystalline alumina using FIB-machined microscopic cantilever beams having a rectangular cross-section. These samples had to be prepared along a sharp $\sim 90^\circ$ edge of the material specimen. In this Subsection, the use of a different chevron-notched microsample sample geometry, which can be produced by micromilling along a single (polished) surface, is demonstrated. This eases sample production significantly and extends the field of application of the chevron-notched sample microtoughness test.

3.1.2.1 Materials and methods

We prepared triangular chevron-notched micro-cantilevers, Figure 3.10, by FIB milling the flat surface of the same fused quartz prism as used in Subsection 3.1.1 [380]. To avoid charging effects during milling, the fused quartz surface was first coated by an ~ 10 nm carbon layer using a Cressington™ 208 Carbon Coater (Watford, UK). Shaping of triangular cantilevers was done with a 30 kV Ga⁺ source in a Zeiss™ NVision™ 40 (Oberkochen, Germany) dual beam instrument with currents of ~ 0.3 nA in final machining stages. The most important milling step is the final stage, in which the chevron-notch and its ligament are produced. To make the notch as thin as possible, milling was done using a low ion current, 10 pA, and in a way, such that the ligament apex is located in the plane of cantilever symmetry roughly at one-half the total height of the triangular cross-section.

As in Subsection 3.1.1 [380], each sample was modelled using finite element simulation to extract its compliance calibration curve. For convenience and efficiency of finite element analysis, the chevron notch was generally offset at some distance (S_S) away from the cantilevers' fixed end.

Machined chevron-notched cantilevers were fractured using the same nanoindentation instrument (TriboIndenter TI950, Hysitron Corporation, Minneapolis, MN, USA) equipped with a cube corner probe (tip radius of ~ 100 nm). Vertical force P was applied in the center of the top cantilever surface at distance S from the notch (Figure 3.10a). All tests were done at room temperature and 20-50% relative humidity in load-controlled mode at loading rates around 2 to 3 $\mu\text{N/s}$. Before and after each test, the cantilever specimen was analysed by Scanning Electron Microscopy (SEM) in order to: measure all relevant specimen dimensions (Table 3-5), confirm that the ligament was properly fabricated and ensure that fracture took place within the notch, Figure 3.10c. The actual load application point in each test was determined by observation of broken cantilevers SEM micrographs, using the imprint left by the nanoindenter probe. Six specimens were tested in this way; of these, two were dismissed as being invalid because of an irregularly machined ligament, and one due to a lack of detectable stable crack propagation in the load-displacement curve. Thus, results presented here are from the three remaining successful tests.

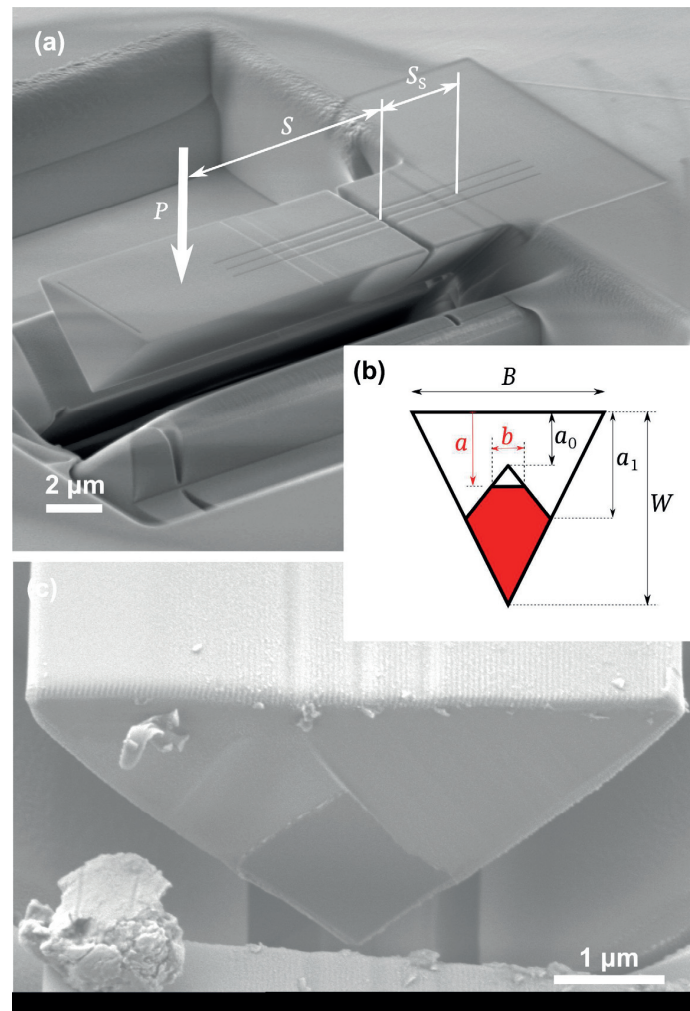


Figure 3.10 (a) Triangular micro-cantilever beam with the chevron notch, as prepared on a flat fused quartz surface by FIB milling. (b) Sketch of chevron notch geometry with characteristic ligament dimensions. The fractured surface of a chevron ligament is assumed to be triangular. Shaded region (in red) represents the unfractured portion of the ligament. (c) Fracture surface of a chevron-notch ligament. (Reproduced from Zagar et al. [381])

Table 3-5 Geometrical dimensions (as defined in Figure 3.10), experimental loading rates \dot{P} , critical (peak) loads P_c , minimum of the geometrical function $F_v(\tilde{a}_c)$ at normalized critical crack length \tilde{a}_c and calculated fracture toughness K_{Ivb} for triangular chevron-notched micro-cantilevers prepared from fused quartz. (Reproduced from Zagar et al. [381])

Sample no.	W μm	B μm	a_0 μm	a_1 μm	S μm	S_S μm	\dot{P} $\mu\text{N/s}$	P_c μN	\tilde{a}_c –	$F_v(\tilde{a}_c)$ –	K_{Ivb} MPa $\text{m}^{1/2}$
1	3.6	5.9	2.0	2.8	8.2	2.2	2	16.7	0.635	435.9	0.658
2	2.7	4.6	1.2	1.9	8.7	2.0	3	15.7	0.546	315.7	0.660
3	3.5	6.1	1.3	2.5	10.3	3.2	3	31.7	0.481	244.3	0.685

3.1.2.2 Results and discussion

Load—displacement responses of those three microfracture tests are shown in Figure 3.11. Responses in Figure 3.11a are corrected for the effect of indentation, by assuming that the displacement measured directly in the test is the sum of the cantilever vertical deflection and the average of two to three measured displacements at load P in conventional nanoindentation tests that were conducted within the (FIB-affected) region of the bulk fused quartz prism close to the fixed end of each cantilever. The material in this region is representative of the material at the cantilever's free end because both have been subjected to roughly the same (comparatively low) ion doses as the result of imaging with a low current FIB (10 pA) upon sample preparation.

Each successful test response featured three different regions. The first is a linear region that represents the elastic cantilever downward deflection free of crack growth. This region extends up to the point where the concentrated tensile stress normal to the notch plane at the apex of the chevron ligament initiates a crack. Crack initiation in fused quartz specimens can be a smooth process; this was the case for two specimens, Figure 3.11a (squares and circles). The linear response then continuously transits into a second, nonlinear, region, in which stable crack propagation occurs, downwards through the ligament. It was also found that crack initiation can be accompanied by a “pop-in” event; this was clearly visible for the third specimen (green curve in Figure 3.11a).

Once initiated, the crack traverses the notch ligament; we define the crack length a using the top of the cantilever beam as the origin, Figure 3.10b. Assuming that the crack front remains straight and symmetrically situated at all times up to position $a = a_1$ defined in Figure 3.10b, the crack front width b is simply given by $b(a) = B(1 - a_1/W)(a - a_0)/(a_1 - a_0)$, where B , W , a_0 and a_1 are defined in Figure 3.10b. As is well known, this increasing front width b serves to stabilize crack growth because it causes the elastic strain energy release rate: $G = P^2/2b (dC/da)$ where dC/da is the change of the specimen compliance C with crack length a , to initially decrease with increasing a .

For brittle, linear elastic materials and under the condition of plane strain (which is commonly assumed to hold for cracks in chevron notched specimens), the stress intensity factor is $K_I = \sqrt{E' G}$, with $E' = E/(1 - \nu^2)$ and E and ν the Young's modulus and the Poisson's ratio of the material, respectively. The stress intensity factor can thus be expressed as $K_I = P/(B\sqrt{W}) \times F_v(\tilde{a})$, where the dimensionless geometrical function is defined in terms of the normalized crack length $\tilde{a} = a/W$ as:

$$F_v(\tilde{a}) = \sqrt{\frac{1}{2(1 - \tilde{a}_1)} \left(\frac{\tilde{a}_1 - \tilde{a}_0}{\tilde{a} - \tilde{a}_0} \right) \frac{dC_v}{d\tilde{a}}} \quad \text{Equation 3-5}$$

In Equation 3-5 the normalized chevron notch geometrical parameters are $\tilde{a}_0 = a_0/W$ and $\tilde{a}_1 = a_1/W$, while the dimensionless compliance of the specimen is $C_v = CE'B$.

As in the previous Subsection 3.1.1 [380], the compliance calibration curve, $C_v(\tilde{a})$, of each sample was calculated by bespoke linear elastic finite element (FE) analysis of the sample knowing its (measured) characteristic dimensions, given in Table 3-5. For each test specimen, a series of thirty FE models was generated in a such a way that the crack length over the series is progressively incremented over the range $a_0 \leq a < a_1$, i.e. each model of the series represents the same specimen geometry at different crack lengths, Figure 3.11b.

The results of FE calculations for tested specimens in Figure 3.11a are shown in Figure 3.11c with open symbols. Data obtained from FE calculations for each specimen were fitted using a fifth-order polynomial function (solid line in Figure 3.11c), which then served as the closed form representation for the specimen dimensionless compliance function $C_v(\tilde{a})$. From this, the geometrical function $F_v(\tilde{a})$ was computed via Equation 3-5. The result is shown by dashed lines in Figure 3.11c.

Typical curves giving the geometrical function $F_v(\tilde{a})$, and therefore the stress intensity factor dependence on crack length, $K_I(\tilde{a})$, for chevron-notched specimen are convex; for constant load P , both functions $F_v(\tilde{a})$ and $K_I(\tilde{a})$ initially decrease with increasing crack length \tilde{a} , reach a minimum at $\tilde{a} = \tilde{a}_c$, and then increase beyond \tilde{a}_c . The applied load P scales with functions $F_v(\tilde{a})$ and $K_I(\tilde{a})$, causing those curves to shift vertically while their shape and the crack length corresponding to the minimum remain the same. At any fixed applied load P it is trivial to see that the crack instability criterion, $dK_I/da \geq 0$, is satisfied at stationary values of $F_v(\tilde{a})$ and $K_I(\tilde{a})$, where, for the critical crack length $\tilde{a} = \tilde{a}_c$, both functions are at their minimum. In the absence of plastic deformation in the material that is tested, the onset of crack instability in a chevron-notched specimen is uniquely predefined by the specimen geometry, which in turn defines the value of $F_v(\tilde{a}_c)$. Therefore, to compute the fracture toughness the only required experimentally measured quantity is the critical (peak) load P_c at which this instability takes place (incidentally, note that this is valid in a load-controlled tests; on the other hand, in displacement-controlled tests the point of instability is often past the maximum measured load P_c). Finally, with measured P_c and the value of $F_v(\tilde{a}_c)$ determined by the (bespoke simulation-derived) compliance calibration curve, the fracture toughness is given as $K_{Ivb} = P_c/(B\sqrt{W}) \times F_v(\tilde{a}_c)$.

Critical loads P_c , measured with the triangular chevron notched micro-cantilevers (Figure 3.11a), and the calculated critical crack lengths \tilde{a}_c and minima $F_v(\tilde{a}_c)$ are summarized in Table 3-5. The fracture toughness of the fused quartz material tested here, averaged over the three tested triangular micro-cantilever specimens, is found to be $K_{Ivb} = 0.67 \pm 0.01 \text{ MPa}\sqrt{\text{m}}$. This result is in good agreement with our previous measurements obtained with rectangular chevron-notched micro-cantilevers (Subsection 3.1.1), namely $K_{Ivb} = 0.65 \pm 0.04 \text{ MPa}\sqrt{\text{m}}$ [380]. The present study thus demonstrates that the chevron-notched microfracture testing method exposed in Subsection 3.1.1 [380] can be transposed to triangular beams; from a practical standpoint this is a significant simplification since triangular beams can be machined by micromilling into a single surface.

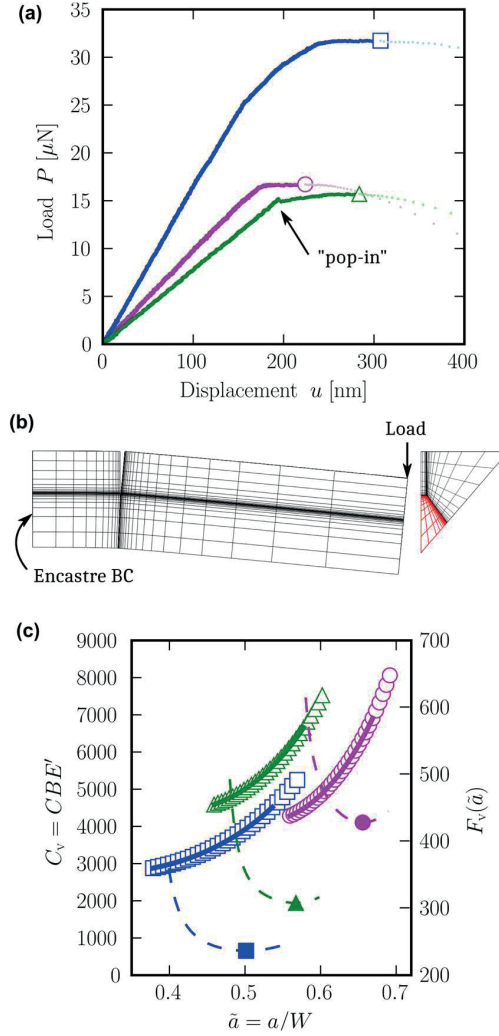


Figure 3.11 (a) Force–displacement response of tested triangular chevron-notched cantilevers corrected for the indentation. The critical (peak) load of each test is indicated with open symbols. (b) Example of the FE mesh (deformation is enhanced by the factor of 100) used for compliance calibration. Shaded region (in red) in half of the cross-sectional view represents the unfractured portion of the ligament. (c) Compliance calibration data for cantilevers tested in (a). Dimensionless compliance, $C_v = CBE'$, as a function of normalized crack length, $\tilde{a} = a/W$, is shown with open symbols (FE calculations) and solid lines (fits). Minimum values, $F_v(\tilde{a}_c)$, of corresponding specimen geometrical functions F_v (dashed lines) are indicated with solid symbols. (Reproduced from Zagar et al. [381])

Note that fused quartz is a material that is strongly susceptible to environmentally assisted slow crack growth (SCG) caused by the presence of moisture in air [403,404]. Interaction between water molecules of air and Si—O bonds in fused quartz near the crack tip when the crack is under load, creates conditions that enable a crack to grow at finite velocity with its tip subjected to stress intensity values that are significantly lower than the (fast) fracture toughness of the material. For example, cracks in fused quartz at room temperature and $\sim 70\%$ relative humidity (corresponding to a water partial pressure of ~ 2.2 kPa) subjected to a stress intensity that is $\sim 75\%$ of the fracture toughness and above (the so-called SCG Region II) grow at a rate of ~ 0.2 mm/s [404]. Because of this, SCG can lead to significant underestimations of the fracture toughness values, since, at the moment of crack instability, the crack might in reality be significantly longer than what was initially measured or assumed; see Ref. [390].

With chevron-notched samples, measured variations in the specimen compliance up to crack instability serve, for brittle linear-elastic materials, as a signature of the crack length evolution. In Figure 3.12, by using the calculated compliance calibration curves of the present triangular chevron-notched specimens, we calculated the crack position, and after smoothing of the resulting curve, the crack velocities in present tests (Figure 3.12b). Then, as shown in Figure 3.12c, one can deduce the crack tip stress intensity factor at each moment (tracked by the applied load) of the test. As seen, although crack tip velocities are low (Figure 3.12b), at no moment does the calculated stress intensity factor K_I in Figure 3.12c fall below K_{Ivb} . In other words, the low measured crack tip velocities are fully consistent with the crack being driven by the applied load, as dictated by the chevron-notched sample geometry, and not by subcritical crack growth mechanisms (if SCG was active K_I would take much smaller values, see data in Ref. [404]). It is concluded from this that there is no trace, in the present tests, of subcritical crack growth mechanisms being operative. This observation, which agrees with data in Subsection 3.1.1 [380], is not what one would expect from theory based on SCG data in the literature [390]. We presently have no simple explanation to offer for this observation.

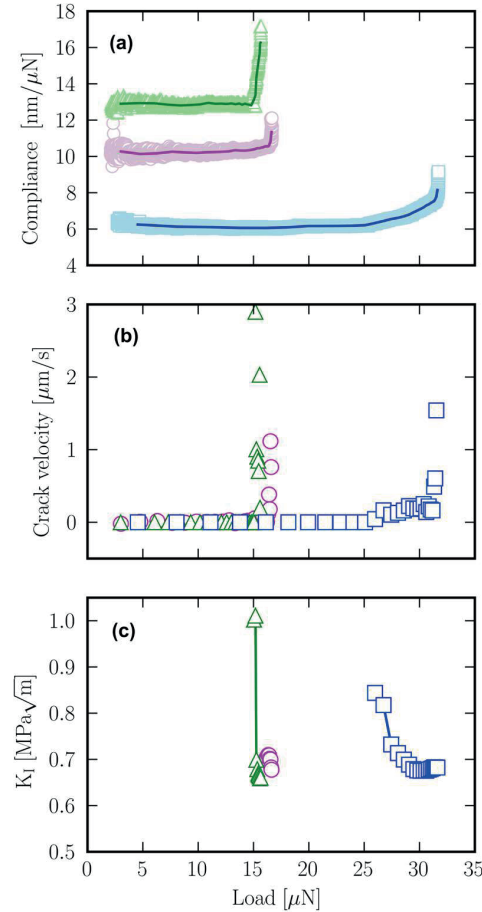


Figure 3.12 (a) Linear elastic compliance as a function of the applied load, up to critical load P_c , as obtained from force—displacement responses in Figure 3.11a (symbols are the same); compliance—load signals after smoothing are indicated with lines. (b) Crack velocity as a function of the load obtained from smooth compliance—load curves in (a). (c) Stress intensity factor at the crack tip versus applied load as calculated from experimental data (Figure 3.11 and Figure 3.12a) using compliance calibration curves.

(Reproduced from Zagar et al. [381])

3.1.2.3 Conclusion

In this Subsection, fracture tests using microscopic chevron-notched fracture toughness samples of triangular cross section were presented. This extends the method presented in Section 3.1.1 (Ref. [380]) to materials accessible from a single surface. The method is convenient for measuring the toughness of brittle, linear-elastic materials that exhibit no significant R -curve and yields results which are unaffected by focused ion-beam milling. A consistent fracture toughness value of $0.67 \pm 0.01 \text{ MPa}\sqrt{\text{m}}$ is obtained using fused quartz, in agreement both with data in Subsection 3.1.1 (Ref. [380]) and with macroscopic test data in the literature. Against expectations, data also show no influence of subcritical crack growth on fracture during the test.

3.2 Chevron-notch tests on silicon particles

The microscopic Chevron-notch fracture toughness test developed using isotropic, benchmark, materials in the previous Section 3.1 was subsequently tried on silicon particles extracted from Al-Si alloys. Early experiments and observations are briefly described in this short Section. These led to the work on silicon wafer in the following Section 3.3.

Silicon particles were extracted from a binary Al-12.6%Si alloy heat treated at 550 °C for 6 days using a process described in detail below in Subsection 4.1.1.2 and further discussed in Subsection 4.1.3.3. In short, the aluminium matrix was first dissolved using a mixture of nitric, phosphoric, and acetic acids, and then particles were collected, filtered, and deposited on a polished steel substrate. This process resulted in dry, isolated, silicon plate-like particles lying on one of their large (111) facets; Figure 3.13 shows an example. Chevron-notched microcantilever beams of triangular cross section were then produced into the silicon particles using FIB milling as described in Section 3.1, see Figure 3.14. A difference, however, was that in this case the particle needed first to be welded to the substrate; otherwise, the particle would simply move (and disappear) upon scanning with the SPM in the nanoindenter before mechanical testing. The welding was done by means of carbon deposition under the electron beam in the SEM/FIB apparatus.

An added degree of complexity with respect to the previous tests on fused quartz and on nanocrystalline alumina fibres (Section 3.1), is that silicon particles are single crystals; hence, anisotropy must be considered. If initial trials proved to be successful, the idea was to first retrieve the particle crystallographic orientation using Electron Back-Scattered Diffraction (EBSD) and then micromachine the specimen aligned along a specific orientation of interest.

Chevron-notch tests on silicon particles (e.g., Figure 3.14) were, however, unsuccessful. The measured load—displacement response was linear up to fracture (Figure 3.14d), indicating an absence of crack formation and growth. This lack of signatures of stable crack growth (i.e. pop-ins or a non-linear curve indicative of an increasingly compliant sample) betrayed crack-initiation issues that rendered tests invalid. It was thus decided to conduct microscopic fracture toughness tests on single crystalline silicon wafers to further study the matter; this is discussed in the next Section.

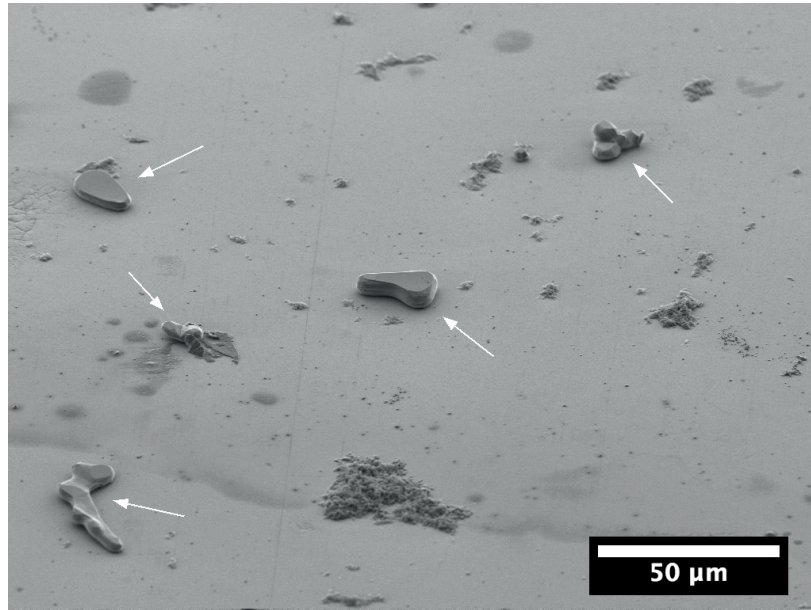


Figure 3.13 Eutectic silicon particles (indicated with white arrows) lying on a polished steel substrate. The particles were extracted from a heat-treated Al-12.6Si alloy by selectively etching the aluminium matrix.

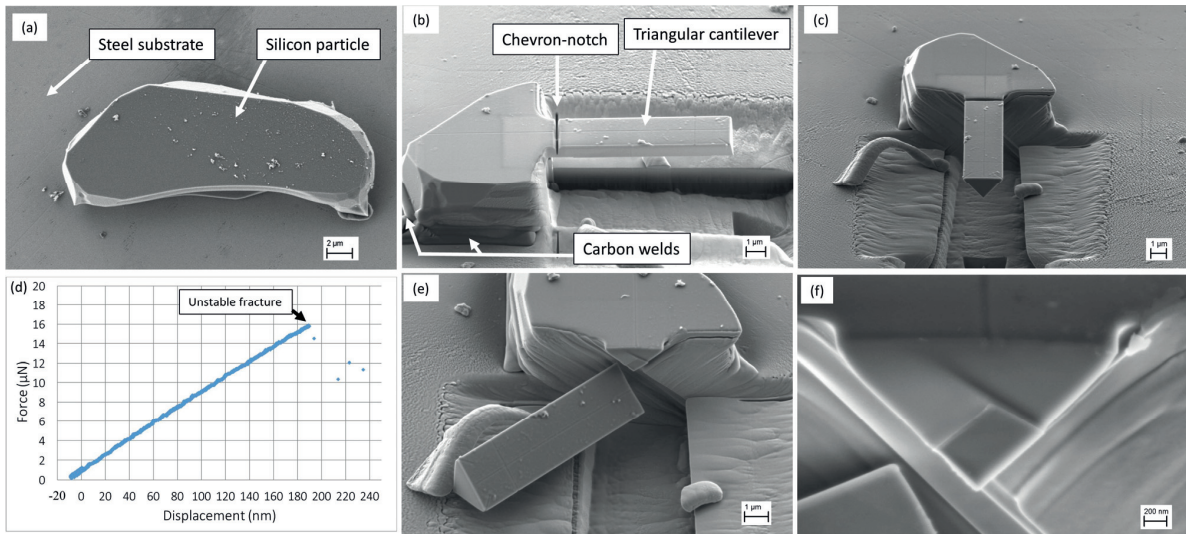


Figure 3.14 Chevron-notch fracture toughness test on a eutectic silicon particle extracted from an Al-12.6Si alloy. (a) Silicon particle lying on a steel substrate. (b) The same particle after FIB-micromachining to produce a cantilever beam of triangular cross section with a chevron notch. To prevent the particle from moving upon testing, it was welded to the substrate using carbon deposition. (c) Front view of the particle ready to be tested. (d) Force—displacement response: no sign of stable crack initiation and growth is observed. (e) Fractured cantilever after the micromechanical testing. (f) Fractography of the notch.

3.3 Chevron and straight-through notch tests on silicon wafer

(Adapted from Ref. [382]: M.G. Mueller, G. Žagar, A. Mortensen, *Stable room-temperature micron-scale crack growth in single-crystalline silicon. Accepted for publication in the Journal of Materials Research, 2017*)

In this Section, room temperature fracture along the (111) plane of electronic grade silicon is probed at the micron-scale using straight-through and chevron notched cantilever beams. A work-around for the crack-initiation issue depicted in the previous Section and confirmed here is found. The main experimental observation is that a growing crack can extend and arrest at different stress intensity factor values within the same specimen. The present data thus provide evidence of variations in the effective Si fracture toughness along the path of a growing crack. This effect could be explained by variations in the extent of limited crack-tip plasticity along the crack path. The present work also shows that the microscopic chevron notch test is, from an experimental point of view, not a convenient method to probe the fracture toughness of silicon because it is difficult with silicon to nucleate a crack at the chevron tip at loads low enough to allow for subsequent stable crack growth.

3.3.1 Materials and Methods

Microscopic cantilever beams of triangular cross-section were carved into the surface of a ($\bar{1}10$) Czochralski silicon wafer slightly p-doped with B (resistivity 1 – 10 Ohm cm) using FIB milling on a Zeiss™ NVision™ 40 (Oberkochen, Germany) SEM/FIB dual-beam system using 30 kV Ga⁺ ions. Currents ranged from 3 nA for the initial rough milling steps down to 700 pA for the final milling steps. Close to the root of each cantilever one of two types of notch was machined: either (i) a chevron-notch (milled at +/- 30° from the top) or (ii) a straight-through notch (milled straight down from the top) was produced by FIB milling with a much lower current of 10 pA, chosen to minimize the notch thickness, Figure 3.15. Specimens and the machined notches were oriented such as to probe the (111) fracture plane with a crack growing in the $[\bar{1}10]$ direction. Once prepared, samples were carefully checked in the SEM/FIB to ensure the absence of redeposited material along or around the notch.

The micromechanical tests were conducted using a TI 950 TriboIndenter® (Hysitron® Corporation, Minneapolis, MN, USA) nanoindentation apparatus, equipped with a cube-corner diamond tip, to apply the load and measure the load-point displacement. Each specimen was aligned to have the loading axis within ± 0.5 degrees of the normal to its top surface; this was achieved using the nanoindenter's Scanning Probe Microscope (SPM) capability and a two-axis goniometric tilt stage (Newport Corp., Irvine, CA) fixed on the positioning stage. The SPM was also used to aim the point of load application at the cantilever's centreline close to its free end. The tests were conducted in the apparatus's "load control" mode. Prior to loading, the nanoindenter tip was put in contact with the sample, holding a load of 1 μ N to measure the drift in the displacement data. The test was started when the observed drift rate was lower than 0.05 nm/s. The loading rate was set to 0.8 μ N/s and kept at that value until fracture; note however that, as discussed below, the tests were not effectively run in an ideal but rather in an over-damped load control mode. At the end of a test, each sample was taken into the SEM to examine its fracture surface, measure the dimensions of the ligament, and identify the point of load application, which was revealed as an indent on the now-disconnected cantilever arm.

The most usual difficulty encountered in the use of CN specimens for the fracture testing of brittle materials (regardless of sample sizes) is that cracks can be difficult to initiate at the tip of the chevron notch. This leads to the frequent observation of rapid fracture at loads well above those that would be required

to propagate the crack across the chevron-shaped ligament. This limitation was observed with the present microscopic silicon samples during preliminary tests of this work on silicon wafer and on silicon particles extracted from an Al-Si alloy (Section 3.2). To ease crack initiation at low applied loads and thus overcome the crack-initiation problem encountered in early attempts (see Discussion for details) the following procedure was used before the fracture test. In the SEM/FIB apparatus, after having produced a cantilever beam with a chevron notch using FIB-milling as described above, a micromanipulator tungsten needle (Kleindiek Nanotechnik GmbH, Reutlingen, Germany) was approached to the cantilever's free end, welded to it with a small carbon deposit and moved cyclically up and down by a distance of roughly $0.5\ \mu\text{m}$ 10 to 15 times, so as to produce slight, elastic bending of the chevron-notched cantilever; Figure 3.16 shows the process. This procedure induces concentrated cyclic strain in the material at the triangular ligament's tip (a region composed of FIB-affected material). The needle was then detached from the cantilever by FIB milling the weld and the cantilever's free end, which shortened the beam by a few micrometres, bringing it to its final geometry. The result of this initial "small chevron notch tip pre-fatigue" step in the sample preparation process was found to be that, when subsequently loading the beam during the fracture toughness test, cracking was initiated at applied loads low enough to enable subsequent stable growth of the crack across the chevron ligament.

The dimensions of all the samples tested in this work, which are defined in Figure 3.15, are given in Table 3-6. Based on that information, bespoke 3D finite element (FE) models were implemented in Abaqus/Standard™ 6.11 software (Dassault Systèmes, Providence, RI, USA) to calculate the compliance calibration functions of CN and STN samples, in a similar way as was done in Section 3.1 (Refs. [380,381]) with the difference, however, that here the material's elastic anisotropy is considered: single crystalline silicon has a cubic-symmetry stiffness matrix with the three independent linear elastic constants, $c_{11} = 166\ \text{GPa}$, $c_{12} = 64\ \text{GPa}$ and $c_{44} = 80\ \text{GPa}$ [164]. The compliance dependence on crack length, $C(a)$, in CN samples is obtained by first calculating a series of the compliance values C at increasing values of crack length a for each cantilever geometry (Figure 3.20a symbols) and subsequently fitting those data with a polynomial function (Figure 3.20a, lines). Note that in all stages of the work (in both calculations and data interpretation) the crack is assumed to be straight. The change of the compliance with respect to the crack length for each CN sample, dC/da , is then obtained by evaluating the derivative of the fitted polynomial.

The released elastic strain energy rate G is finally calculated according to

$$G = \frac{P^2}{2b} \frac{dC}{da} \quad \text{Equation 3-6}$$

where P is the load measured in the test, b is the width of the crack front (see below) and dC/da is the derivative of the compliance function (calculated using bespoke finite element modelling as explained above) evaluated, in the case of CN tests, at the crack length that is derived from the measured compliance, itself extracted from the slope of the line connecting each data point in the indentation-corrected load—displacement curve to the origin.

Because FIB milling of straight-through notches causes removal of the material near the notch ends (Figure 3.15b and Figure 3.22), the geometry of the STN samples resembles that of the CN samples with a finite crack length $a = a_p$ (outlined with dashed line in Figure 3.15b and Figure 3.22). Thus, the compliance calibration function of STN samples was calculated in a similar way as for CN specimens, with the difference that the change of the compliance with respect to the crack length in STN samples is evaluated by the finite difference approximation, i.e. $dC/da = [C(a_p + da) - C(a_p)]/da$ where $C(a_p + da)$

and $C(a_p)$ are obtained from FE calculations with $da = 1$ nm. Scripts that aid in generating Abaqus chevron-notch FE models, used here to obtain the compliance calibration functions, are made freely available for download from the web site of our laboratory [405].

For CN samples, the crack front width b (assumed to be straight) is an increasing function of the crack length, i.e.

$$b = B(1 - a_1/W) \times (a - a_0)/(a_1 - a_0) \quad \text{Equation 3-7}$$

For STN samples, the crack front width is a constant obtained simply by evaluating the expression for b of CN samples at $a = a_p$. For simplicity, Equation 3-6 can be contracted to $G = P^2 g_F(a)$, if we define the geometrical function $g_F(a) = 1/(2b) \times dC/da$ (note that this is simply the dimensional counterpart in units of $[N^{-1}m^{-1}]$ of the geometrical function, $F_v(a/W)$, reported in Section 3.1 and Refs. [380,381]).

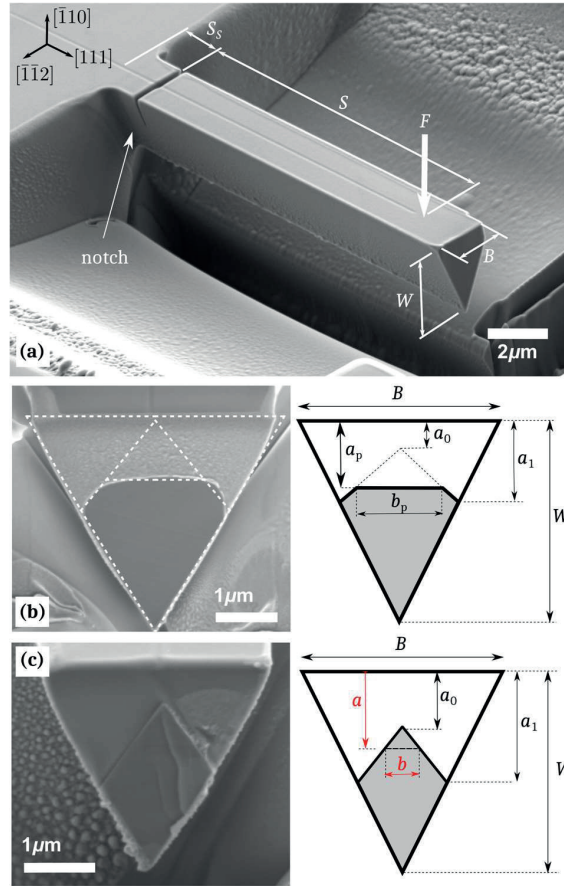


Figure 3.15 (a) General geometry of triangular micro-cantilevers prepared by FIB milling single crystal silicon (110) wafer. (b) Straight-through notch (sample S4, Table 3-6) and (c) chevron notch (sample C2, Table 3-6) fracture surfaces of tested cantilevers (shaded in grey on the right-hand sketches). Straight-through notches are FIB milled perpendicular to the $(\bar{1}10)$ plane, which preferentially removes material near the edges of the notch front. To account for that, the geometry of these samples is approximated in calculations as being chevron-like with static crack length $a = a_p$ (see sketch). (Reproduced from Mueller et al. [382])

Table 3-6 Geometrical parameters of straight-through (S1—S4) and chevron (C1—C3) notched cantilevers, as defined in Figure 3.15. (Reproduced from Mueller et al. [382])

Sample	W [μm]	B [μm]	S [μm]	a_0 [μm]	a_1 [μm]	a_p [μm]	S_s [μm]
S1	3.13	3.03	13.72	0.43	1.42	1.06	3.43
S2	3.94	3.66	11.00	0.01	1.50	1.16	3.50
S3	3.84	3.68	11.40	0.185	1.80	1.24	2.00
S4	4.96	5.08	12.80	0.1	2.24	1.51	2.10
C1	2.86	2.32	11.64	0.57	1.59	-	1.34
C2	3.62	3.26	9.86	0.70	2.04	-	2.10
C3	3.73	3.04	12.41	0.58	1.93	-	2.33

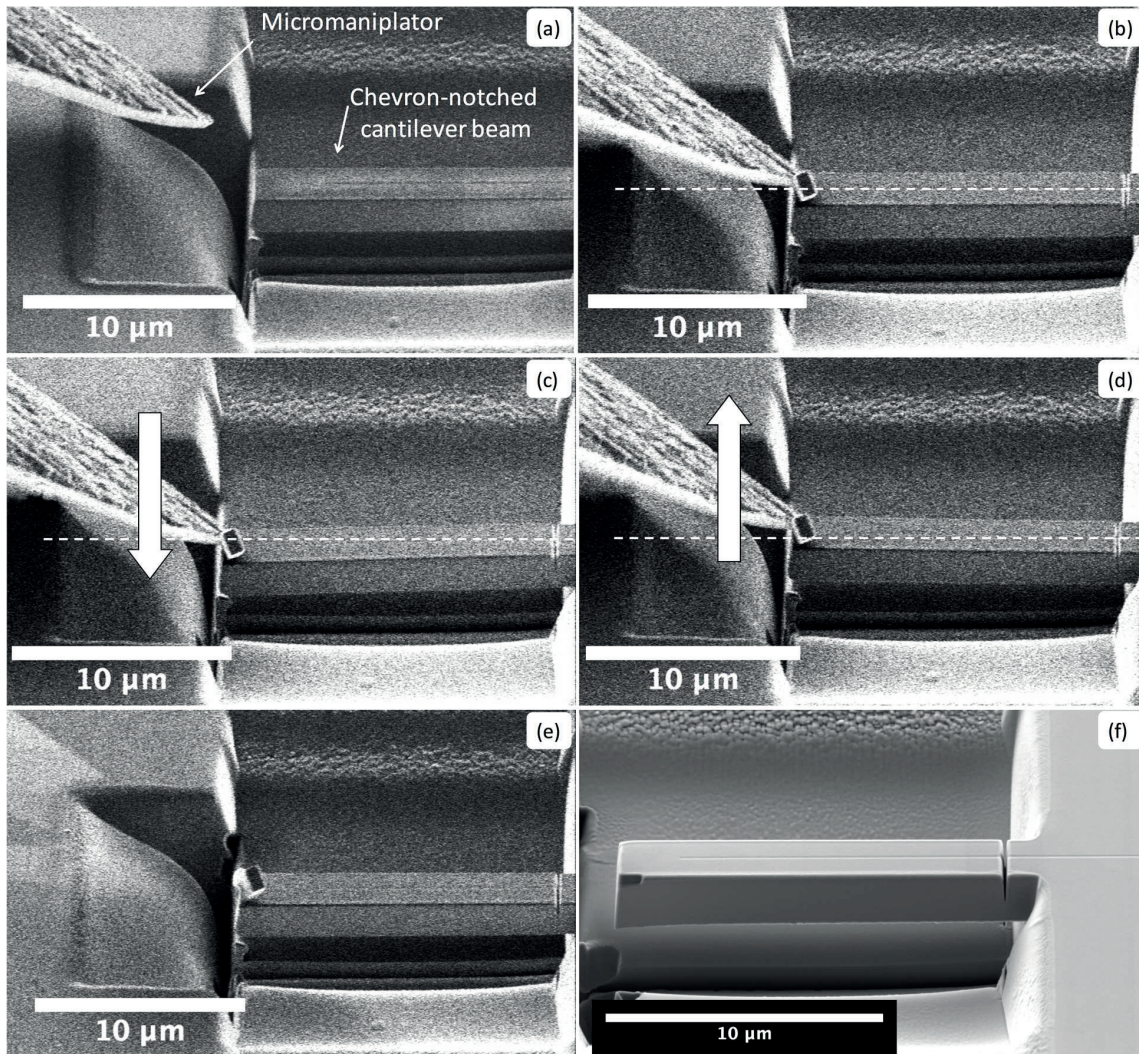


Figure 3.16 Sample C1 during the “small chevron notch pre-fatigue” preparation step to ease crack initiation at the subsequent testing stage. (a) The micromanipulator is approached to the FIB-produced cantilever beam. (b) The micromanipulator is carbon-welded to the beam. The dashed white line is for reference. In (c) and (d) the beam is slightly bent downwards and upwards, respectively. (e) The micromanipulator is detached by FIB milling its tip. (f) The free-end of the cantilever beam is cut by FIB milling, leaving the sample ready for micromechanical testing. (Reproduced from the Supplementary Material of Mueller et al. [382])

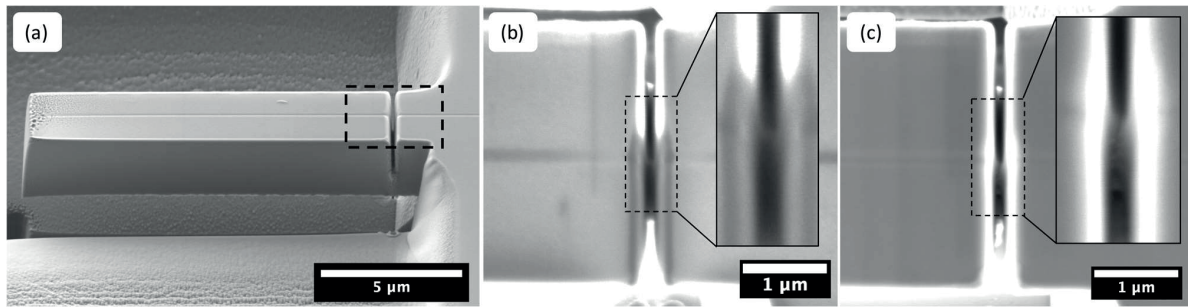


Figure 3.17 (a) SEM image of Sample C2 from a tilted point of view. Close-up views of the notch (dashed square in (a)) before and after the small cyclic pre-deformation step are shown in (b) and (c), respectively, where the view is straight down from the top. Signs of a small crack may be distinguished in (c) at the tip of the triangular ligament. (Reproduced from the Supplementary Material of Mueller et al. [382])

3.3.2 Results

The load—displacement responses corrected for indentation of the STN or CN cantilever beams are shown, respectively, in Figure 3.18 and Figure 3.19. STN curves are linear until the point of sudden fracture, defined by a sudden large load drop and displacement jump (Figure 3.18). Predictions of the finite element model were validated for all four STN samples in that the measured compliance and the calculated compliance match for all samples, Table 3-7, where apparent silicon fracture toughness values computed by assimilating the notches to cracks are also listed. Geometrical functions g_F calculated for CN specimens of this work are given in Figure 3.20b.

With CN specimens (Figure 3.19), loading curves are only linear up to a point where a first, small “pop-in” (load drop and displacement jump) is observed: this is the moment of crack initiation. During pop-ins, displacement of the sample is sudden and rapid; load-displacement data during those phases of the test are therefore not to be trusted, given that the indenter load control loop might not have had the capacity to follow the sample, leading to the possibility that there was temporary loss of contact during the rapid pop-in phase of the event. Thereafter, the curve stabilizes, and continues with a lower slope, betraying an increased compliance as a result of the pop-in event. With Samples C1 and C2 the curves present successive pop-in events appearing prior to the point of final, catastrophic fracture, which is characterized by a final large drop down to zero load.

The portion of the load-displacement curves that stretches between crack initiation and final fracture is indicated in bold for each CN sample in Figure 3.19. The measured compliance as a function of the displacement in that region is plotted in the top row of Figure 3.21. As seen, the compliance increases significantly with each pop-in in Samples C1 and C2, while it only increases slightly between pop-ins. Changes in compliance are signatures of crack growth; thus, pop-ins are sudden crack extensions followed by crack arrest and periods of crack growth at a much slower rate under increasing load. The bottom row of Figure 3.21 shows how the strain energy release rate G (or stress intensity factor K_I in the right-hand axis) varied during the crack growth process in each of Samples C1, C2 and C3; as seen, the data vary significantly from sample to sample.

The fracture surfaces of all STN and CN specimens are globally flat, showing that the general crack propagation plane did not deviate significantly from (111); see Figure 3.15b-c, Figure 3.22 and Figure 3.23. Besides the easily visible terrace-kink feature on Sample C2, in the fracture surfaces several tiny marks parallel or oblique to the expected crack front direction can be distinguished upon examination at high resolution (bottom row of Figure 3.22 and Figure 3.23).

Finally, we note that the justification for taking $G = G_I$ throughout this work comes out of the evaluation of the Mode II contribution to the total strain energy release rate G for the present specimen configurations (for details, see Subsection 3.3.3.4). Results indicate that it reaches, in the worst case, only 5% of the total G value; hence, we deem it negligible. We also neglect the possibility of producing beam twisting either by off-centred loading or because of an off-centred position of the ligament at the notch. This is justified by the *post-mortem* observations in the SEM that, in all cases, the small indent left at the point of load application on the top surface of the post-test disconnected cantilevers was found to be within ~ 50 nm of the cantilever centreline (Figure 3.24), and the ligament at the notch was well-centred within ~ 100 nm.

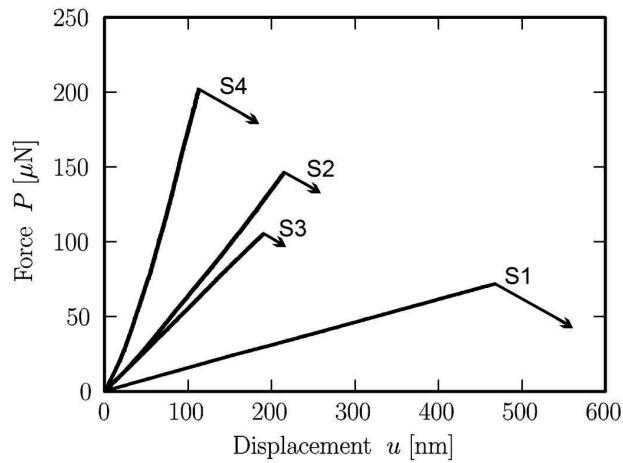


Figure 3.18 Force—displacement response of micro-cantilevers with straight-through notches (STN Samples S1—S4, Table 3-6). All data are corrected for additional displacement caused by tip indentation into the cantilevers. (Reproduced from Mueller et al. [382])

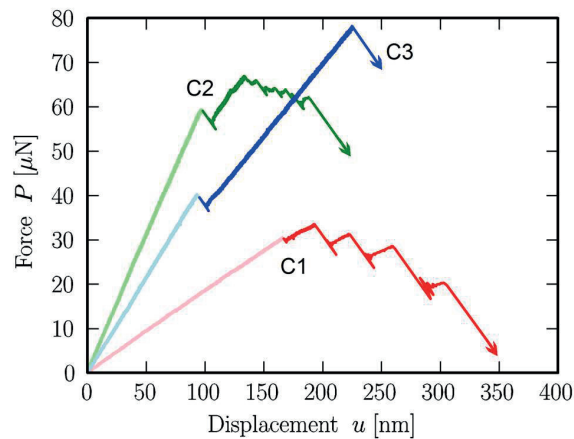


Figure 3.19 Force—displacement response of micro-cantilevers with chevron notch (CN Samples C1—C3, Table 3-6). All data are corrected for displacements due to relative tip indentation into the cantilevers. Region of the response of chevron-notched cantilevers where the crack is growing is indicated with bold lines. (Reproduced from Mueller et al. [382])

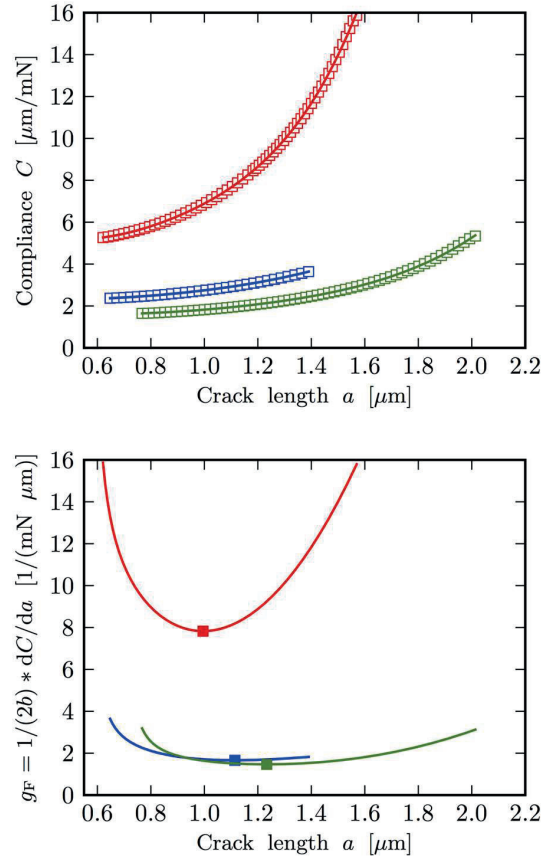


Figure 3.20 Calculated compliance calibration curves of the three chevron-notched cantilever samples: compliance C (a) and geometrical function g_F (b) vs. crack length a for chevron-notched micro-cantilevers samples: C1 (red), C2 (green) and C3 (blue). Square symbol in Panel (b) indicates minimum of g_F . (Reproduced from the Supplementary Material of Mueller et al. [382])

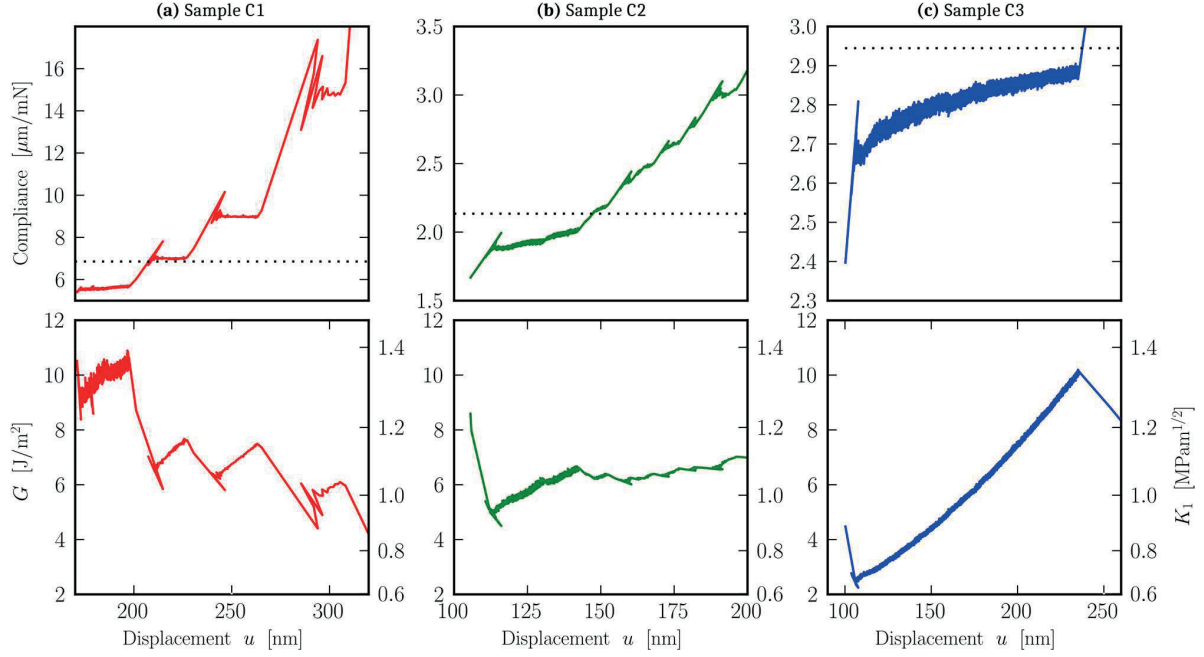


Figure 3.21 (Top row) Linear elastic compliance $C = u/P$ vs. displacement u obtained from CN cantilever responses shown in Figure 3 (only data indicated with a bold line are considered). (Bottom row) Calculated elastic strain energy release rate G versus measured displacement u . For convenience, right-hand scale corresponding to the stress intensity is indicated according to, $K_I = \sqrt{GM_{(111)}}$, where the elastic fracture factor of SC Si for (111) plane $M_{(111)} = 178 \text{ GPa}$ [164]. The dotted line indicates the critical compliance that corresponds to the critical crack length of the chevron-notched geometry. (Reproduced from Mueller et al. [382])

Table 3-7 Experimentally measured fracture load P_c and compliance C_e , and calculated model compliance C_m , geometrical function g_F , critical released elastic energy rate G_c and fracture toughness K_{Ic} for micro-cantilevers having straight-through notch. (Reproduced from Mueller et al. [382])

Sample	P_c [μN]	C_e [$\mu\text{m}/\text{mN}$]	C_m [$\mu\text{m}/\text{mN}$]	g_F [$1/(\text{mN}\sqrt{\mu\text{m}})$]	G_c [J/m^2]	K_{Ic} [$\text{MPa}\sqrt{\text{m}}^{1/2}$]
S1	72	6.54	6.562	2.447	12.69	1.50
S2	146	1.62	1.612	0.308	6.60	1.08
S3	105	1.80	1.824	0.572	6.35	1.06
S4	202	0.85	0.869	0.143	5.83	1.02

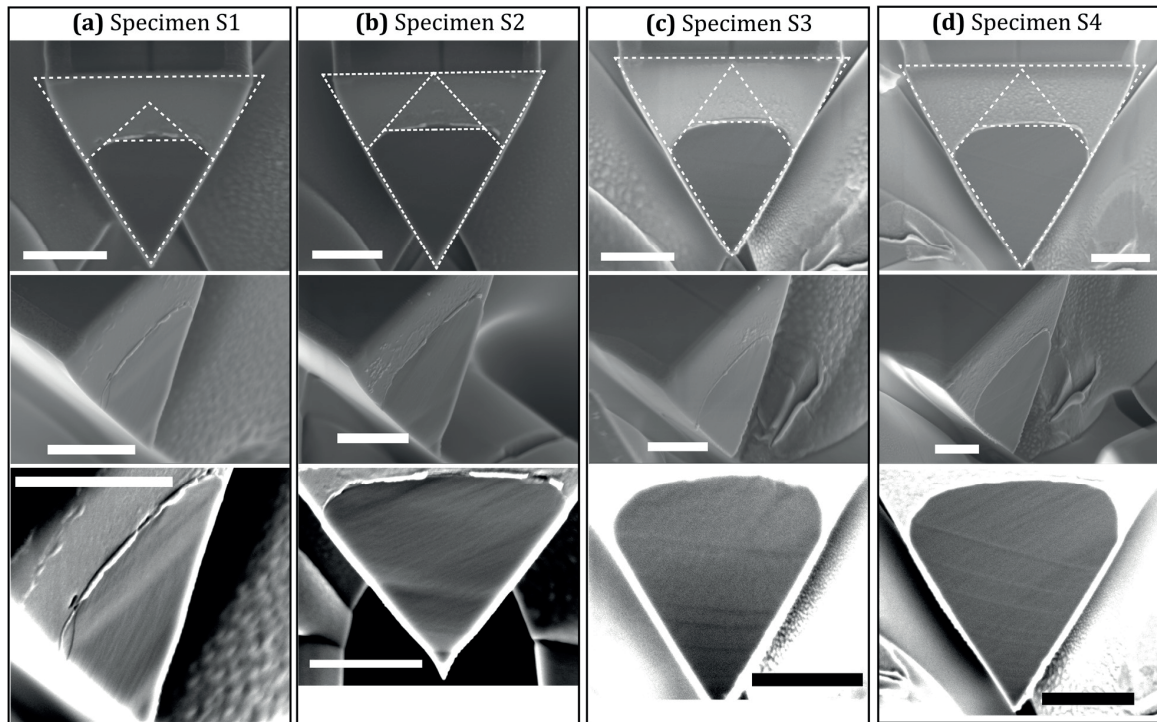


Figure 3.22 Fractured surfaces, all along (111) planes, of the four tested single crystal silicon micro-cantilevers with a straight-through notch (STN). Scale bar in all images represents 1 μm . Columns of images (a) to (d) correspond to different images of the fracture surface of Specimen S1 to S4, respectively. Images on the top and middle rows are taken from different perspectives. Notch geometries used for calculations are superimposed and indicated with a white dashed line in the top-row images. The brightness and contrast of the bottom-row images have been manipulated to enhance the visibility of marks on the fracture surfaces. (Reproduced from the Supplementary Material of Mueller et al. [382])

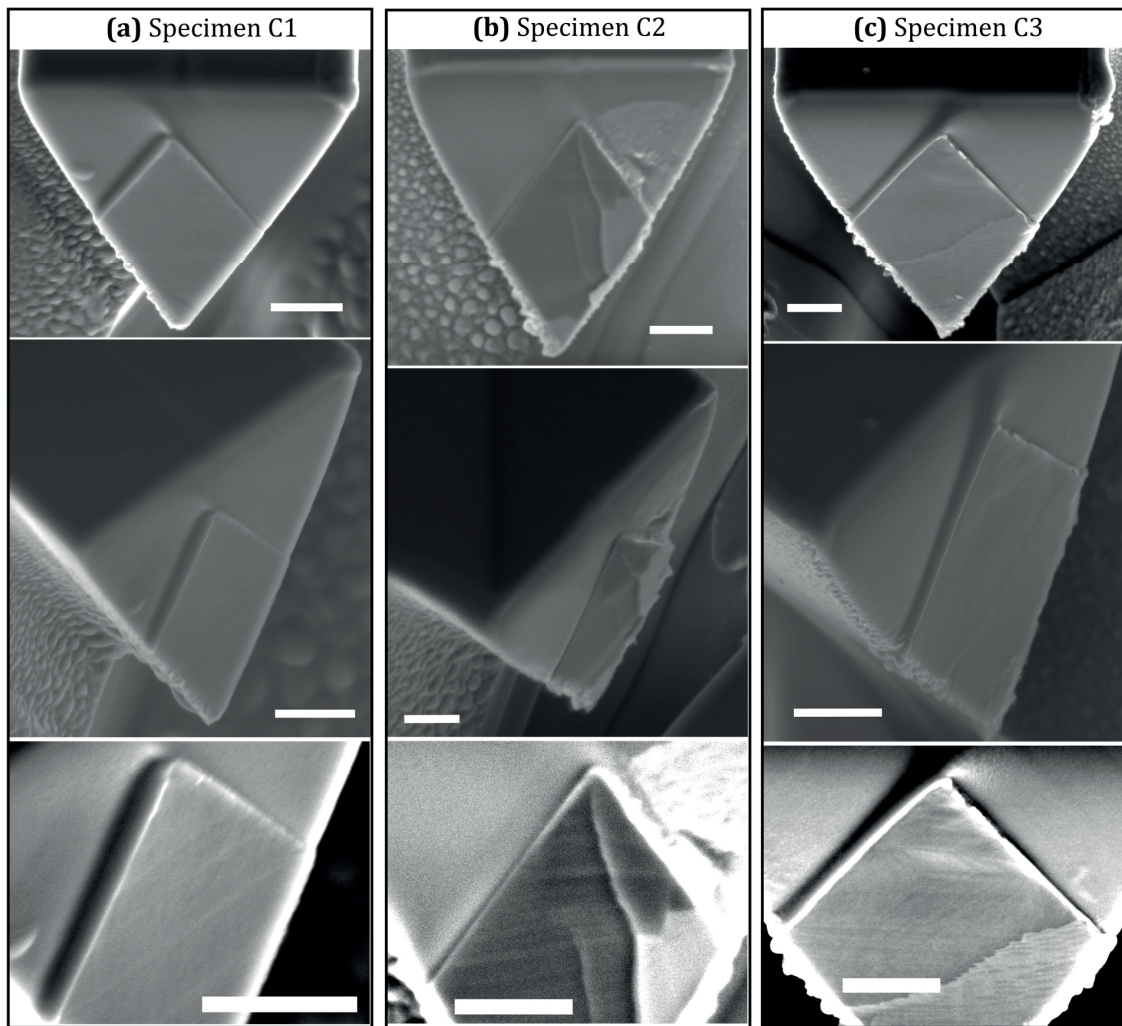


Figure 3.23 Fractured surfaces, (111) planes, of the three tested single crystal silicon micro-cantilevers with a chevron notch (CN). Scale bar in all images represents 0.5 μm . Columns of images (a) to (c) correspond to different images of the fracture surface of Specimens C1 to C3, respectively. Images on the top and middle rows are taken from different perspectives. The brightness and contrast of the bottom-row images have been manipulated to enhance the visibility of marks on the fracture surfaces. (Reproduced from the Supplementary Material of Mueller et al. [382])

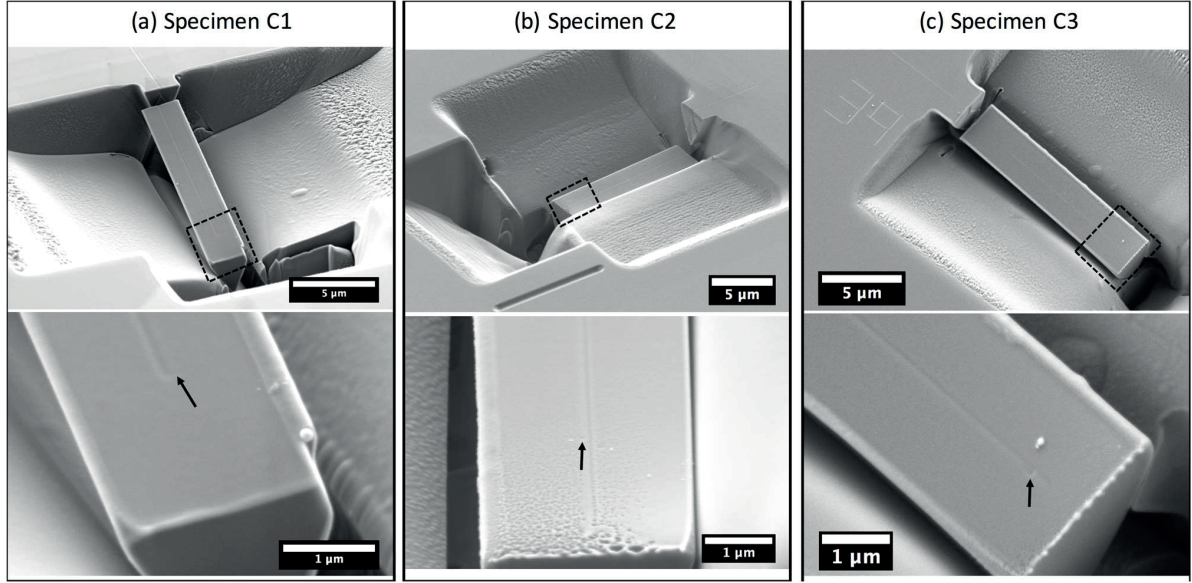


Figure 3.24 Post-test SEM examination of the chevron-notched specimens. The location of the load-application point, identified as a shallow indent, is indicated with black arrows in the lower images, which are close-ups of the area marked with a black, dashed, rectangle in the top images.

3.3.3 Discussion

3.3.3.1 Straight-through notched samples

As is known, using FIB-milled STN specimens to evaluate fracture toughness at a small scale is questionable; reasons for this are three-fold: (i) assimilating a notch to a crack, given the finite notch-tip radius [164], (ii) the fact that the material itself at, and around, the crack tip is modified, to a higher or lesser extent depending on the material, after FIB-milling [274–276] (especially when the incident FIB is perpendicular to the surface [274,276,406], which is how STN samples are mostly produced; see also Section 3.3.3.3) and (iii) ion implantation, which can locally produce residual stresses that alter, to a remarkably large extent in some materials [244], the effective stress field at the notch tip.

Here, measured critical strain energy release rate $G_{Ic(111)}$ values in STN Specimens S2-S4 are near $\approx 6 \text{ J/m}^2$. This value comes close to the result of the pioneering work of Di Maio and Roberts [236] that constitutes, together with the present work, the only (to the best of our knowledge) fracture toughness measurement of the (111) fracture plane in silicon done at the microscopic scale. In Specimen S1, however, a value roughly twice as high was recorded ($G_{Ic(111)} = 12.7 \text{ J/m}^2$), even though no particularity is observed in this specimen with respect to the other three similar specimens, except that it is a bit smaller in size. Overall, the STN results are about twice and four times, respectively, the theoretical fracture energy of Si along (111) planes: $2\gamma_{(111)} = 2.94 \text{ J/m}^2$ [164] and fall above the range of experimental values reported in the literature for the (111) fracture plane in silicon (omitting measurements that used either indentation or ion-beam-notched techniques, see Literature Review on Sections 2.3, 2.5 and Ref. [164]).

This overestimation seems to be in contrast with the work of Jaya et al. [216] on fracture along the (110) plane in silicon, who reported, using notched microscopic specimens, measured fracture toughness values that fall within the expected range for that plane (note that there is a typo in the notch orientation

in [216], which should read “ $(\bar{1}10)[001]$ ” [407]). It is, however, noteworthy that in an earlier contribution the fracture toughness values gleaned using similar notched microscopic specimens in that same plane were far higher [243]. Also, in a separate work, high fracture toughness values were obtained in silicon microscopic STN clamped beams probing a (110) plane [269], prompting the authors to introduce a correction factor to lower the fracture toughness closer to expected values.

In summary, even though it seems that the concerns about the STN technique mentioned above do not always affect results to a large extent in silicon (e.g., Ref. [216] and Samples S2-S4 in this work), the present data confirm that measurements of the toughness in silicon using microscopic STN samples must be taken with extreme caution because of the established potential for (large) overestimations.

3.3.3.2 Crack initiation in microscopic Chevron-notched specimens

The ability to initiate the crack at an early stage of the test and to subsequently grow it in a stable fashion are key requirements for a valid CN test. Early attempts by ourselves to perform microscopic CN fracture toughness tests on $(\bar{1}10)$ and on (111) silicon wafers oriented to probe the (111) $[\bar{1}10]$ or the $(\bar{1}10)[111]$ fracture systems were unsuccessful in that crack initiation was not followed by crack growth and thus occurred at a load higher than the critical load (which in CN samples is defined by their geometry and the material’s fracture toughness). As a result, complete fracture of the samples occurred as soon as a crack was nucleated, rendering the tests invalid.

This crack-initiation problem was not encountered when nanocrystalline alumina or amorphous fused quartz were tested in the same way [380,381]. Reasons why it is present with single-crystalline silicon are unclear. One possible explanation is that difficulty in initiating a crack in silicon results from the nature and/or extent of FIB damage to the machined surface, as the tip of the triangular ligament is a spot highly exposed to the FIB. Amorphization of the silicon at that spot is to be expected [274–276] and FIB damage in the form of gallium implantation is clearly present; we observed the formation of gallium droplets at the notch of Specimen C2 after performing the initial pre-fatigue step, see Figure 3.25 (these droplets were subsequently removed using the FIB before testing the sample). Residual stresses caused by gallium implantation could also play a role, this effect being likely strongly material-specific; for example, Norton et al. [244] estimated the residual stress at the notch of a microscopic STN specimen in alumina to be in the range 12 – 15 GPa in compression over a depth of 20 nm. In one of our early trials on silicon, we introduced a CN sample into a furnace at 500 °C for 30 min under vacuum before the mechanical test (in an attempt to test whether residual stresses were the cause for the difficulty in crack initiation). Here too we found that a droplet had exuded at the notch after the heat-treatment (Figure 3.26; in the subsequent mechanical test this sample did not show stable crack growth and was therefore discarded, as was the use of heat-treatment prior to testing). The difficulty in initiating a crack at the tip of the chevron notch in silicon, and/or the relative ease found in doing so in silica or nano-crystalline alumina [380,381], might thus be related to differences in the nature and level of FIB-induced micro-damage from one material to the other [244].

We therefore explored several approaches to ease crack initiation in silicon CN specimens; among these, the only successful procedure was the “chevron notch tip pre-fatigue” process described above, in the Materials and Methods section (Section 3.3.1). This procedure enabled the production of CN samples that could initiate stable cracks; however, operationally it is not trivial. Half of the cantilevers (four other samples than those tested) were fatally damaged in the process and had to be discarded. Furthermore, its effects are not fully understood (e.g., it might be that the cycling caused migration of implanted Ga

atoms). This said, this preparation step was successful in that it did promote crack initiation at low applied loads in three (Samples C1-C3) out of the four specimens that had survived the preparation and pre-fatigue procedure.

What remains unclear is whether the process produces a (tiny) pre-crack or a different effect at the apex of the chevron notch. In observing the notch at high magnification before and after the process on Sample C2, a pre-crack may arguably be recognized (see Figure 3.17); however, fully clear images of the notches could not be produced and hence we cannot provide a firm conclusion. Measured initial compliances and those calculated via FE match well in all three samples (see Table 3-7), indicating that, if a pre-crack was present, it was sufficiently small not to have a detectable effect on the mechanical response of the beam and hence on the interpretation of the test.

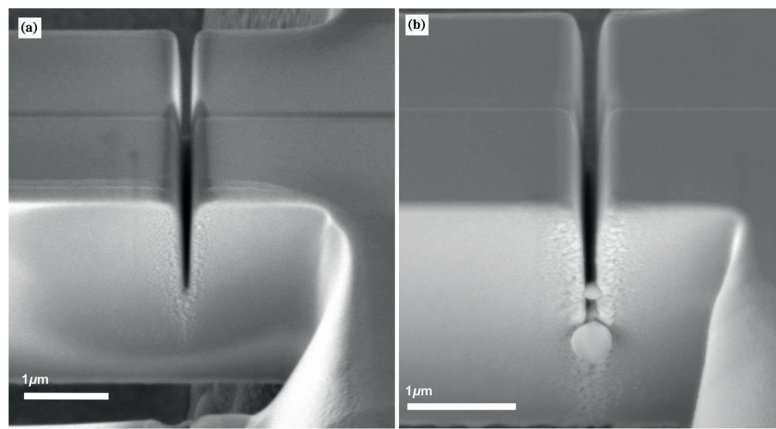


Figure 3.25 CN Sample C2 before (a) and after (b) cyclic elastic deformation. Cyclic deformation of the micro-cantilever resulted in the formation of spherical drops at the notch end. The drop was removed prior to the mechanical test by additional FIB milling under a current of 10 pA. (Reproduced from the Supplementary Material of Mueller et al. [382])

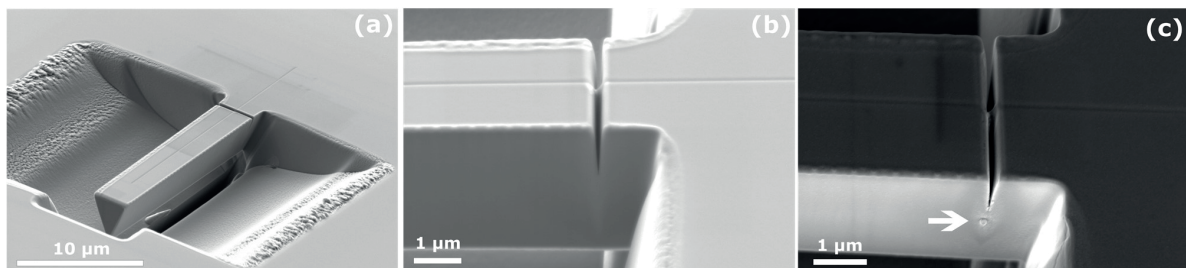


Figure 3.26 SEM images (b) and (c) are close-ups of the chevron-notch of the specimen in (a) before and after subjecting the sample to 500 °C in vacuum, respectively. The arrow in (c) points to a droplet, likely of Ga, that appeared after the heat treatment. This specimen was at a later stage dismissed because a stable crack could not be initiated upon mechanical testing. (Reproduced from the Supplementary Material of Mueller et al. [382])

3.3.3.3 Crack growth and fracture toughness

In a perfectly load-controlled chevron-notch fracture toughness test the geometry alone defines a specific crack length up to which a crack grows stably, and beyond which the sample fractures completely and suddenly, regardless of the material as long as its fracture toughness is constant. The point of instability is defined by the crack location at which the stress intensity factor has ceased to decrease with

increasing crack length. In other words, the critical crack length, a_c , is at the minimum of the function $g_F(a)$, itself computed from a compliance calibration procedure.

The test data for the silicon CN samples of this work, however, show deviations from this expected behaviour. Namely, Samples C1 and C2 show that stable crack growth occurred also beyond the critical point at $a > a_c$ (see Figure 3.21, where dotted lines indicate the compliance corresponding to the critical crack lengths) and that instability was reached at a lower load after passing the maximum value (Figure 3.19). Moreover, Samples C1 and C2 also feature several pop-ins, which are indications of sudden crack extension followed by crack arrest. Close examination of the load as a function of time in these tests reveals that after each pop-in, the load immediately dropped and the set point in load was re-sought very slowly by the nanoindenter, indicating an over-damped machine response. Such sluggish load-control most likely allowed the crack to immediately lose its driving force after a pop-in and hence to arrest, such that, due to the imperfect load control, the present tests have characteristics of displacement-controlled tests. Now, as seen in Figure 3.21 bottom row, neither the values of G at which the crack suddenly extends nor the G values at which the crack arrests are the same across successive pop-ins; rather, values are scattered over the range $G_{Ic(111)} \approx 5 - 7.7 \text{ J/m}^2$ (excluding the first crack extension of Sample C1 at 10.8 J/m^2). These values are about twice the theoretical fracture energy of (111), $2\gamma_{(111)} = 2.94 \text{ J/m}^2$ [164].

The response of Sample C3 is altogether different. Here, other than at crack initiation, there is no succession of jump-like crack advances (Figure 3.19); rather, the load and the associated apparent compliance increase continuously after crack initiation (Figure 3.21c top row; this can also be seen directly on Figure 3.19 using a ruler). This increase in compliance can be interpreted in two possible ways. In the first interpretation, the compliance increase is attributed to stable crack growth, which progresses smoothly at a slow rate. The corresponding variation in strain energy release rate is over the range $G_{Ic(111)} \approx 2.5 - 10.3 \text{ J/m}^2$, ending with the latter value before the onset of rapid crack growth (Figure 3.21c bottom row). In a second interpretation of the C3 test, the apparent change in compliance is caused by drift in the displacement measurement (note that the drift rate is assessed prior to loading but its instantaneous value during a test is unknown). One can then evaluate the fracture toughness using the crack length calculated from the compliance right after the crack was initiated (Figure 3.21c) and the measured forces corresponding to the initial crack arrest and to the final fracture events; this gives $G_{Ic(111)} \approx 2.5 \text{ J/m}^2$ and $G_{Ic(111)} \approx 10.7 \text{ J/m}^2$, respectively. As seen, regardless of whether stable crack growth took place or not in Sample C3 (after crack initiation), one obtains similar extreme values of $G_{Ic(111)}$; the reason for this is the weak dependence of g_F with crack length near the minimum of g_F in this specimen (see Figure 3.20b). We note in passing that the toughness value at crack arrest is close to $2\gamma_{(111)}$.

Several studies have documented that the thickness of the amorphous layer on a side-wall (a wall parallel to the ion beam) produced by milling with a 30 kV Ga⁺ FIB is in the range 20 – 30 nm at saturation [274–276]; this is what can be expected at the edges of the triangular ligament in the CN specimens tested in this work. Hence, except at the beginning of stable crack propagation, the proportion of damaged material along the crack front is small and becomes even smaller as the crack advances (because b increases linearly with a , see Figure 3.15 and Equation 3-7). The amorphous FIB-induced damage layer is thus not expected to pollute toughness measurements produced by a developed crack in a CN specimen. This is contrary to STN specimens, which probe the onset of propagation of a notch made of FIB-milled material, furthermore known to be thicker since in milling STN notches the ion beam is applied

perpendicularly to the silicon (in this case the amorphous layer is ~ 60 nm [274,276], and the silicon structure can actually be affected down to a depth of 230 nm [406]).

Summing up, we find that, also with the CN geometry and despite the expectation that this test is unaffected by FIB-damage, erratic values, well above the expected value of $2\gamma_{(111)} = 2.94$ J/m² [164] are measured, with the exception of values at crack arrest in Specimen C3. Also, we note that the apparent fracture toughness values measured using CN samples are comparable to the values obtained from STN samples.

The finding that a growing crack in the (111) plane can propagate at a certain apparent critical stress intensity value and then arrest at a lower value, both values being higher than $2\gamma_{(111)}$, is in line with results reported by John [350], where similar behaviour and G_{Ic} ranging from ~ 4.6 to ~ 5.4 J/m² for Si in the same fracture system as in this work were measured at room temperature and also at -196°C using much larger (millimetre-wide) double cantilever specimens in displacement-controlled testing [350]. Thus, it is unlikely that the erratic crack growth leading to the scatter in fracture toughness was a consequence of the small sample size or a result of FIB damage.

As a candidate reason for the erratic response obtained in CN specimens, we studied the possibility that the “small chevron notch pre-fatigue” preparation step introduces extensive plastic deformation into the material through which the crack grows during the test. Using the largest beam-end displacements gathered from SEM images during the preparation step (e.g. Figure 3.16) and the FE models constructed to calculate the compliance calibration curves, the stress field at the chevron ligament was estimated for Specimen C1. In these simulations, silicon was taken as isotropic, ideally elastoplastic, with Young modulus $E = 163$ GPa, Poisson ratio 0.223 [164] and yield stress 7.6 GPa (based on compression measurements of fully crystalline nanopillars [342]). As shown in Figure 3.27(a) for the maximum deformation during the pre-fatigue step, only in a very thin layer of material at the top tip of the ligament does the von Mises equivalent stress exceed the critical value for the onset of plasticity. This means that a small amount of plasticity (e.g., the generation of a limited number of dislocations) might occur at that location, particularly if a pre-crack is produced. On the other hand, the great majority of material along which the crack grows during the mechanical test has not seen stresses high enough to introduce defects (dislocations) during the preparation step. This analysis was also done for the maximum load reached upon the initial loading in the tests (the load before the first pop-in in Figure 3.19), leading to the same conclusion (Figure 3.27 (b)). Hence, the effect of the pre-fatigue step or the initial sample loading is unlikely to be the cause for the erratic responses of the different CN samples. Results show that extensive plasticity is very unlikely in the great majority of the ligament, except at the very tip of the triangular ligament, where stress might be high enough to introduce some dislocations, which might have travelled some distance into the specimen (particularly if a pre-crack was created in the pre-fatigue process).

A likely explanation for the erratic response is, therefore, that it resulted from the fact that, in both Ref. [350] and the present work, Si toughness measurements were produced using growing cracks. This might have caused some, limited but finite, amount of dislocation emission and subsequent interaction with growing cracks. It was recently observed by TEM that dislocations are emitted at the tip of sharp cracks grown by microindentation in Si at room temperature [376] (Figure 2.52, a phenomenon that was also suggested to hold for many brittle materials in Ref. [377]). It is thus possible that, as was also suggested in Ref. [350], the emission of dislocations at the tip of growing cracks, and the ensuing finite and variable crack tip shielding, cause a departure in measured toughness values upward of the expected value for the onset of the propagation of a pristine crack.

Specifically, if we assume in a simple back-of-the-envelope calculation that advancing a crack in silicon will cause the nucleation of a new dislocation every time a increases by Δa , we can estimate that the increment ΔG_c in the work of fracture that is linked to dislocation emission is roughly $\mu b^2/(\Delta a)$. With μ taken equal to the shear modulus of polycrystalline silicon (64.9 GPa) and b the dislocation Burgers vector (0.383 nm) [408], we can solve for the value Δa needed to account for the difference between the theoretical fracture toughness value in silicon ($\approx 3 \text{ J/m}^2$ for (111)) and the values measured here (which fluctuate around 6 J/m^2). We arrive at $\Delta a \approx 3 \text{ nm}$, which is close to the distance measured between dislocations that were observed just ahead of a crack tip produced at room temperature in silicon and observed in Ref. [376] (see Figure 2.52).

We thus propose that the tips of growing cracks in present samples might stochastically emit a few dislocations and encounter previously emitted dislocations along the crack path, causing in the process variations in the apparent toughness linked with the number, nature, and orientation of the dislocations involved in those events. This could explain the observed variable excess in critical strain energy release rate that is required for the propagation of cracks in (111) silicon over and above the Griffith value $2\gamma_{(111)} = 2.94 \text{ J/m}^2$, because crack tips in present samples could stochastically emit a few dislocations along the crack path, variations in the apparent toughness being caused by variations in the number, nature, and orientation of the dislocations. One question this interpretation would raise is whether or not the FIB-affected layer of material at the edges of the ligament (and thus at the borders of the crack front) in the present CN tests play a role in this process, by enhancing the level of dislocation activity, similarly to what was identified in FIB-produced silicon nanopillars [342].

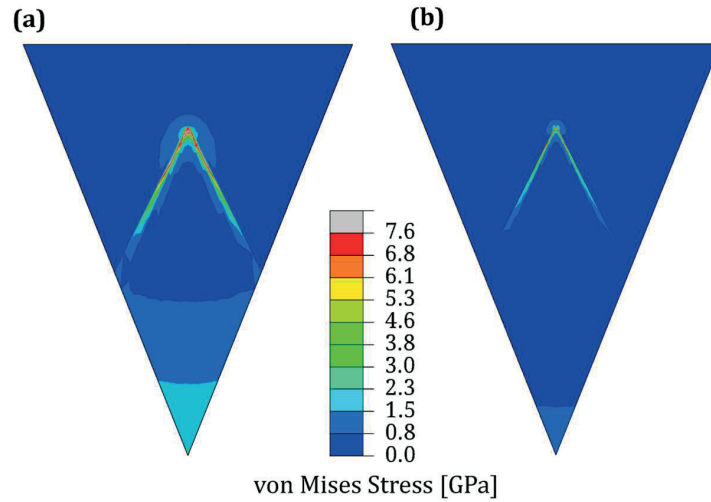


Figure 3.27 Von Mises stress distribution in the chevron ligament of Sample C1 at (a) the maximal displacement recorded during the pre-fatigue preparation step and (b) immediately before the crack initiation pop-in during the micromechanical test. The results are obtained for isotropic, elastic-perfectly plastic silicon (see the main text for material parameters). Plastic yielding (von Mises stress exceeding 7.6 GPa) is found in a very narrow region near the edges at the top part of the chevron notch. (Reproduced from the Supplementary Material of Mueller et al. [382])

3.3.3.4 Influence of Mode II in the interpretation of CN and STN tests

An alternative reason why the apparent Mode I fracture toughness values might be too high could originate from the fact that cantilever samples unavoidably have some shear stress present within the notch

plane. If this shear stress is large enough, it might lead to a contribution of Mode II cracking in the test data.

Since in the presence of Mode I and Mode II crack loading the total strain energy release rate is the sum of the energy rates for each of the two modes, $G = G_I + G_{II}$, Mode I propagation requires the total G to be higher by G_{II} than it need be for pure Mode I loading. Since values for G computed above via compliance calibration function correspond (given the use of a full three-dimensional finite element model) to the total released strain energy rates, maintaining the driving force for Mode I fracture in the presence of Mode II loading requires somewhat higher load P . The magnitude of this overloading essentially depends on the sample's Mode I and II crack stress singularity strengths, i.e. the Mode I and II crack stress intensity factors, K_I and K_{II} , respectively.

To estimate K_I and K_{II} for our cantilever samples we revert to FE calculations. We use the same FE models as for the compliance calibration, but now with more refined mesh around the crack front and the quarter point elements located immediately next to the crack front. This modelling strategy is commonly used to improve and obtain the theoretically expected crack stress singularity, i.e. $\sigma \propto 1/\sqrt{r}$, where r is the radial distance from the crack front [385]. Since the normal to the notch plane in our models is aligned with the z -axis and the crack propagation direction is along the y -axis (see Figure 3.28a, inset), the stress components of interest for estimating the crack stress intensity factors are $\sigma_{33}(y)$ for Mode I and $\sigma_{32}(y)$ for Mode II. The theoretical expressions for the near-field stress distributions of Mode I and Mode II cracks are well known and can be found, for example, in the book of Anderson [385]. The stress distribution along the symmetry line, y , within the notch ligament, are theoretically expected to be: $\sigma_{33}(y) = K_I/\sqrt{2\pi y}$ for Mode I and $\sigma_{32}(y) = K_{II}/\sqrt{2\pi y}$ for Mode II. The angle-dependent part in these expressions vanished since we are considering the stress distributions along the crack propagation direction for which the angle $\theta = 0$.

In Figure 3.28a and b, we show in linear and logarithmic plots respectively, the dependence of the stress components σ_{33} (filled symbols) and σ_{32} (open symbols) on the distance from the crack front y along the symmetry line of a chevron notch ligament, as obtained from FE models for chevron-notched Sample C1. Stress distributions are plotted for several values of the relative crack length $\hat{a} = (a - a_0)/(a_1 - a_0)$. Fits of the expected theoretical expressions to the FEM data in the vicinity of crack fronts, with K_I and K_{II} being the free fitting parameters, are indicated in Figure 3.28a and b with solid lines for σ_{33} and a dashed line for σ_{32} . As seen, FE models reproduce reasonably well expected stress distributions; this is truer for σ_{33} than for σ_{32} . For Sample C1, the ratios K_I/K_{II} , obtained after fitting FEM data, at each relative crack length \hat{a} are shown in Figure 3.28c with circles. Similarly obtained ratios K_I/K_{II} for chevron-notched Samples C2 (squares) and C3 (triangle) are also shown in Figure 3.28c. As seen, the ratios of Mode I to Mode II crack stress singularities for the three samples are reasonably similar.

For small cracks, the ratio K_I/K_{II} is quite high indicating a clear dominance of Mode I over Mode II. As the crack gets longer, the ratio K_I/K_{II} is settling to a constant value near ~ 4.5 . Writing $G = K^2/M$, where M is the elastic stress factor (e.g. the Young's modulus in case of isotropic materials), a ratio value $K_I/K_{II} \approx 4.5$ suggests that $G_I \approx 20 G_{II}$. Mode I thus accounts for more than $\sim 95\%$ of the total G . Considering all other sources of error, it can be concluded that the importance of Mode II for the present chevron-notched cantilever samples can be neglected. Thus, the increase of here measured G 's due to the presence of Mode II crack loading is small.

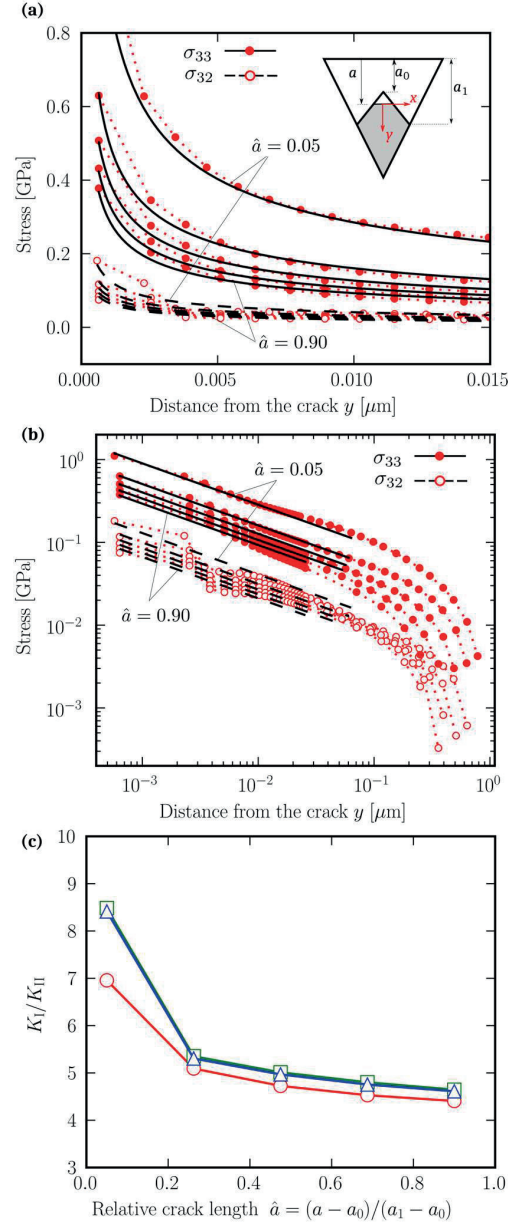


Figure 3.28 (a) Linear and (b) logarithmic plot of the normal (σ_{33}) and the shear (σ_{32}) stress as a function of the distance from the crack, y , along the line of symmetry in the chevron notch plane of the cantilever specimen C1 at several relative crack lengths, $\hat{a} = (a - a_0)/(a_1 - a_0)$. Stress distributions obtained by FEM at $\hat{a} = 0.05, 0.26, 0.48, 0.69$ and 0.90 are shown with filled (σ_{33}) and open (σ_{32}) circles. Fitted near-field crack singularity expressions are indicated with solid (σ_{33}) and dashed (σ_{32}) lines. (c) Ratio of the stress intensity factors, K_I/K_{II} , as a function of the relative crack length \hat{a} for chevron-notched specimens C1 (circle) C2 (square) and C3 (triangle). (Reproduced from the Supplementary Material of Mueller et al. [382])

3.3.4 Conclusion

The fracture toughness of silicon at room temperature was probed at the microscopic scale using triangular cantilever beams with either straight-through (STN) or chevron (CN) notches along the (111) fracture plane with a $[\bar{1}10]$ crack growth direction. CN tests reveal crack extension and arrest together with

a jerky evolution of the fracture toughness during crack growth of a (short) crack. The mechanism responsible for this is at present undetermined; a strong candidate is stochastic crack tip dislocation activity producing crack-tip shielding, which can also account for the fact that measured fracture toughness values (both here and in practically every study in the literature) exceed the theoretical fracture energy $2\gamma_{(111)}$. A second conclusion of this work is that the microscopic CN test, which promotes stable crack growth and is hence free from the artefacts of the STN test (and might be used in a far more extensive testing program aiming to generate statistically significant data on the stochastics of growing cracks in silicon), has in single-crystalline silicon crack initiation issues that make it inconvenient for this particular material.

Chapter 4 Strength

This Chapter tackles the question of the mechanical strength of silicon particles within Al-Si alloys. In Section 4.1, a microscopic 3-point bending test is developed and used to probe Si particles extracted from a binary, eutectic, Al-Si alloy. In Section 4.2, silicon particles within an industrially important Al-Si-Mg alloy are probed using a different, *in-situ*, micromechanical test, which is complementary to the previous 3-point bending test and was inspired by the method of *C-shaped* sample testing (Refs. [348,409], see Figure 2.49 and Figure 4.15). As will be seen, a main finding of the micromechanical tests on silicon particles is the realization that they can be very strong but feature identifiable deleterious surface defects. Thus, in Section 4.3 the defects are investigated using FIB-serial sectioning to gain insight into their origin.

Disclaimer: This Chapter contains extracts, including literal reproduction of full paragraphs and figures, of the following publications, which the author has produced together with colleagues working on this project: Mueller et al. [410] (Section 4.1), Mueller et al. [411] (Section 4.2) and Mueller et al. [412] (Section 4.3). The author was the main contributor to all experimental work, finite element modelling, and writing in these publications, except for the TEM examinations in Section 4.1.3.3, which were carried out by Dr. M. Fornabaio.

4.1 Microscopic 3-point bending test of silicon particles

(Adapted from Ref. [410]: M.G. Mueller, M. Fornabaio, G. Žagar, A. Mortensen, *Microscopic strength of silicon particles in an aluminium–silicon alloy*, *Acta Materialia*. 105 (2016) 165–175. doi:10.1016/j.actamat.2015.12.006)

As illustrated in detail in the Introduction and the Literature Review (Chapter 1 and Chapter 2), the strength of the silicon phase in Al-Si alloys has been mostly assessed using approaches that measure averaged back-calculated phase properties. Observed differences in measured strength values have been interpreted in terms of average geometrical and morphological features of the Si phase such as size, aspect ratio and interconnectivity. Reasons why Si particles are as strong or as weak as they are found to be, or in other words structure/property relations in these particles viewed as a material with its own strength-limiting defects, have not yet been explored in depth. In this Section, a microscopic three-point bending test that measures the strength of faceted particles of high aspect ratio is developed and used to probe individual coarsened plate-like silicon particles extracted from the eutectic Al-12.6%Si alloy. Focused ion beam (FIB) milling is used in sample preparation; as will be seen, the tapered beam cross-section and multistep preparation procedure used here ensure that the particle surface area subject to tension in mechanical testing is free of ion beam damage. Results in this Section show that coarsened silicon particles in aluminium can reach strength values on the order of 9 GPa when they are free of visible surface defects; such high strength values are comparable to what has been reported for electronic-grade silicon specimens of the same size. By contrast, tests on eutectic silicon particles that feature visible surface defects, notably pinholes or boundary grooves, result in much lower particle strength values.

4.1.1 Method

4.1.1.1 Principle of the test

The flexural strength of plate-like silicon extracted from a binary Al-Si alloy is measured in this work using a microscopic three-point bending test conducted on particles that have been removed from the alloy by selective leaching the aluminium matrix. Prior to leaching, the alloy is heat-treated to coarsen the particles; this causes them to adopt naturally a variety of plate-like shapes showing flat surfaces oriented along (111) planes of the Si crystal [94,100,104,106]. We use one such flat surface, as it presents itself after etching, as the probed surface subjected to peak tensile stress during the bend test.

The sides of the specimens are shaped by focused ion-milling to turn the particles into straight beams amenable to bend testing: this inevitably causes material in the corners of the lower beam surface to be altered by the ion beam. In early measurements conducted with beams that had parallel sides and rectangular cross-sections, we found that fracture surfaces can betray crack initiation at, or near, the beam corner, i.e. from a portion of irradiated and gallium-implanted material which is likely not to be representative of silicon as it is within the alloy (Figure 4.1). This problem was alleviated by giving the beams a trapezoidal (tapered) cross-section, with the wider side of the beam subjected to tension during the test. This alters the stress distribution, causing tensile stresses to decrease as one approaches the edge of the beam. Figure 4.2 illustrates this by showing results of finite element simulations, conducted as described below, on two beams: one with a near-rectangular cross section and the other with a cross section typical of tests conducted here. As seen, whereas in the former the first principal stress is uniform along the X axis, in the latter the stress at the mid-span edge is 10% lower than the peak stress and decreases rapidly in the Z direction. This is representative of all specimens tested in this work: the minimum difference in computed stress between the edge and the peak stress in the centre was always between 10% and 20%. With such trapezoidal beams, thus, the region of the samples that is exposed to peak values of applied tensile stress during the test does not include material that was altered by focused ion beam milling, which is situated along the sidewalls of the sample. This is an important feature of the present test method, which we describe in more specific detail in the following Subsections.

We note in passing that such trapezoidally tapered specimens are often used in fracture toughness testing; however, in such tests the taper is oriented the other way around (i.e. with the narrower end at the location of peak tensile stress). This is practiced where crack growth stability is sought, since in the inverse orientation, as the crack advances, its front broadens, decreasing the driving force. This is ultimately exploited in the well-known chevron-notch fracture toughness test first introduced by Barker [386], developed into standards [383] and used to measure fracture toughness at microscopic scale in Chapter 3 [380,381,390]. By contrast, here the goal is to measure strength and hence it is accepted that the taper will, in the present orientation, accelerate crack growth once incipient cracks become unstable.

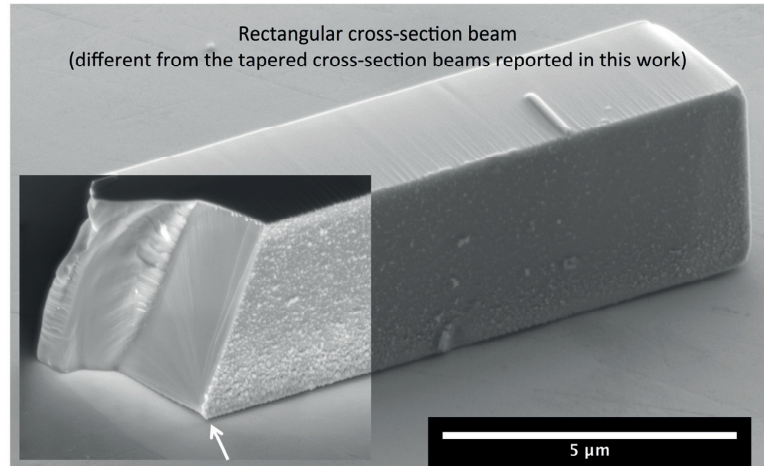


Figure 4.1 Fractured half-beam and fracture surface of a rectangular cross-section specimen produced in early phases of the work described in this Section. The fracture origin is at a FIB-damaged edge of the beam (indicated with a white arrow). Throughout the rest of the present body of work a tapered cross-section design was used instead, to prevent fracture from starting from the edges as shown here. (Reproduced from the Supplementary Material of Mueller et al. [410])

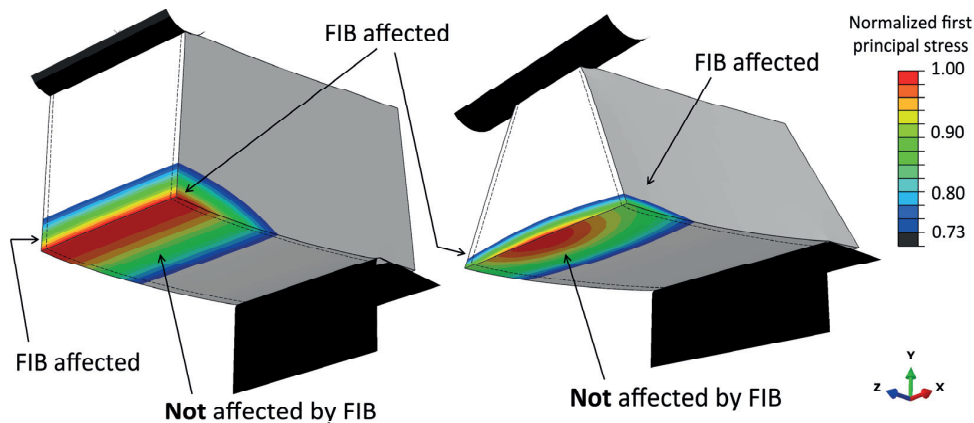


Figure 4.2 Illustration of the difference in the maximum principal stress distribution between a rectangular (left) and a trapezoidal (right) cross-section three-point bending specimen (cut view through mid-span plane). The design with a trapezoidal cross-section was thus used here to keep the higher maximum stresses away from the edges of the beam, which are affected by ion milling. (Reproduced from Mueller et al. [410])

4.1.1.2 Material

The silicon particles probed in this body of work (Section 4.1) belong to a commercially pure near-eutectic Al-Si alloy (which is the same used in Section 3.2), which was first produced as a cast ingot by Alusuisse Technology & Management AG (Neuhausen am Rheinfall, Switzerland). Chemical analysis provided along with the alloy gives 12.6 ± 0.4 wt. % Si, with 0.033 ± 0.002 wt. % Fe as the main impurity and <0.003 wt. % of Cu, Mn, Mg, Cr, Ni, Zn and Ti. The as-received alloy microstructure largely consists of lamellar Al-Si eutectic containing interconnected silicon plate-like particles, plus small amounts of (i)

relatively equiaxed and larger primary silicon particles, (ii) primary α -aluminium dendrites and (iii) pores.

This alloy was heat-treated for 7 days at 550 °C to coarsen and disconnect from each other the eutectic silicon plate-like particles, which as a result became also somewhat more regular in shape, Figure 4.3. Silicon particles were then extracted from the alloy by selectively dissolving the aluminium matrix for 1 week at room temperature in a solution prepared using H_3PO_4 85%, CH_3COOH 100% and HNO_3 70% mixed in volume ratio 83:5.5:5.5. The solution containing the extracted silicon particles was then filtered using qualitative filter paper grade 413 (VWR International bvba, Leuven, Belgium). Particles captured on the filter paper were rinsed several times, first with water, and finally with ethanol. The particles were then recovered within ethanol from the filter paper and were, in this wet condition, spread over a flat polished quenched K990 steel substrate of hardness 950 HV/100 (Böhler International GmbH, Vienna, Austria). The ethanol quickly evaporated, leaving dry silicon particles lying on the steel substrate.

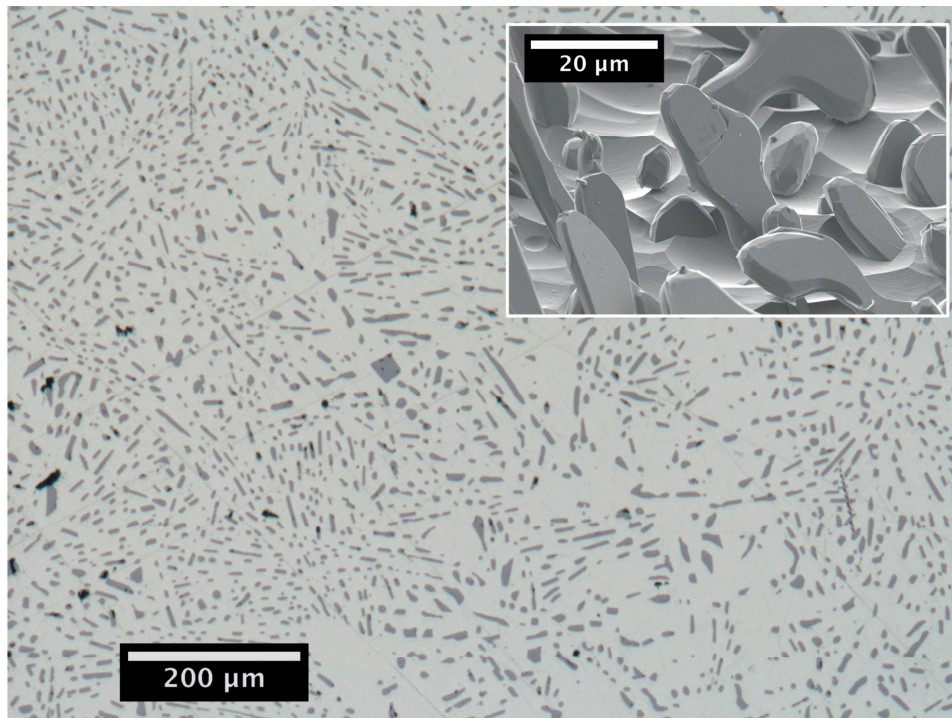


Figure 4.3 Optical micrograph of the heat-treated near-eutectic Al-Si alloy used in this work. Inset: SEM image of a few eutectic silicon particles such as the ones probed in this work after selectively etching the aluminium phase to expose them. (Reproduced from Mueller et al. [410])

4.1.1.3 Test specimen preparation

The bend specimen preparation method is summarized in Figure 4.4. The steel substrate with silicon particles resting along its surface was introduced in a Zeiss™ NVision™ 40 (Oberkochen, Germany) dual beam (SEM/FIB) instrument. One or a few plate-like particles were selected (Figure 4.4a) and shaped into a beam by 30kV Ga^+ Focused Ion Beam (FIB) milling. To produce its trapezoidal cross-section, the sample was tilted so that the angle between the FIB and the top surface of the particle was 70° to mill one side of the particle (Figure 4.4b) and 110° to mill the other side (Figure 4.4c). The FIB currents used ranged from 3 nA in initial rough-milling steps down to 80 pA in the last milling steps, notably to finish the sides of the beam.

Once each silicon beam was milled, a carbon FIB-induced deposit was applied to weld the beam to a micromanipulator needle (Figure 4.4d). The beam was then lifted (Figure 4.4f) and deposited onto a rectangular hole previously dug elsewhere by FIB milling the surface of the steel substrate (Figure 4.4e). Thin carbon welds were then made to (gently) fix the silicon beam to the substrate (Figure 4.4g) before releasing the silicon beam from the needle; this was done by FIB milling the weld holding them together (Figure 4.4h).

A typical specimen ready for testing, prepared from the eutectic particle in Figure 4.5a, is shown in Figure 4.5b. Note that, in this process and in this testing configuration, the particle surface that will later be subjected to tensile stress was never contacted by the FIB, and was furthermore protected, by the underlying steel, from being coated with redeposited matter while the beam was being machined.

Apart from the regular specimens just described, four specimens were prepared so as to subject to tension a surface along which a flaw was spotted by SEM imaging; one such example is Figure 4.6e. These four flaw-containing particles (Figure 4.6a-d) had to be turned over before milling, such that their flawed surface was made to contact the steel surface before carving the three-point bend specimen. To achieve this, the particle was first welded to the micromanipulator needle with a carbon deposit. Then, the silicon particle was transported and welded to the edge of a stainless steel razor blade. The razor blade was next extracted from the SEM/FIB instrument, flipped upside-down by hand, re-introduced in the microscope, the silicon particle rewelded to the micromanipulator needle, separated from the blade, transported, and placed along the steel substrate. Thereafter, it was machined with its defect-containing surface contacting the steel, following the procedure described above and summarized in Figure 4.4.

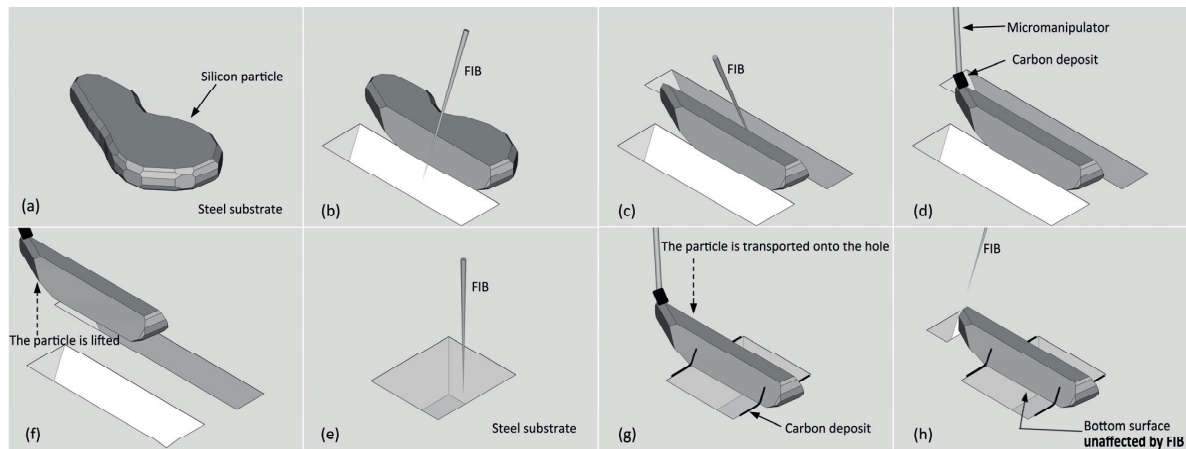


Figure 4.4 Scheme of the preparation of a microscopic three-point bending specimen from a silicon particle extracted from the Al-Si alloy. (Reproduced from Mueller et al. [410])

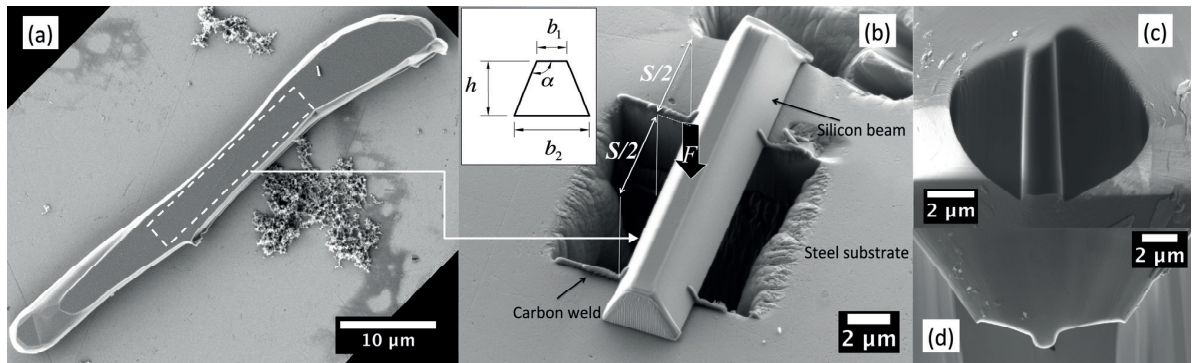


Figure 4.5 (a) Eutectic silicon plate-like particle extracted from the Al-Si alloy, lying on a steel substrate. (b) Microscopic three-point bending specimen (S8 in Table 4-1) ready to be tested prepared from the particle in (a). FIB milling, transportation with a micromanipulator and carbon FIB induced depositing were used for the preparation; however, the bottom surface of the specimen is unaffected by these. Relevant geometrical dimensions are indicated on the image and on the inset. Bottom-view (c) and side-view (d) of the nanoindenter diamond tip used for the microscopic three-point bending tests. (Reproduced from Mueller et al. [410])

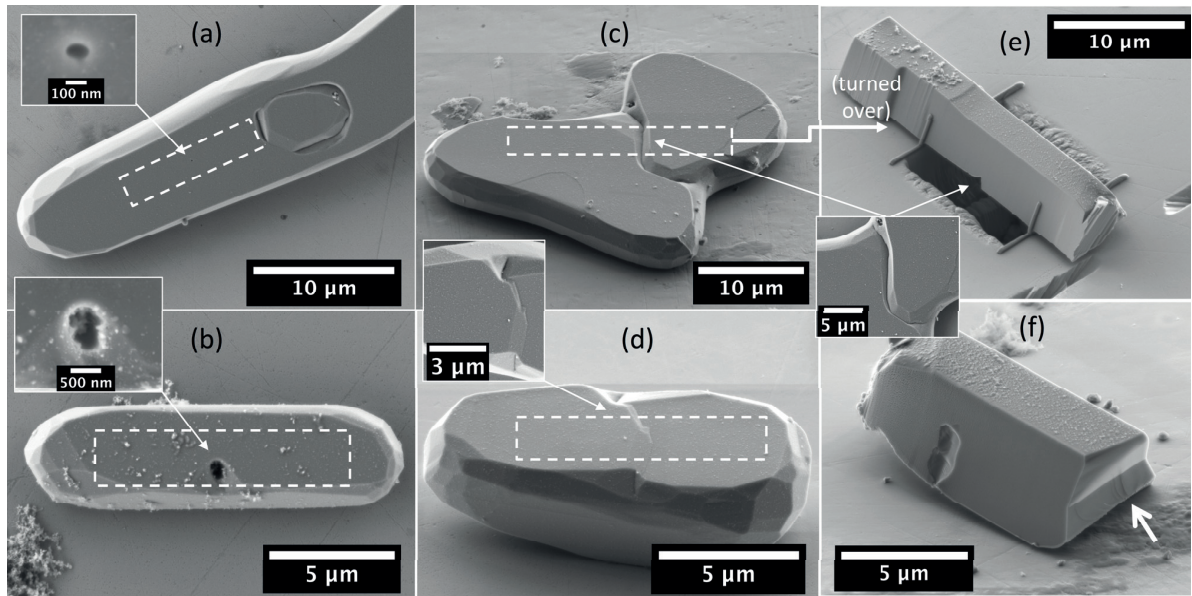


Figure 4.6 (a-d) Eutectic silicon particles extracted from the Al-Si alloy featuring distinctive surface defects: a small pore in (a), a larger pore in (b), a deep trench-like interface in (c) and a shallow stepped interface in (d). These particles were turned over before producing a three-point bending specimen out of each, to probe the strength of their defect-containing surface. One such specimen (S11 in Table 4-1) is shown in (e); it was prepared from the particle in (c). Image (f) is the fractured half-beam and fracture surface after the three-point bending test of the specimen in (e). The fracture origin in (f) is indicated with a white arrow. (Reproduced from Mueller et al. [410])

4.1.1.4 Testing procedure

Micrometric three-point bending tests were conducted, using a TI 950 TriboIndenter® (Hysitron® Corporation, Minneapolis, MN, USA) nanoindentation apparatus, on the machined beams resting over a

square hole cut into the steel substrate. To this end, the steel substrate with the FIB-prepared specimen(s) was first mounted on top of a rotation-tilt stage (Newport Corp., Irvine, CA, USA) that was fixed on the nanoindenter positioning stage. Parallelism between the tip and the specimen was achieved within ± 0.5 degrees by iteratively making a shallow indent in the steel substrate, scanning the indent with the Scanning Probe Microscope (SPM) of the NanoDMA™ transducer and correcting the tilt with the rotation-tilt stage. Once parallelism was achieved, the bend tests were carried out using the 3D OmniProbe™ transducer in displacement control mode at 60 nm/s. Load was applied up to fracture, with 1 to 4 partial unloading/reloading sequences in-between. The nanoindenter probe that was used to conduct these three-point bend tests was a diamond probe custom-shaped by FIB-milling to feature, at its tip, a cylindrical ridge with a diameter of ~ 1.5 μm and a length of ~ 8.5 μm , Figure 4.5c-d.

4.1.2 Results

4.1.2.1 General response

A representative measured load—displacement curve is shown in Figure 4.7. Initially, up to a displacement of ~ 250 nm, the signal is ill-defined and features a few load drops. This portion of the curve is likely a signature of specimen accommodation and of the thin carbon welds on the side of the bent silicon beam being chipped off (see Figure 4.6f, which shows craters along the sides of a beam where the welds were located). This interpretation is suggested by the observation (e.g. Figure 4.5b and Figure 4.6e) that the specimen and steel substrate preparation procedure tends to leave a gap of some tens or hundreds of nanometres between the specimen and the substrate. After this first transient regime, the load increases steadily with displacement, at first with an increasing slope (a signature of indentation effects) and then linearly, suggesting that the deflection is now dominated by bending of the beam. This steady-slope loading curve then continues up to a maximum force F_{max} followed by a sudden load-drop and a jump in displacement, which evidently corresponds to fracture of the bending beam. The curve in Figure 4.7 shows also a partial unloading-reloading cycle, which was conducted starting from a load near 6 mN in the range of displacements between 400 and 500 nm: the slight difference in slope between this and the monotonic loading curve shows that some irreversible deformation takes place during loading. In some specimens, this difference was more pronounced: these were specimens with greater amounts of powder-like material along their surface (see for example Figure 4.6b and Figure 4.6f). Separate observations in the SEM (not shown here) of indented locations where such fine particulate material covered silicon particle surfaces show that this layer of nanoscopic powder-like particles deforms plastically under the indenter, explaining, together with some possible plastic deformation of the silicon under the indenter, the slightly higher compliance upon initial loading of the sample.

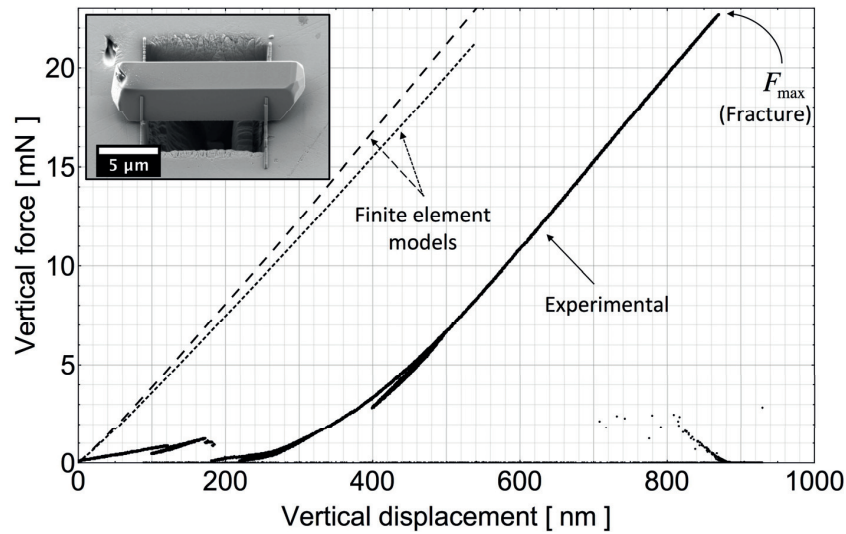


Figure 4.7 Typical measured load—displacement response of a microscopic three-point bending test of the silicon specimen shown in the inset (specimen S1 in Table 4-1). Responses calculated by finite element modelling with rigid supports (long-dashed line) and with elastic supports (short-dashed line) are also shown (corresponding to the models in Figure 4.8a and Figure 4.8b respectively). (Reproduced from Mueller et al. [410])

4.1.2.2 Stress analysis and sensitivity analysis

Each individual three-point bending specimen was analysed by means of a bespoke quasi-static three-dimensional Finite Element (FE) model using Abaqus/Standard™ 6.11 software (Dassault Systèmes, Providence, RI, USA), Figure 4.8. The indenter was modelled as a cylindrical rigid analytical surface of diameter 1.5 μm . The dimensions of each silicon bending beam (h , b_1 and b_2) and of the corresponding hole in the steel defining the span S were obtained from SEM images of each sample, in place before testing. Despite the careful FIB-machining procedure (Figure 4.4), small deviations from symmetry in the geometry of silicon bending specimens were unavoidable. When such deviations were noted, they were neglected and the specimens were assumed to be symmetric.

It is known that the large facets of plate-like Si particles in aluminium are $\{111\}$ planes and that the particles contain multiple $\{111\}$ twins parallel to their large facets [94,100,104,106]. Here, simulations were run using linear elastic constants $C_{11} = 165.6$ GPa, $C_{12} = 63.9$ GPa and $C_{44} = 79.5$ GPa [413] and assuming that the silicon beams are single crystals free of twins with $[111]$ in the Y direction (Figure 4.8). The (unknown) orientation of the silicon beam axis (i.e. the Z direction in Figure 4.8), on the other hand, was arbitrarily chosen since the (111) plane in diamond cubic crystal structures is elastically isotropic [414].

In finite element modelling, two alternatives were used for the steel supports that define the span: (i) rigid analytical surfaces (Figure 4.8a), and (ii) isotropic linear elastic material of Young's modulus 210 GPa and Poisson's ratio 0.3 (Figure 4.8b). As for the geometry of the support, in both cases the edge was filleted with a radius of 150 nm. In Figure 4.7 the load—displacement responses resulting from these two models are indicated in dashed lines. The response is obviously more compliant when the support is considered to be elastic; however, when the peak load is reached, the difference in maximum first principal stress value for the two configurations is less than 1%. Given this negligible difference and the fact that the model with rigid analytical surfaces (Figure 4.8b) is computationally far less demanding,

this type of model was implemented and used in data interpretation of the ensemble of samples tested here.

The model with elastic supports (Figure 4.8b) was nevertheless used to investigate numerically the influence of possible misalignments using the specimen in Figure 4.7. Separate simulations were run with misalignments having magnitudes that represent extreme cases of reasonable experimental imprecision, namely: (i) the indenter rotated 5° about the Y axis (i.e. beam axis and indenter ridge not perpendicular, Figure 4.9a); (ii) the supports rotated 5° about the Y axis (i.e. beam axis and support edges not perpendicular, Figure 4.9b); (iii) the indenter rotated 2° about the Z axis (i.e. loss of parallel contact between the indenter and the beam, Figure 4.9c); and (iv) the indenter off-centre by $1\text{ }\mu\text{m}$ in the Z direction (i.e. lateral misalignment, Figure 4.9d). Results show that for Cases (i), (ii) and (iii) the maximum first principal stress varies by less than 2%. Only for Case (iv) is the influence more important: for $1\text{ }\mu\text{m}$ of lateral misalignment the calculated maximum first principal stress at F_{max} is 5% lower than with a well-aligned sample. This type of misalignment was therefore also simulated for the specimen with the shortest span (specimen S5 in Table 4-1), this being the sample most affected by lateral misalignment; here, a $1\text{ }\mu\text{m}$ misalignment leads to an error slightly lower than 10%. An interesting observation in running these calculations was that in all cases of misalignment (in particular for the lateral misalignment) the simulation predicted a *lower* peak stress at given load than it did for the perfectly centred and aligned system. These sources of error are therefore taken as being ones that lead to *overestimate* the peak stress within the sample when it is calculated using the bespoke finite element model knowing the peak load F_{max} that is reached when it fractures.

The friction coefficient μ in the models was taken as 0.2 both for the beam-supports [415] and the beam-indenter contacts. To evaluate the influence of this parameter, simulations were run for several specimens also with $\mu = 0.1$ and 0.3. Results show that the maximum first principal stress at F_{max} does not change by more than 5% compared to the result with $\mu = 0.2$.

Also, the sensitivity to possible errors in the determination of dimensions was evaluated by running simulations for the specimen in Figure 4.7 varying widths b_1 and b_2 , height h and span S , one at the time, by $\pm 5\%$. Results indicate that such errors in width and span lead to approximately $\pm 5\%$ error in the resulting maximum first principal stress at the load of fracture, whereas $\pm 5\%$ error in the determination of the height h leads to approximately $\pm 10\%$ error in the computed stress.

Summarizing the results of the sensitivity analysis described above, we conclude that misalignments can overestimate the calculated strength value of a specimen by at most 10%, that uncertainty in the friction coefficient can lead to a $\pm 5\%$ error, and that errors in the measurement of dimensions lead to a $\pm 10\%$ uncertainty in the computed particle strength. Pooling results of these calculations, we deem it reasonable to consider that strength values reported here could be overestimated by up to about 15% and underestimated by up to about 10% of the reported values. Those are therefore the magnitudes of the error bars used in Figure 4.10.

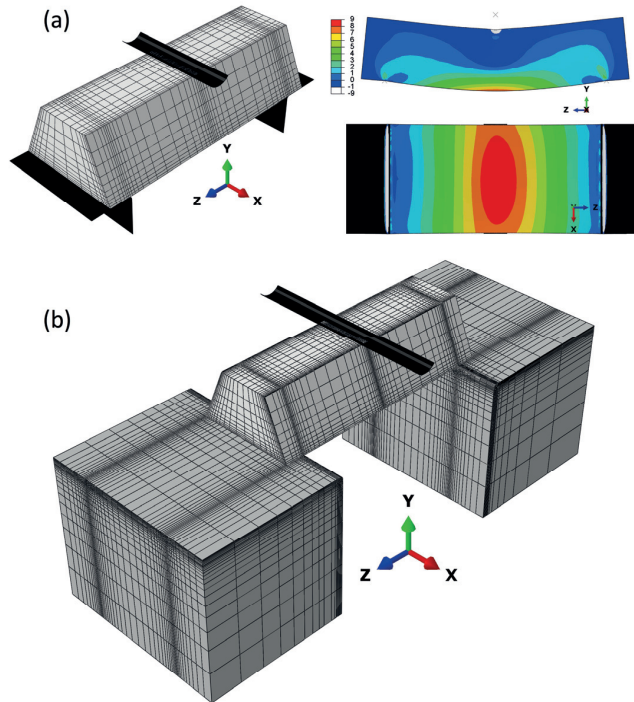


Figure 4.8 Finite element models of the microscopic three-point bending test on silicon particles (Specimen S1 in Table 4-1). The model in (a), where the supports are rigid surfaces, was used to obtain the maximum first principal stress of each tested specimen. The model in (b), where the supports are elastic, was used to analyse the influence of various possible misalignments. The stress field shown in (a) is the first (tensile) principal stress in GPa. The values are largest at the centre of the bottom surface and decrease towards the edges in the X-direction as a consequence of the tapered cross-section. (Reproduced from Mueller et al. [410])

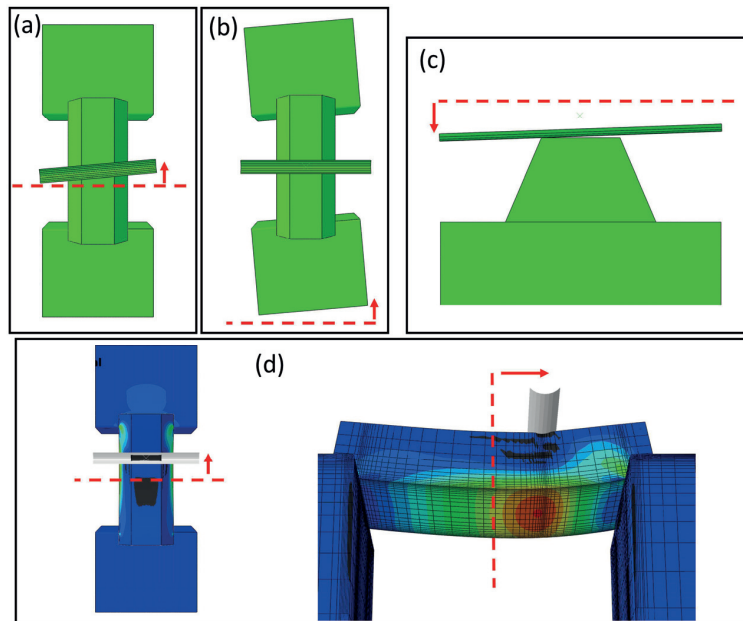


Figure 4.9 Finite element models of different misaligned testing configurations that were considered to evaluate uncertainty sources of the microscopic 3-point bending test.

4.1.2.3 Measurements and test results

Three-point bending tests were carried out on ten specimens such as that in Figure 4.5b, whose bottom surfaces –the surfaces subjected to the maximum tensile stress– were not observed before testing. *A priori*, not having observed signs of defects along the sample sides before or after ion-milling, these can be assumed to be free of large flaws (as data later confirm, see below). An additional four tests were conducted using specimens that contained a clearly identified defect along the tested surface, Figure 4.6a-d. These required identification of the defect along the upper, visible, surface of the Si particle, followed by an operation in which the samples were turned over before being carved and tested with the flaw on their lower surface (see Section 4.1.1.3).

Measurements and results are collected in Table 4-1. Here, the flexural strength is evaluated at F_{\max} using two calculation schemes: (i) the maximum first principal stress calculated from the bespoke FE model of each specimen assuming rigid supports (σ_{FE}), or (ii) Simple Beam Theory (σ_{SBT} , see below).

After testing, fractographic analysis was in general not possible because all but the weakest specimen (S11 in Table 4-1, shown in Figure 4.6c-e-f) could not be found after fracture along the steel substrate. In some cases, small debris was found scattered around the test site, whereas in other cases no remaining portion of the specimen could be found at all. In fact, the only fractured half-beam that could be found after testing (Figure 4.6f) was situated approximately 600 μm away from the test site. These observations suggest that, for all but one sample, the specimens shattered into a few or many small pieces that were dispersed by release of the high stored elastic energy density stored within the samples upon fracture.

4.1.3 Discussion

4.1.3.1 Flexural strength of the silicon plate-like particles

The particle flexural strength is evaluated as the calculated maximum first principal stress at the experimentally measured load at fracture. This means that Mode I failure is assumed throughout this work. Resulting values of σ_{FE} are plotted in Figure 4.10, using uncertainty bars corresponding to +10% and -15%, this being an educated approximation based on the analysis of uncertainties detailed above, versus the effective area A_{eff} that was subjected to tensile stress in the sample in question, defined as follows on the assumption that the particle strength is governed by Weibull statistics.

In plotting the data in terms of A_{eff} (Figure 4.10), we implicitly assume that fracture is only caused by surface defects. Moreover, in what follows we also assume that fracture only occurs from the bottom surface of the beams, i.e. we neglect the possibility of fracture occurring from their sides (this assumption being motivated by the fact that the bending beams have a trapezoidal cross-section, see Figure 4.2). Along this line of thought, one can seek whether the present bending strength data can be expressed in terms of the two-parameter Weibull cumulative distribution function, according to which the probability that a bent sample breaks at or before reaching an arbitrary reference stress σ_r is given by [416]

$$P(\sigma_r, A_{\text{eff}}) = 1 - \text{Exp} \left(- \frac{A_{\text{eff}}}{A_0} \left(\frac{\sigma_r}{\sigma_0} \right)^m \right), \quad \text{Equation 4-1}$$

where

$$A_{\text{eff}} = \iint_{\sigma_1 > 0} \left(\frac{\sigma_1}{\sigma_r} \right)^m dA, \quad \text{Equation 4-2}$$

is the effective area, calculated by integrating the tensile component of the first principal stress σ_1 over the surface subjected to tension (i.e. over the bottom surface) to the power of m . Here, the Weibull modulus m and $A_0 \sigma_0^m$ are two independent material parameters. Defining a "Weibull stress" $\sigma_W = (A_{\text{eff}} \sigma_r^m)^{1/m}$ (note that the units of σ_W are $([\text{length}]^2 [\text{stress}]^m)^{1/m}$) and correspondingly $\sigma_{W0} = (A_0 \sigma_0^m)^{1/m}$, Equation 4-1 can then be recast as

$$P(\sigma_W) = 1 - \text{Exp} \left(- \left(\frac{\sigma_W}{\sigma_{W0}} \right)^m \right). \quad \text{Equation 4-3}$$

In using the stress field at the load of fracture from the finite element simulations to interpret data, we insert $\sigma_r = \max(\sigma_1) = \sigma_{FE}$ into Equation 4-2, and we assign a fracture probability to each experiment using the probability estimator function $P_i = (i - 0.5)/N$, where $i \in [1, \dots, N]$ is the ranked specimen index and N the total number of specimens. With this, we numerically solve the associated maximum likelihood problem to calculate m and σ_{W0} .

Weibull parameters are estimated in this way using data from Specimens S1 to S10 in Table 4-1 (i.e. excluding particles selected for identified defects), giving $m = 5.86$ and $\sigma_{W0} = 12.41 (\mu\text{m}^2 \text{GPa}^{5.86})^{1/5.86}$; the fit is shown as an inset in Figure 4.10. Note that this Weibull modulus must be viewed as highly approximate given the small sample size (10 tests) and the assumptions made in the analysis. Nevertheless, it is a reasonable value for a brittle material such as Si, which in turn allows estimating on a reasonable basis the magnitude of the effective surface area being probed in these experiments. From this result it follows that, if the average A_{eff} is taken as the characteristic area A_0 , i.e. $A_0 = 7.1 \mu\text{m}^2$, then the characteristic strength σ_0 equals 8.8 GPa.

Strength values measured with the ten samples that were not selected for the presence of a given defect (Samples S1 to S10, filled circles in Figure 4.10) show a significant scatter range but invariably reach very high values of peak stress upon fracture: bending strengths vary roughly between 6 and 12 GPa. Scatter in the value of the samples' bending strength has two obvious potential sources, namely the statistical distribution (in size and in shape) of flaws that act as the origin for fracture, and the directional anisotropy of the fracture toughness of monocrystalline silicon [164,260,349,417].

These measured strengths far exceed fracture stress values that have been either estimated using mean-field methods or measured directly on silicon particles within aluminium: the literature review in Section 2.2 shows that work to date has yielded values in the range from roughly 200 to 3000 MPa. Still, values measured here, although much higher, are not outlandish. There have been a great number of measurements of the fracture strength in small-scale samples of (generally single-crystalline) electronic grade silicon produced by lithographic methods or in silicon nanowires; a comprehensive review was recently written by Del Rio et al. [164]. Such samples give fracture strength values that have a marked dependency on sample size (e.g. Fig. 28 in Ref. [164] and Fig. 10 in Ref. [418]): the strength of relatively large specimens often lies in the range from 1 to 4 GPa (e.g. [419–426]) while as the specimen size becomes smaller, the fracture strength has been reported to exceed 10 GPa [65,427], at times significantly [379,428] (see Section 2.5), approaching silicon's theoretical strength of 21–23 GPa along $\langle 111 \rangle$ tensile directions [46,378]. Noteworthy in the literature is the study by Namazu et al. [65], who produced and tested bend beams of similarly trapezoidal cross-section (this being a result of anisotropic wet etching) spanning a wide range of sizes. Their data were expressed in terms of Weibull strength statistics using

the area-based expression in Equation 4-1. Transposing their fracture statistics data to the present sample size ranges gives the three fracture probability lines in Figure 4.10. As seen, present data are broadly compatible with the data of Namazu et al. [65].

To sum up, the present test data show that Si platelets tested for bend strength along plate surfaces, reach strength values consistent with what is measured in high-perfection single-crystalline silicon samples produced by deposition and etching processes typical of the Microelectromechanical Systems (MEMS) industry.

In contrast, the four specimens prepared from visible-flaw containing particles (Figure 4.6a-d, specimens S11 to S14 in Table 4-1) gave strength values significantly lower than Specimens S1 to S10 (Table 4-1), Figure 4.10. Among these four samples, the specimen containing the deepest trench-like surface feature (Figure 4.6e, likely a twin boundary groove or a line where two ridges limiting the growth of {111} facets were blocked before coalescing) was the weakest; this was the only sample for which a half-beam was found after fracture (Figure 4.6f). In this fractured half-beam, it can be observed that fracture started at the defect and initiated away from the edges (white arrow in Figure 4.6f). The fracture path then produced a zigzag surface towards the upper surface. This upper surface is a {111} plane, which is known to be the family of planes with the lowest surface energy [210,349] and the easiest cleavage planes in silicon (followed closely by the {110} planes in $\langle 110 \rangle$) [260,349,417,429,430]. Noting also that {111} planes are 19.5° from each other, the walls of the trench and the zigzag planes of the fracture path are probably {111} planes. In Figure 4.6f one can also observe the chipping-off of material around the carbon weld bead, which occurred by locally breaking the silicon around the weld rather than along the carbon deposit-silicon interphase.

Having determined that microstructural defects at the surface of the plate-like silicon particles decrease considerably their strength, a statistical analysis of the occurrence of defects was carried out to have an insight into the possible relevance of such defects on particle fracture in the alloy. A total of 225 randomly selected plate-like silicon particles extracted from the alloy were examined in the SEM. The observable defects (i.e. surface defects on the SEM-accessible surface(s) of each particle) were here classified into three types and it was then counted how many particles featured each type of defect, see Figure 4.11. Another characteristic weakening feature of silicon particles, namely *necks* (parts of the particles of significantly reduced cross section), were also included in this analysis. The result indicates that pores (e.g. Figure 4.6a and Figure 4.6b) are present in 32% of the particles, necks in 26%, trench-like interfaces (e.g. Figure 4.6c) in 52% and step-like interfaces (e.g. Figure 4.6d) in 12% of all examined particles, whereas no noticeable flaw could be observed in 30% of the particles. The results of this analysis shows that most silicon particles within the alloy feature defects. Indeed, roughly half of them feature at least one trench-like interface similar to that in the weakest specimen in Figure 4.10.

The facts that silicon particles with defects are weaker - likely due to stress concentration effects - and that weakening defects occur in great numbers within the alloy is probably what reconciles the silicon particle strength values measured in this work with the far lower strength values calculated by indirect means in previous work (reviewed in Section 2.2).

Table 4-1 Dimensions (S to α), experimentally measured force at fracture (F_{\max}) and calculated flexural strength by Simple Beam Theory (σ_{SBT}) and by Finite Element analysis (σ_{FE}) of microscopic three-point bending tests of plate-like eutectic silicon particles extracted from the Al-Si alloy. Specimens marked with (*) are ones that probe particles containing visible flaws. (Reproduced from Mueller et al. [410])

Specimen ID	S [μm]	h [μm]	b_1 [μm]	b_2 [μm]	α [$^\circ$]	F_{\max} [mN]	σ_{SBT} [GPa]	σ_{FE} [GPa]
S1	10.6	3.0	2.8	5.4	113	22.7	9.3	8.7
S2	9.7	2.2	2.6	4.7	116	14.9	11.5	10.9
S3	11.8	4.5	2.0	5.6	112	33.8	7.2	6.6
S4	11.8	4.2	1.6	5.0	112	23.4	6.5	6.0
S5	7.1	2.3	0.9	2.9	113	14.1	13.2	11.9
S6	11.8	3.5	1.6	4.6	113	14.5	6.1	5.7
S7	10.6	4.5	2.1	5.8	112	50.8	9.1	8.3
S8	9.5	2.8	0.9	3.6	116	11.6	8.6	8.0
S9	9.5	2.7	1.4	3.6	113	13.9	9.9	9.1
S10	7.4	2.0	1.2	3.0	114	7.5	9.3	8.7
S11 (*)	12.9	3.8	2.8	6.2	114	4.1	1.1	1.1
S12 (*)	9.5	3.8	2.4	6.0	116	22.6	5.0	4.7
S13 (*)	7.1	2.4	0.9	2.9	113	3.2	2.7	2.6
S14 (*)	7.4	4.3	0.8	4.5	113	18.8	3.9	3.6

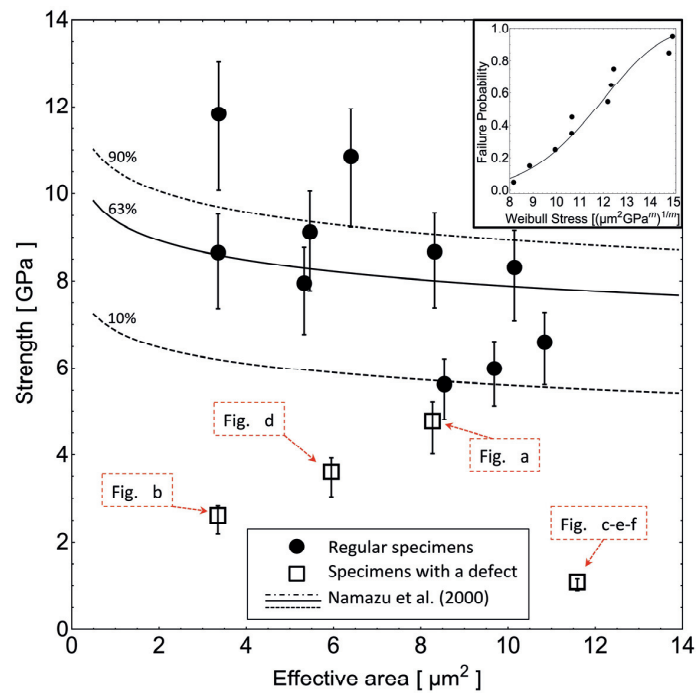


Figure 4.10 Flexural strength (evaluated as the maximum first principal stress calculated from finite element model of each specimen) versus the specimen effective probed area for "regular" three-point bending specimens (black dots) and for specimens produced with a visible defect along the lower beam surface (hollow squares; their indications with letters a—f refers to the corresponding images in Figure 4.6). The error bars are +10% and -15%, which is an estimate of the pooled uncertainty arising from the sensitivity analysis (see main text). Strength of electronic grade silicon as reported by Namazu et al. [65] is shown with lines indicating 10%, 63% and 90% of failure probability. Inset: Weibull fit of regular specimens. (Adapted from Mueller et al. [410])

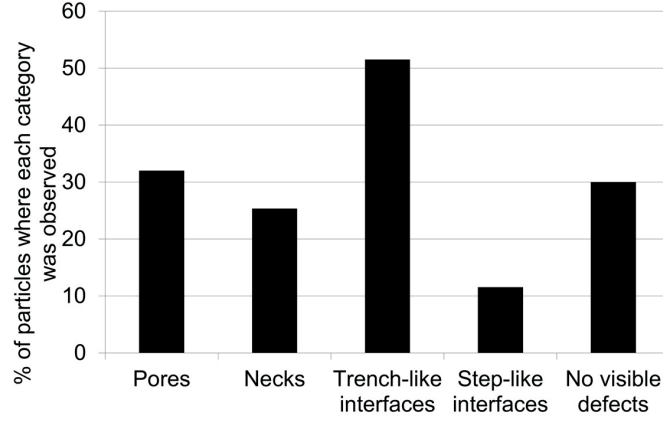


Figure 4.11 Occurrence of different types of surface defects and necks on eutectic silicon plate-like particles extracted from heat-treated Al-12.6Si.

4.1.3.2 Re-evaluation using Simple Beam Theory

We have used bespoke finite element models to evaluate the strength of each three-point bending specimen and to analyse statistically the results (see above); however, the testing method exposed here is obviously easier to implement if data can be interpreted using analytical methods. To explore whether this is a viable approach, in this subsection we revisit the data analysis using a rougher, straightforward approach based on Simple Beam Theory (SBT). We do so –despite the fact that specimens in this work cannot be considered to be slender– to show that such a simple approach can also be used to evaluate data from three-point bending experiments on specimens with tapered cross-section such as those produced and tested here.

According to SBT, in a three-point bending configuration the maximum tensile stress occurs at mid-span and is $\sigma_{\text{SBT}} = M y / I$, where $M = F_{\text{max}} S / 4$ is the applied moment at mid-span, $y = (h/3)(2b_1 + b_2)/(b_1 + b_2)$ is the distance from the neutral axis to the bottom surface and $I = (h^3/36)(b_1^2 + 4b_1b_2 + b_2^2)/(b_1 + b_2)$ is the moment of inertia about the axis that passes through the centroid of the trapezoidal cross-section in the X direction (see Figure 4.5 for a definition of geometrical parameters in preceding expressions). As can be seen in Table 4-1, σ_{SBT} values for the tests in this work are between 3 and 11% higher than σ_{FE} values. In other words, using SBT in data analysis would lead to an additional error of the same sign (i.e. overestimation of the strength) and comparable magnitude as uncertainty arising from the various types of misalignment (Section 4.1.2.2).

As was done above using results of FE simulations, here too we can analyse strength data in terms of two-parameter Weibull statistics assuming that fracture is caused by flaws on the bottom surface of the specimens. In this case, we take $\sigma_r = \sigma_{\text{SBT}}$, and $\sigma_1(z) = \frac{\sigma_{\text{SBT}}}{S/2} z$ as given by SBT. Replacing these into

Equation 4-2 leads to $A_{\text{eff}} = b_2 2 \int_0^{S/2} \left(\frac{\sigma(z)}{\sigma_{\text{SBT}}} \right)^m dz = \frac{S b_2}{m+1}$, whereas the "Weibull stress" now reads $\sigma_W = (A_{\text{eff}} \sigma_{\text{SBT}}^m)^{1/m}$. The solution to the maximum likelihood problem of finding the Weibull parameters in Equation 4-3 using data from Specimens S1 to S10 gives with this approach $m = 5.84$ and $\sigma_{W0} = 13.25(\mu\text{m}^2 \text{GPa}^{5.84})^{1/5.84}$. It follows that if the average A_{eff} is taken as the characteristic area A_0 , i.e. $A_0 = 6.8 \mu\text{m}^2$, then the characteristic strength $\sigma_0 = 9.5 \text{ GPa}$.

These results obtained using SBT compared to those obtained using the outputs of finite element modelling (Section 4.1.3.1) indicate that the estimated Weibull modulus is the same for both approaches, whereas the effective areas and the strength values are under- and overestimated, respectively, by at most 10%. Therefore, if one lacks the time or means to conduct bespoke finite element analysis to interpret tests conducted according to the procedure developed in this work, SBT provides rapid and simple access to relatively precise data.

4.1.3.3 Influence of the etching procedure

In this work, the surfaces of the silicon particles probed for strength were not affected by focused ion beam milling; however, the potential effect of the etching procedure that was used in sample preparation has to be addressed.

When silicon is exposed to acidic media that do not contain fluorine ions, a nanometric passivating layer of silicon oxide forms immediately along its surface, thereafter preventing further oxidation [431]. Oxide layers $\sim 1 - 3$ nm thick have been measured for silicon immersed in aqueous HNO_3 solutions at room temperature and it has been furthermore determined that the thickness does not increase with time even under an applied anodic voltage of 5 V [432,433]. In phosphoric acid and in acetic acid, anodic voltages of a few or a few tens of V must similarly be applied to increase the oxide thickness on silicon [431]. In a study on surface treatments of a Al-Si-Mg alloy it was determined that a short (2 minute) exposure to phosphoric acid leaves silicon particles within the alloy unaffected, and that aluminium phosphate is not deposited on the particle surface, given that they are cathodic when compared to both the Al matrix and Mg_2Si particles [434].

Solutions based on a mixture of nitric, phosphoric and acetic acids, in similar proportions as in the etchant used here, are typical aluminium wet-etching solutions that have been used for decades in microfabrication [435–438]. Aluminium is known to be etched in these solutions through a two-step mechanism [436,437]: the nitric acid reacts with aluminium producing aluminium oxide, which is then dissolved by the phosphoric acid. The acetic acid buffers the solution and improves wetting. These solutions are known not to etch silicon microcomponents nor silicon oxide (or very slowly, even at 50 °C) [435,437,438].

Still, exposure times typical of microfabrication are much shorter than the 7 days used here to extract particles tested in this work (note, however, that this is an upper limit of the time spent by the particles in contact with the solution, as silicon particles from the alloy were progressively exposed by the slowly advancing etching front). Therefore, to get an insight on the thickness of the oxide layer of the particles tested here in three-point bending, a TEM lamella was prepared using FIB milling, from a particle that had been subjected to the etching procedure used here to extract particles from the alloy (Figure 4.12). The observed oxide thickness was ~ 30 nm (Figure 4.13). We note in passing that, upon TEM examination, we observed the presence of Al-rich nanoprecipitates inside the silicon particle such as those discussed in Section 2.1 and shown in Figure 2.23. In a study on fracture of silicon nanospheres of size in the order of 100 nm, Mook et al. [219] suggested that the thickness of the oxide layer around the nanospheres could account for the size of crack-initiating defects. Now, if we solve for strength σ in $K_{\text{IC}} = \sigma\sqrt{\pi a}$, with $a = 30$ nm and $K_{\text{IC}} = 0.9 \text{ MPa}\sqrt{\text{m}}$ as is typical of silicon [216,260,417], one obtains $\sigma \approx 3 \text{ GPa}$, which is below values of strength measured here for specimens without large flaws, i.e. specimens S1 to S10 (Table 4-1 and Figure 4.10). This leads to conclude that the layer of oxide formed during etching did not govern the strength of the Si particles tested here, since measured strength values correspond to critical flaws even smaller than the oxide thickness. It is, on the other hand, possible that the oxide layer

could have healed small cracks along the Si particle surfaces; however, the presence of such cracks along the surface of individual Si crystals is unlikely as they would be healed by Si diffusion along the Al/Si interface or through the aluminium phase during the Si particle coarsening heat treatment.

We thus deem the influence of larger flaws on the strength of the Si particles measured here to be representative of the behaviour of Si particles within the coarsened Al-12.6%Si alloy from which they were extracted.

We also studied the possibility that Si particle surface defects might have been produced by the etching procedure used in this work. To this end, we extracted particles from the alloy also by electroetching with sodium chloride and with nitric acid as electrolytes. We found no indication of a difference in the observable particle defects with etching procedure, giving confidence that the observed defects are present originally in the silicon particles within the alloy.

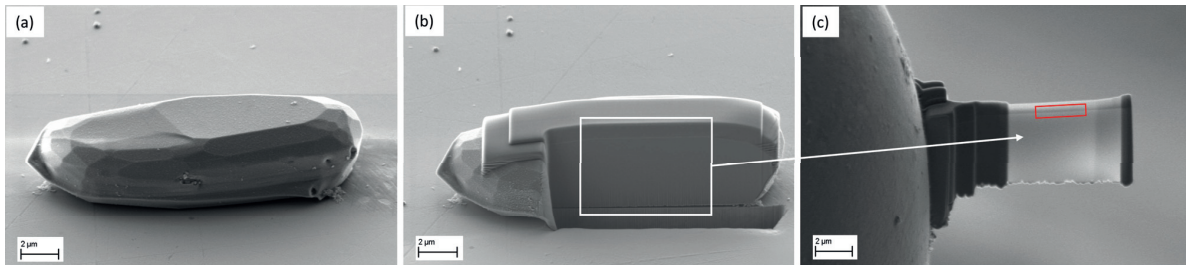


Figure 4.12 (a) Eutectic silicon particle extracted from the Al-12.6Si alloy. (b) Image during the process of producing a TEM lamella out of the particle using FIB. Note that a protective layer of carbon was deposited on top of the particle. (c) SEM image of the prepared TEM lamella. The red rectangle indicates the area at the particle-carbon layer interface that is imaged in Figure 4.13.

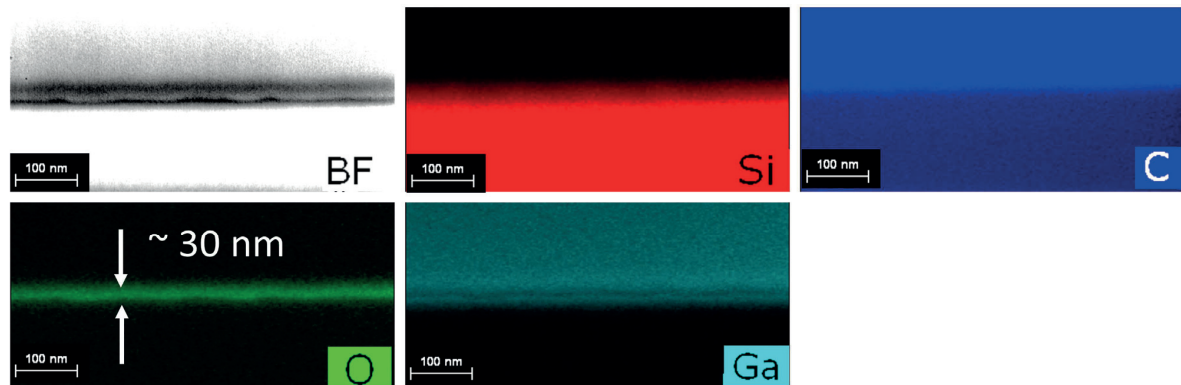


Figure 4.13 Bright field TEM image and EDS element maps of the area in the red rectangle in Figure 4.12c. The thickness of the oxygen-containing layer is found to be about 30 nm.

4.1.4 Conclusion

A microscopic three-point bending test is developed to measure the flexural strength of hard reinforcing particles of high aspect ratio. Although focused ion beam milling is used in sample preparation, the particle surface probed in tension is pristine, in the sense that it is not affected by focused ion beam milling or by redeposition of milled matter. This is achieved on one hand through a specific specimen preparation procedure and on the other hand through the use of a tapered bend beam cross-section, which focuses the stress at the centre of the bottom surface of the bending beam while reducing it at the edges.

Bespoke finite element modelling is used to access the peak stress at fracture. Misalignment can lead to overestimate calculated strength values by at most 10%, the most critical source of error being deviations of the indenter placement point from the beam span centre. This level of error is of the same order as uncertainty resulting from error in sample dimension measurement. Alternatively, simple beam theory can be used to interpret data; this leads to overestimate resulting strengths by about 10%, largely as a consequence of the rather short span of the specimens.

Results on coarsened eutectic silicon particles extracted from Al-12.6wt.%Si show that:

- coarsened Si particles can be very strong, with a characteristic strength around 9 GPa when bend particles of effective surface area near $7 \mu\text{m}^2$ are tested; and that
- when such particles contain microstructural flaws, such as pin-holes and particularly trench-like interfaces along their facets, their strength is strongly diminished.

Given the high particle strength values that are recorded in the absence of such flaws, their elimination from Si particles in Al-Si alloys should be a potent pathway to strongly improved strength and ductility in 3xx series aluminium casting alloys.

4.2 In-situ strength measurements of individual silicon particles

(Adapted from Ref. [411]: M.G. Mueller, G. Žagar, A. Mortensen, *In-situ strength of individual silicon particles within an aluminium casting alloy (Submitted, 2017)*)

In this Section, measurements of local strength are performed *in-situ* on individual silicon particles that constitute the second phase of aluminium alloy A356. Particles are shaped using Focused Ion Beam (FIB) milling such that, upon the application of a compressive force on the particle, a volume of material unaffected by FIB milling is subjected to bending. The volume of material subjected to peak tensile stress is situated along the edge of the flat Si particles; as such, these tests are complementary to tests in Section 4.1, where material subjected to peak tensile stress is situated along the flat sides of the Si particles. Data confirm what was found in Section 4.1: (i) silicon particles in this commercial aluminium casting alloy are shown to be capable of locally sustaining tensile stresses (as high as 16 GPa), i.e., approaching theoretical strength and (ii) the reason why such strengths are not reached by most alloy Si particles is shown to be the presence of specific surface defects. The most deleterious defects are grooves at the interfaces between merged silicon crystals; therefore, the present data confirm that eliminating these might lead to significantly enhanced strength and ductility in this widely-used casting alloy family.

4.2.1 Materials and Methods

4.2.1.1 Material

The particles probed in this work are Si particles produced in the course of conventional alloy processing within aluminium casting alloy A356 (Alu Metall Guss AG, Gontenschwil, Switzerland), of composition limits: 6.5 to 7.5 wt.% Si, 0.25 to 0.45 wt.% Mg, max 0.20 wt.% Fe, max 0.20 wt.% Cu, max 0.10 wt.% Mn, max 0.10 wt.% Zn, max 0.20 wt.% Ti, max 0.05 wt.% of others (each), max 0.15 wt.% others (total), balance Al. The alloy was remelted and cast as a rod 15 cm high and 2 cm in diameter using a copper permanent mould. Heat-treatment was then conducted at 540 °C for 6 h, these being standard

parameters for the solutionizing step of this alloy's T6 heat-treatment schedule [439]. The resulting microstructure is shown in Figure 4.14a on a polished section of the material, where the silicon particles are dark and the α -aluminium phase is bright.

To expose the silicon particles within the microstructure, the aluminium phase was selectively dissolved to a depth of a few tens of micrometres by soaking a polished sample of the alloy in a mixture of phosphoric acid 85%, acetic acid 100% and nitric acid 70% in volume ratios 83:5.5:5.5 for 2 hours. Figure 4.14b-c shows the topography after this deep-etching procedure, where the partly protruding silicon particles are readily visible.

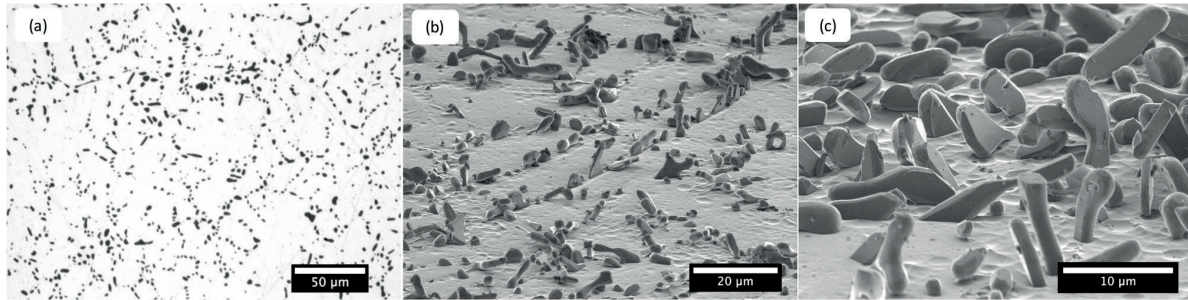


Figure 4.14 Microstructure of the alloy A356 heat-treated 6 hours at 540 °C used in this work. (a) Optical micrograph of a polished section. (b-c) SEM images showing silicon particles exposed after a deep-etching procedure. (Reproduced from Mueller et al. [411])

4.2.1.2 Generalities of the method

We probe the strength of individual particles a few micrometres in size, produced within the alloy after standard alloy processing steps detailed above. As will be seen, test geometries on different particles vary; however, the general idea in all cases is that the particle be shaped using a Focused Ion Beam (FIB) such that a well-defined part of the particle that was not ion-milled be subjected to bending upon the application of a compressive force using the tip of an instrumented (tungsten) needle. This defines a portion of the particle surface that is subjected to tensile stress, which is where fracture will eventually take place.

A main premise of the method is that the surface where strength is probed be left in its pristine condition; it thus must be unaffected by FIB milling and its shape thus cannot be altered. This, together with the fact that particles are all different from each other, both morphologically and in terms of their disposition in space, makes it impossible to prepare specimens of the same shape and the same dimensions out of the many different particles within the alloy. Instead, each particle is shaped individually exploiting its own characteristics. This makes each specimen probed in this work unique in terms of its geometry. There are, nevertheless, two common features to most particles tested here (exceptions are described in the next subsection). One is a deep, rectangular, notch micromilled with the FIB so as to define a remaining ligament that will be subjected to bending upon the subsequent mechanical testing (Figure 4.16c). The second is a roof at the top of the particle, introduced to ease load application.

This particle strength test method is an adaptation of a notched sample test that was developed using the Nextel 610™ alumina fibres shown in Figure 3.4 as a test bench material [409]. The work in Ref. [409], which was done within the ERC project of which this thesis is part (see Section 1.3), extended to the microscopic scale the concept of machining a deep blunt notch to produce, upon the application of a compressive force, bending in a pristine ligament of material (this microtest was inspired by the work

of Wereszczak et al. [348] on ceramic bearings discussed in Section 2.4). Figure 4.15 shows an example of what we call a *C-shape* test on an alumina fibre [409].

There are, nevertheless, important differences between the methodology that was developed in Ref. [409] and that of the present Section. Namely, the particles tested here are randomly oriented and significantly more irregular morphologically. Also, they are nearly one order of magnitude smaller. Furthermore, a main difference between the present test and that in Ref. [409] is the kind of data that are used to determine the particle strength: in Ref. [409] tests were conducted within a nanoindentation apparatus (in air) and the record of load—displacement was used to feed bespoke finite element models, while in this Section test were conducted within the SEM and we use SEM images acquired during the test to calculate the stress state, as detailed below. The reason for these differences is that the small size and irregular shapes of particles tested here make it essential to be able to see the sample in real time and have sufficient tilt and rotation capability in performing sample positioning and alignment adjustments prior to mechanical testing. Therefore, particles in this work are tested within a SEM; an added advantage is then that a live video recording of the test can be produced.

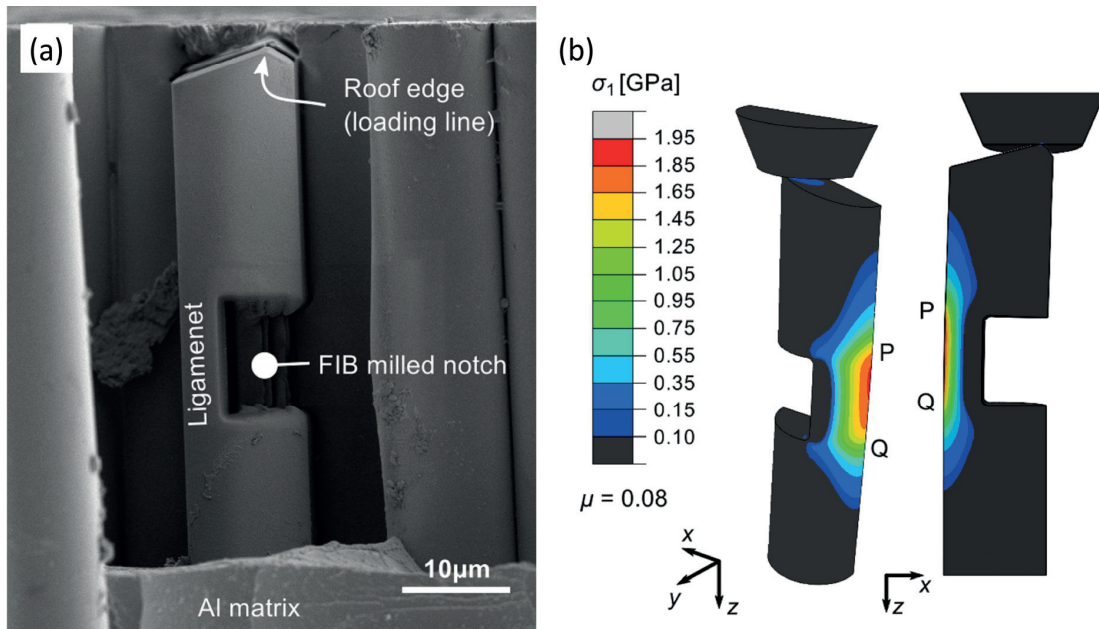


Figure 4.15 *C-shape* test of a nanocrystalline alumina fibre exposed by deep-etching from a composite wire, itself shown in lower magnification in Figure 3.4. The fibre ready to be tested is shown in (a). Mechanical testing is conducted within a nanoindentation apparatus (in air), by loading the fibre tip up to fracture with a diamond flat punch. The interpretation scheme uses the load—displacement measurement and bespoke finite element model of the tested fibre section to compute the stress field at fracture, shown in (b), from which a measurement of local strength within the ligament material can be extracted. (Figure adapted from Ref. [409])

4.2.1.3 Sample preparation and testing

Selected plate-like silicon particles were individually micromachined using Focused Ion Beam milling with 30 kV Ga⁺ ions in a Zeiss NVision 40 SEM/FIB dual-beam apparatus (Oberkochen, Germany). Due to limitations of the set-up, only particles tilted at least 26° with respect to the normal of the alloy sample surface could be shaped with the FIB and tested (details of this can be found in the Supplementary Material of Ref. [411]). As described in the previous Subsection the particles were shaped so as to produce

bending upon load application within a well-defined volume of material, whose surface subjected to tension is unaffected by FIB milling (Figure 4.16).

For each particle, the sample was thus rotated and tilted such as to have the incident FIB perpendicular to one of the particle's large, flat, facets, which are known to be (111) planes [100,106,104,94]. Therefore, the ligament was, in all samples tested here, located along the edge of the plate-like particle. Moreover, because one of the goals of the present work was to measure the severity of the different types of surface defects of silicon particles, most specimens were produced in such a way as to probe particle edges containing an identified defect.

Most of the particles were prepared with a notch milled in this way using the FIB; however, there are two exceptions. One is the particle in Figure 4.21h: this particle was tested as a simple cantilever beam that could be easily produced by virtue of its natural morphology. FIB-milling on this particle was therefore only applied at the lower side of the cantilever, so as to make its thickness reasonably uniform. Upon testing, fracture occurred at the interface between silicon crystals that were meeting at the root of the cantilever; the particle strength at that location was evaluated using simple beam theory assuming a rectangular beam cross-section. The second exception is a particle that also consisted in two silicon crystals merged together along a visible interface (Figure 4.20). This particle's shape and disposition in space made it amenable for testing such that, upon the application of a load on its top, the volume of material around the interface was naturally subjected to bending. No FIB milling was thus used to prepare that particular specimen.

The *in-situ* tests were done in a Zeiss Merlin SEM apparatus (Oberkochen, Germany) using a FT-NMT03 Nanomechanical Testing System from Femtotools (Buchs ZH, Switzerland) mounted with a tungsten needle. Proper alignment was achieved using the rotation and tilt capabilities of the testing device stage (see Figure 4.17). Loading was done in displacement control at a constant speed in the range 0.01 – 0.04 $\mu\text{m/s}$, up to sample fracture. All tests were video-recorded and films are available in the Supplementary Material of Ref. [411].

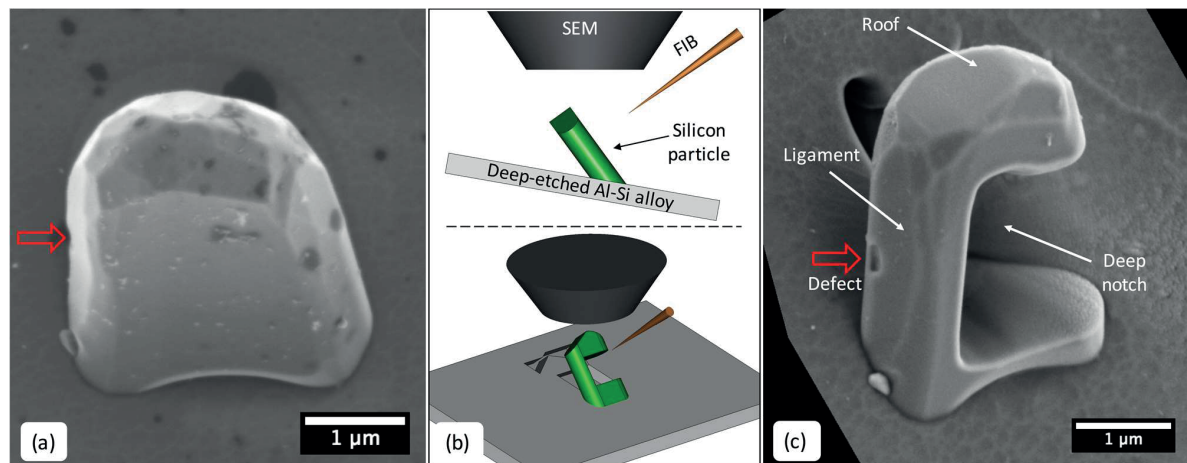


Figure 4.16 Sample fabrication procedure (Specimen #10 in Figure 4.24). (a) Original silicon particle. (b) Sketch of the FIB milling process used to produce a C-shaped specimen out of the silicon particle (side and perspective views). (c) Resulting C-shaped particle ready to be tested. A surface pinhole defect is indicated with red arrows; note that it is located along a surface that is unaffected by the FIB and that it is stressed in tension upon the subsequent micromechanical test. (Reproduced from Mueller et al. [411])

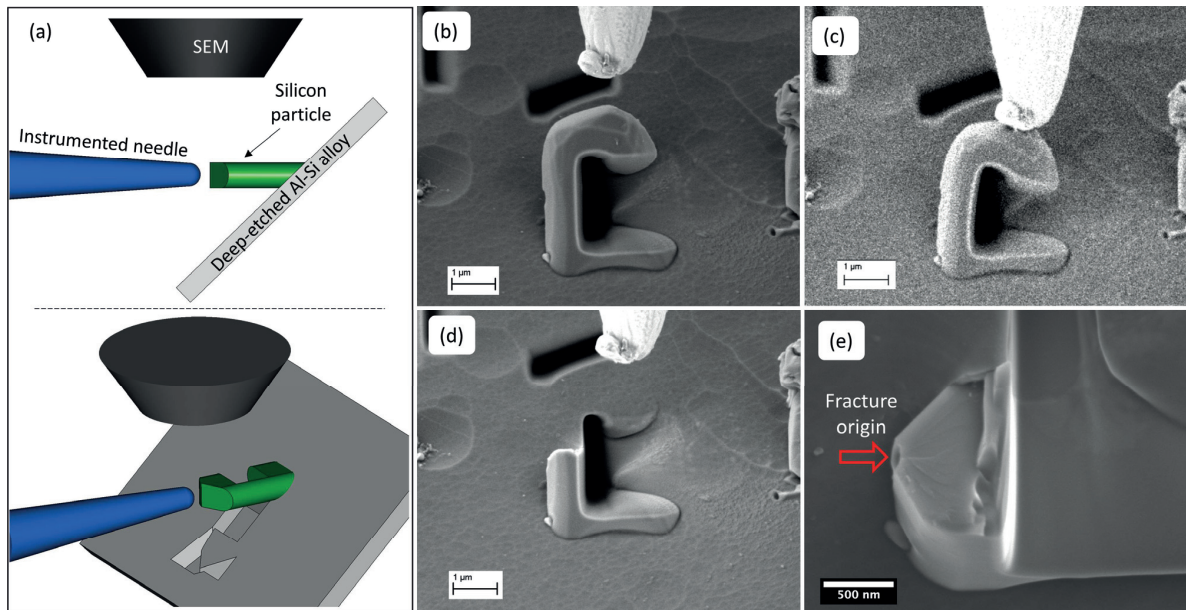


Figure 4.17 Testing procedure (Specimen #10 in Figure 4.24). (a) Sketch of the *in-situ* micromechanical test (side and perspective views). (b) The C-shaped particle of Figure 4.16 and the instrumented tungsten tip before testing. (c) Last frame before fracture during testing. (d) Fractured particle after testing. (e) Fractography of the particle showing the surface defect that originated fracture (red arrow). (Reproduced from Mueller et al. [411])

4.2.1.4 Test interpretation

To calculate the particle strength, bespoke 3D finite element (FE) half-models of each specimen were constructed using the Abaqus FEA 6.11 (Dassault Systèmes S.A., Vélizy-Villacoublay, France) software, using as input notched particle dimensions measured from SEM images. The cross section of the ligament, which is a critical part of the model because this is where the largest deformation takes place, was modelled according to the following criteria.

In the few cases where the tensile surface of the ligament was (approximately) flat (e.g. Figure 4.21 b and e), the cross section was taken to be a rectangle. In the more usual case where the surface was somewhat rounded or faceted, a semi elliptic approximation of the rounded or faceted edge was used (e.g. Figure 4.18 and Figure 4.19). The surface defects on the particles, e.g., pinholes or interfaces, were not introduced in the models. Silicon was modelled as elastically isotropic with a Young's modulus 168.9 GPa and Poisson ratio 0.262; these are the isotropic, in-plane, properties of the (111) plane in silicon [414]. This choice is justified by the fact that the large facets of silicon plate-like particles in Al-Si alloys are known to be (111) planes [100,106,104,94] and also by the fact that most deformation in the particles tested here occurs within that plane. The validity of using elastic constants of high-purity electronic-grade silicon to model the elastic behaviour of microscopic, eutectic, silicon particles from Al-Si alloys was confirmed in the Section 4.1, where measured and modelled load—displacement responses largely matched in microscopic 3-point bending tests of such particles.

The encastre boundary condition was applied to the base of each half-model; this base was typically situated at the particle-aluminium interface, while a symmetric boundary condition was applied in the Z plane (half-model plane of symmetry parallel to the particle's largest facet). Despite the fact that the micromechanical system used here is capable of measuring axial forces, this set of data was not used to

drive the FE models because the point of load application is ill-defined (the needle's tip radius is relatively large) and also because it changes throughout the test (due to relative lateral displacement between the tip and the particle, see for example Figure 4.23). Instead, interpretation was based on frames of the recorded SEM video. Namely, the bespoke FE model of each specimen was driven by the displacement of a specific edge, measured from frames before starting to load and at the critical moment, which was set as a boundary condition in the finite element model. The selected edge, perpendicular to the particle large facets, was typically located at the top of the particle, away from the ligament, in a part that undergoes exclusively rigid translations. In Figure 4.18f and Figure 4.19f the relevant edge and the imposed displacement are indicated with black spots and a black arrow. The undeformed and deformed shapes resulting from the FE model were finally compared with the corresponding SEM images to check that the deformation of the whole particle –and particularly that of the ligament– were mutually consistent; this was systematically the case in data of this work. These shapes are indicated in blue and in red, respectively, for each particle in Figure 4.18 to Figure 4.21.

Tests were also analysed using an alternative, rough yet much simpler, analytical approach. According to classical beam bending theory, the maximum stress σ of a straight bent beam deformed to a radius of curvature ρ (measured at the neutral axis) is given by

$$\sigma = \frac{E y}{\rho} \quad \text{Equation 4-4}$$

where E is the Young's modulus, here taken as 168.9 GPa; this being the (isotropic) modulus of Si along the (111) plane, and y is the distance from the neutral axis to the outermost surface. Here, the actual shape of the particle ligament cross section was not taken into account; instead, the ligament was considered to be symmetric and unaffected by FIB milling along its compressive surface; the neutral axis was thus taken to pass through the middle of the ligament's cross section; in other words, we take $y = t / 2$, where t is the (measured) ligament thickness. SEM images were used to determine t in the undeformed state and ρ at the critical deformation (i.e. from an image taken right before catastrophic failure). A representative example of the curvature measurement, ρ , is shown in Figure 4.22a1-a2. For simplicity, measurements of ρ were done on the specimen's outermost surface rather than on the neutral axis as it was observed that the former, which is easier to identify in SEM images, described fairly accurately the curvature of the ligament at any position along its thickness, justifying the underlying assumption that deformation along the ligament's outer surface was relatively uniform, see Figure 4.22a2. In this approach particle strength was then taken as the maximum stress at failure, as computed from Equation 4-4. Finally, note that in Specimen #2 (Figure 4.22b1—b2), the initial shape of the ligament was naturally curved. To account for the initial curvature (of the stress-free particle), first a stress was computed using Equation 4-4 with ρ being the initial curvature, which was then subtracted from the stress computed with ρ being the critical curvature.

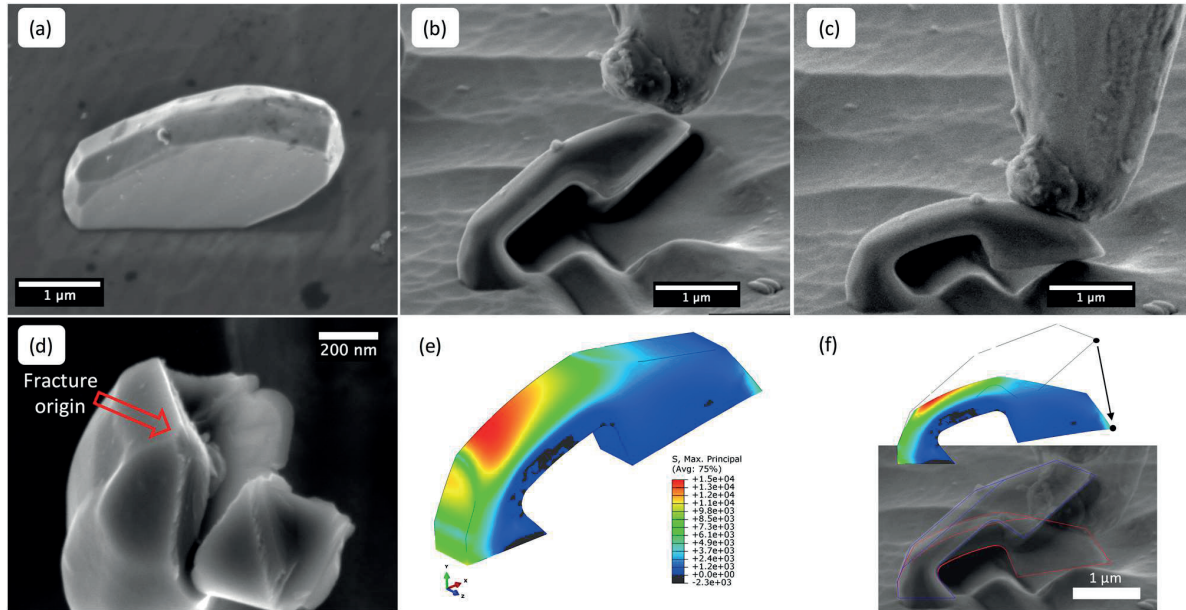


Figure 4.18 A step-by-step example of the methodology used in this work to probe the strength of individual silicon particles of the alloy (Specimen #7 in Figure 4.24). (a) The original silicon particle from a perspective view. (b) Same particle after shaping using FIB milling, ready to be tested. (c) Last frame of the video recorded upon mechanical testing, immediately before particle fracture. (d) Fractography of the sample. (e) Linear elastic finite element modelling results of the deformed particle. (f) Superimposed SEM images and results of the FE model of the particle before the test (undeformed) and at the critical moment (deformed). (Reproduced from Mueller et al. [411])

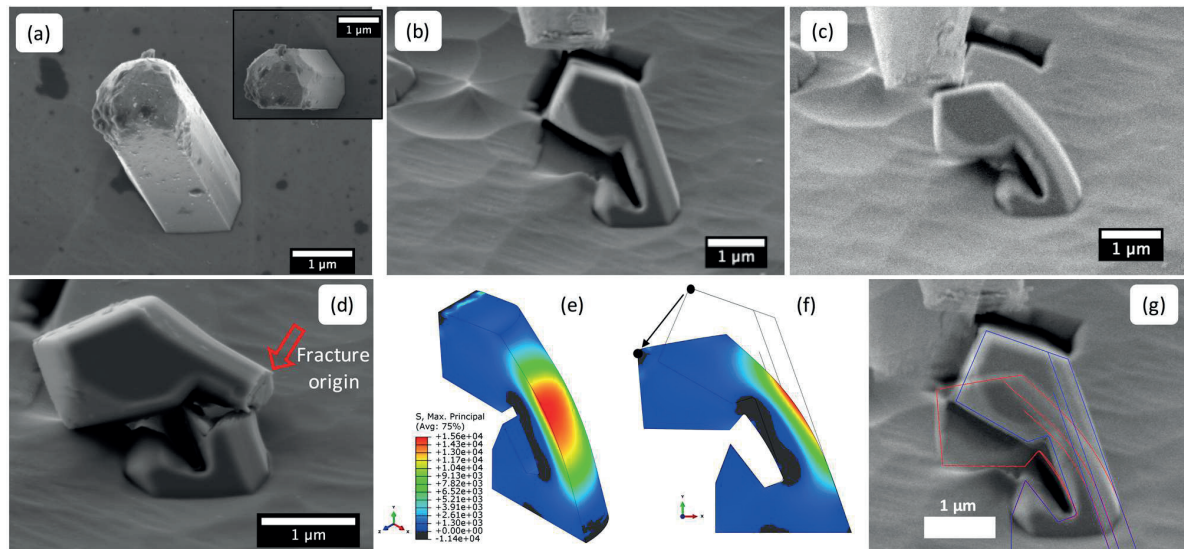


Figure 4.19 A second step-by-step example of the methodology used in this work (Specimen #1 in Figure 4.24). (a) The original silicon particle from a perspective view (and from a top view in the inset). (b) The particle ready to be tested. (c) Last frame before particle fracture. (d) Fractured particle. (e-f) Finite element modelling results of the deformed particle. (g) Superimposed SEM images and the shapes resulting from the FE model. (Reproduced from Mueller et al. [411])

4.2.2 Results

A total of 15 particles were tested in this work; these are shown in Figure 4.16 to Figure 4.23. Figure 4.18 and Figure 4.19 show two step-by-step examples of the method: the selection of a given particle, its shape after FIB milling, the micromechanical test, the fracture surface, the analysis by finite element modelling and finally the cross-check for consistency between modelled and actual particle shapes. While in some of the probed surfaces no defect could be distinguished by SEM examination (e.g. Figure 4.19, Figure 4.21a and Figure 4.22), in most specimens one of the following was detected:

- a surface pinhole (Figure 4.16, Figure 4.17 and Figure 4.21e),
- an interface between two silicon crystals (Figure 4.21g-h-i and Figure 4.20),
- a burr-like feature running diagonally along the particle edge (Figure 4.21d),
- a (111) twin boundary producing either a slight ridge or groove along the edge (Figure 4.18 and Figure 4.21c),
- a tiny feature attached to the surface (labelled here “surface scale”, Figure 4.21f).

Moreover, two samples were tested in which the surface subjected to tension was intentionally flattened with the FIB prior to testing, so as to probe whether the strength of such a FIB-produced surface is affected by ion-milling (Figure 4.21b and Figure 4.23).

The measured strength values (based on the bespoke FE analysis) are given in Figure 4.24 (tabulated data can be found in Table 4-2). In the graph, samples are separated into groups according to the specific characteristics of the probed surface, namely samples with no apparent defect, samples with a FIB-produced surface or samples featuring one of the different types of particle defects listed above. In several tests, it was noted that particle fracture had initiated at a location subjected to a first principal stress that was not the highest within the specimen. For those cases, two values of strength are reported in Figure 4.24: (i) the maximum of the first principal stress in the ligament at the moment of fracture (full squares), and (ii) the value of the first principal stress at the moment of fracture at the location where fracture actually initiated (hollow squares). An example of such a particle is Specimen #15 (Figure 4.21f), whose fractographic analysis indicates that the crack leading to fracture took off from a spot on the side of the ligament where a rare feature (here called a *surface scale*) was present. Another example is Specimen #2 (Figure 4.22b1—b4), in which fracture originated in a spot subjected to significantly lower stress than the maximum stress in the specimen (though, in this case, no specific defect could be identified upon fractographic examination).

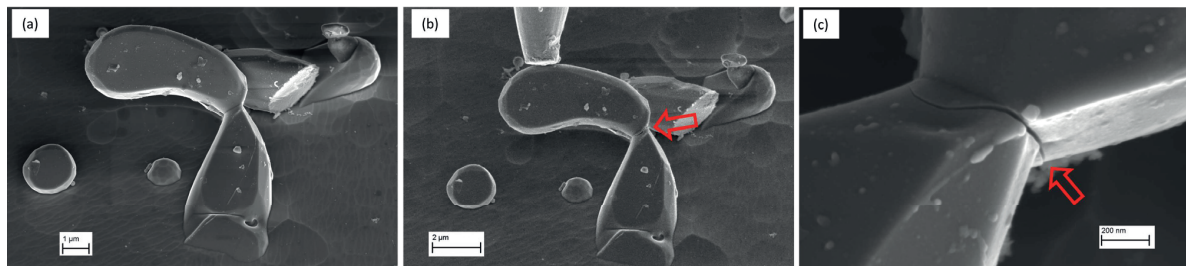


Figure 4.20 (a) A particle (Specimen #14 in Figure 4.24) featuring an interface that could be readily probed (no FIB-milling was required to prepare this sample). (b) The particle right after fracture. (c) Close-up, from a tilted angle, of the point of fracture, situated at a grooved silicon-silicon interface.

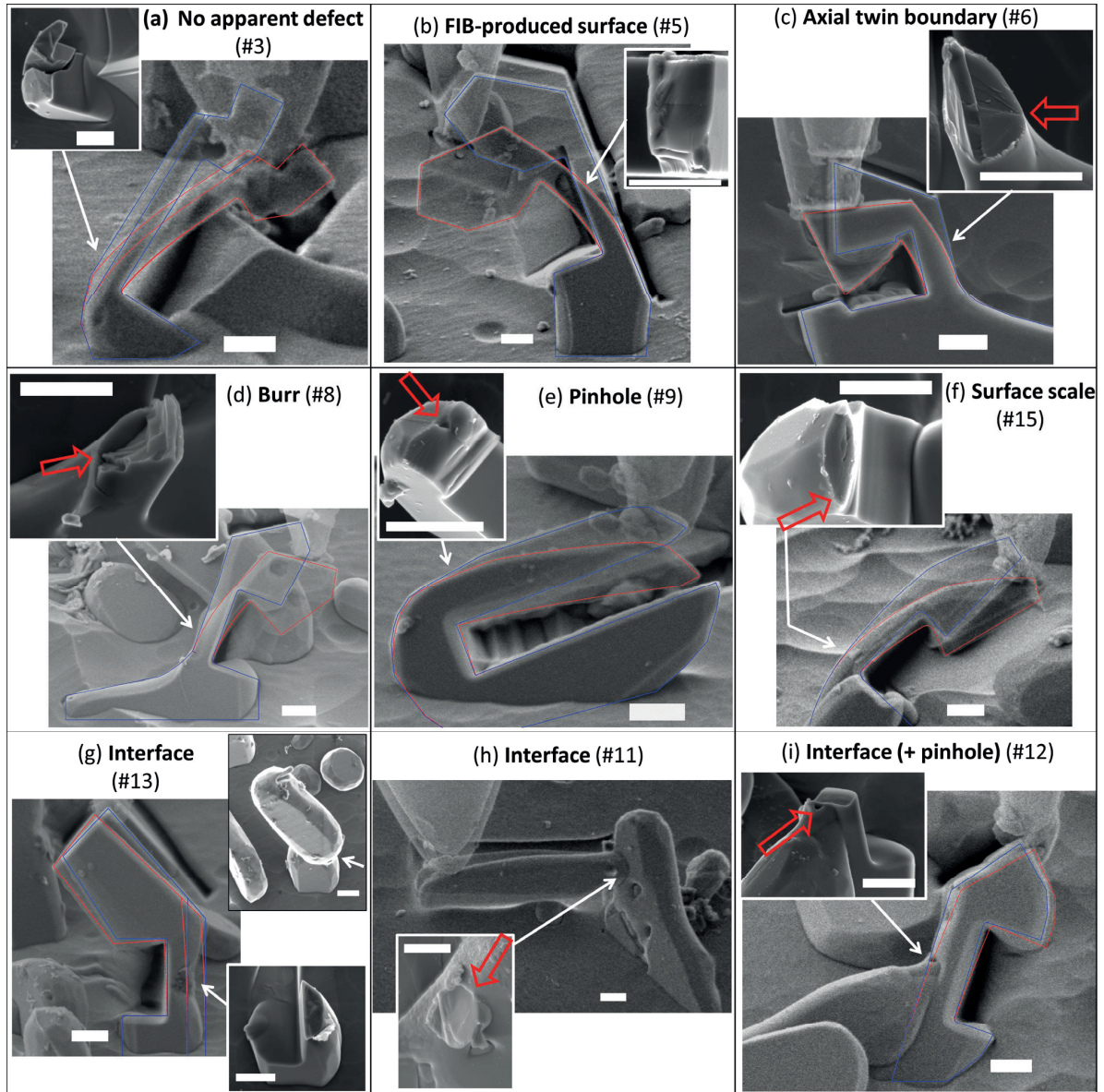


Figure 4.21 A representative selection of the particles tested in this work (each specimen is identified with a number, #nn, which is used correspondingly in Figure 4.24). In each subfigure (a-i), the undeformed and the deformed (just before fracture) images of each particle are superimposed. The corresponding shapes extracted from the finite element model (FEM) are also superimposed in blue and red, respectively –except for specimen (h), as this was only analysed using simple beam theory–. The fracture surface of each particle is shown as an inset in a white frame. The scale bar is 1 μm . Particles in (c-i) feature various surface defects that naturally occur in silicon particles within the alloy. On the other hand, no defect could be distinguished on the tensile surface of particle (a). The specimen in (b) was prepared deliberately such as to probe the strength of a surface milled with the FIB. (Reproduced from Mueller et al. [411])

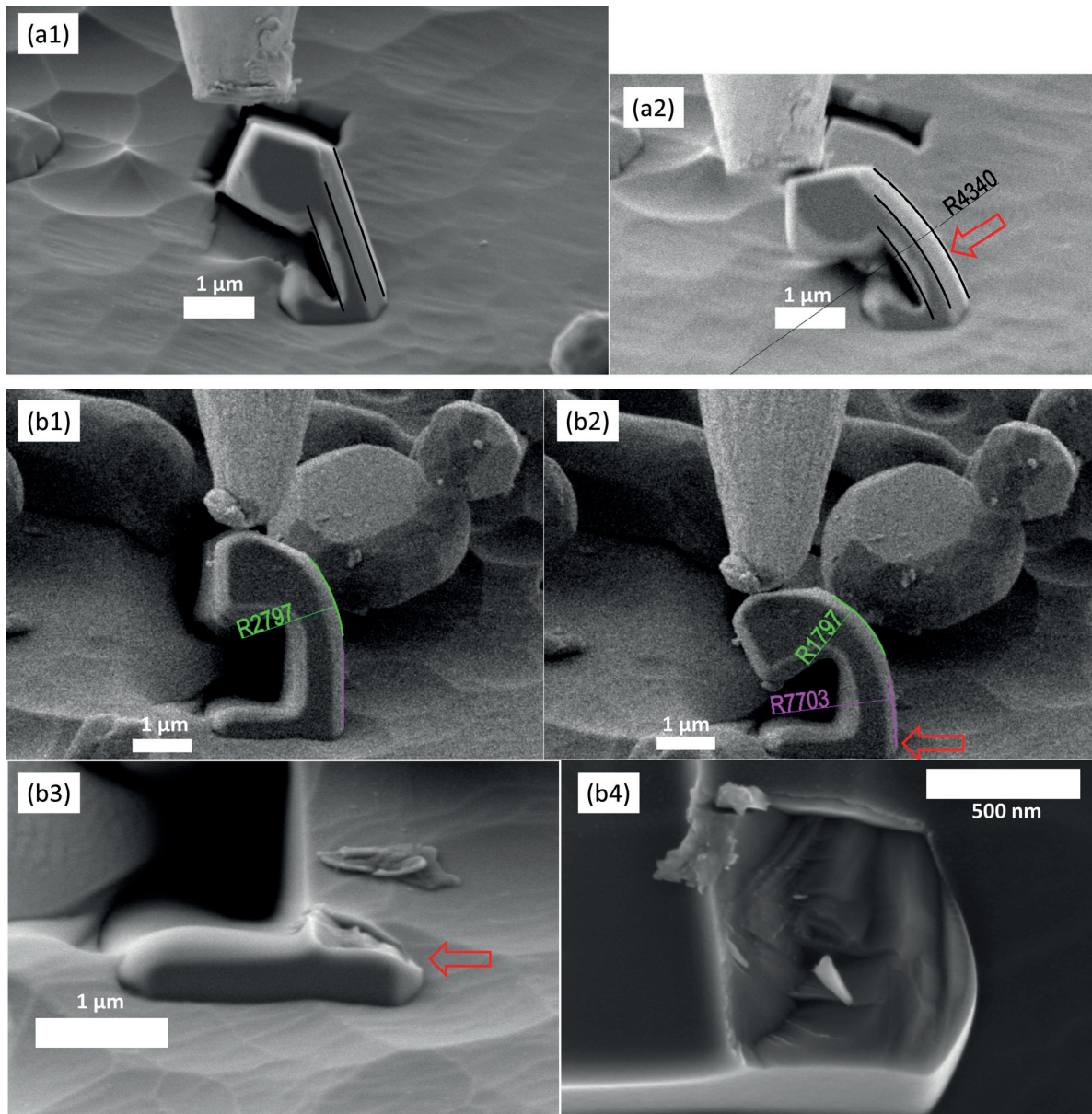


Figure 4.22 An alternative, simple, way to estimate the specimen fracture stress is based on curvature measurements (Equation 4-4), here exemplified with Specimen #1 (a1—a2) and with Specimen #2 (b1—b4). The location of maximum stress in Specimen #2 is indicated in green (b1—b2); to account for the initial curvature (of the stress-free particle), first a stress was computed using Equation 4-4 with ρ being the initial curvature (measured in b1), which was then subtracted from the stress computed with ρ being the critical curvature (measured in b2). Note that, as seen in b3—b4, the specimen fractured in a location of lower stress (a critical defect could not be identified, though): the critical stress at that location was estimated from the curvature measurement indicated in purple. The radii of curvature indicated in the images are in nm. Results are tabulated in Table 4-2.

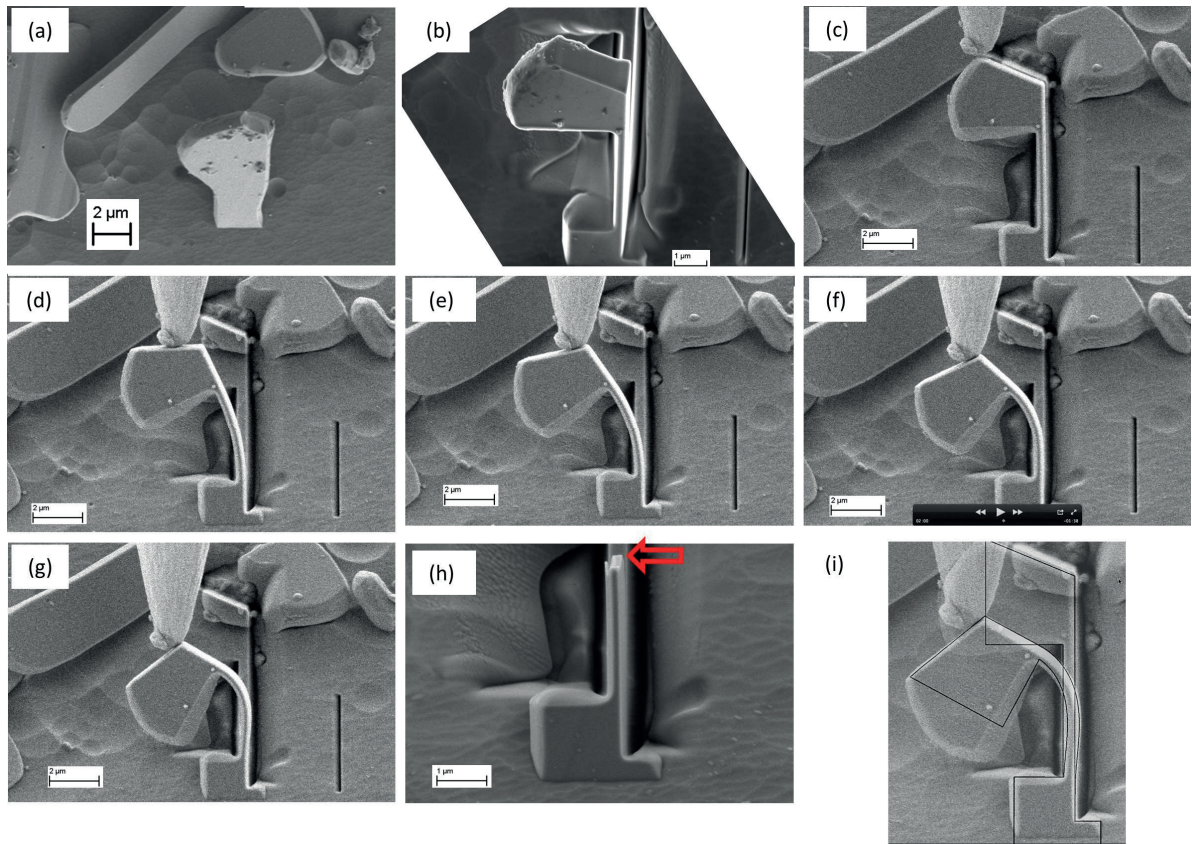


Figure 4.23 Test on a particle (Specimen #4 in Figure 4.24) featuring a FIB-milled tensile surface (the particle before and after preparation is shown in (a) and (b), respectively). Image (g) is the moment before catastrophic failure. The fractured particle is shown in (h). Note that the load application point and the deflection of the ligament change substantially throughout the test (c)—(g). The interpretation approach based on FEM used in this Section nevertheless captures well the particle deformation; this is shown in (i), where the initial and critical shapes extracted from the FEM calculations are superimposed to the experimental SEM images.

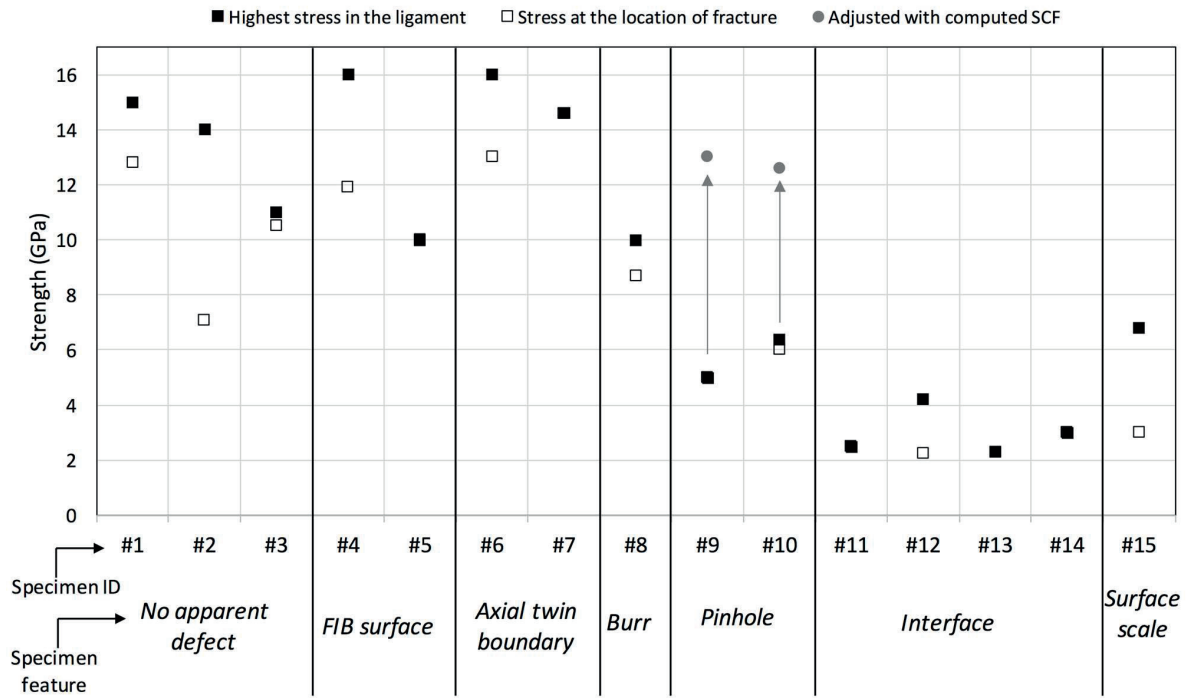


Figure 4.24 Measured strength of individual silicon particles (Specimens #1—#15), which are classified according to the type of feature on their probed surface (see examples in Figure 4.21 and data in Table 4-2). Results from finite element model (FEM) calculations are reported with squares. Full squares indicate the maximum value of the first principal stress in the ligament at fracture. Specimens that have full squares only are specimens that fractured at the location of maximum first principal stress. Specimens in which fracture originated at a location of lower stress are reported also with hollow squares, which indicate the first principal stress at the location where fracture actually originated. For particles featuring “pinholes” (Specimens #9 and #10), arrows and grey circles indicate the stress concentration effect of those defects calculated as the value in full squares multiplied by the corresponding stress concentration factor (SCF), itself computed from Ref. [440] (see main text in Section 4.2.3.2). (Reproduced from Mueller et al. [411])

Table 4-2 Data from the eutectic silicon particles probed in this work. Columns 1 and 2 indicate the specimen ID# and the characteristics of the surface probed in tension. Dimensions of the particle sections subjected to the highest deformations (i.e. the ligaments) are indicated in Columns 3 through 5. Column 6 indicates whether the surface probed in tension (i.e. the outermost surface of the ligament) was considered flat or curved in the bespoke 3D finite element models (FEM). Columns 7 and 8 indicate results from the FEM and Columns 9 and 10 indicate results from curvature measurements (Equation 4-4 in the main text).

Specimen #	Feature on the tensile surface	Particle thickness (nm)	Ligament length (nm)	Ligament width (nm)	Shape of the surface in tension – FEM ^(f)	Max FPS ^(e) in the ligament – FEM ^(f) (GPa)	FPS ^(e) at fracture location – FEM ^(f) (GPa)	Max stress in the ligament – analytical ^(g) (GPa)	Stress at fracture location – analytical ^(g) (GPa)
1	No apparent defect	1434	1057	608	Curved	15	12.8	12.4	N/A ^(d)
2	No apparent defect	834	1345	800	Curved	14	7.1	13.5	8.8
3	No apparent defect	1589	3070	740	Curved	11	10.5	9.0	N/A ^(d)
4	FIB surface	1439	3810	357	Flat	16	11.9	13.2	N/A ^(d)
5	FIB surface	1265	3078	796	Flat	10	10	9.0	N/A ^(d)
6	Axial twin boundary	1266	1303	669	Curved	16	13	13.6	N/A ^(d)
7	Axial twin boundary	810	1141	478	Curved	14.6	14.6	16.5	N/A ^(d)
8	Burr	1300	2096	629	Curved	10	8.7	10.4	N/A ^(d)
9	Pinhole	798	N/A ^(a)	N/A ^(a)	Flat	5	5	N/A ^(c)	N/A ^(d)
10	Pinhole	1269	1942	856	Curved	6.4	6	5.9	N/A ^(d)
11	Grooved interface	1004	N/A ^(a)	N/A ^(a)	Flat	N/A ^(d)	N/A ^(d)	2.5 ^(h)	2.5 ^(h)
12	Grooved interface	1308	2360	896	Curved	4.2	2.3	N/A ^(c)	N/A ^(d)
13	Grooved interface	1400	2065	957	Curved	2.3	2.3	N/A ^(c)	N/A ^(d)
14	Grooved interface	1213	N/A ^(b)	N/A ^(b)	Flat	3	3	N/A ^(c)	N/A ^(d)
15	Surface scale	1347	2504	663	Curved	6.8	3	7.5	N/A ^(d)

Notes:

- (a) The specimen is a cantilever beam.
- (b) Micromachining a notch was not necessary for this specimen.
- (c) Deformation of the specimen was too small to allow for reliably measuring its radius of curvature when loaded.
- (d) This value was not measured.
- (e) FPS: First Principal Stress.
- (f) FEM: Finite Element Model.
- (g) Based on Eq. 4-4.
- (h) Calculated using Simple Beam Theory as $(6 FL) / (bh^2)$ with $F = 162 \mu\text{N}$, $L = 6.5 \mu\text{m}$, $b = 1 \mu\text{m}$ and $h = 1.6 \mu\text{m}$.

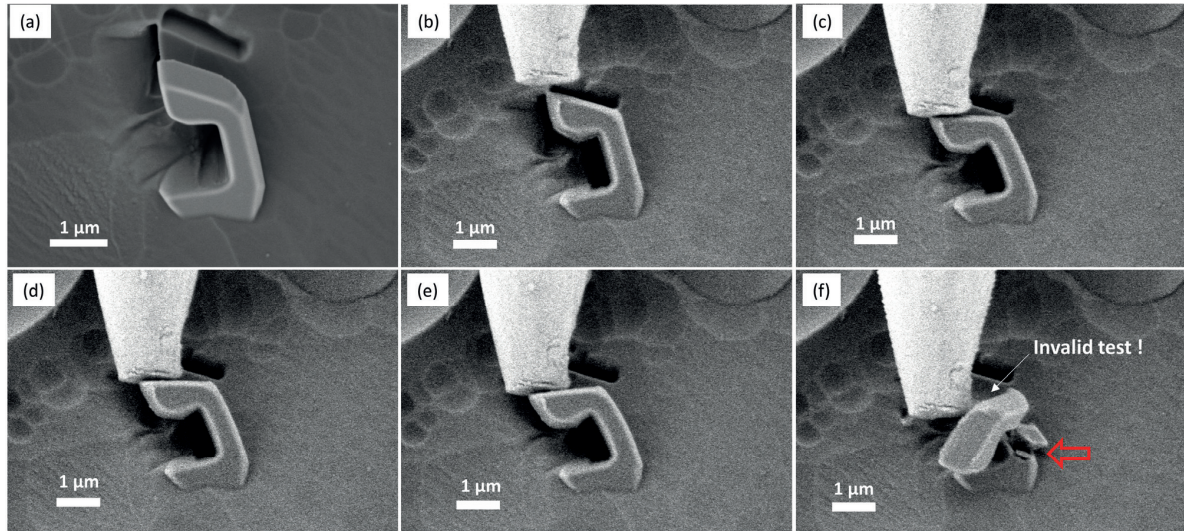


Figure 4.25 (a)–(f) A sample that twisted before catastrophic failure, rendering the test invalid. Note the slight shift of the tungsten needle towards the back between (c) and (d).

4.2.3 Discussion

4.2.3.1 The method and its precision

This work uses a method to measure strength that is an adaptation of the notched particle test of Ref. [409], designed to test individual samples of microscopic, irregular, second phases in alloys and composites (e.g., [441]). The method offers a few advantages with respect to the microscopic three-point bending test [410,442] that was previously used to probe larger silicon particles extracted from an eutectic, binary, Al-Si alloy (Section 4.1 [410]). One is the obvious benefit that comes with performing the test in the SEM, namely that preparation and the test progression can directly be observed. For example, SEM video recording permitted identifying (and more easily discharging) unsuccessful tests (e.g., Figure 4.25 shows an unsuccessful test in which the tungsten needle slipped sideways and produced particle fracture by twisting). The micromachining, using the FIB, of a specimen is furthermore much faster — despite the need for careful alignment — and it is easier to probe smaller particles. Plus, it is easier to aim the test so as to probe a given surface feature on a particle; this is simply achieved by milling a notch opposite to an observed feature. And finally, fractographic examination can always be done because at least one part of the broken particle always stays in place after the test, permitting the identification of the fracture initiation site (in contrast, both ends of microbend bars in Section 4.1 [410] tended to fly off upon fracture). On the other hand, the present test is less well adapted than that in Section 4.1 [410] to the testing of the large facets in plate-like particles – in that sense, the method developed here and that of Section 4.1 [410] are complementary, as they allow to probe the strength along complementary sections of the silicon particle surface.

Prior to discussing the results in this work and their meaning we estimate the accuracy and precision of the tests. Due to the small size of the specimens, a main factor that affects the precision of the measurements is uncertainty in the dimensions measured from SEM images. We estimate this uncertainty as ± 20 nm, this being mainly as a result of the “edge-effect” on SEM images. In this sense, the dimensions of the ligament are the most critical values because this is where most deformation takes place and dimensions are typically submicronic. A maximum limit to the influence of this factor on the global precision of the method can be estimated by taking representative dimensions of the smallest ligaments tested here,

namely 400 x 800 nm, as the cross section of a bar in simple bending. Knowing from simple beam theory that the maximum tensile stress in the beam is $\sigma = (Mh)/(2I)$ where M is the applied moment, $I = bh^3/12$ is the area moment of inertia, and b and h are the width and height of the cross section, respectively, then $er_\sigma^2 = er_M^2 + er_h^2 + er_I^2$ with $er_I^2 = er_b^2 + 3er_h^2$, where er_X is the relative random error of Variable X . Letting $er_M = 0$, $er_h = 20 \text{ nm} / 400 \text{ nm}$ and $er_b = 20 \text{ nm} / 800 \text{ nm}$ leads to the relative random error in measured strength values equal to $er_\sigma \cong 10\%$.

Another factor that can affect accuracy is the particle morphology simplification that is adopted in the finite element model of the test. Namely, ligament cross sections are taken as idealized geometries, with either a semi-elliptical or a flat side, as described above Section 4.2.1.4. In reality, particle edges are sometimes faceted and are not necessarily symmetrical. In addition, the FIB milling process itself generates a small asymmetry because the removal of material is not perfectly parallel to the incoming ion beam axis (and is thus not accurately perpendicular to the large (111) facets in the particles): there is, instead, a 2-3° taper. Moreover, the alignment procedures (shown in Figures S1 and S2 of the Supplementary Material of Ref. [411]), even though carefully performed, could also result in slight misalignments of the same order. These factors, which are hard to quantify globally, can be a source for additional slight error (including overestimation) in the present strength measurements.

Other factors related to the finite element model must also be considered as possible sources of inaccuracy. One is the use of linear instead of higher order elasticity. In principle, this could lead to an overestimation of the stresses when deformations are very large; however, tensile data on silicon nanowires [294] suggests that the linear assumption is safe since the measured stress-strain responses in Ref. [294] were linear up to fracture, which occurred at values exceeding those measured in the present work. Another factor to consider is the encastre boundary condition applied on the particle base: this does not seem to affect much the maximum first principal stress in the models, if one uses as a guide simulations of several tests in which particles were also modelled with longer bases. The reason is that deformation is highly localized at the ligament. In line with this, it is worth noting that we have not observed any sign of deformation of the aluminium around the particle base in any of the experiments.

While the main interpretation scheme in this body of work is based on coupling displacements measured from SEM images with bespoke FE models (described in Subsection 4.2.1.4 and discussed above), the simple, analytical, approach based on Equation 4-4 was also applied. The analytical model computations of strength fall within 20% of the FE results (Table 4-2). Thus, unless a higher precision is sought, the simple analytical approach based on engineering beam theory can be a quick and convenient approach to interpret this kind of tests because it avoids running time- and resources-consuming FEM calculations on data that will often vary, for other reasons, by much more than 20%. Note, however, that measurements of the curvature of deformed particles could only be made on ligaments that were substantially bent, which means that only particles that were subject to relatively high stress (over roughly 6 GPa) could be evaluated in this way: the ligament of the weakest particles bent too little to extract a meaningful radius of curvature from the SEM images (e.g., Figure 4.21 g and i).

From the above, it seems a reasonable estimation that the present strength measurements (Figure 4.24) are accurate to within 20%. This is sufficient precision to ensure the robustness of trends obtained in this work and hence of the conclusions that follow from the present Si particle strength data, discussed next.

4.2.3.2 Silicon deformation and particle strength

This work presents direct evidence that silicon particles in Al-based casting alloys can attain very high levels of elastic deformation at the microscopic scale. This is seen on those particles where no particular surface feature could be spotted, on those featuring shallow surface indications of a twin boundary along the axis of the ligament and on those where the surface subjected to tension was milled with the FIB (e.g. Figure 4.18, Figure 4.19, Figure 4.21b and c.). The affirmation that the deformation was exclusively elastic is based on the fact that every time a test was aborted, which happened many times (either on purpose or simply because mispositioning of the tip was noted and needed correction), the particles fully returned back to their initial position upon retraction of the tip. In turn, the observed large elastic deformations also show that silicon particles can locally reach extremely high strength values: i.e. tensile stresses up to 16 GPa were measured, a value not too far from $\langle 111 \rangle$ silicon's ideal strength in tension (21–23 GPa [46,378]).

Comparable (in some cases higher) strength values and purely elastic response have been measured on silicon nanowires ~ 100 nm in diameter grown by a vapour-liquid-solid process tested in bending [297,379] and in tension [294], and on nanometric bending beams ~ 250 nm thick prepared by photolithography [65]. Note that in the cited works, as well as in the present work, linear elasticity was assumed [65,297,379] or observed [294] in Si deformed to such high strain levels. Despite the difference in global dimensions between the nanowires in the literature and the eutectic silicon particles tested in this work, the fact that they reach similarly high strength values can be understood by the fact that the actual surface area that is probed is comparable. For example, Zhang et al. [294] obtained $\sim 13\%$ of strain on several $\langle 110 \rangle$ -oriented Si nanowires of diameter in the range 80 to 150 nm and roughly $2 \mu\text{m}$ long tested in tension. The surface area of these nanowires adds to roughly 0.6 to $0.8 \mu\text{m}^2$ and the strength is ~ 17 GPa (using a Young's modulus of 130 GPa [294]). This can be compared to the surface of specimens of the present work that attained the highest strength values (Specimens #1 to #8 in Figure 4.24 and in Table 4-2). A rough –yet illustrative– estimation of the surface area subjected to tension on those specimens can be taken as the length of each ligament multiplied by its width (i.e. the ligament surface, considered flat, opposite to the notch). This gives values in the range $0.9 - 5.5 \mu\text{m}^2$; as seen, not only strength values but also probed surface areas are roughly of the same order of magnitude in the present study and in nanowires of Ref. [294]. Other strength measurements in the literature of Si nanowires some tens of nanometres in diameter give lower values: up to 12 GPa for specimen surface areas of roughly $0.1 \mu\text{m}^2$ [428,443]. The reason for these lower values was proposed to be the fact that nanowires grown in the $\langle 111 \rangle$ direction (e.g., Refs [428,443]) feature less smooth surfaces than $\langle 110 \rangle$ -oriented nanowires [294], which once more reflects the fact that strength is controlled by surface features.

We also find in this work that certain silicon particle surface defects are stress concentration sites that decrease markedly the particle strength. These defects, some of which had been recognized in earlier studies (Section 4.1 above and Section 4.3 below [410,412]), occur in large numbers across the particle population of Al-Si alloys. The present results show that the most deleterious defects are those that are here categorized as *interfaces*; namely, grooved edges at the particle surface where two silicon crystals merge together forming one particle. These defects lower the strength down to 2 to 3 GPa, which is roughly a factor 5 to 6 from the strongest particles measured in this work, Figure 4.24. Stress concentration factors (SCF) of that order imply that these grooves must be very sharp (i.e. the radius of curvature at their bottom, which we were not able to measure in this work, must be very small).

A specimen featuring a rare defect that we call here “surface scale” also showed very low strength; however, this result could unfortunately not be reproduced because no other particle with a similar defect could be spotted and tested.

“Pinhole” defects, which are caused by alloy impurities such as Fe and Ti [412], are found to decrease particle strength down to 5 or 6 GPa, which betrays a SCF of ~ 2 to 3. For comparison, an expression for the SCF of a semi-elliptical surface pit characterized by its depth a and its radius c can be found in the work of Cerit et al. [440] (note, however, that the loading mode is uniaxial tension in Ref. [440] instead of bending as in the present work). Measurements based on SEM images of the pinhole of Specimen #10 (Figure 4.16 and Figure 4.17) give $a \approx 70$ nm and $c \approx 80$ nm, which yields a SCF according to Ref. [440] of ~ 2.1 . In the case of Specimen #9 (Figure 4.21e), $a \approx 120$ nm and $c \approx 50$ nm, leading to SCF of ~ 2.6 . The effect on strength of the calculated SCF is shown in Figure 4.24 with grey circles for these two particles. As seen, the strength values obtained here are realistic given the shape of these defects.

Surface “burrs”, which are produced at aluminium grain boundaries upon heat treatment [412], are found to be less critical, as expected given their ridge-like shape. Finally, FIB-machined surfaces and shallow axial grooves produced by (111) twin boundaries do not act as stress raisers and hence do not affect particle strength, see Figure 4.24.

Present results can be compared to the microscopic three-point bending investigation of Section 4.1 [410], in which the local strength of coarsened eutectic silicon particles extracted from a binary Al-12.6%Si alloy was probed. Besides the testing approaches and the alloys’ composition, other important differences between both studies include the size of the eutectic silicon particles that were probed (which were roughly 10 times larger in Ref. [410] than in the present work), and most importantly the fact that in Ref. [410] particles were tested along their large (111) facets, whereas in the present work particles are tested along their edges; testing methods of this work and of Ref. [410] are thus complementary in that they probe two complementary portions of the particle surface. Strength results of surface defect-free particles are scattered in both studies; yet, it can be noted that they give somewhat higher strength values in the present work than in Ref. [410] (~ 7 to 15 GPa vs. ~ 6 to 12 GPa). This might be a consequence of the smaller volume (or surface area) of material that is probed here. On the other hand, the strength of particles featuring similar “pinhole” defects are close across both studies (~ 5 to 6 GPa vs. 4.7 GPa) indicating that particle strength is then governed by the stress concentration effect associated with the defect. Similarly, the local strength of particles featuring interfaces measured here (~ 2 to 3 GPa) falls within the values of the two particles featuring interfaces that were probed in Ref. [410] (1.1 GPa and 3.6 GPa), although in this case the differences are larger, probably reflecting the differences in the geometry of the probed interfaces. Overall, both studies agree in that (i) silicon particles can achieve high, near-theoretical, local strength values, and (ii) surface defects on the silicon particles strongly decrease particle strength. We note in passing that the surface defects on silicon particles within Al-Si alloys are not related to the etching procedure (this is demonstrated in Section 4.3 below [412]) and that the etchant is expected to produce a surface layer of only a couple of nanometres of silicon oxide (see discussion in Section 4.1.3.3 while noting that the etching times were significantly shorter in this Section than in Section 4.1).

Previous estimations of the strength of the silicon particles in aluminium (see Section 2.2) give values in the range 0.1 – 3.5 GPa [13,29,40–45,50,163]. These values were, in some of those publications, deemed reasonable on the basis that they compare roughly with the strength of 2 GPa measured on silicon whiskers in the late 1950’s [296]; however, they are significantly lower than the highest strength values measured in the present work, which reflect better, we believe, the actual potential of the silicon

particles as a reinforcing phase for aluminium. Indeed, the high strength measured here on some silicon particles reflects the great degree of surface perfection that these eutectic particles, nucleated and grown during alloy solidification and subsequent solid-state heat-treatment, can attain (which is comparable to that of silicon nanowires). Given that particle fracture is the main mechanism during the first stage of damage in this class of alloys when they are subjected to stress [444,14,13,12,19], it would therefore be beneficial to alloy strength and ductility to prevent, through appropriate processing schedules yet to be designed, the formation of the most deleterious particle defects identified here, namely (grooved) interfaces, which result in particular from the joining of growing or coarsening Si particles.

4.2.4 Conclusion

In-situ measurements of local strength on individual, microscopic, silicon particles within cast aluminium Alloy A356 were performed using a micromechanical testing method that probes in tension a portion of the particle surface that is unaffected by artefacts arising from FIB milling. Results show that:

- the local strength of these particles can be very high, reaching 16 GPa,
- in the absence of visible defects, along FIB-machined surfaces or near defects that do not produce strong stress concentration, particles were found to fracture at surface stresses in the range from 7 to 15 GPa, while
- the presence of defects that act as stress concentration sites lowers substantially particle strength, to values in the range from 2 to 6 GPa.

The most important defect is found to be at the triple line where aluminium meets a silicon-silicon grain boundary, as this produces grooves along the particle surfaces. These defects, occurring in large numbers within particles in Al-Si alloys, lower particle strength down to only a few GPa. It follows that one way of improving mechanical properties of Al-Si alloys is the avoidance of this particular type of defect.

4.3 Investigation on the origin of particle defects

(Adapted from Ref. [412]: M.G. Mueller, M. Fornabaio, A. Mortensen, *Silicon particle pinhole defects in aluminium-silicon alloys*, *J Mater Sci.* 52 (2017) 858–868. doi:10.1007/s10853-016-0381-y)

In Sections 4.1 and 4.2 it was shown that silicon particles in heat-treated Al-Si casting alloys can contain flaws such as surface pinholes and grooves, which cause varying degrees of reduction in the in-situ particle fracture strength and hence influence the mechanical properties of this class of alloys. In this Section, the formation of one class of such strength-limiting flaws in solidified and coarsened Si particles, namely surface pinholes, is shown to be caused by alloy impurities such as Fe and Ti in both binary eutectic Al-Si alloys and also in casting alloy A356. This is evidenced by using Focused Ion Beam serial sectioning tomography coupled with Energy-Dispersive X-Ray Spectroscopy, and confirmed by the observation that a high-purity Al-Si alloy presents a significantly lower proportion of pinholes along the surface of the silicon phase than does an alloy of commercial purity. A similar correlation between alloy purity and the formation of another, more severe strength-limiting particle defect, namely grooved interfaces, was on the other hand not found.

4.3.1 Introduction and examination of fractured particles

In Sections 4.1 and 4.2, the strength of individual silicon particles was measured directly using a novel microscopic 3-point bending technique [410] or an ‘C-shape’ test in a SEM [411]. These approaches treat

individual particles as separate samples of material, each with their own microstructure and strength-limiting flaws. The probed particles, which were extracted from a coarsened eutectic Al-Si alloy by deep etching in one case, and exposed out of a polished and deep-etched surface of a Al-Si-Mg alloy in the other case, could be classified into two groups: (i) those in which the surface subjected to tensile stress contained no pre-identified defects, and (ii) those that had a distinct microstructural defect visible along the tested surface (see Figure 4.6 and Figure 4.21). Results show that silicon particles from the first group have very high local strength values, commensurate with strength values found in specimens of the same size produced from electronic grade silicon [65] and thus approaching the theoretical strength of silicon. Particles from the second group were, on the other hand, found to be much weaker. The implication is that silicon particles within Al-Si casting alloys can be very strong, but many of them feature defects along their surface that strongly reduce the particle strength, notably because they act as stress concentrators.

Examples of silicon particles in binary Al-12.6%Si and A356 alloys in either as-cast or heat-treated conditions are shown in Figure 4.26. The presence of defects on the particles such as surface holes or "pinholes" of various sizes (indicated with white arrows), surface step- or groove-like interfaces, burrs and necks is evident along the particle surfaces, in both alloy conditions. Figure 4.27 shows fractured silicon particles from macroscopic specimens of each alloy, in either condition, which were deformed in tension before selectively deep-etching the aluminium phase for SEM examination of the particles. Surface pinholes and internal "cavities" (the latter seen along the fracture surfaces in Figure 4.27 f and g) are here too indicated with white arrows. In most of these particles the fracture origin can be identified by examining the beach-marks and/or by following the river pattern on the particle fracture surface: these point to a stress-concentrating defect along the particle surface. Pinholes (or similar defects) were the fracture origin of particles in Figure 4.27 b, c, d, h and, arguably, a. The particle in Figure 4.27e fractured at a location situated along a neck (see low-magnification image in the inset); here, the precise fracture origin is a shallow surface groove, which is likely related to a twin plane. The particles in Figure 4.27 f and i broke at interfaces, the latter a deeply grooved one. All those flaws are important factors affecting the strength of the silicon particles within the alloy, and hence govern in turn the strength or toughness of the Al-Si based alloy.

SEM examination of defects on silicon particles such as those in Sections 4.1 and 4.2, and in Figure 4.26 and Figure 4.27, was made possible after subjecting each alloy to a deep-etching procedure, so as to selectively dissolve the primary aluminium phase over a depth of a few micrometres and expose silicon particles that were present within the microstructure. Even though the etching procedures, described in the next section, are generally known to be harmless to silicon (other than producing some nanometre-thick surface oxidation, see the discussion in Subsection 4.1.3.3), it is not granted that the surface defects observed on silicon particles after etching were not modified by the etching procedure, particularly if they were the seat of (removed) variations in the composition of the particle or if the defects neighboured second phases that were also dissolved. In the extreme, pinholes might even be suspected to be the result of a pitting corrosion mechanism during the deep etching procedure, rather than being intrinsic particle defects.

To alleviate the limitations and concerns linked to the use of an etching procedure, in this work we investigate the (strength-limiting) Si particle defects identified earlier using FIB-tomographic examination of the microstructures within polished samples of two Al-Si alloys. Results reveal the presence of small intermetallic particles at the root of surface pinholes and in internal "cavities" within the silicon particles. Other defects, namely grooves and burrs, are on the other hand not linked to such impurities. To corroborate that surface pinholes are the result of the presence of impurities, an Al-Si alloy of very

high purity was also produced and compared to a lower purity alloy using a statistical survey of defects found along exposed Si particles.

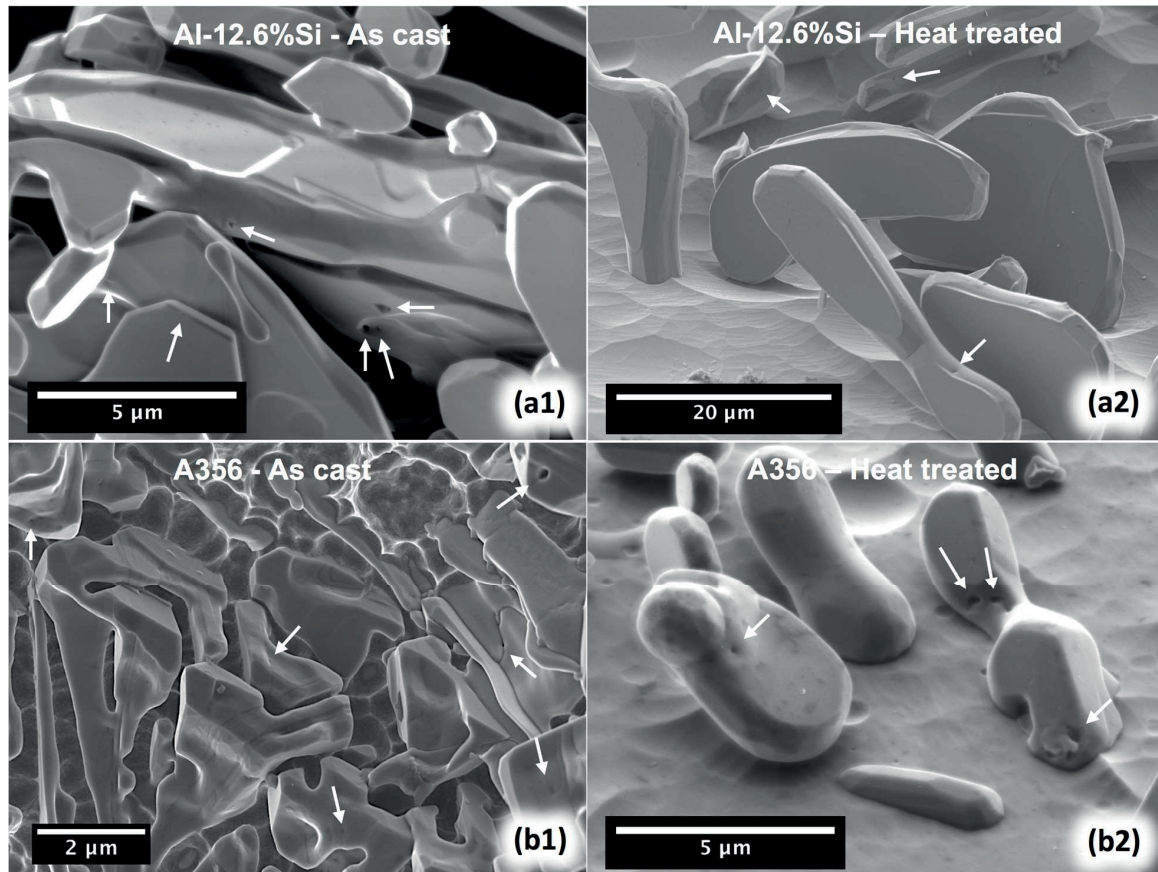


Figure 4.26 SEM images of silicon particles from an Al-12.6 %Si alloy (a1–a2) and from alloy A356 (b1–b2) exposed by selectively dissolving the aluminium matrix of the alloys in either the as-cast or heat-treated conditions. Several defects on the particles are observable (see main text); among them pinholes are indicated with white arrows. (Reproduced from Mueller et al. [412])

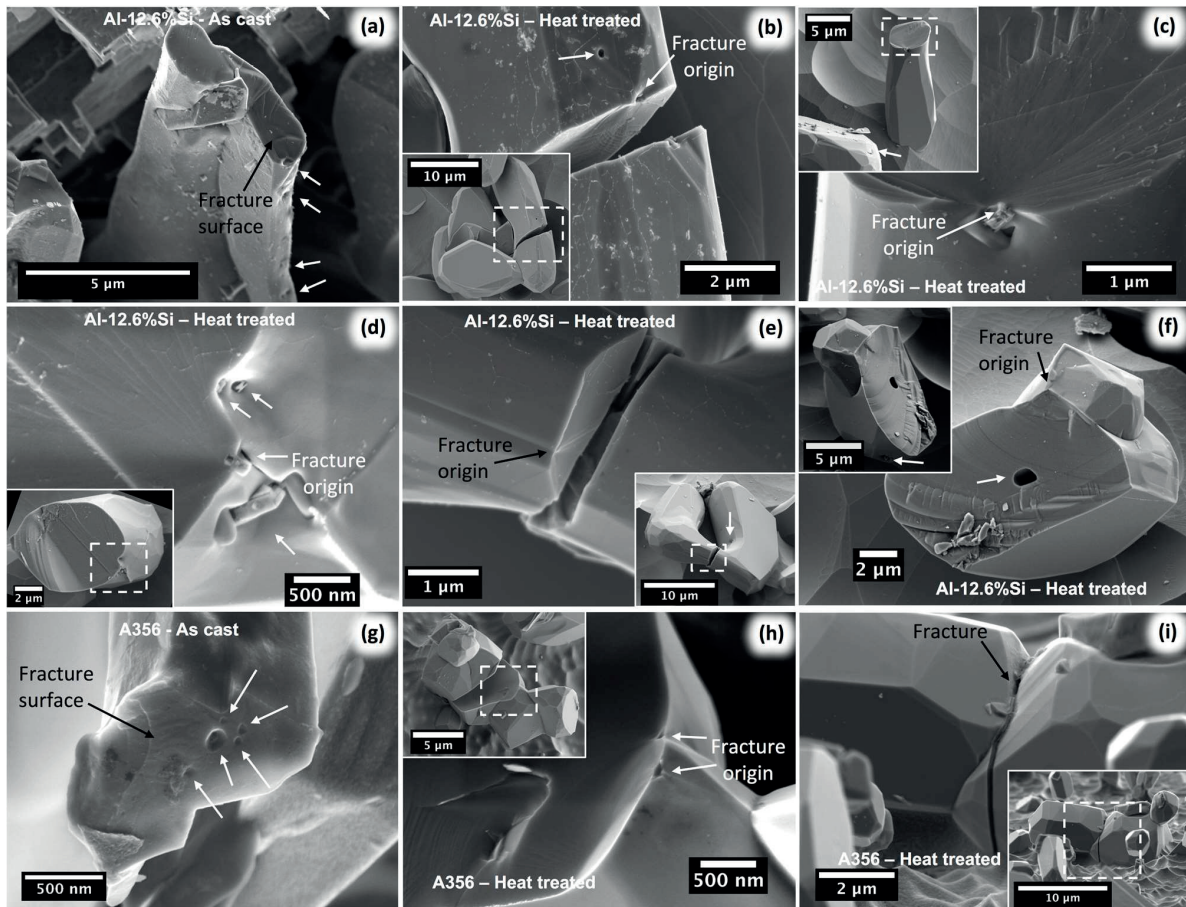


Figure 4.27 Fractured silicon particles from Al-12.6 %Si and alloy A356, in the as-cast and heat-treated conditions. The alloy samples were deformed in tension, followed by aluminium selective etching to expose the silicon particles for subsequent examination in the SEM. Surface pinholes (or similar surface defects) and internal cavities along fracture surfaces are indicated with white arrows. In the insets, a lower magnification image of the fractured particle is shown. In most particles, the fracture origin can be identified and is found to be a stress-concentrating defect on the silicon particles: pinholes in (a), (b), (c), (d) and (h), a shallow-groove linked to a twin boundary in (e) and deep grooved interfaces in (f) and (i). (Reproduced from Mueller et al. [412])

4.3.2 Materials and methods

Two alloys, namely a binary eutectic Al-12.6 %Si alloy—also referred to as a standard-purity eutectic alloy—and a A356 alloy, were used to examine the silicon particles within their microstructure using FIB-tomography coupled with Energy-Dispersive X-ray Spectroscopy (EDXS) analysis. The chemical composition of these two alloys is given in Table 4-3. For Al-12.6 %Si, the as-cast condition refers to the state in which it was delivered by the producer, Alusuisse Technology & Management AG (Neuhausen am Rheinfall, Switzerland), within cast ingots roughly 40 cm × 9 cm × 2 cm in size. The heat-treated condition refers for this alloy to exposure for 7 days to 550 °C, a heat-treatment that was conducted with a goal to coarsen the silicon particles. The A356 alloy (from Alu Metall Guss AG, Gontenschwil, Switzerland) was cast by ourselves into a copper permanent mould producing a rod 15 cm high and 2 cm in diameter. Its heat-treatment was conducted at 540 °C during 6 h, followed by air cooling.

The FIB-tomographic examination was carried out along the surface of polished samples of the two alloys described above, in either the as-cast or heat-treated conditions. Progressive cross sections of silicon particles and their surrounding aluminium matrix were produced by ion-milling using 30 kV Ga⁺ ions and imaged using a secondary electron in-lens detector (which gives contrast based particularly on the electronic properties of the elements in a given phase). The apparatus used was a Zeiss™ NVision™ 40 (Oberkochen, Germany) SEM/FIB dual-beam system. Local chemical analyses were conducted using qualitative EDXS at an electron acceleration voltage of 10 kV to identify the chemical elements of the observed phases (80 mm² X-Max™ silicon drift detector from Oxford Instruments, Tubney Wood, Abingdon, Oxfordshire, UK). No automated FIB milling methods were used in this work; instead, the SEM/FIB operator controlled the progressive sectioning. In this way, the thickness of each successive section could be adjusted (between about 100 nm up to about 700 nm) according to the observed presence or absence of interesting features within the particle under investigation. When a defect was spotted, its nature (i.e. whether it was a surface pinhole or a surface grooved interface for example) could be deduced by the analysis of successive cross sections.

Moreover, a control experiment was performed with a goal to compare the occurrence frequency of pinholes on the silicon particles of the standard-purity eutectic alloy with that of this type of defects on the particles of a high-purity eutectic alloy (as shown in the next sections, the main finding of this work is that impurities cause pinholes on silicon particles). This high-purity eutectic alloy was produced in an induction furnace under an argon atmosphere using a carbon crucible and a steel mould 15 cm tall of 2 × 2 cm square cross section. The mould was open at the bottom, where a large copper piece was attached for enhanced heat extraction by direct contact with the solidifying alloy. The crucible and the mould were beforehand coated with boron nitride. The raw materials were 5N6 aluminium (from Alcoa, Pittsburgh PR, USA) (see its chemical analysis in Table 4-4) mixed with 12.6 wt.% of polycrystalline silicon flakes of purity 5 N or higher (from Wacker Chemie AG, Munich, Germany). The temperature, measured on the crucible, was cycled 4 times between 650 °C and 900 °C to enhance dissolution of the silicon flakes and to homogenise the melt before casting at 800 °C. The alloy was subsequently heat-treated in the same way as the standard-purity Al-12.6 %Si alloy (i.e. 7 days at 550 °C).

The control experiment consisted in individually examining, using the SEM, 225 silicon particles extracted from each of the standard-purity or the high-purity eutectic alloys in the heat-treated condition, and then counting how many of them featured pinhole defects on their visible surfaces. Results from the same measurement conducted with the standard-purity alloy have already been reported in Section 4.1 [410].

The procedure used to extract particles from the alloys and to place them along a flat surface is based on chemical etching (using a solution prepared with H₃PO₄ 85 %, CH₃COOH 100 % and HNO₃ 70 % mixed in volume ratio 83:5.5:5.5 as described in detail in Section 4.1.1.2) or electro-chemical etching (using HNO₃ 6.5 % or NaCl in water as electrolyte) to selectively dissolve the aluminium matrix, then filtering the solution containing extracted particles by passing it through a filter paper to recover the particles, washing them with deionised water and ethanol and finally spreading them on a flat substrate that could be brought to the SEM after drying.

Table 4-3 Chemical composition in wt.% of the alloys used in this work for FIB-tomography and EDX examination. (Reproduced from Mueller et al. [412])

Alloy	Si	Mg	Cu	Fe	Mn	Cr	Ni	Ti	Zn	other (total)	Al
Al-12.6%Si	12.6±0.4	< 0.003	< 0.003	0.033 ± 0.002	< 0.003	< 0.003	< 0.003	< 0.003	< 0.003		bal
A356	6.5 - 7.5	0.25 - 0.45	0.2 max	0.2 max	0.1 max	0.05 max	0.05 max	0.2 max	0.1 max	0.15 max	bal

Table 4-4 Chemical composition in ppm of the 5N6 aluminium used, together with high-purity silicon, to produce the high-purity Al-12.6 %Si alloy. (Reproduced from Mueller et al. [412])

Li	<0.002	Ti	0.14	Fe	0.26	As	<0.009	Sb	<0.009	Ca	<0.2
B	0.019	V	0.056	Ni	<0.004	Zr	0.018	La	0.0056	Si	1.4
Mg	0.92	Cr	0.11	Cu	0.24	Ag	<0.01	Ce	0.041	Al	bal
P	0.056	Mn	0.087	Zn	<0.01	Sn	<0.02	Na	<0.1		

4.3.3 Results

4.3.3.1 FIB-tomography

In the heat-treated standard-purity Al-12.6 %Si alloy, a total of 14 silicon particles embedded within the aluminium matrix were partially or fully sectioned using FIB-tomography. In 6 of those 14 silicon particles, a Fe-rich intermetallic particle containing also Al and Si and having submicronic dimensions was found at the bottom of what could be identified as a metal-filled surface hole (or “pinhole”); Figure 4.28a gives an example. Also, in this alloy no such Fe-rich particle was found to be fully encapsulated by a silicon particle, and only one was found to be surrounded by aluminium (i.e. not to be in contact with Si).

In the same sample, ten other small intermetallic particles containing Al, Ti and Cr were also found; two of these were located at the root of surface pinholes on silicon particles (one is shown in Figure 4.28b). Of the remaining eight intermetallic particles, seven were located inside silicon particles, while one was embedded within the aluminium-rich phase. These particles were even smaller than the Fe-rich intermetallic particles mentioned above: their size was on the order of 100 nm. Given their small size, it is likely that many other particles of this kind were missed due to the relatively thick sectioning that was used. On their EDXS spectra, a small peak corresponding to Si was also present; however, it is not possible to tell whether that Si signal originated from the small intermetallic particle, from the silicon particle around it or whether it is simply an artefact (e.g. an internal fluorescence peak).

Intermetallic particles similarly located within surface pinholes or fully embedded inside silicon particles were also found in the heat-treated A356 alloy. Several Fe-rich particles of size on the order of 100 nm were found to be fully embedded within different silicon particles; one example is shown in Figure 4.29a1 and the corresponding EDXS spectrum of the Fe-rich particle is given in Figure 4.29a2. The cavities on the fracture surface of a silicon particle of this alloy shown in Figure 4.27g are possibly linked to such nanoscopic Fe-rich internal precipitates, which disappeared together with the aluminium matrix during the etching procedure. Moreover, Figure 4.29b1 shows a Ti-rich intermetallic particle within a surface hole on a silicon particle. In Figure 4.29b2, the EDXS spectrum of the intermetallic particle shows the presence of Ti, V and arguably some Ni. Measured Al, Si and Mg peaks could come from the intermetallic particle, but potentially also from the phases around it (the silicon particle and the aluminium

matrix). We note in passing that a particle smaller than 100 nm with its EDXS spectrum showing the presence of P, Al, Si and Mg was found within a silicon particle (data not shown); this could be a particle onto which silicon nucleated heterogeneously, see Section 2.1 [109,108,117].

FIB-tomographic examinations were also done on the standard-purity Al-12.6 %Si alloy in the as-cast condition. There again, Fe-rich intermetallics were found to be connected to silicon particles; however, in this condition their shape was very irregular, see Figure 4.29c. Similarly, Figure 4.29d shows a silicon particle of the as-cast A356 alloy featuring irregular Fe-rich intermetallic particles, both along its surface and within a surface hole.

Such irregular intermetallic particle shapes were not observed in the heat-treated alloys, indicating that the intermetallic phases also undergo strong morphological changes upon heat-treatment (as do silicon particles). We note in passing that Fe- or Ti-rich intermetallics were not easy to find on silicon particles after deep-etching, suggesting that the intermetallics are mostly removed together with the aluminium matrix in the etching process. In other words, structures such as that in Figure 4.29d were a rather rare occurrence after deep-etching; instead, silicon surface pinholes are generally found to be empty when an etching procedure is used to extract and examine the silicon phase.

Apart from surface pinholes and internal defects, we identified and examined eight groove- or step-like defects and four ridge-like features (or “burrs”) on the Al–Si interface of different embedded silicon particles of both alloys after heat-treatment. An example of a groove-/step-like interface is shown in Figure 4.30, where the white arrows indicate the defect along successive sections. Two examples of burrs can be observed in the cross section shown in Figure 4.28b1, one of which is magnified in Figure 4.28b2. Along such embedded surface grooves, steps or ridges, nothing but aluminium and silicon were detected.

4.3.3.2 Control experiment

A statistical comparison between the occurrence frequency of pinholes between high-purity and standard-purity eutectic binary Al–Si alloys was also conducted as a control experiment. Particles extracted by deep-etching from either alloy and spread on a flat substrate were examined one by one with the SEM to check whether they had any pinhole on their SEM-accessible surfaces. It was found that 32 % of the particles from the standard-purity alloy feature at least one surface pinhole (Figure 4.11, [410]), while only 6 % of the particles from the high-purity alloy do. Note that these numbers underestimate the actual proportion of particles featuring pinholes because particle facets in contact with the flat substrate were not accessible for SEM examination, such that it was impossible to know whether pinholes were present on those facets or not. Such bias, nevertheless, is similar for both alloys and thus the observed difference between them is conclusive.

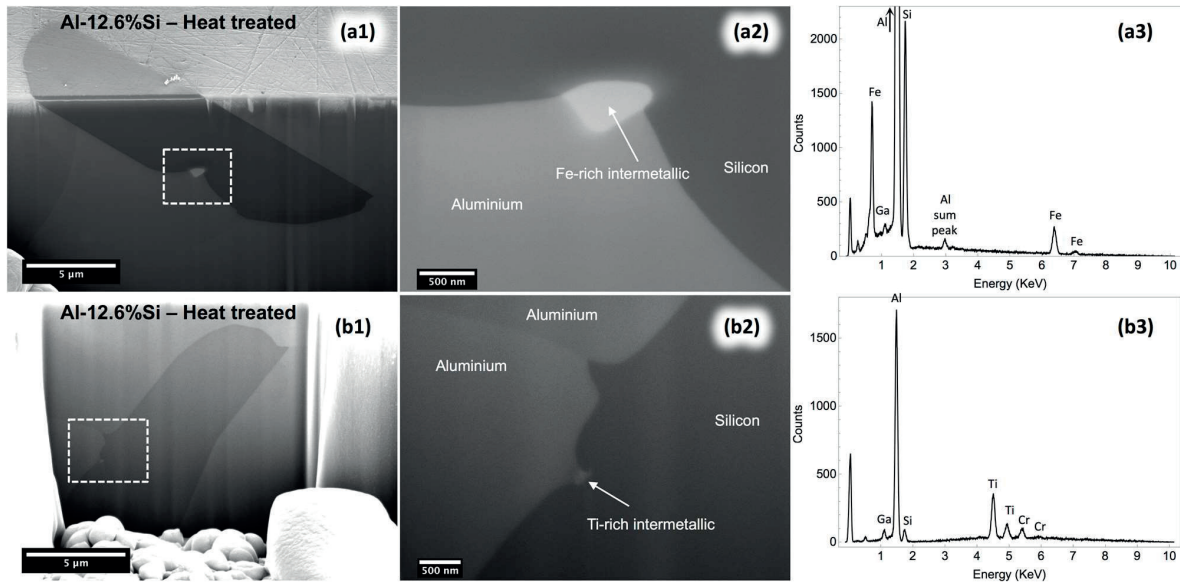


Figure 4.28 SEM images obtained from cross sections of silicon particles embedded within the primary aluminium phase, produced by FIB milling. The alloy is Al-12.6 %Si. Images (a2) and (b2) are close-ups of the area indicated in (a1) and (b1), respectively, which correspond to pinholes on the surface of the silicon particles. EDX spectra (a3) and (b3) correspond to the intermetallic particles indicated with an arrow on images (a2) and (b2), respectively. In images (b1) and (b2), a *burr-like ridge* on the silicon surface can also be observed. (Reproduced from Mueller et al. [412])

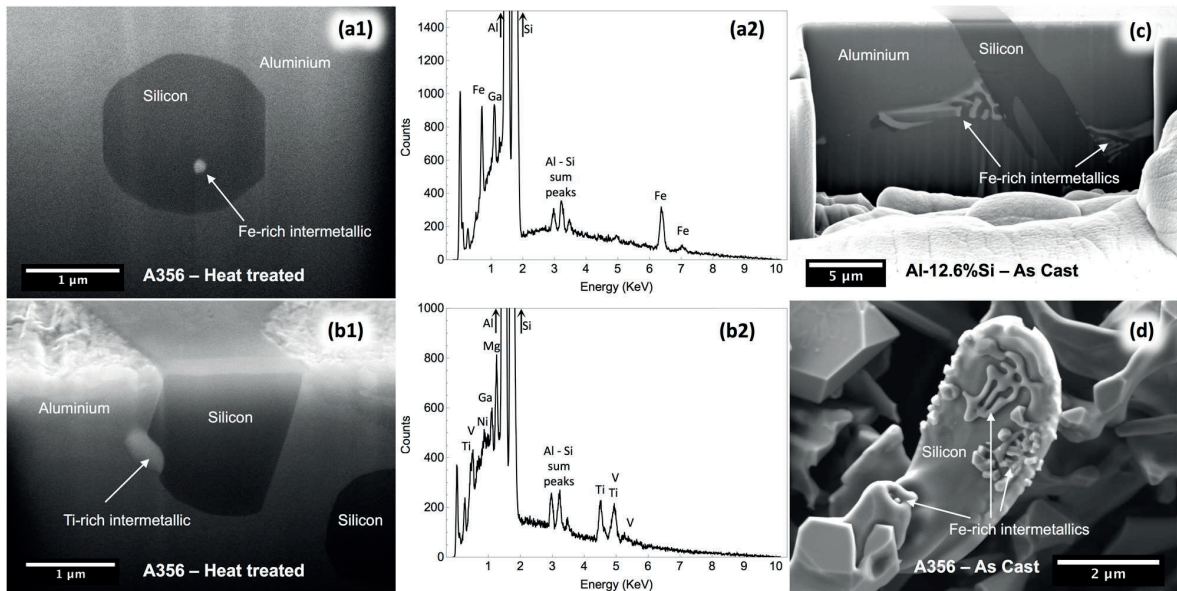


Figure 4.29 (a)–(c) SEM images of silicon particles within the aluminium–silicon alloys obtained from cross sections produced by FIB milling. (a1) and (b1) show an intermetallic particle inside silicon and in a surface feature, respectively, in a A356 heat-treated alloy. (a2) and (b2) are the EDX spectra corresponding the intermetallic particles indicated with an arrow in (a1) and (b1), respectively. (c) Cross section of a silicon particle within aluminium showing the presence of irregular (eutectic) Fe-rich intermetallic phase in the as-cast Al-12.6 %Si alloy. (d) SEM image of a silicon particle extracted by deep-etching from the as-cast A356 alloy showing irregular (eutectic) Fe-rich intermetallic phase on its surface and in a shallow pin-hole defect. (Reproduced from Mueller et al. [412])

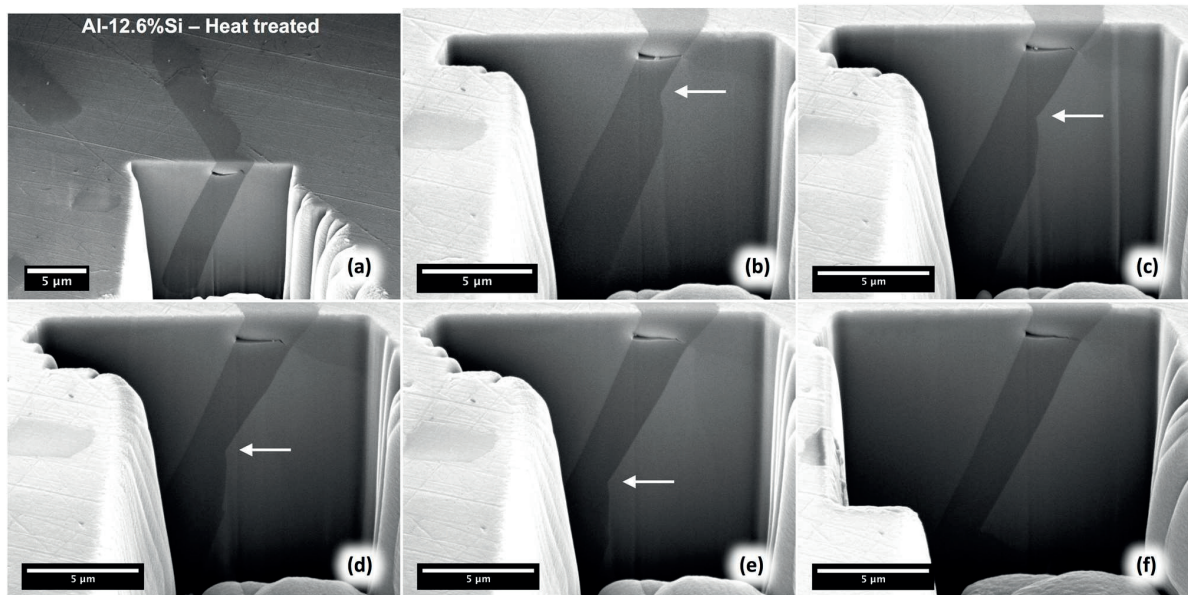


Figure 4.30 (a)–(f) Successive cross sections produced by FIB milling of a silicon particle within aluminium, imaged using the SEM. The white arrows indicate a groove-/step-like interface; here, no intermetallic particle became apparent. (Reproduced from Mueller et al. [412])

4.3.4 Discussion

The FIB-tomography investigation shows conclusively that, at the root of surface pinholes and inside internal defects of silicon particles, there are Fe-rich or Ti-rich intermetallics. Moreover, the control experiment shows that far fewer pinholes exist along the surface of silicon particles within a high-purity alloy compared to a standard-purity alloy, which further demonstrates the link between the occurrence of those flaws and the presence of Fe- or Ti-containing intermetallic second phases.

Fe and Ti impurities are therefore linked with the formation of this particular strength-reducing Si particle defect. Whether this is one of the main mechanisms by which those impurities reduce the mechanical properties of aluminium casting alloys could, on the other hand, not be determined here, for two reasons: (i) these impurities exert other influences on the alloy microstructure (e.g., they also appear as large brittle intermetallic particles and can affect the Si particle size and distribution), and (ii) there are other, more strongly strength-limiting, defects in Si particles that do not seem to be triggered by the presence of Fe, Ti or other impurities. Grooves, which are shown here not to be correlated with the presence of intermetallic precipitates, are one important example.

In Al-Si alloys, Fe-rich intermetallics are virtually always present to some degree: Fe, which has very limited solid solubility [147,445] in aluminium alloys, is one of the main alloy impurities (it is sometimes also used as a deliberate alloying element in hypereutectic Al-Si alloys [446]). The most common and important known Fe-intermetallic is the β - Al_5FeSi phase. This normally forms large and elongated platelets [447], which are at times connected, at times not, to silicon particles [448] and are known to severely reduce the alloy ductility [21]. Another common Fe-containing phase is the α - $\text{Al}_3\text{Fe}_2\text{Si}$ intermetallic, which has a Chinese-script morphology [445]. Also small Fe-rich particles (closer to those observed in the present work) have been observed before using Electron Back-Scatter Diffraction in Al-Si alloys [112,449]. In fact, there are many other intermetallic phases that can form in the Al-Si-Fe system [118,445,450] and their number increases significantly when other alloying elements such as Cu, Mg,

Mn, Ti or Ni are present [149,450]. We have not sought here to identify the exact crystallographic nature of the various small intermetallic particles that were found within Si pinholes, in part because there is uncertainty on their composition with the method used here: quantitative EDXS results can be affected by the surrounding phases, given the small size of the intermetallic particles compared to the interaction volume of 10 kV electrons.

Ti, Cr and V are impurities normally found in aluminium alloys, though in lesser proportion than Fe. In particular Ti is widely used for grain refinement, notably through added Al-Ti-B grain-refining master alloys [451]. Even though the exact mechanisms of grain refinement in aluminium wrought and casting alloys are not yet fully understood, it is known that operative phases are TiAl_3 and TiB_2 [452,453] (the EDXS analysis in this work unfortunately cannot detect B). A number of intermetallic phases containing different combinations of Ti, Cr, Zr, V, Al, Si, Mg and Cu have also been identified in a recent study on an Al-Si casting alloy [454]; this is in line with our findings of Ti-Cr and Ti-V together with Al forming intermetallic phases in the present alloy.

It is interesting that small particles such as those Fe- or Ti-containing intermetallics are able to pin the Al-Si interface so strongly as to form circular holes that are, at times, many particle diameters deep, see Figure 4.26 to Figure 4.28. Likely, this betrays values of the interfacial energy between those intermetallics and silicon that exceed the interfacial energy between those intermetallics and aluminium (2D “contact angles” of Si on the intermetallic, Figure 4.28 and Figure 4.29, suggest this; note, however, that one must be careful with the transposition to 3D of values measured along individual 2D sections). Another cause for the formation of relatively deep pinholes might be the likely anisotropic distribution of the solid Al-Si interfacial energy with interface orientation. This will in turn create torque terms, which could prevent Al-Si interfaces from meeting to engulf intermetallic nanoparticles within the much larger coarsening Si particles.

Another feature that can be noted, particularly on the edges of coarsened silicon particles, is ridges resembling burrs, Figure 4.26a2. Their presence is easily explained as a result of local capillary equilibration along the triple line formed where an aluminium grain boundary meets the Al-Si interface; see Figure 4.28b1–b2. With Al-Si interfacial energies on the order of 0.26 to 0.40 J/m² (from the values for Si with liquid aluminium at the eutectic temperature [455–457]) and aluminium grain boundary energies roughly between 0.2 and 0.6 J/m² [458,459], given the long hold times and high temperatures of heat-treatment, the formation of broad ridges characteristic of equilibration with a finite dihedral angle in the middle of the range between 0 and 180° makes sense. Along the linear burr-like ridges no intermetallic particles were observed; this was also the case for the grooves and the steps. While it remains a possibility that impurities smaller than can be caught at the resolution of the present technique (i.e. in the order of a couple of tens of nanometres) might actually exist there, there is a clear difference between what was found along these kinds of defects, and what was found at the bottom of surface pinholes, where intermetallic particles were readily visible and could be identified as the cause underlying formation of that particular class of strength-limiting silicon particle defect.

4.3.5 Conclusions

In conclusion, this body of work complements Sections 4.1 and 4.2, in which the strength of individual silicon particles from Al-Si alloys was measured to show that there are identifiable, specific defects that weaken Si particles in aluminium casting alloys. It is demonstrated here, using FIB-tomography and EDXS examination of Al-12.6 %Si and A356 alloys, that:

- (i) Burr-like defects exist on the edges of some coarsened silicon particles. These are a consequence of capillary force equilibration where aluminium grain boundaries meet the particles (and are not associated with the presence of other second phases).
- (ii) Groove- and step-like defects on silicon particles are also not linked to impurity-containing intermetallic particles; their existence is therefore likely related to mechanisms of Si particle growth or coarsening.
- (iii) Pinholes found along the surface of etched silicon particles are not voids but contain, in the alloy, submicronic Fe-rich or Ti-rich intermetallic particles at their root, and are otherwise filled with the aluminium-rich primary phase.

The well-known deleterious influence of impurities in aluminium casting alloys is thus twofold: not only are impurity-containing intermetallics weak second phases that promote the early onset of internal damage, but they also form stress-concentrating “pinhole” defects that contribute, together with other silicon particle defects found here not to be connected to those impurities, to decrease the silicon particle fracture strength to values below the ideal strength of Si.

Chapter 5 Summary and conclusions

In this Chapter, a summary of the work developed in the previous Chapters is presented in Section 5.1, followed by the statement of the main conclusions of this thesis in Section 5.2.

5.1 Summary

At the time the present project started, the state of the art of micromechanics of two-phase (brittle-ductile) materials included significant progress in modelling the relations between local and global mechanical properties, several existing experimental approaches to measure average phase properties, and an important body of work on the properties of the ductile phase at small scale. There was, however, still a lack of direct assessment of the local fracture properties of the brittle phase in such alloys or composites. This applies specifically to Al-Si-based casting alloys, where the fracture of brittle, microscopic, silicon particles strongly affects the alloys' mechanical properties.

In view of this, the present work focused on:

- developing micromechanical testing techniques to probe the fracture toughness and the local strength of hard, brittle, particulate, second phases in alloys and composite materials; and
- studying, notably using those techniques, the local fracture properties of eutectic silicon particles that constitute the main second phase in Al-Si alloys.

To measure fracture toughness at the micron-scale, a *microscopic chevron notch fracture toughness test* was developed using two benchmark materials, namely a bulk sample of fused quartz, whose fracture toughness is well-documented in the literature and thus enabled checking the accuracy of the novel method, and nanocrystalline alumina fibres 12 μm in diameter, which are material samples that are closer (but simpler) than reinforcing particles such as silicon particles in Al-Si alloys.

The chevron notch test has a fundamental advantage over common existing methods that use a pre-notch to simulate a sharp crack. Namely, fracture toughness is measured on an actual (sharp) crack: by virtue of the geometry of the chevron notch, a crack is first initiated and then undergoes stable growth before reaching the point of instability (in a valid test).

A main experimental challenge was shown to be the proper micromachining of a sufficiently thin and sharp notch that would enable crack initiation at applied loads low enough to allow for subsequent stable crack growth. Indeed, preliminary attempts to measure the fracture toughness of eutectic plate-like silicon particles that were extracted from an Al-Si alloy were unsuccessful because stable crack initiation could not be achieved. This problem was also consistently encountered in tests on material from a single crystalline silicon wafer. In this material, after trying many different approaches to initiate a stable crack in the chevron-notched samples, a fairly effective but tedious work-around was found. It consisted in applying small, cyclic, elastic deformation to the cantilever with a micromanipulator in the SEM/FIB

apparatus before the actual mechanical test in the nanoindenter. The specific mechanism by which this promotes crack initiation at the notch at relatively low loads could not be positively determined.

In this way, a limited number of valid microscopic chevron notch tests on single crystalline silicon wafer could be produced. Results indicate that stable crack growth in the (111) fracture plane of silicon can proceed as a series of erratic crack extension and crack arrest events. Consecutive crack extension episodes, which provide measurements of the material fracture toughness, are found not to necessarily occur at a constant critical strain energy release rate value.

The proposed responsible mechanism for this complex crack growth behaviour is the presence of limited (but finite), stochastic, dislocation activity at the crack tip, producing varying levels of crack tip shielding. This is also consistent with the fact that fracture energy values of the (111) fracture plane of silicon, measured here and also in the literature, are typically over and above the expected value in a perfectly brittle material, of twice the surface energy.

To measure local strength, a microscopic 3-point bending technique was developed and used to probe coarsened, plate-like, eutectic silicon particles extracted from a heat-treated Al-12.6Si alloy. Using a trapezoidal cross section beam design and by virtue of the specific way in which specimens are prepared, the particle surface subjected to tension upon testing is free from FIB damage even though FIB-milling is used in sample preparation. From the measured fracture force, particle strength can be calculated using two possible approaches: bespoke finite element modelling, and an analytical expression from simple beam theory.

An alternative microscopic local strength test method was also developed and used to probe eutectic silicon particles protruding from the surface of a deep-etched sample of heat-treated Al-7Si-Mg (A356) alloy. Most tested particles were beforehand micromachined into a *C-shape* using FIB-milling. Tests were run *in-situ* within an SEM using an instrumented needle to deform individual particles, which produces tensile stress states that eventually lead to fracture along a particle surface region that is free from ion beam-induced artefacts.

Strength results from those two tests show that the measured values depend strongly on the presence or absence of certain surface defects (which have been identified in this thesis), as follows.

In the case of silicon plate-like eutectic particles without visible defects on their probed surface, local strength values up to 9 GPa for probed effective surface area of $\sim 7 \mu\text{m}^2$ were measured using the microscopic 3-point bending method on particles extracted from a heat-treated Al-12.6Si alloy. Moreover, particles roughly 10 times smaller of a heat-treated A356 alloy tested *in-situ* in an SEM resulted in similar strength values in the range 7 – 16 GPa along defect-free surfaces.

Such high strength values, which approach silicon's theoretical strength and are comparable to strength measurements reported in the literature on ultra-pure silicon samples of similar size shaped using lithographic techniques, had not been reported before for silicon particles within Al-Si alloys.

In contrast, significantly lower local strength values are measured on particles that feature visible surface defects. The main strength-limiting defects on silicon particles were identified as:

- surface grooves, typically at interfaces between two silicon crystals, and
- surface *pinholes*.

Other, less detrimental, defects identified were:

- surface steps,
- shallow grooves or ridges produced by twin boundaries at particle edges, and
- surface burrs.

These observations are in agreement with SEM examinations of the fracture surfaces of silicon particles within Al-Si samples deformed macroscopically in tension. Here, visible particle surface defects were frequently observed to be crack initiation sites.

Finally, a study using FIB-milling cross-sectioning coupled with EDX analyses on silicon particles within Al-Si showed that:

- *Pinholes*, as well as internal cavities, are filled with an intermetallic phase and are thus connected to the presence of alloy impurities, namely Fe and Ti.
- In contrast, no intermetallic phases were detected in surface grooves and around surface steps, hence their occurrence is likely a consequence of particle growth and coarsening.
- Surface burrs are produced upon heat treatment at the point where a α -Al grain boundary meets a silicon particle.

5.2 General conclusions

- The chevron notch fracture toughness test is extended to the microscale. The main advantage over existing microfracture methods is that it probes the material's resistance to the growth of a real, sharp, crack.
- This test method, which was successfully demonstrated on two benchmark materials, is inconvenient to probe silicon because early crack initiation and stable crack growth are difficult to achieve in this specific material.
- Two novel techniques are exposed towards measuring the local strength of silicon particles within heat-treated Al-Si alloys, namely a microscopic 3-point bending test, and an *in-situ C-shape* test.
- Most silicon particles in the studied Al-Si alloys feature visible surface defects, some of which strongly decrease particle strength.
- The most deleterious defects, i.e. surface grooves produced at interfaces between two silicon crystals, are most probably related to particle growth and coarsening mechanisms. On the other hand, *pinhole* defects are caused by the presence of alloy impurities, namely Fe and Ti.
- Defect-free particles within Al-Si can be as strong as ultra-pure silicon at the microscale, and approach the theoretical strength of Si, reflecting the true potential of silicon particles as reinforcements in Al-Si alloys if particle strength-limiting defects identified in this work can be suppressed.

Chapter 6 Outlook

This brief perspective of the work presented in this thesis will consider methods- and material-related aspects separately in the following paragraphs.

In the author's viewpoint, future developments on small-scale fracture toughness testing should stick to the concept that crack growth resistance must be measured on *real* cracks. Even though achieving this at microscopic scale is a substantial challenge compared to testing pre-notched samples, the methodology developed here (i.e. the miniature chevron notch test) is an example of the fact that it can be accomplished even in brittle materials. It would be interesting to explore other more effective and convenient ways to achieve this. In particular, strategies to ease crack initiation at low loads should be developed. These could be based on probing more stable structures such as clamped bending beams, for example. In this line, a design using the chevron notch approach in bowtie-shaped clamped beams was published very recently [248]. Alternatively, new micromachining technologies and/or methods may become available by which less damage and a sharper apex at the chevron notch could be produced.

Regarding the fracture toughness of silicon second-phase particles in Al-Si alloys, a measurement thereof would be valuable because this property is sometimes used in micromechanical modelling. Values that are considered are typically those measured on ultra-pure single crystalline silicon; however, silicon particles in alloys are known not to be that pure (e.g., they can contain aluminium nanoprecipitates, see Figure 2.23). Unfortunately, the present work was not able to give a fracture toughness measurement of silicon particles. In principle, the crack-initiation work-around used to probe single crystalline silicon wafer (Section 3.3) could be applied to produce fracture toughness measurements of silicon particles following a procedure such as in Section 3.2. This was not done in this work simply due to resources limitations (time and SEM/FIB accessibility). Priority was given to the investigation of particle strength rather than to fracture toughness measurements because the former is a property that can be improved significantly by metallurgical processes (aiming at avoiding particle defects) whereas less can *a priori* be done to enhance the Si particle fracture toughness.

Micromechanical strength testing of brittle second-phases in alloys or reinforcing phases in composites will likely be an active topic in the following years, driven by enabling technologies and techniques that become increasingly available. In this sense, the main idea of the microscopic *C-shape* test, which is to produce bending in a pristine volume of material upon the application of a compressive force (inspired from a macroscopic test developed for ceramic bearings [348]), can be readily exploited on many other particles or short fibres used as reinforcement in metal matrix composites (e.g., Al_2O_3 , SiC or B_4C ; in fact, the present work on *C-shape* testing of Si particles was conducted in parallel with the thesis of my colleague Vaclav Pejchal, who developed an alternative version of this test to measure the strength of alumina reinforcements [441]). Appropriate techniques to characterize the strength of microscopic particles depend on the specific shape of the particles. For example, to probe platelets, the microscopic 3-point bending test developed here is appropriate (if possible done in an SEM to ease alignment) and has

been already applied elsewhere recently in the literature [442]. Awareness of the deleterious effect on strength of stress-concentrating defects shall also be of interest to developments in processing routes.

A main conclusion of this thesis is that an objective of future alloy development of coarsened Al-Si alloys could be the avoidance of silicon particle strength-limiting defects that were here identified. This would delay the onset of particle fracture and hence enhance the strength and ductility of this important class of alloys. To avoid pinhole defects, it was shown here that a high purity composition is required. This, unfortunately, is cost-prohibitive for most industrial applications. Efforts should therefore rather be focused on avoiding the most deleterious defects, which are particle-particle interfaces and other particle surface grooves. This is a challenging undertaking because these defects seem to be produced on precipitated particles no matter the alloy cooling rate and heat treatment. Indeed, in side-excursions done in the context of this thesis, the presence of defects was observed even in the two following extreme cases: in melt spun Al-Si ribbon (i.e. very high solidification rate) subjected to only a few minutes of heat treatment, and in alloys solidified very slowly in a furnace. It was also observed that defects do not disappear after extremely long heat treatments (several weeks).

To tackle this challenge, the mechanisms by which these type of strength-limiting particle defects occur need first to be better understood. One could pursue the idea of finding alloying elements that discourage the merging of growing silicon crystals, for example by affecting the energetics of the Si/Al interfacial or Si/Si grain boundary energies. On the other hand, if the formation of these particle defects cannot be avoided, an alternative line of research could be based on exploring ways of fracturing the weak particles into separated, stronger, particles during processing, healing afterwards the crack formed between the two. To achieve this, a potential approach could be stirring (i.e. shearing) vigorously the alloy in semi-solid (*mushy*) state, as is done in semi-solid metal casting processes (e.g., rheocasting and thixocasting). These processes, which are applied to alloys with compositions having a solidification temperature range (i.e. a solid-liquid region in the phase diagram), break up the dendrites of the primary phase and hence lead to more globular and homogeneous microstructures. Although in principle this approach seems unsuitable to break up the eutectic silicon phase too, claims have been made that also Al-Si alloys of eutectic composition can be rheocast [460] and eutectic silicon fragmentation has been reported on a rheocast hypereutectic Al-Si alloy [461].

Alternatively, it could be envisaged to fracture intentionally the weakest eutectic particles within the alloy in the solid state (i.e. after casting). This might be achieved using, for example, a powerful ultrasound horn to produce strong vibrations, which would produce periods of tensile stress within the particles that shall be high enough to produce particle fracture at particle stress concentration sites. Such an approach would require a subsequent step, namely the healing of the damage by filling with aluminium the cracks formed due to particle fracture, which may potentially be achieved through heat treatment. Incidentally, note that ultrasonic treatments on Al-Si alloys have been the subject of past research efforts, where its use was to treat the melts with the objective of obtaining finer microstructures. To the author's best knowledge, there are no reported works in the literature that explore the above-described idea of using a strong ultrasonic horn on solidified alloys to deliberately introduce damage on weak spots that could subsequently be healed resulting in an alloy with enhanced mechanical properties.

References

- [1] Aluminium in cars: Unlocking the light-weighting potential, European Aluminum Association, 2012.
- [2] Aluminium in cars, European Aluminum Association, 2007.
- [3] 2015 North American Light Vehicle Aluminum Content Study, Ducker Worldwide, 2014.
- [4] V.S. Zolotarevsky, N.A. Belov, M.V. Glazoff, Casting Aluminum Alloys, Elsevier, Oxford, 2007.
- [5] S. Otarawanna, A.K. Dahle, 6 - Casting of aluminium alloys, in: R. Lumley (Ed.), Fundamentals of Aluminium Metallurgy, Woodhead Publishing, 2011: pp. 141–154. doi:10.1533/9780857090256.1.141.
- [6] J. Hannagan, Global aluminium industry overview, (2014).
- [7] Industry Statistics (November 2016 Report), The Aluminium Association, 2016.
- [8] D.R. Lide, CRC Handbook of Chemistry and Physics, 84th Edition, CRC Press, 2003.
- [9] J.G. Kaufman, E.L. Rooy, Aluminum Alloy Castings: Properties, Processes And Applications, illustrated edition, ASM International, 2004.
- [10] S. Li, D. Apelian, Hot Tearing of Aluminum Alloys, Inter Metalcast. 5 (2011) 23–40. doi:10.1007/BF03355505.
- [11] M. Lebyodkin, A. Deschamps, Y. Bréchet, Influence of second-phase morphology and topology on mechanical and fracture properties of Al-Si alloys, Materials Science and Engineering A. 234–236 (1997) 481–484.
- [12] Q.G. Wang, C.H. Cáceres, The fracture mode in Al-Si-Mg casting alloys, Materials Science and Engineering: A. 241 (1998) 72–82. doi:10.1016/S0921-5093(97)00476-0.
- [13] C.H. Cáceres, J.R. Griffiths, Damage by the cracking of silicon particles in an Al-7Si-0.4Mg casting alloy, Acta Mater. 44 (1996) 25–33.
- [14] A. Mocellin, Y. Brechet, R. Fougères, Fracture of an Osprey™ AlSiFe alloy: A microstructure based model for fracture of microheterogeneous materials, Acta Metallurgica et Materialia. 43 (1995) 1135–1140. doi:10.1016/0956-7151(94)00327-E.
- [15] G. Guiglionda, W.J. Poole, The role of damage on the deformation and fracture of Al-Si eutectic alloys, Materials Science and Engineering: A. 336 (2002) 159–169. doi:10.1016/S0921-5093(01)01971-2.
- [16] R. Doglione, J.L. Douziech, C. Berdin, D. François, Tensile damage stages in cast A356-T6 aluminium alloy, Mater. Sci. Technol. 18 (2002) 554–562. doi:10.1179/026708302225001660.
- [17] M. Warmuzek, Aluminum-Silicon Casting Alloys: Atlas of Microfractographs, 2004.
- [18] H. Mae, X. Teng, Y. Bai, T. Wierzbicki, Comparison of ductile fracture properties of aluminum castings: Sand mold vs. metal mold, International Journal of Solids and Structures. 45 (2008) 1430–1444. doi:10.1016/j.ijsolstr.2007.10.016.
- [19] R. Doglione, In Situ Investigations on the Ductility of an Al-Si-Mg Casting Alloy, JOM. 64 (2012) 51–57. doi:10.1007/s11837-011-0231-y.
- [20] L. Zeng, J. Sakamoto, A. Fujii, H. Noguchi, Role of eutectic silicon particles in fatigue crack initiation and propagation and fatigue strength characteristics of cast aluminum alloy A356, Engineering Fracture Mechanics. 115 (2014) 1–12. doi:10.1016/j.engfrac-mech.2013.11.016.

- [21] M. Javidani, D. Larouche, Application of cast Al-Si alloys in internal combustion engine components, *International Materials Reviews*. 59 (2014) 132–158. doi:10.1179/1743280413Y.0000000027.
- [22] Z. Chen, X. Hao, Y. Wang, K. Zhao, In-situ Observation of Tensile Fracture in A357 Casting Alloys, *Journal of Materials Science & Technology*. 30 (2014) 139–145. doi:10.1016/j.jmst.2013.04.014.
- [23] N.D. Alexopoulos, M. Tiriyakiog˘lu, A.N. Vasilakos, S.K. Kourkoulis, The effect of Cu, Ag, Sm and Sr additions on the statistical distributions of Si particles and tensile properties in A357–T6 alloy castings, *Materials Science and Engineering: A*. 604 (2014) 40–45. doi:10.1016/j.msea.2014.02.084.
- [24] Z. Asghar, G. Requena, Three dimensional post-mortem study of damage after compression of cast Al-Si alloys, *Materials Science and Engineering: A*. 591 (2014) 136–143. doi:10.1016/j.msea.2013.10.067.
- [25] S. Joseph, S. Kumar, V.S. Bhadram, C. Narayana, Stress states in individual Si particles of a cast Al-Si alloy: Micro-Raman analysis and microstructure based modeling, *Journal of Alloys and Compounds*. 625 (2015) 296–308. doi:10.1016/j.jallcom.2014.10.207.
- [26] M. Karbalaee Akbari, H.R. Baharvandi, K. Shirvanimoghaddam, Tensile and fracture behavior of nano/micro TiB₂ particle reinforced casting A356 aluminum alloy composites, *Materials & Design*. 66, Part A (2015) 150–161. doi:10.1016/j.matdes.2014.10.048.
- [27] D.K. Ward, W.A. Curtin, Y. Qi, Aluminum–silicon interfaces and nanocomposites: A molecular dynamics study, *Composites Science and Technology*. 66 (2006) 1151–1161. doi:10.1016/j.compscitech.2005.10.024.
- [28] K. Gall, N. Yang, M. Horstemeyer, D.L. McDowell, J. Fan, The debonding and fracture of Si particles during the fatigue of a cast Al-Si alloy, *Metall and Mat Trans A*. 30 (1999) 3079–3088. doi:10.1007/s11661-999-0218-2.
- [29] S. Joseph, S. Kumar, A systematic investigation of fracture mechanisms in Al-Si based eutectic alloy—Effect of Si modification, *Materials Science and Engineering: A*. 588 (2013) 111–124. doi:10.1016/j.msea.2013.09.019.
- [30] S. Dezecot, M. Brochu, Microstructural characterization and high cycle fatigue behavior of investment cast A357 aluminum alloy, *International Journal of Fatigue*. 77 (2015) 154–159. doi:10.1016/j.ijfatigue.2015.03.004.
- [31] C. Nayhumwa, N.R. Green, J. Campbell, Influence of casting technique and hot isostatic pressing on the fatigue of an Al-7Si-Mg alloy, *Metall and Mat Trans A*. 32 (2001) 349–358. doi:10.1007/s11661-001-0266-8.
- [32] J.M. Boileau, J.E. Allison, The effect of solidification time and heat treatment on the fatigue properties of a cast 319 aluminum alloy, *Metall and Mat Trans A*. 34 (2003) 1807–1820. doi:10.1007/s11661-003-0147-4.
- [33] J. Campbell, *Castings*, Second Edition, 2 edition, Butterworth-Heinemann, Amsterdam, 2003.
- [34] N.D. Alexopoulos, M. Tiriyakiog˘lu, A.N. Vasilakos, S.K. Kourkoulis, The effect of Cu, Ag, Sm and Sr additions on the statistical distributions of Si particles and tensile properties in A357–T6 alloy castings, *Materials Science and Engineering: A*. 604 (2014) 40–45. doi:10.1016/j.msea.2014.02.084.
- [35] N. Chawla, K.K. Chawla, *Metal Matrix Composites*, Springer, 2006.
- [36] A. Mortensen, J. Llorca, Metal matrix composites, *Annual Review of Materials Research*. 40 (2010).
- [37] D.S. Wilkinson, W. Pompe, M. Oeschner, Modeling the mechanical behaviour of heterogeneous multi-phase materials, *Progress in Materials Science*. 46 (2001) 379–405. doi:10.1016/S0079-6425(00)00008-6.

- [38] J.L. Chaboche, P. Kanouté, A. Roos, On the capabilities of mean-field approaches for the description of plasticity in metal matrix composites, *International Journal of Plasticity*. 21 (2005) 1409–1434. doi:10.1016/j.ijplas.2004.07.001.
- [39] R.W. Coade, J.R. Griffiths, B.A. Parker, P.J. Stevens, Inclusion stresses in a two-phase alloy deformed to a plastic strain of 1%, *Philosophical Magazine A*. 44 (1981) 357–372. doi:10.1080/01418618108239538.
- [40] T.R. Finlayson, J.R. Griffiths, D.M. Viano, M.E. Fitzpatrick, E.C. Oliver, Q.G. Wang, Stresses in the eutectic silicon particles of strontium-modified A356 castings loaded in tension, in: P.N. Crepeau, M. Tiryakioglu, J. Campbell (Eds.), *Shape Casting: The 2nd International Symposium*, Minerals, Metals & Materials Society, Warrendale, 2007: pp. 127–134.
- [41] M.T. Kiser, F.W. Zok, D.S. Wilkinson, Plastic flow and fracture of a particulate metal matrix composite, *Acta Materialia*. 44 (1996) 3465–3476. doi:10.1016/1359-6454(96)00028-6.
- [42] Q.G. Wang, C.H. Caceres, J.R. Griffiths, Damage by eutectic particle cracking in aluminum casting alloys A356/357, *Metall and Mat Trans A*. 34 (2003) 2901–2912. doi:10.1007/s11661-003-0190-1.
- [43] S. Nishido, M. Kaneso, T. Kobayashi, H. Toda, Role of Si particle damage on fatigue characteristics of cast Al–Si alloys, *International Journal of Cast Metals Research*. 17 (2004) 345–350. doi:10.1179/136404604225022702.
- [44] G. Huber, Y. Brechet, T. Pardoen, Predictive model for void nucleation and void growth controlled ductility in quasi-eutectic cast aluminium alloys, *Acta Materialia*. 53 (2005) 2739–2749. doi:10.1016/j.actamat.2005.02.037.
- [45] A.R. Riahi, A.T. Alpas, Fracture of silicon-rich particles during sliding contact of Al–Si alloys, *Materials Science and Engineering A*. 441 (2006) 326–330.
- [46] S.M.-M. Dubois, G.-M. Rignanese, T. Pardoen, J.-C. Charlier, Ideal strength of silicon: An ab initio study, *Phys. Rev. B*. 74 (2006) 235203. doi:10.1103/PhysRevB.74.235203.
- [47] Q.G. Wang, Microstructural effects on the tensile and fracture behavior of aluminum casting alloys A356/357, *Metall and Mat Trans A*. 34 (2003) 2887–2899. doi:10.1007/s11661-003-0189-7.
- [48] J. Campbell, Entrainment defects, *Mater. Sci. Technol.* 22 (2006) 127–145. doi:10.1179/174328406X74248.
- [49] J. Knott, Commentaries on “Entrainment defects” by J. Campbell, *Mater. Sci. Technol.* 22 (2006) 999–1008. doi:10.1179/174328406X109221.
- [50] S.J. Harris, A. O’Neill, J. Boileau, W. Donlon, X. Su, B.S. Majumdar, Application of the Raman technique to measure stress states in individual Si particles in a cast Al–Si alloy, *Acta Mater.* 55 (2007) 1681–1693. doi:10.1016/j.actamat.2006.10.028.
- [51] J. Campbell, Cavitation During Superplastic Forming, *Materials*. 4 (2011) 1271–1286. doi:10.3390/ma4071271.
- [52] S. Groh, B. Devincere, L.P. Kubin, A. Roos, F. Feyel, J.-L. Chaboche, Size effects in metal matrix composites, *Materials Science and Engineering: A*. 400–401 (2005) 279–282. doi:10.1016/j.msea.2005.03.062.
- [53] O. Kraft, P.A. Gruber, R. Mönig, D. Weygand, Plasticity in Confined Dimensions, *Annual Review of Materials Research*. 40 (2010) 293–317.
- [54] J.A. El-Awady, Unravelling the physics of size-dependent dislocation-mediated plasticity, *Nature Communications*. 6 (2015) 5926. doi:10.1038/ncomms6926.
- [55] R. Mueller, A. Rossoll, L. Weber, M.A.M. Bourke, D.C. Dunand, A. Mortensen, Tensile flow stress of ceramic particle-reinforced metal in the presence of particle cracking, *Acta Materialia*. 56 (2008) 4402–4416.

- [56] M. Slámová, Y. Bréchet, C. Verdu, R. Fougères, F. Louchet, Al-Si Alloys as a Model System for Damage Accumulation in Composite Materials, *Physica Status Solidi (a)*. 168 (1998) 117–127. doi:10.1002/(SICI)1521-396X(199807)168:1<117::AID-PSSA117>3.0.CO;2-X.
- [57] J.-Y. Buffière, E. Maire, P. Cloetens, G. Lormand, R. Fougères, Characterization of internal damage in a MMCp using X-ray synchrotron phase contrast microtomography, *Acta Materialia*. 47 (1999) 1613–1625. doi:10.1016/S1359-6454(99)00024-5.
- [58] Y. Rozenblat, D. Portnikov, A. Levy, H. Kalman, S. Aman, J. Tomas, Strength distribution of particles under compression, *Powder Technology*. 208 (2011) 215–224. doi:10.1016/j.powtec.2010.12.023.
- [59] C. Couroyer, M. Ghadiri, P. Laval, N. Brunard, F. Kolenda, Methodology for Investigating the Mechanical Strength of Reforming Catalyst Beads, *Oil & Gas Science and Technology - Rev. IFP*. 55 (2000) 67–85. doi:10.2516/ogst:2000004.
- [60] C. Subero-Couroyer, M. Ghadiri, N. Brunard, F. Kolenda, Analysis of catalyst particle strength by impact testing: The effect of manufacturing process parameters on the particle strength, *Powder Technology*. 160 (2005) 67–80. doi:10.1016/j.powtec.2005.08.005.
- [61] ASTM D4179 – 11 Standard Test Method for Single Pellet Crush Strength of Formed Catalysts and Catalyst Carriers, 2011.
- [62] M. Yoshida, H. Ogiso, S. Nakano, J. Akedo, Compression test system for a single submicrometer particle, *Review of Scientific Instruments*. 76 (2005) 093905. doi:10.1063/1.2038187.
- [63] S. Zhao, Y. Gan, M. Kamlah, T. Kennerknecht, R. Rolli, Influence of plate material on the contact strength of Li₄SiO₄ pebbles in crush tests and evaluation of the contact strength in pebble-pebble contact, *Engineering Fracture Mechanics*. (2012). doi:10.1016/j.engfracmech.2012.05.011.
- [64] S. Antonyuk, S. Heinrich, J. Tomas, N.G. Deen, M.S. van Buijtenen, J. a M. Kuipers, Energy absorption during compression and impact of dry elastic-plastic spherical granules, *Granular Matter*. 12 (2010) 15–47. doi:10.1007/s10035-009-0161-3.
- [65] T. Namazu, Y. Isono, T. Tanaka, Evaluation of size effect on mechanical properties of single crystal silicon by nanoscale bending test using AFM, *J. Microelectromech. Syst.* 9 (2000) 450–459. doi:10.1109/84.896765.
- [66] A.M. Fitzgerald, D.M. Pierce, B.M. Huigens, C.D. White, A General Methodology to Predict the Reliability of Single-Crystal Silicon MEMS Devices, *Journal of Microelectromechanical Systems*. 18 (2009) 962–970. doi:10.1109/JMEMS.2009.2020467.
- [67] C. Eberl, X. Wang, D.S. Gianola, T.D. Nguyen, M.Y. He, A.G. Evans, K.J. Hemker, In Situ Measurement of the Toughness of the Interface Between a Thermal Barrier Coating and a Ni Alloy, *J. Am. Ceram. Soc.* 94 (2011) s120–s127. doi:10.1111/j.1551-2916.2011.04588.x.
- [68] S. Zhang, X. Zhang, Toughness evaluation of hard coatings and thin films, *Thin Solid Films*. 520 (2012) 2375–2389. doi:10.1016/j.tsf.2011.09.036.
- [69] A. Loganathan, A.S. Gandhi, Toughness evolution in Gd- and Y-stabilized zirconia thermal barrier materials upon high-temperature exposure, *J Mater Sci.* 52 (2017) 7199–7206. doi:10.1007/s10853-017-0956-2.
- [70] M.T. Lessmann, A. Calvo, C.D. Hardie, M. Porton, N. Ordás, C. García-Rosales, P.M. Mumery, Fracture strength testing of a self-passivating tungsten alloy at the micrometre scale, *Philosophical Magazine*. 96 (2016) 3570–3585. doi:10.1080/14786435.2016.1177229.
- [71] Global passenger vehicle standards, The International Council on Clean Transportation. (n.d.). <http://www.theicct.org/global-pv-standards-chart-library> (accessed March 3, 2017).

- [72] Ford launches plasma-sprayed cylinder bores on 2011 Shelby V8 - SAE International, (n.d.). <http://articles.sae.org/7624/> (accessed April 21, 2017).
- [73] Superior Industries Inc - OEM Aluminum Wheel Manufacturer, (n.d.). <http://www.supind.com/> (accessed April 21, 2017).
- [74] Aluminium pistons of the highest quality, (n.d.). <http://www.almet-pistons.com/aluminium-pistons/> (accessed April 21, 2017).
- [75] Rhino VW Aluminum Transmission Case - DRE-301111, (n.d.). <https://dunebuggywarehouse.com/rhino-vw-aluminum-transmission-case-ac301111.html> (accessed April 21, 2017).
- [76] L. Pedersen, L. Arnberg, The effect of solution heat treatment and quenching rates on mechanical properties and microstructures in AlSiMg foundry alloys, *Metall and Mat Trans A*. 32 (2001) 525–532. doi:10.1007/s11661-001-0069-y.
- [77] J.R. Davis, *ASM Speciality Handbook - Aluminium and Aluminum Alloys (some parts only)*, ASM International, 1993.
- [78] L.F. Mondolfo, *Aluminum alloys: structure and properties*, Butterworths, 1976.
- [79] I.L.S. C. H. Caceres, Strength-ductility behaviour of Al-Si-Cu-Mg casting alloys in T6 temper, *International Journal of Cast Metals Research*. 15 (2003).
- [80] R. Lumley, ed., *Fundamentals of Aluminium Metallurgy: Production, Processing and Applications*, Elsevier, 2010.
- [81] S. Otarawanna, A.K. Dahle, 6 - Casting of aluminium alloys, in: R. Lumley (Ed.), *Fundamentals of Aluminium Metallurgy*, Woodhead Publishing, 2011: pp. 141–154.
- [82] J.L. Murray, A.J. McAlister, The Al-Si (Aluminum-Silicon) system, *Bulletin of Alloy Phase Diagrams*. 5 (1984) 74. doi:10.1007/BF02868729.
- [83] S.R. Wang, Y.Z. Wang, L.Y. Yang, R. Ma, Y. Wang, Solute Redistribution Resulting in Growth of Primary Silicon in Cast Hypoeutectic Al-Si Alloys, *Applied Mechanics and Materials*. 121–126 (2011) 367–371. doi:10.4028/www.scientific.net/AMM.121-126.367.
- [84] J.H. Li, X.D. Wang, T.H. Ludwig, Y. Tsunekawa, L. Arnberg, J.Z. Jiang, P. Schumacher, Modification of eutectic Si in Al-Si alloys with Eu addition, *Acta Materialia*. 84 (2015) 153–163. doi:10.1016/j.actamat.2014.10.064.
- [85] C. Caceres, C. Davidson, J. Griffiths, The Deformation and Fracture-Behavior of an Al-Si-Mg Casting Alloy, *Mater. Sci. Eng. A-Struct. Mater. Prop. Microstruct. Process.* 197 (1995) 171–179. doi:10.1016/0921-5093(94)09775-5.
- [86] C.H. Caceres, C.J. Davidson, J.R. Griffiths, Q.G. Wang, The effect of Mg on the microstructure and mechanical behavior of Al-Si-Mg casting alloys, *Metallurgical and Materials Transactions A*. 30 (1999) 2611–2618. doi:10.1007/s11661-999-0301-8.
- [87] E. Ogris, A. Wahlen, H. Lüchinger, P.J. Uggowitzer, On the silicon spheroidization in Al-Si alloys, *Journal of Light Metals*. 2 (2002) 263–269.
- [88] M. Haghshenas, A. Zarei-Hanzaki, H. Sabetghadam, The room temperature mechanical properties of a thermo-mechanically processed Thixocast A356 aluminum alloy, *Journal of Alloys and Compounds*. 477 (2009) 250–255. doi:10.1016/j.jallcom.2008.10.090.
- [89] S.K. Shaha, F. Czerwinski, W. Kasprzak, J. Friedman, D.L. Chen, Improving High-Temperature Tensile and Low-Cycle Fatigue Behavior of Al-Si-Cu-Mg Alloys Through Micro-additions of Ti, V, and Zr, *Metall and Mat Trans A*. 46 (2015) 3063–3078. doi:10.1007/s11661-015-2880-x.
- [90] M.G. Day, A. Hellawell, Microstructure and Crystallography of Aluminium-Silicon Eutectic Alloys, *Proceedings of the Royal Society of London Series a-Mathematical and Physical Sciences*. 305 (1968) 473–491. doi:10.1098/rspa.1968.0128.
- [91] S. Lu, A. Hellawell, Growth Mechanisms of Silicon in Al-Si Alloys, *J. Cryst. Growth*. 73 (1985) 316–328. doi:10.1016/0022-0248(85)90308-2.

- [92] G.K. Sigworth, The Modification of Al-Si Casting Alloys: Important Practical and Theoretical Aspects, *Int. J. Met.* 2 (2008) 19–41.
- [93] F. Lasagni, A. Lasagni, E. Marks, C. Holzapfel, F. Mücklich, H.P. Degischer, Three-dimensional characterization of “as-cast” and solution-treated AlSi12(Sr) alloys by high-resolution FIB tomography, *Acta Materialia*. 55 (2007) 3875–3882. doi:10.1016/j.actamat.2007.03.004.
- [94] X. Liu, Y. Zhang, B. Beausir, F. Liu, C. Esling, F. Yu, X. Zhao, L. Zuo, Twin-controlled growth of eutectic Si in unmodified and Sr-modified Al–12.7%Si alloys investigated by SEM/EBSD, *Acta Materialia*. 97 (2015) 338–347. doi:10.1016/j.actamat.2015.06.041.
- [95] R.-Y. Wang, W.-H. Lu, L.M. Hogan, Twin related silicon crystals in Al-Si alloys and their growth mechanism, *Materials Science and Technology*. 11 (1995) 441–449.
- [96] R.Y. Wang, W.H. Li, L.M. Hogan, Faceted growth of silicon crystals in Al-Si alloys, *Metall. Mater. Trans. A-Phys. Metall. Mater. Sci.* 28 (1997) 1233–1243. doi:10.1007/s11661-997-0289-x.
- [97] O. Atasoy, F. Yilmaz, R. Elliott, Growth Structures in Aluminum Silicon Alloys .1. the Coupled Zone, *J. Cryst. Growth*. 66 (1984) 137–146. doi:10.1016/0022-0248(84)90084-8.
- [98] C.L. Xu, Q.C. Jiang, Morphologies of primary silicon in hypereutectic Al-Si alloys with melt overheating temperature and cooling rate, *Materials Science and Engineering A*. 437 (2006) 451–455. doi:10.1016/j.msea.2006.07.088.
- [99] C.L. Xu, H.Y. Wang, C. Liu, Q.C. Jiang, Growth of octahedral primary silicon in cast hypereutectic Al-Si alloys, *Journal of Crystal Growth*. 291 (2006) 540–547. doi:10.1016/j.jcrysgro.2006.03.044.
- [100] K. Kobayashi, L. Hogan, The Crystal-Growth of Silicon in Al-Si Alloys, *J. Mater. Sci.* 20 (1985) 1961–1975. doi:10.1007/BF01112278.
- [101] M. Shamsuzzoha, L.M. Hogan, Crystal morphology of unmodified aluminium-silicon eutectic microstructures, *Journal of Crystal Growth*. 76 (1986) 429–439. doi:10.1016/0022-0248(86)90390-8.
- [102] K. Fujiwara, K. Maeda, N. Usami, K. Nakajima, Growth Mechanism of Si-Faceted Dendrites, *Phys. Rev. Lett.* 101 (2008) 055503. doi:10.1103/PhysRevLett.101.055503.
- [103] A. Mazahery, M.O. Shabani, Modification Mechanism and Microstructural Characteristics of Eutectic Si in Casting Al-Si Alloys: A Review on Experimental and Numerical Studies, *JOM*. 66 (2014) 726–738. doi:10.1007/s11837-014-0968-1.
- [104] S.-Z. Lu, A. Hellawell, The mechanism of silicon modification in aluminum-silicon alloys: Impurity induced twinning, *Metallurgical Transactions A*. 18 (1987) 1721–1733.
- [105] M. Shamsuzzoha, L.M. Hogan, D.J. Smith, P.A. Deymier, A transmission and high-resolution electron microscope study of cozonally twinned growth of eutectic silicon in unmodified Al-Si alloys, *Journal of Crystal Growth*. 112 (1991) 635–643. doi:10.1016/0022-0248(91)90119-P.
- [106] S. Lu, A. Hellawell, Growth Mechanisms of Silicon in Al-Si Alloys, *J. Cryst. Growth*. 73 (1985) 316–328. doi:10.1016/0022-0248(85)90308-2.
- [107] T.H. Ludwig, P.L. Schaffer, L. Arnberg, Influence of Phosphorus on the Nucleation of Eutectic Silicon in Al-Si Alloys, *Metall and Mat Trans A*. 44 (2013) 5796–5805. doi:10.1007/s11661-013-1945-y.
- [108] K. Nogita, S.D. McDonald, K. Tsujimoto, K. Yasuda, A.K. Dahle, Aluminium phosphide as a eutectic grain nucleus in hypoeutectic Al-Si alloys, *Journal of Electron Microscopy*. 53 (2004) 361–369.

- [109] C.R. Ho, B. Cantor, Heterogeneous nucleation of solidification of Si in Al-Si and Al-Si-P alloys, *Acta Metallurgica et Materialia*. 43 (1995) 3231–3246. doi:10.1016/0956-7151(94)00480-6.
- [110] S.D. McDonald, K. Nogita, A.K. Dahle, Eutectic nucleation in Al-Si alloys, *Acta Mater.* 52 (2004) 4273–4280. doi:10.1016/j.actamat.2004.05.043.
- [111] J.H. Li, M.Z. Zarif, M. Albu, B.J. McKay, F. Hofer, P. Schumacher, Nucleation kinetics of entrained eutectic Si in Al–5Si alloys, *Acta Materialia*. 72 (2014) 80–98. doi:10.1016/j.actamat.2014.03.030.
- [112] S. Shankar, Y.W. Riddle, M.M. Makhlof, Nucleation mechanism of the eutectic phases in aluminum-silicon hypoeutectic alloys, *Acta Materialia*. 52 (2004) 4447–4460.
- [113] A.K. Dahle, M. Hillert, Discussion of “Nucleation mechanism of eutectic phases in aluminum-silicon hypoeutectic alloys,” *Metall. Mater. Trans. A-Phys. Metall. Mater. Sci.* 36A (2005) 1612–1613. doi:10.1007/s11661-005-0253-6.
- [114] S. Shankar, Y.W. Riddle, M.M. Makhlof, Discussion of “Nucleation mechanism of eutectic phases in aluminum-silicon hypoeutectic alloys” - Authors’ reply, *Metall. Mater. Trans. A-Phys. Metall. Mater. Sci.* 36A (2005) 1613–1617. doi:10.1007/s11661-005-0254-5.
- [115] A.K. Dahle, M. Hillert, Reply to discussion on “Nucleation mechanism of eutectic phases in aluminum-silicon hypoeutectic alloys,” *Metallurgical and Materials Transactions A: Physical Metallurgy and Materials Science*. 37 (2006) 1353.
- [116] S. Shankar, M.M. Makhlof, Authors’ reply to reply of discussion on “Nucleation mechanism of eutectic phases in aluminum-silicon hypoeutectic alloys,” *Metallurgical and Materials Transactions A: Physical Metallurgy and Materials Science*. 37 (2006) 1353–1356.
- [117] S.-M. Liang, R. Schmid-Fetzer, Nucleants of Eutectic Silicon in Al-Si Hypoeutectic Alloys: β -(Al, Fe, Si) or AlP Phase, *Metall and Mat Trans A*. 45 (2014) 5308–5312. doi:10.1007/s11661-014-2522-8.
- [118] W. Khalifa, F.H. Samuel, J.E. Gruzleski, Iron intermetallic phases in the Al corner of the Al-Si-Fe system, *Metall. Mater. Trans. A-Phys. Metall. Mater. Sci.* 34A (2003) 807–825. doi:10.1007/s11661-003-0116-y.
- [119] S. Nafisi, R. Ghomashchi, H. Vali, Eutectic nucleation in hypoeutectic Al-Si alloys, *Materials Characterization*. 59 (2008) 1466–1473. doi:10.1016/j.matchar.2008.01.014.
- [120] A.K. Dahle, K. Nogita, S.D. McDonald, J.W. Zindel, L.M. Hogan, Eutectic nucleation and growth in hypoeutectic Al-Si alloys at different strontium levels, *Metall and Mat Trans A*. 32 (2001) 949–960. doi:10.1007/s11661-001-0352-y.
- [121] K. Nogita, A.K. Dahle, Eutectic solidification in hypoeutectic Al-Si alloys: electron backscatter diffraction analysis, *Mater. Charact.* 46 (2001) 305–310. doi:10.1016/S1044-5803(00)00109-1.
- [122] J. Campbell, Discussion of “Effect of Strontium and Phosphorus on Eutectic Al-Si Nucleation and Formation of β -Al₅FeSi in Hypoeutectic Al-Si Foundry Alloys”*, *Metall and Mat Trans A*. 40 (2009) 1009–1010. doi:10.1007/s11661-009-9804-6.
- [123] J. Campbell, The Modification of Al-Si Casting Alloys: Important Practical and Theoretical Aspects Reply, *Int. J. Met.* 3 (2009) 71–72.
- [124] G.K. Sigworth, The Modification of Al-Si Casting Alloys: Important Practical and Theoretical Aspects Reply, *Int. J. Met.* 3 (2009) 68–70.
- [125] H. Singh, A.M. Gokhale, A. Tewari, S. Zhang, Y. Mao, Three-dimensional visualization and quantitative characterization of primary silicon particles in an Al–Si base alloy, *Scripta Materialia*. 61 (2009) 441–444. doi:10.1016/j.scriptamat.2009.04.040.
- [126] D.R. Hamilton, R.G. Seidensticker, Propagation Mechanism of Germanium Dendrites, *Journal of Applied Physics*. 31 (1960) 1165–1168. doi:doi:10.1063/1.1735796.

- [127] R. Wagner, On the Growth of Germanium Dendrites, *Acta Metallurgica*. 8 (1960) 57–60. doi:10.1016/0001-6160(60)90145-0.
- [128] K. Fujiwara, H. Fukuda, N. Usami, K. Nakajima, S. Uda, Growth mechanism of the Si $\{110\}$ faceted dendrite, *Phys. Rev. B*. 81 (2010) 224106. doi:10.1103/PhysRevB.81.224106.
- [129] M. Hillert, Discussion of “Eutectic solidification of Al-Si alloys,” *Metall. Mater. Trans. A-Phys. Metall. Mater. Sci.* 34A (2003) 2688–2690. doi:10.1007/s11661-003-0030-3.
- [130] S. Hegde, K.N. Prabhu, Modification of eutectic silicon in Al-Si alloys, *Journal of Materials Science*. 43 (2008) 3009–3027.
- [131] Y.H. Cho, H.-C. Lee, K.H. Oh, A.K. Dahle, Effect of strontium and phosphorus on eutectic Al-Si nucleation and formation of beta-Al(5)FeSi in hypoeutectic Al-Si foundry alloys, *Metall. Mater. Trans. A-Phys. Metall. Mater. Sci.* 39A (2008) 2435–2448. doi:10.1007/s11661-008-9580-8.
- [132] M. Shamsuzzoha, L.M. Hogan, The twinned growth of silicon in chill-modified Al-Si eutectic, *Journal of Crystal Growth*. 82 (1987) 598–610. doi:10.1016/S0022-0248(87)80004-0.
- [133] E. Sjölander, S. Seifeddine, The heat treatment of Al-Si-Cu-Mg casting alloys, *Journal of Materials Processing Technology*. 210 (2010) 1249–1259.
- [134] C.H. Liu, J.H. Chen, C. Li, C.L. Wu, D.Z. Li, Y.Y. Li, Multiple silicon nanotwins formed on the eutectic silicon particles in Al-Si alloys, *Scripta Materialia*. 64 (2011) 339–342. doi:10.1016/j.scriptamat.2010.10.030.
- [135] G. Requena, G. Garcés, S. Danko, T. Pirling, E. Boller, The effect of eutectic Si on the strength of short-fibre-reinforced Al, *Acta Materialia*. 57 (2009) 3199–3210. doi:10.1016/j.actamat.2009.03.030.
- [136] D.L. Zhang, L.H. Zheng, D.H. StJohn, Effect of a short solution treatment time on microstructure and mechanical properties of modified Al-7wt.%Si-0.3wt.%Mg alloy, *Journal of Light Metals*. 2 (2002) 27–36.
- [137] M. Tiryakioğlu, The effect of solution treatment and artificial aging on the work hardening characteristics of a cast Al-7%Si-0.6%Mg alloy, *Materials Science and Engineering: A*. 427 (2006) 154–159. doi:10.1016/j.msea.2006.04.011.
- [138] M. Tiryakioğlu, Si particle size and aspect ratio distributions in an Al-7%Si-0.6%Mg alloy during solution treatment, *Materials Science and Engineering: A*. 473 (2008) 1–6. doi:10.1016/j.msea.2007.03.044.
- [139] W.J. Poole, E.J. Dowdle, Experimental measurements of damage evolution in Al-Si eutectic alloys, *Scripta Materialia*. 39 (1998) 1281–1287. doi:10.1016/S1359-6462(98)00326-1.
- [140] Z. Asghar, G. Requena, H.P. Degischer, P. Cloetens, Three-dimensional study of Ni aluminides in an AlSi12 alloy by means of light optical and synchrotron microtomography, *Acta Materialia*. 57 (2009) 4125–4132. doi:10.1016/j.actamat.2009.05.010.
- [141] G. Sharma, R.V. Ramanujan, G.P. Tiwari, Instability mechanisms in lamellar microstructures, *Acta Mater.* 48 (2000) 875–889. doi:10.1016/S1359-6454(99)00378-X.
- [142] S.J. Andersen, O. Jensrud, I. Johansen, H.J. Roven, R. Høier, Si-particles in an AlNiSiMn alloy, *Micron and Microscopica Acta*. 23 (1992) 135–136. doi:10.1016/0739-6260(92)90105-M.
- [143] W.T. Donlon, Precipitation of aluminum in the silicon phase contained in W319 and 356 aluminum alloys, *Metall. Mater. Trans. A-Phys. Metall. Mater. Sci.* 34 (2003) 523–529. doi:10.1007/s11661-003-0088-y.
- [144] Z.H. Jia, L. Arnberg, P. Åsholt, B. Barlas, T. Iveland, TEM investigations of aluminum precipitate in eutectic Si of A356 based alloys, in: *EMC 2008 14th European Microscopy Congress 1–5 September 2008, Aachen, Germany, Springer, Berlin, Heidelberg, 2008*: pp. 435–436. doi:10.1007/978-3-540-85226-1_218.

- [145] Z.H. Jia, L. Arnberg, S.J. Andersen, J.C. Walmsley, On nanoscale Al precipitates forming in eutectic Si particles in Al–Si–Mg cast alloys, *Scripta Materialia*. 61 (2009) 500–503. doi:10.1016/j.scriptamat.2009.05.009.
- [146] S.C. Hogg, C.J.D. Hetherington, H.V. Atkinson, Aluminium precipitates in the primary silicon of as-sprayformed hypereutectic aluminium-silicon alloys, *Philosophical Magazine Letters*. 80 (2000) 477–482. doi:10.1080/09500830050057170.
- [147] L. Zhang, J. Gao, L.N.W. Damoah, D.G. Robertson, Removal of Iron from Aluminum: A Review, *Miner. Process Extr. Metall. Rev.* 33 (2012) 99–157. doi:10.1080/08827508.2010.542211.
- [148] C.J. Simensen, T.L. Rolfsen, Production of π -AlMgSiFe crystals, *Z. Metallk.* 88 (1997) 142–146.
- [149] C.-L. Chen, R.C. Thomson, The combined use of EBSD and EDX analyses for the identification of complex intermetallic phases in multicomponent Al–Si piston alloys, *Journal of Alloys and Compounds*. 490 (2010) 293–300. doi:10.1016/j.jallcom.2009.09.181.
- [150] A. Kelly, W. Tyson, Tensile Properties of Fibre-Reinforced Metals - Copper/Tungsten and Copper/Molybdenum, *J. Mech. Phys. Solids*. 13 (1965) 329–. doi:10.1016/0022-5096(65)90035-9.
- [151] Y. Brechet, J.D. Embury, S. Tao, L. Luo, Damage initiation in metal matrix composites, *Acta Metallurgica et Materialia*. 39 (1991) 1781–1786. doi:10.1016/0956-7151(91)90146-R.
- [152] S. Corbin, D. Wilkinson, Influence of Matrix Strength and Damage Accumulation on the Mechanical Response of a Particulate Metal-Matrix Composite, *Acta Metall. Mater.* 42 (1994) 1329–1335. doi:10.1016/0956-7151(94)90149-X.
- [153] J.-Y. Buffiere, E. Maire, C. Verdu, P. Cloetens, M. Pateyron, G. Peix, J. Baruchel, Damage assessment in an Al/SiC composite during monotonic tensile tests using synchrotron X-ray microtomography, *Materials Science and Engineering: A*. 234–236 (1997) 633–635. doi:10.1016/S0921-5093(97)00302-X.
- [154] L. Babout, Y. Brechet, E. Maire, R. Fougères, On the competition between particle fracture and particle decohesion in metal matrix composites, *Acta Materialia*. 52 (2004) 4517–4525. doi:10.1016/j.actamat.2004.06.009.
- [155] A. Miserez, R. Müller, A. Rossoll, L. Weber, A. Mortensen, Particle reinforced metals of high ceramic content, *Materials Science and Engineering A*. 387–389 (2004) 822–831.
- [156] M. Slámová, Y. Bréchet, C. Verdu, R. Fougères, F. Louchet, Al–Si Alloys as a Model System for Damage Accumulation in Composite Materials, *Physica Status Solidi (a)*. 168 (1998) 117–127. doi:10.1002/(SICI)1521-396X(199807)168:1<117::AID-PSSA117>3.0.CO;2-X.
- [157] W.J. Poole, N. Charras, An experimental study on the effect of damage on the stress–strain behaviour for Al–Si model composites, *Materials Science and Engineering: A*. 406 (2005) 300–308. doi:10.1016/j.msea.2005.06.041.
- [158] G. Guiglionda, W. Poole, The role of damage on the deformation and fracture of Al–Si eutectic alloys, *Materials Science and Engineering: A*. 336 (2002) 159–169. doi:10.1016/S0921-5093(01)01971-2.
- [159] Q.G. Wang, Plastic deformation behavior of aluminum casting alloys A356/357, *Metallurgical and Materials Transactions A*. 35 (2004) 2707–2718. doi:10.1007/s11661-004-0216-3.
- [160] C.H. Cáceres, J.R. Griffiths, P. Reiner, The influence of microstructure on the Bauschinger effect in an Al–Si–Mg casting alloy, *Acta Mater.* 44 (1996) 15–23. doi:10.1016/1359-6454(95)00171-6.
- [161] J.R. Brockenbrough, F.W. Zok, On the role of particle cracking in flow and fracture of metal matrix composites, *Acta Metallurgica et Materialia*. 43 (1995) 11–20. doi:10.1016/0956-7151(95)90256-2.

- [162] J.-W. Yeh, W.-P. Liu, The cracking mechanism of silicon particles in an A357 aluminum alloy, *MMTA*. 27 (1996) 3558–3568. doi:10.1007/BF02595447.
- [163] C. Berdin, A. Ouglova, V. Djafari, R. Doglione, Secondary foundry alloy damage and particle fracture, *Materials Science and Engineering: A*. 357 (2003) 328–336. doi:10.1016/S0921-5093(03)00202-8.
- [164] F.W. DelRio, R.F. Cook, B.L. Boyce, Fracture strength of micro- and nano-scale silicon components, *Appl. Phys. Rev.* 2 (2015) 021303. doi:10.1063/1.4919540.
- [165] E. Maire, V. Carmona, J. Courbon, W. Ludwig, Fast X-ray tomography and acoustic emission study of damage in metals during continuous tensile tests, *Acta Materialia*. 55 (2007) 6806–6815. doi:10.1016/j.actamat.2007.08.043.
- [166] J.J. Williams, Z. Flom, A.A. Amell, N. Chawla, X. Xiao, F. De Carlo, Damage evolution in SiC particle reinforced Al alloy matrix composites by X-ray synchrotron tomography, *Acta Materialia*. 58 (2010) 6194–6205. doi:10.1016/j.actamat.2010.07.039.
- [167] E. Maire, P.J. Withers, Quantitative X-ray tomography, *International Materials Reviews*. 59 (2014) 1–43. doi:10.1179/1743280413Y.0000000023.
- [168] J.-Y. Buffière, E. Maire, P. Cloetens, G. Lormand, R. Fougères, Characterization of internal damage in a MMCp using X-ray synchrotron phase contrast microtomography, *Acta Materialia*. 47 (1999) 1613–1625. doi:10.1016/S1359-6454(99)00024-5.
- [169] A.R. Riahi, T. Perry, A.T. Alpas, Scuffing resistances of Al-Si alloys: effects of etching condition, surface roughness and particle morphology, *Mater. Sci. Eng. A-Struct. Mater. Prop. Microstruct. Process.* 343 (2003) 76–81. doi:10.1016/S0921-5093(02)00322-2.
- [170] M. Chen, X. Meng-Burany, T.A. Perry, A.T. Alpas, Micromechanisms and mechanics of ultra-mild wear in Al-Si alloys, *Acta Materialia*. 56 (2008) 5605–5616. doi:10.1016/j.actamat.2008.07.043.
- [171] Y. Wang, S.C. Tung, Scuffing and wear behavior of aluminum piston skirt coatings against aluminum cylinder bore, *Wear*. 225–229 (1999) 1100–1108.
- [172] S. Narayanan, S.R. Kalidindi, L.S. Schadler, Determination of unknown stress states in silicon wafers using microlaser Raman spectroscopy, *Journal of Applied Physics*. 82 (1997) 2595–2602. doi:10.1063/1.366072.
- [173] Q.G. Wang, M. Praud, A. Needleman, K.S. Kim, J.R. Griffiths, C.J. Davidson, C.H. Caceres, A.A. Benzerga, Size effects in aluminium alloy castings, *Acta Mater.* 58 (2010) 3006–3013. doi:10.1016/j.actamat.2010.01.032.
- [174] R.F. Cook, G.M. Pharr, Direct Observation and Analysis of Indentation Cracking in Glasses and Ceramics, *Journal of the American Ceramic Society*. 73 (1990) 787–817. doi:10.1111/j.1151-2916.1990.tb05119.x.
- [175] A.G. Evans, E.A. Charles, Fracture Toughness Determinations by Indentation, *J Am Ceram Soc.* 59 (1976) 371–372. doi:10.1111/j.1151-2916.1976.tb10991.x.
- [176] F.C. Frank, B.R. Lawn, On the Theory of Hertzian Fracture, *Proceedings of the Royal Society of London. Series A, Mathematical and Physical Sciences*. 299 (1967) 291–306.
- [177] R. Warren, Measurement of the fracture properties of brittle solids by hertzian indentation, *Acta Metallurgica*. 26 (1978) 1759–1769. doi:10.1016/0001-6160(78)90087-1.
- [178] P.D. Warren, Determining the fracture toughness of brittle materials by Hertzian indentation, *Journal of the European Ceramic Society*. 15 (1995) 201–207. doi:10.1016/0955-2219(95)93941-U.
- [179] B.R. Lawn, A.G. Evans, D.B. Marshall, Elastic/Plastic Indentation Damage in Ceramics: The Median/Radial Crack System, *Journal of the American Ceramic Society*. 63 (1980) 574–581. doi:10.1111/j.1151-2916.1980.tb10768.x.
- [180] G. r. Anstis, P. Chantikul, B. r. Lawn, D. b. Marshall, A Critical Evaluation of Indentation Techniques for Measuring Fracture Toughness: I, Direct Crack Measurements, *Journal of*

- the American Ceramic Society. 64 (1981) 533–538. doi:10.1111/j.1151-2916.1981.tb10320.x.
- [181] K. Niihara, A fracture mechanics analysis of indentation-induced Palmqvist crack in ceramics, *J Mater Sci Lett.* 2 (1983) 221–223. doi:10.1007/BF00725625.
- [182] M. Laugier, The Elastic Plastic Indentation of Ceramics, *J. Mater. Sci. Lett.* 4 (1985) 1539–1541. doi:10.1007/BF00721390.
- [183] Y. Tang, A. Yonezu, N. Ogasawara, N. Chiba, X. Chen, On radial crack and half-penny crack induced by Vickers indentation, *Proceedings of the Royal Society of London A: Mathematical, Physical and Engineering Sciences.* 464 (2008) 2967–2984. doi:10.1098/rspa.2008.0077.
- [184] R.D. Dukino, M.V. Swain, Comparative Measurement of Indentation Fracture Toughness with Berkovich and Vickers Indenters, *Journal of the American Ceramic Society.* 75 (1992) 3299–3304. doi:10.1111/j.1151-2916.1992.tb04425.x.
- [185] D.S. Harding, W.C. Oliver, G.M. Pharr, Cracking During Nanoindentation and its Use in the Measurement of Fracture Toughness, *MRS Online Proceedings Library.* 356 (1994). doi:10.1557/PROC-356-663.
- [186] T. Zhang, Y. Feng, R. Yang, P. Jiang, A method to determine fracture toughness using cube-corner indentation, *Scripta Materialia.* 62 (2010) 199–201. doi:10.1016/j.scriptamat.2009.10.025.
- [187] X. Li, D. Diao, B. Bhushan, Fracture mechanisms of thin amorphous carbon films in nanoindentation, *Acta Materialia.* 45 (1997) 4453–4461. doi:10.1016/S1359-6454(97)00143-2.
- [188] J. Chen, On the determination of coating toughness during nanoindentation, *Surface and Coatings Technology.* 206 (2012) 3064–3068. doi:10.1016/j.surfcoat.2011.12.006.
- [189] J. Chen, Indentation-based methods to assess fracture toughness for thin coatings, *J. Phys. D: Appl. Phys.* 45 (2012) 203001. doi:10.1088/0022-3727/45/20/203001.
- [190] F.F. Schlich, R. Spolenak, Size- and phase-dependent mechanical properties of ultrathin Si films on polyimide substrates, *Acta Materialia.* 110 (2016) 122–130. doi:10.1016/j.actamat.2016.03.028.
- [191] C.M. Perrott, On the indentation fracture of cemented carbide II — the nature of surface fracture toughness, *Wear.* 47 (1978) 81–91.
- [192] M.T. Laugier, Toughness determination of some ceramic tool materials using the method of Hertzian indentation fracture, *J Mater Sci Lett.* 4 (1985) 1542–1544. doi:10.1007/BF00721391.
- [193] F. Sergejev, M. Antonov, Comparative study on indentation fracture toughness measurements of cemented carbides, *Proc. Estonian Acad. Sci. Eng.* 12 (2006) 388–398.
- [194] D. Casellas, J. Caro, S. Molas, J.M. Prado, I. Valls, Fracture toughness of carbides in tool steels evaluated by nanoindentation, *Acta Mater.* 55 (2007) 4277–4286. doi:10.1016/j.actamat.2007.03.028.
- [195] B. Wong, R.J. Holbrook, Microindentation for Fracture and Stress-Corrosion Cracking Studies in Single-Crystal Silicon, *J. Electrochem. Soc.* 134 (1987) 2254–2256. doi:10.1149/1.2100861.
- [196] F. Ericson, S. Johansson, J. Schweitz, Hardness and Fracture-Toughness of Semiconducting Materials Studied by Indentation and Erosion Techniques, *Mater. Sci. Eng. A-Struct. Mater. Prop. Microstruct. Process.* 105 (1988) 131–141. doi:10.1016/0025-5416(88)90489-2.
- [197] F. Ebrahimi, L. Kalwani, Fracture anisotropy in silicon single crystal, *Materials Science and Engineering: A.* 268 (1999) 116–126. doi:10.1016/S0921-5093(99)00077-5.

- [198] R.W. Fancher, C.M. Watkins, M.G. Norton, D.F. Bahr, E.W. Osborne, Grain growth and mechanical properties in bulk polycrystalline silicon, *Journal of Materials Science*. 36 (2001) 5441–5446. doi:10.1023/A:1012425529753.
- [199] J.G. Swadener, M. Nastasi, Effect of dopants on the fracture toughness of silicon, *Journal of Materials Science Letters*. 21 (2002) 1363–1365. doi:10.1023/A:1019772717743.
- [200] Z. Xia, W.A. Curtin, B.W. Sheldon, A new method to evaluate the fracture toughness of thin films, *Acta Materialia*. 52 (2004) 3507–3517. doi:10.1016/j.actamat.2004.04.004.
- [201] M. Tanaka, K. Higashida, H. Nakashima, H. Takagi, M. Fujiwara, Orientation dependence of fracture toughness measured by indentation methods and its relation to surface energy in single crystal silicon, *Int J Fract*. 139 (2006) 383–394. doi:10.1007/s10704-006-0021-7.
- [202] C.M. Pecnik, D. Courty, D. Muff, R. Spolenak, Fracture toughness of esthetic dental coating systems by nanoindentation and FIB sectional analysis, *Journal of the Mechanical Behavior of Biomedical Materials*. 47 (2015) 1–11. doi:10.1016/j.jmbbm.2015.03.006.
- [203] R. Morrell, Fracture toughness testing for advanced technical ceramics: internationally agreed good practice, *Advances in Applied Ceramics*. 105 (2006) 88–98. doi:10.1179/174367606X84422.
- [204] G.D. Quinn, R.C. Bradt, On the Vickers indentation fracture toughness test, *J. Am. Ceram. Soc.* 90 (2007) 673–680. doi:10.1111/j.1551-2916.2006.01482.x.
- [205] D. Munz, T. Fett, *Ceramics: Mechanical Properties, Failure Behaviour, Materials Selection*, Corrected edition, Springer, Berlin ; New York, 2001.
- [206] G. Geandier, S. Denis, A. Mocellin, Float glass fracture toughness determination by Hertzian contact: experiments and analysis, *Journal of Non-Crystalline Solids*. 318 (2003) 284–295. doi:10.1016/S0022-3093(02)01886-0.
- [207] F. Petit, A.C. Sartieaux, M. Gonon, F. Cambier, Fracture toughness and residual stress measurements in tempered glass by Hertzian indentation, *Acta Materialia*. 55 (2007) 2765–2774. doi:10.1016/j.actamat.2006.12.014.
- [208] G.M. Pharr, W.C. Oliver, D.R. Clarke, Hysteresis and discontinuity in the indentation load-displacement behavior of silicon, *Scripta Metallurgica*. 23 (1989) 1949–1952. doi:10.1016/0036-9748(89)90488-2.
- [209] G. m. Pharr, W. c. Oliver, D. s. Harding, New evidence for a pressure-induced phase transformation during the indentation of silicon, *Journal of Materials Research*. 6 (1991) 1129–1130. doi:10.1557/JMR.1991.1129.
- [210] M. Ganchenkova, R.M. Nieminen, Chapter Eleven - Mechanical Properties of Silicon Microstructures, in: *Handbook of Silicon Based MEMS Materials and Technologies*, William Andrew Publishing, Boston, 2010: pp. 179–219.
- [211] S. Zhang, D. Sun, Y. Fu, H. Du, Toughness measurement of thin films: a critical review, *Surf Coat Tech*. 198 (2005) 74–84. doi:10.1016/j.surfcoat.2004.10.021.
- [212] S. Bhattacharya, A.R. Riahi, A.T. Alpas, Indentation-induced subsurface damage in silicon particles of Al-Si alloys, *Materials Science and Engineering: A*. 527 (2009) 387–396. doi:10.1016/j.msea.2009.08.052.
- [213] S. Bhattacharya, A.T. Alpas, Role of sliding-induced tribofilms on fracture of particles in aluminium-silicon alloys, *Wear*. 301 (2013) 707–716. doi:10.1016/j.wear.2013.01.081.
- [214] M. Sebastiani, K.E. Johanns, E.G. Herbert, F. Carassiti, G.M. Pharr, A novel pillar indentation splitting test for measuring fracture toughness of thin ceramic coatings, *Philosophical Magazine*. 95 (2015) 1928–1944. doi:10.1080/14786435.2014.913110.
- [215] M. Sebastiani, K.E. Johanns, E.G. Herbert, G.M. Pharr, Measurement of fracture toughness by nanoindentation methods: Recent advances and future challenges, *Current Opinion in*

- Solid State and Materials Science. 19 (2015) 324–333. doi:10.1016/j.cossms.2015.04.003.
- [216] B.N. Jaya, C. Kirchlechner, G. Dehm, Can microscale fracture tests provide reliable fracture toughness values? A case study in silicon, *Journal of Materials Research*. 30 (2015) 686–698. doi:10.1557/jmr.2015.2.
- [217] J.P. Best, J. Zechner, J.M. Wheeler, R. Schoeppner, M. Morstein, J. Michler, Small-scale fracture toughness of ceramic thin films: the effects of specimen geometry, ion beam notching and high temperature on chromium nitride toughness evaluation, *Philosophical Magazine*. 0 (2016) 1–18. doi:10.1080/14786435.2016.1223891.
- [218] M. Sebastiani, E. Bemporad, F. Carassiti, N. Schwarzer, Residual stress measurement at the micrometer scale: focused ion beam (FIB) milling and nanoindentation testing, *Philosophical Magazine*. 91 (2011) 1121–1136. doi:10.1080/14786431003800883.
- [219] W.M. Mook, J.D. Nowak, C.R. Perrey, C.B. Carter, R. Mukherjee, S.L. Girshick, P.H. McMurry, W.W. Gerberich, Compressive stress effects on nanoparticle modulus and fracture, *Phys. Rev. B*. 75 (2007) 214112. doi:10.1103/PhysRevB.75.214112.
- [220] J. Deneen Nowak, W.M. Mook, A.M. Minor, W.W. Gerberich, C.B. Carter, Fracturing a nanoparticle, *Philosophical Magazine*. 87 (2007) 29–37.
- [221] F. Östlund, K. Rzepiejewska-Malyska, K. Leifer, L.M. Hale, Y. Tang, R. Ballarini, W.W. Gerberich, J. Michler, Brittle-to-Ductile Transition in Uniaxial Compression of Silicon Pillars at Room Temperature, *Adv Funct Mater*. 19 (2009) 2439–2444. doi:10.1002/adfm.200900418.
- [222] S. Zhang, D. Sun, Y. Fu, H. Du, Toughness measurement of ceramic thin films by two-step uniaxial tensile method, *Thin Solid Films*. 469–470 (2004) 233–238. doi:10.1016/j.tsf.2004.08.094.
- [223] Z. Chen, B. Cotterell, W. Wang, The fracture of brittle thin films on compliant substrates in flexible displays, *Engineering Fracture Mechanics*. 69 (2002) 597–603. doi:10.1016/S0013-7944(01)00104-7.
- [224] R. Ballarini, R.L. Mullen, Y. Yin, H. Kahn, S. Stemmer, A.H. Heuer, The Fracture Toughness of Polysilicon Microdevices: A First Report, *Journal of Materials Research*. 12 (1997) 915–922. doi:10.1557/JMR.1997.0131.
- [225] O. Kraft, R. Schwaiger, W. d. Nix, Measurement of Mechanical Properties in Small Dimensions by Microbeam Deflection, *MRS Online Proceedings Library*. 518 (1998). doi:10.1557/PROC-518-39.
- [226] H.D. Espinosa, B.C. Prorok, M. Fischer, A methodology for determining mechanical properties of freestanding thin films and MEMS materials, *Journal of the Mechanics and Physics of Solids*. 51 (2003) 47–67. doi:10.1016/S0022-5096(02)00062-5.
- [227] J.J. Bellante, H. Kahn, R. Ballarini, C.A. Zorman, M. Mehregany, A.H. Heuer, Fracture toughness of polycrystalline silicon carbide thin films, *Appl. Phys. Lett.* 86 (2005) 071920. doi:10.1063/1.1864246.
- [228] H.D. Espinosa, B. Peng, A new methodology to investigate fracture toughness of freestanding MEMS and advanced materials in thin film form, *J Microelectromech S.* 14 (2005) 153–159. doi:10.1109/JMEMS.2004.839013.
- [229] V. Hatty, H. Kahn, J. Trevino, C.A. Zorman, M. Mehregany, R. Ballarini, A.H. Heuer, Fracture toughness of low-pressure chemical-vapor-deposited polycrystalline silicon carbide thin films, *J. Appl. Phys.* 99 (2006) 013517. doi:10.1163/1.2158135.
- [230] H.D. Espinosa, B. Peng, N. Moldovan, T.A. Friedmann, X. Xiao, D.C. Mancini, O. Auciello, J. Carlisle, C.A. Zorman, M. Merhegany, Elasticity, strength, and toughness of single crystal silicon carbide, ultrananocrystalline diamond, and hydrogen-free tetrahedral amorphous carbon, *Appl. Phys. Lett.* 89 (2006) 073111. doi:10.1063/1.2336220.

- [231] S.W. Cho, K. Jonnalagadda, I. Chasiotis, Mode I and mixed mode fracture of polysilicon for MEMS, *Fatigue and Fracture of Engineering Materials and Structures*. 30 (2007) 21–31. doi:10.1111/j.1460-2695.2006.01086.x.
- [232] Y. Xiang, J. McKinnell, W.-M. Ang, J.J. Vlassak, Measuring the fracture toughness of ultra-thin films with application to AlTa coatings, *Int J Fract.* 144 (2007) 173–179. doi:10.1007/s10704-007-9095-0.
- [233] K. Jonnalagadda, S.W. Cho, I. Chasiotis, T. Friedmann, J. Sullivan, Effect of intrinsic stress gradient on the effective mode-I fracture toughness of amorphous diamond-like carbon films for MEMS, *Journal of the Mechanics and Physics of Solids*. 56 (2008) 388–401. doi:10.1016/j.jmps.2007.05.013.
- [234] H. Hosokawa, A.V. Desai, M.A. Haque, Plane stress fracture toughness of freestanding nanoscale thin films, *Thin Solid Films*. 516 (2008) 6444–6447. doi:10.1016/j.tsf.2008.03.005.
- [235] X.D. Li, B. Bhushan, K. Takashima, C.W. Baek, Y.K. Kim, Mechanical characterization of micro/nanoscale structures for MEMS/NEMS applications using nanoindentation techniques, *Ultramicroscopy*. 97 (2003) 481–494. doi:10.1016/S0304-3991(03)00077-9.
- [236] D. Di Maio, S.G. Roberts, Measuring fracture toughness of coatings using focused-ion-beam-machined microbeams, *J Mater Res.* 20 (2005) 299–302. doi:10.1557/JMR.2005.0048.
- [237] K. Matoy, H. Schönherr, T. Detzel, T. Schöberl, R. Pippan, C. Motz, G. Dehm, A comparative micro-cantilever study of the mechanical behavior of silicon based passivation films, *Thin Solid Films*. 518 (2009) 247–256. doi:10.1016/j.tsf.2009.07.143.
- [238] K. Matoy, T. Detzel, M. Müller, C. Motz, G. Dehm, Interface fracture properties of thin films studied by using the micro-cantilever deflection technique, *Surf Coat Tech.* 204 (2009) 878–881. doi:10.1016/j.surfcoat.2009.09.013.
- [239] K. Matoy, H. Schönherr, T. Detzel, G. Dehm, Micron-sized fracture experiments on amorphous SiO_x films and SiO_x/SiN_x multi-layers, *Thin Solid Films*. 518 (2010) 5796–5801. doi:10.1016/j.tsf.2010.05.114.
- [240] F. Iqbal, J. Ast, M. Göken, K. Durst, In situ micro-cantilever tests to study fracture properties of NiAl single crystals, *Acta Mater.* 60 (2012) 1193–1200. doi:10.1016/j.actamat.2011.10.060.
- [241] S. Wurster, C. Motz, R. Pippan, Characterization of the fracture toughness of micro-sized tungsten single crystal notched specimens, *Philos Mag.* 92 (2012) 1803–1825. doi:10.1080/14786435.2012.658449.
- [242] J. Ast, T. Przybilla, V. Maier, K. Durst, M. Göken, Microcantilever bending experiments in NiAl – Evaluation, size effects, and crack tip plasticity, *Journal of Materials Research*. 29 (2014) 2129–2140. doi:10.1557/jmr.2014.240.
- [243] B.N. Jaya, V. Jayaram, Crack stability in edge-notched clamped beam specimens: modeling and experiments, *Int J Fract.* 188 (2014) 213–228. doi:10.1007/s10704-014-9956-2.
- [244] A.D. Norton, S. Falco, N. Young, J. Severs, R.I. Todd, Microcantilever investigation of fracture toughness and subcritical crack growth on the scale of the microstructure in Al₂O₃, *Journal of the European Ceramic Society*. 35 (2015) 4521–4533. doi:10.1016/j.jeurceramsoc.2015.08.023.
- [245] M.D. Abad, S. Parker, D. Frazer, M.R. de Figueiredo, A. Lupinacci, K. Kikuchi, P. Hosemann, Evaluation of the Mechanical Properties of Naturally Grown Multilayered Oxides Formed on HCM12A Using Small Scale Mechanical Testing, *Oxid Met.* 84 (2015) 211–231. doi:10.1007/s11085-015-9551-6.

- [246] B.N. Jaya, J.M. Wheeler, J. Wehrs, J.P. Best, R. Soler, J. Michler, C. Kirchlechner, G. Dehm, Micro-scale fracture behavior of single crystal silicon beams at elevated temperatures, *Nano Letters*. 16 (2016) 7597–7603. doi:10.1021/acs.nanolett.6b03461.
- [247] C. Bohnert, N.J. Schmitt, S.M. Weygand, O. Kraft, R. Schwaiger, Fracture toughness characterization of single-crystalline tungsten using notched micro-cantilever specimens, *International Journal of Plasticity*. 81 (2016) 1–17. doi:10.1016/j.ijplas.2016.01.014.
- [248] F.Y. Cui, R.P. Vinci, A chevron-notched bowtie micro-beam bend test for fracture toughness measurement of brittle materials, *Scripta Materialia*. 132 (2017) 53–57. doi:10.1016/j.scriptamat.2017.01.031.
- [249] R. Treml, D. Kozic, R. Schöngrundner, O. Kolednik, H.-P. Gänser, R. Brunner, D. Kiener, Miniaturized fracture experiments to determine the toughness of individual films in a multilayer system, *Extreme Mechanics Letters*. 8 (2016) 235–244. doi:10.1016/j.eml.2016.01.004.
- [250] Y. Zou, P. Okle, H. Yu, T. Sumigawa, T. Kitamura, S. Maiti, W. Steurer, R. Spolenak, Fracture properties of a refractory high-entropy alloy: In situ micro-cantilever and atom probe tomography studies, *Scripta Materialia*. 128 (2017) 95–99. doi:10.1016/j.scriptamat.2016.09.036.
- [251] S. Liu, J.M. Wheeler, P.R. Howie, X.T. Zeng, J. Michler, W.J. Clegg, Measuring the fracture resistance of hard coatings, *Appl Phys Lett*. 102 (2013) 171907. doi:10.1063/1.4803928.
- [252] N. Jaya B, V. Jayaram, S.K. Biswas, A new method for fracture toughness determination of graded (Pt,Ni)Al bond coats by microbeam bend tests, *Philosophical Magazine*. 92 (2012) 3326–3345. doi:10.1080/14786435.2012.669068.
- [253] B.N. Jaya, V. Jayaram, Fracture Testing at Small-Length Scales: From Plasticity in Si to Brittleness in Pt, *JOM*. 68 (2015) 94–108. doi:10.1007/s11837-015-1489-2.
- [254] W.N. Sharpe, B. Yuan, R.L. Edwards, Fracture Tests Of Polysilicon Film, *MRS Online Proceedings Library Archive*. 505 (1997). doi:10.1557/PROC-505-51.
- [255] T. Tsuchiya, J. Sakata, Y. Taga, Tensile Strength and Fracture Toughness of Surface Micro-machined Polycrystalline Silicon Thin Films Prepared Under Various Conditions, *MRS Online Proceedings Library Archive*. 505 (1997). doi:10.1557/PROC-505-285.
- [256] R. Ballarini, R.L. Mullen, H. Kahn, A.H. Heuer, The Fracture Toughness of Polysilicon Microdevices, *MRS Online Proceedings Library Archive*. 518 (1998). doi:10.1557/PROC-518-137.
- [257] S. Koyama, K. Takashima, Y. Higo, Fracture Toughness Measurement of a Micro-Sized Single Crystal Silicon, *Key Eng Mat*. 297–300 (2005) 292–298. doi:10.4028/www.scientific.net/KEM.297-300.292.
- [258] J. Bagdahn, J. Schischka, M. Petzold, W.N. Sharpe, Fracture toughness and fatigue investigations of polycrystalline silicon, in: R. Ramesham (Ed.), *Reliability, Testing and Characterization of Mems/Moems*, SPIE -Int Soc Optical Engineering, Bellingham, 2001: pp. 161–168.
- [259] T.P. Halford, K. Takashima, Y. Higo, P. Bowen, Fracture tests of micro-sized TiAl specimens, *Fatigue Fract Eng M*. 28 (2005) 695–701. doi:10.1111/j.1460-2695.2005.00893.x.
- [260] X. Li, T. Kasai, S. Nakao, T. Ando, M. Shikida, K. Sato, H. Tanaka, Anisotropy in fracture of single crystal silicon film characterized under uniaxial tensile condition, *Sensor Actuat A-Phys*. 117 (2005) 143–150. doi:10.1016/j.sna.2004.06.003.
- [261] X. Li, T. Kasai, S. Nakao, H. Tanaka, T. Ando, M. Shikida, K. Sato, Measurement for fracture toughness of single crystal silicon film with tensile test, *Sensor Actuat A-Phys*. 119 (2005) 229–235. doi:10.1016/j.sna.2003.10.063.

- [262] T. Ando, X. Li, S. Nakao, T. Kasai, H. Tanaka, M. Shikida, K. Sato, Fracture toughness measurement of thin-film silicon, *Fatigue Fract Eng M.* 28 (2005) 687–694. doi:10.1111/j.1460-2695.2005.00920.x.
- [263] S. Massl, W. Thomma, J. Keckes, R. Pippan, Investigation of fracture properties of magnetron-sputtered TiN films by means of a FIB-based cantilever bending technique, *Acta Mater.* 57 (2009) 1768–1776. doi:10.1016/j.actamat.2008.12.018.
- [264] B. Merle, M. Göken, Fracture toughness of silicon nitride thin films of different thicknesses as measured by bulge tests, *Acta Mater.* 59 (2011) 1772–1779. doi:10.1016/j.actamat.2010.11.043.
- [265] D.E.J. Armstrong, A.J. Wilkinson, S.G. Roberts, Micro-mechanical measurements of fracture toughness of bismuth embrittled copper grain boundaries, *Phil Mag Lett.* 91 (2011) 394–400. doi:10.1080/09500839.2011.573813.
- [266] D.E.J. Armstrong, A.S.M.A. Haseeb, S.G. Roberts, A.J. Wilkinson, K. Bade, Nanoindentation and micro-mechanical fracture toughness of electrodeposited nanocrystalline Ni–W alloy films, *Thin Solid Films.* 520 (2012) 4369–4372. doi:10.1016/j.tsf.2012.02.059.
- [267] N. Jaya, S. Bhowmick, S. Asif, O. I. Warren, V. Jayaram, S.K. Biswas, Fracture Properties of Diffusion Aluminide Bond Coats: An In Situ SEM Study of Microbeam Bending, *Microsc Microanal.* 19 (2013) 1836–1837. doi:10.1017/S1431927613011173.
- [268] E. Hintsala, D. Kiener, J. Jackson, W.W. Gerberich, In-Situ Measurements of Free-Standing, Ultra-Thin Film Cracking in Bending, *Experimental Mechanics.* 55 (2015) 1681–1690. doi:10.1007/s11340-015-0069-2.
- [269] E.D. Hintsala, S. Bhowmick, X. Yueyue, R. Ballarini, S.A.S. Asif, W.W. Gerberich, Temperature dependent fracture initiation in microscale silicon, *Scripta Materialia.* 130 (2017) 78–82. doi:10.1016/j.scriptamat.2016.11.016.
- [270] J. Bagdahn, W.N. Sharpe, O. Jadaan, Fracture strength of polysilicon at stress concentrations, *J Microelectromech S.* 12 (2003) 302–312. doi:10.1109/JMEMS.2003.814130.
- [271] S. Nakao, T. Ando, M. Shikida, K. Sato, Effect of temperature on fracture toughness in a single-crystal-silicon film and transition in its fracture mode, *J Micromech Microeng.* 18 (2008) 015026. doi:10.1088/0960-1317/18/1/015026.
- [272] S. Kamiya, H. Nagasawa, K. Yamanobe, M. Saka, A comparative study of the mechanical strength of chemical vapor-deposited diamond and physical vapor-deposited hard coatings, *Thin Solid Films.* 473 (2005) 123–131. doi:10.1016/j.tsf.2004.05.135.
- [273] H. Kahn, N. Tayebi, R. Ballarini, R.L. Mullen, A.H. Heuer, Fracture toughness of polysilicon MEMS devices, *Sensor Actuat A-Phys.* 82 (2000) 274–280. doi:10.1016/S0924-4247(99)00366-0.
- [274] S. Rubanov, P.R. Munroe, FIB-induced damage in silicon, *Journal of Microscopy.* 214 (2004) 213–221. doi:10.1111/j.0022-2720.2004.01327.x.
- [275] L.A. Giannuzzi, R. Geurts, J. Ringnalda, 2 keV Ga⁺ FIB Milling for Reducing Amorphous Damage in Silicon, *Microscopy and Microanalysis.* 11 (2005) 828–829. doi:10.1017/S1431927605507797.
- [276] S. Rubanov, Damage Layers in Si vs. Ion Dose during 30 keV FIB Milling, *Microscopy and Microanalysis.* 15 (2009) 358–359. doi:10.1017/S1431927609098638.
- [277] D. Liu, P.E.J. Flewitt, The Measurement of Mechanical Properties of Thermal Barrier Coatings by Micro-Cantilever Tests, *Key Eng Mat.* 525–526 (2012) 13–16. doi:10.4028/www.scientific.net/KEM.525-526.13.
- [278] R. Ballarini, H. Kahn, N. Tayebi, A.H. Heuer, Effects of microstructure on the strength and fracture toughness of polysilicon: A wafer level testing approach, in: 2001: pp. 37–51.
- [279] H. Kahn, A.H. Heuer, R. Ballarini, On-chip testing of mechanical properties of MEMS devices, *MRS Bull.* 26 (2001) 300–301. doi:10.1557/mrs2001.64.

- [280] I. Chasiotis, S.W. Cho, K. Jonnalagadda, Fracture Toughness and Subcritical Crack Growth in Polycrystalline Silicon, *J Appl Mech.* 73 (2005) 714–722. doi:10.1115/1.2172268.
- [281] S.W. Cho, K. Jonnalagadda, I. Chasiotis, Mode I and mixed mode fracture of polysilicon for MEMS, *Fatigue Fract Eng M.* 30 (2007) 21–31. doi:10.1111/j.1460-2695.2006.01086.x.
- [282] Y. Ichikawa, S. Maekawa, K. Takashima, M. Shimojo, Y. Higo, M.V. Swain, Fracture Behavior of Micro-Sized Ni-P Amorphous Alloy Specimens, *MRS Online Proceedings Library.* 605 (1999). doi:10.1557/PROC-605-273.
- [283] K. Takashima, Y. Higo, Fatigue and fracture of a Ni-P amorphous alloy thin film on the micrometer scale, *Fatigue Fract Eng M.* 28 (2005) 703–710. doi:10.1111/j.1460-2695.2005.00923.x.
- [284] Y. Yang, S. Allameh, B. Boyce, K.S. Chan, W.O. Soboyejo, An Experimental Study of Fracture of LIGA Ni Micro-Electro-Mechanical Systems Thin Films, *Metall and Mat Trans A.* 38 (2007) 1223–1230. doi:10.1007/s11661-007-9147-0.
- [285] D.I. Son, J.J. Kim, D.I. Kwon, Fracture Behavior of Single and Polycrystalline Silicon Films for MEMS Applications, *Key Eng Mat.* (2005) 551–556. doi:10.4028/www.scientific.net/KEM.297-300.551.
- [286] S.S. Brenner, Tensile Strength of Whiskers, *Journal of Applied Physics.* 27 (1956) 1484–1491. doi:10.1063/1.1722294.
- [287] D.T. Read, J.W. Dally, A new method for measuring the strength and ductility of thin films, *Journal of Materials Research.* 8 (1993) 1542–1549. doi:10.1557/JMR.1993.1542.
- [288] M.A. Haque, M.T.A. Saif, In-situ tensile testing of nano-scale specimens in SEM and TEM, *Experimental Mechanics.* 42 (2002) 123–128. doi:10.1007/BF02411059.
- [289] T. Tsuchiya, Tensile testing of silicon thin films, *Fatigue Fract. Eng. Mater. Struct.* 28 (2005) 665–674. doi:10.1111/j.1460-2695.2005.00910.x.
- [290] B.L. Boyce, J.M. Grazier, T.E. Buchheit, M.J. Shaw, Strength Distributions in Polycrystalline Silicon MEMS, *Journal of Microelectromechanical Systems.* 16 (2007) 179–190. doi:10.1109/JMEMS.2007.892794.
- [291] D.S. Gianola, C. Eberl, Micro- and nanoscale tensile testing of materials, *JOM.* 61 (2009) 24. doi:10.1007/s11837-009-0037-3.
- [292] Y. Zhu, F. Xu, Q. Qin, W.Y. Fung, W. Lu, Mechanical Properties of Vapor–Liquid–Solid Synthesized Silicon Nanowires, *Nano Lett.* 9 (2009) 3934–3939. doi:10.1021/nl902132w.
- [293] T. Fujii, T. Namazu, K. Sudoh, S. Sakakihara, S. Inoue, Focused Ion Beam Induced Surface Damage Effect on the Mechanical Properties of Silicon Nanowires, *J. Eng. Mater. Technol.-Trans. ASME.* 135 (2013) 041002. doi:10.1115/1.4024545.
- [294] H. Zhang, J. Tersoff, S. Xu, H. Chen, Q. Zhang, K. Zhang, Y. Yang, C.-S. Lee, K.-N. Tu, J. Li, Y. Lu, Approaching the ideal elastic strain limit in silicon nanowires, *Science Advances.* 2 (2016) e1501382. doi:10.1126/sciadv.1501382.
- [295] C. Herring, J.K. Galt, Elastic and Plastic Properties of Very Small Metal Specimens, *Phys. Rev.* 85 (1952) 1060–1061. doi:10.1103/PhysRev.85.1060.2.
- [296] G.L. Pearson, W.T. Read Jr., W.L. Feldmann, Deformation and fracture of small silicon crystals, *Acta Metallurgica.* 5 (1957) 181–191. doi:10.1016/0001-6160(57)90164-5.
- [297] G. Stan, S. Krylyuk, A.V. Davydov, I. Levin, R.F. Cook, Ultimate Bending Strength of Si Nanowires, *Nano Lett.* 12 (2012) 2599–2604. doi:10.1021/nl300957a.
- [298] T.P. Weihs, S. Hong, J.C. Bravman, W.D. Nix, Mechanical deflection of cantilever microbeams: A new technique for testing the mechanical properties of thin films, *Journal of Materials Research.* 3 (1988) 931–942. doi:10.1557/JMR.1988.0931.

-
- [299] M. f. Doerner, W. d. Nix, A method for interpreting the data from depth-sensing indentation instruments, *Journal of Materials Research*. 1 (1986) 601–609. doi:10.1557/JMR.1986.0601.
 - [300] W.C. Oliver, G.M. Pharr, An Improved technique for determining hardness and elastic modulus using load and displacement sensing indentation experiments, *Journal of Materials Research*. 7 (1992) 1564–1580.
 - [301] M.D. Uchic, D.M. Dimiduk, J.N. Florando, W.D. Nix, Sample dimensions influence strength and crystal plasticity, *Science*. 305 (2004) 986–989.
 - [302] M.D. Uchic, D.A. Dimiduk, A methodology to investigate size scale effects in crystalline plasticity using uniaxial compression testing, *Mater. Sci. Eng. A-Struct. Mater. Prop. Microstruct. Process*. 400 (2005) 268–278. doi:10.1016/j.msea.2005.03.082.
 - [303] P.R. Howie, S. Korte, W.J. Clegg, Fracture modes in micropillar compression of brittle crystals, *Journal of Materials Research*. 27 (2012) 141–151. doi:10.1557/jmr.2011.256.
 - [304] G.D. Quinn, E. Fuller, D. Xiang, A. Jillavenkatesa, L. Ma, D. Smith, J. Beall, A Novel Test Method for Measuring Mechanical Properties at the Small-Scale: The Theta Specimen, in: E. LaraCurzio (Ed.), *Mechanical Properties and Performance of Engineering Ceramics and Composites*, Amer Ceramic Soc, Westerville, 2005: pp. 117–126.
 - [305] M.S. Gaither, F.W. DelRio, R.S. Gates, E.R. Fuller Jr., R.F. Cook, Strength distribution of single-crystal silicon theta-like specimens, *Scripta Materialia*. 63 (2010) 422–425. doi:10.1016/j.scriptamat.2010.04.047.
 - [306] M.S. Gaither, R.S. Gates, R. Kirkpatrick, R.F. Cook, F.W. DelRio, Etching Process Effects on Surface Structure, Fracture Strength, and Reliability of Single-Crystal Silicon Theta-Like Specimens, *Journal of Microelectromechanical Systems*. 22 (2013) 589–602. doi:10.1109/JMEMS.2012.2234724.
 - [307] S. Hong, T.P. Weihs, J.C. Bravman, W.D. Nix, Measuring stiffnesses and residual stresses of silicon nitride thin films, *JEM*. 19 (1990) 903. doi:10.1007/BF02652915.
 - [308] J.J. Vlassak, W.D. Nix, A new bulge test technique for the determination of Young's modulus and Poisson's ratio of thin films, *Journal of Materials Research*. 7 (1992) 3242–3249. doi:10.1557/JMR.1992.3242.
 - [309] F.R. Brotzen, Mechanical testing of thin films, *International Materials Reviews*. 39 (1994) 24–45. doi:10.1179/imr.1994.39.1.24.
 - [310] K.S. Chen, A. Ayon, S.M. Spearing, Controlling and testing the fracture strength of silicon on the mesoscale, *J. Am. Ceram. Soc*. 83 (2000) 1476–1484.
 - [311] Y. Xiang, X. Chen, J.J. Vlassak, Plane-strain Bulge Test for Thin Films, *Journal of Materials Research*. 20 (2005) 2360–2370. doi:10.1557/jmr.2005.0313.
 - [312] C. Eberl, D.S. Gianola, K.J. Hemker, Mechanical Characterization of Coatings Using Microbeam Bending and Digital Image Correlation Techniques, *Exp Mech*. 50 (2010) 85–97. doi:10.1007/s11340-008-9187-4.
 - [313] O. Kraft, C.A. Volkert, Mechanical Testing of Thin Films and Small Structures, *Adv. Eng. Mater.* 3 (2001) 99–110. doi:10.1002/1527-2648(200103)3:3<99::AID-ADEM99>3.0.CO;2-2.
 - [314] K.J. Hemker, W.N. Sharpe, Microscale Characterization of Mechanical Properties, *Annual Review of Materials Research*. 37 (2007) 93–126. doi:10.1146/annurev.matsci.36.062705.134551.
 - [315] M.F. Pantano, H.D. Espinosa, L. Pagnotta, Mechanical characterization of materials at small length scales, *J. Mech. Sci. Technol*. 26 (2012) 545–561. doi:10.1007/s12206-011-1214-1.
 - [316] Z. Gyulai, Festigkeits- und Plastizitätseigenschaften von NaCl-Nadelkristallen, *Z. Physik*. 138 (1954) 317–321. doi:10.1007/BF01340676.

- [317] R.L. Eisner, Tensile tests on silicon whiskers, *Acta Metallurgica*. 3 (1955) 414–415. doi:10.1016/0001-6160(55)90051-1.
- [318] W.W. Webb, W.D. Forgeng, Mechanical behavior of microcrystals, *Acta Metallurgica*. 6 (1958) 462–469.
- [319] G. Stan, S. Krylyuk, A.V. Davydov, R.F. Cook, Bending manipulation and measurements of fracture strength of silicon and oxidized silicon nanowires by atomic force microscopy, *Journal of Materials Research*. 27 (2012) 562–570. doi:10.1557/jmr.2011.354.
- [320] M. Trueba, D. Gonzalez, M.R. Elizalde, J.M. Martínez-Esnaola, M.T. Hernandez, H. Li, D. Pantuso, I. Ocaña, Assessment of mechanical properties of metallic thin-films through micro-beam testing, *Thin Solid Films*. 571, Part 2 (2014) 296–301. doi:10.1016/j.tsf.2014.02.094.
- [321] C.J. Wilson, P.A. Beck, Fracture testing of bulk silicon microcantilever beams subjected to a side load, *Journal of Microelectromechanical Systems*. 5 (1996) 142–150. doi:10.1109/84.536620.
- [322] A.J. Griffin, F.R. Brotzen, C.F. Dunn, Mechanical testing of thin metallic films, *Thin Solid Films*. 220 (1992) 265–270. doi:10.1016/0040-6090(92)90583-W.
- [323] F. Ericson, J.-Å. Schweitz, Micromechanical fracture strength of silicon, *Journal of Applied Physics*. 68 (1990) 5840–5844. doi:10.1063/1.346957.
- [324] A. Pajares, M. Chumakov, B.R. Lawn, Strength of silicon containing nanoscale flaws, *J. Mater. Res.* 19 (2004) 657–660. doi:10.1557/jmr.2004.19.2.657.
- [325] R. Mougnot, D. Maugis, Fracture indentation beneath flat and spherical punches, *J Mater Sci*. 20 (1985) 4354–4376. doi:10.1007/BF00559324.
- [326] A.C. Fischer-Cripps, *Introduction to Contact Mechanics*, Springer Science & Business Media, 2007.
- [327] Y.W. Bao, S.B. Su, J.J. Yang, L. Sun, J.H. Gong, Nondestructively determining local strength and residual stress of glass by Hertzian indentation, *Acta Materialia*. 50 (2002) 4659–4666. doi:10.1016/S1359-6454(02)00316-6.
- [328] R. Wang, N. Katsube, R.R. Seghi, S.I. Rokhlin, Failure probability of borosilicate glass under Hertz indentation load, *Journal of Materials Science*. 38 (2003) 1589–1596. doi:10.1023/A:1023290618573.
- [329] P.R.M. Ayesha J. Haq, Phase transformations in (111) Si after spherical indentation, *Journal of Materials Research*. 24 (2009) 1967–1975. doi:10.1557/jmr.2009.0249.
- [330] K. Yoshii, H. Takagi, M. Umeno, H. Kawabe, A tensile testing machine for evaporated thin metal films, *J. Phys. E: Sci. Instrum.* 16 (1983) 127. doi:10.1088/0022-3735/16/2/005.
- [331] T.J. Balk, C. Eberl, Y. Sun, K.J. Hemker, D.S. Gianola, Tensile and compressive microspecimen testing of bulk nanoporous gold, *JOM*. 61 (2009) 26. doi:10.1007/s11837-009-0176-6.
- [332] J. Sharpe, W.N., B. Yuan, R.L. Edwards, A new technique for measuring the mechanical properties of thin films, *Microelectromechanical Systems, Journal of*. 6 (1997) 193–199. doi:10.1109/84.623107.
- [333] T. Yi, L. Li, C.-J. Kim, Microscale material testing of single crystalline silicon: process effects on surface morphology and tensile strength, *Sensors and Actuators A: Physical*. 83 (2000) 172–178. doi:10.1016/S0924-4247(00)00350-2.
- [334] P.E. Cantonwine, Strength of thermally exposed alumina fibers Part I Single filament behavior, *Journal of Materials Science*. 38 (2003) 461–470. doi:10.1023/A:1021867530979.
- [335] P.E. Cantonwine, Processing and properties of an alumina composite fiber /, (1999). <http://search.lib.virginia.edu/catalog/u3520059>.
- [336] F. Cottier, M.G. Mueller, *Study of the strength of alumina fibres*, EPFL, Lausanne, 2013.

- [337] J.W. Ma, W.J. Lee, J.M. Bae, K.S. Jeong, S.H. Oh, J.H. Kim, S.-H. Kim, J.-H. Seo, J.-P. Ahn, H. Kim, M.-H. Cho, Carrier Mobility Enhancement of Tensile Strained Si and SiGe Nanowires via Surface Defect Engineering, *Nano Lett.* 15 (2015) 7204–7210. doi:10.1021/acs.nanolett.5b01634.
- [338] B. Moser, K. Wasmer, L. Barbieri, J. Michler, Strength and fracture of Si micropillars: A new scanning electron microscopy-based micro-compression test, *J. Mater. Res.* 22 (2007) 1004–1011. doi:10.1557/JMR.2007.0140.
- [339] J.M. Wheeler, R. Raghavan, J. Wehrs, Y. Zhang, R. Erni, J. Michler, Approaching the Limits of Strength: Measuring the Uniaxial Compressive Strength of Diamond at Small Scales, *Nano Lett.* 16 (2016) 812–816. doi:10.1021/acs.nanolett.5b04989.
- [340] S.H. Shim, H. Bei, M.K. Miller, G.M. Pharr, E.P. George, Effects of Focused Ion Beam Milling on the Compressive Behavior of Directionally Solidified Micro-Pillars and the Nanoindentation Response of an Electro-Polished Surface, *Acta Materialia*. 57 (2009). doi:10.1016/j.actamat.2008.09.033.
- [341] M. Dietiker, S. Buzzi, G. Pigozzi, J.F. Löffler, R. Spolenak, Deformation behavior of gold nano-pillars prepared by nanoimprinting and focused ion-beam milling, *Acta Materialia*. 59 (2011) 2180–2192. doi:10.1016/j.actamat.2010.12.019.
- [342] Y. Wang, D. Xie, X. Ning, Z. Shan, Thermal treatment-induced ductile-to-brittle transition of submicron-sized Si pillars fabricated by focused ion beam, *Appl. Phys. Lett.* 106 (2015) 081905. doi:10.1063/1.4913241.
- [343] Y.-C. Wang, W. Zhang, L.-Y. Wang, Z. Zhuang, E. Ma, J. Li, Z.-W. Shan, In situ TEM study of deformation-induced crystalline-to-amorphous transition in silicon, *NPG Asia Mater.* 8 (2016) e291. doi:10.1038/am.2016.92.
- [344] Y. Rozenblat, D. Portnikov, A. Levy, H. Kalman, S. Aman, J. Tomas, Strength distribution of particles under compression, *Powder Technology*. 208 (2011) 215–224. doi:10.1016/j.powtec.2010.12.023.
- [345] L. Ribas, G.C. Cordeiro, R.D. Toledo Filho, L.M. Tavares, Measuring the strength of irregularly-shaped fine particles in a microcompression tester, *Minerals Engineering*. 65 (2014) 149–155. doi:10.1016/j.mineng.2014.05.021.
- [346] J.J. Swab, J. Yu, R. Gamble, S. Kilczewski, Analysis of the diametral compression method for determining the tensile strength of transparent magnesium aluminate spinel, *Int J Fract.* 172 (2011) 187–192. doi:10.1007/s10704-011-9655-1.
- [347] V. Pejchal, G. Žagar, R. Charvet, C. Dénéréaz, A. Mortensen, Compression testing spherical particles for strength: Theory of the meridian crack test and implementation for microscopic fused quartz, *Journal of the Mechanics and Physics of Solids*. 99 (2017) 70–92. doi:10.1016/j.jmps.2016.11.009.
- [348] A.A. Wereszczak, T.P. Kirkland, O.M. Jadaan, Strength Measurement of Ceramic Spheres Using a Diametrically Compressed “C-Sphere” Specimen, *Journal of the American Ceramic Society*. 90 (2007) 1843–1849. doi:10.1111/j.1551-2916.2007.01639.x.
- [349] R. Pérez, P. Gumbsch, Directional Anisotropy in the Cleavage Fracture of Silicon, *Phys. Rev. Lett.* 84 (2000) 5347–5350. doi:10.1103/PhysRevLett.84.5347.
- [350] C.S. John, The brittle-to-ductile transition in pre-cleaved silicon single crystals, *Philosophical Magazine*. 32 (1975) 1193–1212. doi:10.1080/14786437508228099.
- [351] J. Samuels, S. Roberts, P. Hirsch, The brittle-to-ductile transition in silicon, *Materials Science and Engineering: A*. 105–106, Part 1 (1988) 39–46. doi:10.1016/0025-5416(88)90478-8.
- [352] M. Brede, The brittle-to-ductile transition in silicon, *Acta Metallurgica et Materialia*. 41 (1993) 211–228. doi:10.1016/0956-7151(93)90353-T.

- [353] B.J. Gally, A.S. Argon, Brittle-to-ductile transitions in the fracture of silicon single crystals by dynamic crack arrest, *Philosophical Magazine A*. 81 (2001) 699–740. doi:10.1080/01418610108212168.
- [354] L. Zhao, D. Bardel, A. Maynadier, D. Nelias, Crack initiation behavior in single crystalline silicon, *Scripta Materialia*. 130 (2017) 83–86. doi:10.1016/j.scriptamat.2016.11.015.
- [355] M.J. Buehler, H. Tang, A.C.T. van Duin, W.A. Goddard, Threshold Crack Speed Controls Dynamical Fracture of Silicon Single Crystals, *Phys. Rev. Lett.* 99 (2007) 165502. doi:10.1103/PhysRevLett.99.165502.
- [356] A. Gleizer, D. Sherman, The cleavage energy at initiation of (110) silicon, *Int J Fract.* 187 (2014) 1–14. doi:10.1007/s10704-013-9882-8.
- [357] A.M. Fitzgerald, R.S. Iyer, R. h. Dauskardt, T.W. Kenny, Subcritical Crack Growth in Single-crystal Silicon Using Micromachined Specimens, *Journal of Materials Research*. 17 (2002) 683–692. doi:10.1557/JMR.2002.0097.
- [358] D. Sherman, M. Markovitz, O. Barkai, Dynamic instabilities in {1 1 1} silicon, *Journal of the Mechanics and Physics of Solids*. 56 (2008) 376–387. doi:10.1016/j.jmps.2007.05.010.
- [359] T. Cramer, A. Wanner, P. Gumbsch, Energy Dissipation and Path Instabilities in Dynamic Fracture of Silicon Single Crystals, *Phys. Rev. Lett.* 85 (2000) 788–791. doi:10.1103/PhysRevLett.85.788.
- [360] J.J.M.J. Y. L. Tsai, Fractal fracture of single crystal silicon, *Journal of Materials Research*. 6 (1991) 1248–1263. doi:10.1557/JMR.1991.1248.
- [361] F. Shi, Z. Song, P.N. Ross, G.A. Somorjai, R.O. Ritchie, K. Komvopoulos, Failure mechanisms of single-crystal silicon electrodes in lithium-ion batteries, *Nature Communications*. 7 (2016) 11886. doi:10.1038/ncomms11886.
- [362] J. Gilman, Direct Measurements of the Surface Energies of Crystals, *Journal of Applied Physics*. 31 (1960) 2208–2218. doi:10.1063/1.1735524.
- [363] R.J. Jaccodine, Surface Energy of Germanium and Silicon, *J. Electrochem. Soc.* 110 (1963) 524–527. doi:10.1149/1.2425806.
- [364] P.B. Hirsch, S.G. Roberts, The brittle-ductile transition in silicon, *Philosophical Magazine A*. 64 (1991) 55–80. doi:10.1080/01418619108206126.
- [365] W. w. Gerberich, J. Michler, W. m. Mook, R. Ghisleni, F. Östlund, D. d. Stauffer, R. Ballarini, Scale effects for strength, ductility, and toughness in “brittle” materials, *Journal of Materials Research*. 24 (2009) 898–906. doi:10.1557/jmr.2009.0143.
- [366] D. Chrobak, N. Tymiak, A. Beaber, O. Ugurlu, W.W. Gerberich, R. Nowak, Deconfinement leads to changes in the nanoscale plasticity of silicon, *Nat Nano*. 6 (2011) 480–484. doi:10.1038/nnano.2011.118.
- [367] W.W. Gerberich, D.D. Stauffer, A.R. Beaber, N.I. Tymiak, A brittleness transition in silicon due to scale, *J Mater Res*. 27 (2012) 552–561. doi:10.1557/jmr.2011.348.
- [368] W.W. Gerberich, W.M. Mook, C.R. Perrey, C.B. Carter, M.I. Baskes, R. Mukherjee, A. Gidwani, J. Heberlein, P.H. McMurry, S.L. Girshick, Superhard silicon nanospheres, *Journal of the Mechanics and Physics of Solids*. 51 (2003) 979–992.
- [369] A.M. Minor, E.T. Lilleodden, M. Jin, E.A. Stach, D.C. Chrzan, J.W. Morris, Room temperature dislocation plasticity in silicon, *Philos. Mag.* 85 (2005) 323–330. doi:10.1080/14786430412331315680.
- [370] X.D. Han, K. Zheng, Y.F. Zhang, X.N. Zhang, Z. Zhang, Z.L. Wang, Low-Temperature In Situ Large-Strain Plasticity of Silicon Nanowires, *Adv. Mater.* 19 (2007) 2112–2118. doi:10.1002/adma.200602705.
- [371] K. Zheng, C. Wang, Y.-Q. Cheng, Y. Yue, X. Han, Z. Zhang, Z. Shan, S.X. Mao, M. Ye, Y. Yin, E. Ma, Electron-beam-assisted superplastic shaping of nanoscale amorphous silica, *Nat Commun*. 1 (2010) 24. doi:10.1038/ncomms1021.

- [372] J. Zang, L. Bao, R.A. Webb, X. Li, Electron Beam Irradiation Stiffens Zinc Tin Oxide Nanowires, *Nano Lett.* 11 (2011) 4885–4889. doi:10.1021/nl2027519.
- [373] B.R. Lawn, B.J. Hockey, S.M. Wiederhorn, Atomically sharp cracks in brittle solids - An electron microscopy study, *Journal of Materials Science.* 15 (1980) 1207–1223. doi:10.1007/BF00551810.
- [374] M. Tanaka, K. Higashida, T. Kishikawa, T. Morikawa, HVEM/AFM Observation of Hinge-Type Plastic Zones Associated with Cracks in Silicon Crystals, *Materials Transactions.* 43 (2002) 2169–2172.
- [375] E. Langer, D. Katzer, Dislocation emission from moving cleavage cracks in silicon at room temperature, *J Mater Sci Lett.* 13 (1994) 1256–1257. doi:10.1007/BF00270953.
- [376] D.R. Adhika, M. Tanaka, T. Daio, K. Higashida, Crack tip shielding observed with high-resolution transmission electron microscopy, *Microscopy (Tokyo).* 64 (2015) 335–340. doi:10.1093/jmicro/dfv032.
- [377] W.W. Gerberich, W.M. Mook, C.B. Carter, R. Ballarini, A crack extension force correlation for hard materials, *Int J Fract.* 148 (2007) 109–114. doi:10.1007/s10704-008-9177-7.
- [378] D. Roundy, M.L. Cohen, Ideal strength of diamond, Si, and Ge, *Phys. Rev. B.* 64 (2001) 212103. doi:10.1103/PhysRevB.64.212103.
- [379] S. Hoffmann, I. Utke, B. Moser, J. Michler, S.H. Christiansen, V. Schmidt, S. Senz, P. Werner, U. Gösele, C. Ballif, Measurement of the Bending Strength of Vapor–Liquid–Solid Grown Silicon Nanowires, *Nano Lett.* 6 (2006) 622–625. doi:10.1021/nl052223z.
- [380] M.G. Mueller, V. Pejchal, G. Žagar, A. Singh, M. Cantoni, A. Mortensen, Fracture toughness testing of nanocrystalline alumina and fused quartz using chevron-notched microbeams, *Acta Materialia.* 86 (2015) 385–395. doi:10.1016/j.actamat.2014.12.016.
- [381] G. Žagar, V. Pejchal, M.G. Mueller, L. Michelet, A. Mortensen, Fracture toughness measurement in fused quartz using triangular chevron-notched micro-cantilevers, *Scripta Materialia.* 112 (2016) 132–135. doi:10.1016/j.scriptamat.2015.09.032.
- [382] M.G. Mueller, G. Žagar, A. Mortensen, Stable room-temperature micron-scale crack growth in single-crystalline silicon (Accepted for publication), *Journal of Materials Research.* (2017). doi:10.1557/jmr.2017.238.
- [383] ASTM C1421-10 Test Methods for Determination of Fracture Toughness of Advanced Ceramics at Ambient Temperature, ASTM Standard C1421 – 10, 2010.
- [384] I. Bar-On, G. Quinn, J. Salem, M. Jenkins, Development of ASTM C 1421-99 Standard Test Methods for Determination of Fracture Toughness of Advanced Ceramics, in: R. Chona (Ed.), *Fatigue and Fracture Mechanics: 32nd Volume*, ASTM International, 100 Barr Harbor Drive, PO Box C700, West Conshohocken, PA 19428-2959, 2002: pp. 315–315–21.
- [385] T.L. Anderson, *Fracture mechanics: fundamentals and applications*, Taylor & Francis, Boca Raton, FL, 2005.
- [386] L. Barker, Simplified Method for Measuring Plane Strain Fracture Toughness, *Eng Fract Mech.* 9 (1977) 361–369. doi:10.1016/0013-7944(77)90028-5.
- [387] P.E. Cantonwine, Strength of thermally exposed alumina fibers Part I: Single filament behavior, *J Mater Sci.* 38 (2003) 461–470. doi:10.1023/A:1021867530979.
- [388] K. Minoshima, T. Terada, K. Komai, Influence of nanometre-sized notch and water on the fracture behaviour of single crystal silicon microelements, *Fatigue Fract Eng M.* 23 (2000) 1033–1040. doi:10.1111/j.1460-2695.2000.00354.x.
- [389] B. Lawn, *Fracture of brittle solids*, 2nd ed., 1993.
- [390] G. Žagar, A. Singh, V. Pejchal, M.G. Mueller, A. Mortensen, On measuring fracture toughness under load control in the presence of slow crack growth, *Journal of the European Ceramic Society.* 35 (2015) 3155–3166. doi:10.1016/j.jeurceramsoc.2015.04.004.

- [391] A.R. Ingraffea, C. Manu, Stress-intensity factor computation in three dimensions with quarter-point elements, *Int J Fract.* 15 (1980) 1427–1445. doi:10.1002/nme.1620151002.
- [392] A. Carpinteri, Stress intensity factors for straight-fronted edge cracks in round bars, *Eng Fract Mech.* 42 (1992) 1035–1040. doi:10.1016/0013-7944(92)90142-2.
- [393] R. Kolhe, C.Y. Hui, A.T. Zehnder, Effects of finite notch width on the fracture of chevron-notched specimens, *Int. J. Fract.* 94 (1998) 189–198. doi:10.1023/A:1007451005263.
- [394] D.. Wilson, L. Visser, High performance oxide fibers for metal and ceramic composites, *Composites Part A.* 32 (2001) 1143–1153. doi:10.1016/S1359-835X(00)00176-7.
- [395] M. Asmani, C. Kermel, A. Leriche, M. Ourak, Influence of porosity on Young's modulus and Poisson's ratio in alumina ceramics, *J Eur Ceram Soc.* 21 (2001) 1081–1086. doi:10.1016/S0955-2219(00)00314-9.
- [396] L. Barker, Short Bar Specimens for KIC Measurements, in: *Fracture Mechanics Applied to Brittle Materials*, American Society for Testing and Materials, S. W. Freiman, 1979: pp. 73–82.
- [397] T. Scholz, G.A. Schneider, J. Muñoz-Saldaña, M.V. Swain, Fracture toughness from submicron derived indentation cracks, *Appl Phys Lett.* 84 (2004) 3055–3057. doi:10.1063/1.1711164.
- [398] S.M. Wiederhorn, H. Johnson, A.M. Diness, A.H. Heuer, Fracture of Glass in Vacuum, *J Am Ceram Soc.* 57 (1974) 336–341. doi:10.1111/j.1151-2916.1974.tb10917.x.
- [399] J.J. Mecholsky, R.W. Rice, S.W. Freiman, Prediction of Fracture Energy and Flaw Size in Glasses from Measurements of Mirror Size, *J Am Ceram Soc.* 57 (1974) 440–443. doi:10.1111/j.1151-2916.1974.tb11377.x.
- [400] J.A. Salem, Transparent Armor Ceramics as Spacecraft Windows, *J Am Ceram Soc.* 96 (2013) 281–289. doi:10.1111/jace.12089.
- [401] J.P. Lucas, N.R. Moody, S.L. Robinson, J. Hanrock, R.Q. Hwang, Determining fracture toughness of vitreous silica glass, *Scripta Metallurgica et Materialia.* 32 (1995) 743–748. doi:10.1016/0956-716X(95)91596-H.
- [402] P. Chantikul, S.J. Bennison, B.R. Lawn, Role of Grain Size in the Strength and R-Curve Properties of Alumina, *J Am Ceram Soc.* 73 (1990) 2419–2427. doi:10.1111/j.1151-2916.1990.tb07607.x.
- [403] S.M. Wiederhorn, Moisture assisted crack growth in ceramics, *Int J Fract.* 4 (1968) 171–177. doi:10.1007/BF00188945.
- [404] T.I. Suratwala, R.A. Steele, Anomalous temperature dependence of sub-critical crack growth in silica glass, *Journal of Non-Crystalline Solids.* 316 (2003) 174–182. doi:10.1016/S0022-3093(02)01799-4.
- [405] LMM | EPFL - Open Science, (n.d.). <http://lmm.epfl.ch/page-143871-en.html> (accessed May 19, 2017).
- [406] P. Roediger, H.D. Wanzenboeck, S. Waid, G. Hochleitner, E. Bertagnolli, Focused-ion-beam-inflicted surface amorphization and gallium implantation—new insights and removal by focused-electron-beam-induced etching, *Nanotechnology.* 22 (2011) 235302. doi:10.1088/0957-4484/22/23/235302.
- [407] B.N. Jaya, Private communication, (2016).
- [408] L. Kubin, *Dislocations, Mesoscale Simulations and Plastic Flow*, Oxford University Press, Oxford, New York, 2013.
- [409] G. Žagar, V. Pejchal, M.G. Mueller, A. Rossoll, M. Cantoni, A. Mortensen, The local strength of microscopic alumina reinforcements, *Acta Materialia.* 100 (2015) 215–223. doi:10.1016/j.actamat.2015.08.026.

- [410] M.G. Mueller, M. Fornabaio, G. Žagar, A. Mortensen, Microscopic strength of silicon particles in an aluminium–silicon alloy, *Acta Materialia*. 105 (2016) 165–175. doi:10.1016/j.actamat.2015.12.006.
- [411] M.G. Mueller, G. Žagar, A. Mortensen, In-situ strength of individual silicon particles within an aluminium casting alloy (Submitted), (2017).
- [412] M.G. Mueller, M. Fornabaio, A. Mortensen, Silicon particle pinhole defects in aluminium–silicon alloys, *J Mater Sci*. 52 (2017) 858–868. doi:10.1007/s10853-016-0381-y.
- [413] H.J. McSkimin, P.A. Jr, Elastic Moduli of Silicon vs Hydrostatic Pressure at 25.0°C and –195.8°C, *Journal of Applied Physics*. 35 (1964) 2161–2165. doi:10.1063/1.1702809.
- [414] W.A. Brantley, Calculated elastic constants for stress problems associated with semiconductor devices, *Journal of Applied Physics*. 44 (1973) 534–535. doi:10.1063/1.1661935.
- [415] Z. Yang, H.P. Zhang, M. Marder, Dynamics of static friction between steel and silicon, *PNAS*. 105 (2008) 13264–13268. doi:10.1073/pnas.0806174105.
- [416] R. Danzer, T. Lube, P. Supancic, R. Damani, Fracture of Ceramics, *Advanced Engineering Materials*. 10 (2008) 275–298. doi:10.1002/adem.200700347.
- [417] C. Chen, M. Leipold, Fracture-Toughness of Silicon, *Am. Ceram. Soc. Bull.* 59 (1980) 469–472.
- [418] T. Fujii, T. Namazu, K. Sudoh, S. Sakakihara, S. Inoue, Focused Ion Beam Induced Surface Damage Effect on the Mechanical Properties of Silicon Nanowires, *J. Eng. Mater. Technol.-Trans. ASME*. 135 (2013) 041002. doi:10.1115/1.4024545.
- [419] I. Chasiotis, Mechanics of thin films and microdevices, *IEEE Transactions on Device and Materials Reliability*. 4 (2004) 176–188. doi:10.1109/TDMR.2004.829901.
- [420] T. Tsuchiya, Tensile testing of silicon thin films, *Fatigue Fract. Eng. Mater. Struct.* 28 (2005) 665–674. doi:10.1111/j.1460-2695.2005.00910.x.
- [421] R. Boroch, J. Wiaranowski, R. Mueller-Fiedler, M. Ebert, J. Bagdahn, Characterization of strength properties of thin polycrystalline silicon films for MEMS applications, *Fatigue & Fracture of Engineering Materials & Structures*. 30 (2007) 2–12. doi:10.1111/j.1460-2695.2006.01055.x.
- [422] B.L. Boyce, J.M. Grazier, T.E. Buchheit, M.J. Shaw, Strength Distributions in Polycrystalline Silicon MEMS, *Journal of Microelectromechanical Systems*. 16 (2007) 179–190. doi:10.1109/JMEMS.2007.892794.
- [423] B.L. Boyce, M.J. Shaw, P. Lu, M.T. Dugger, Stronger silicon for microsystems, *Acta Materialia*. 58 (2010) 439–448. doi:10.1016/j.actamat.2009.09.022.
- [424] M.S. Gaither, F.W. DelRio, R.S. Gates, E.R. Fuller Jr., R.F. Cook, Strength distribution of single-crystal silicon theta-like specimens, *Scripta Materialia*. 63 (2010) 422–425. doi:10.1016/j.scriptamat.2010.04.047.
- [425] A.L. Hartzell, M.G. Da Silva, H.R. Shea, *MEMS Reliability*, Springer, New York, 2011. doi:10.1007/978-1-4419-6018-4.
- [426] O. Borrero-Lopez, M. Hoffman, Measurement of fracture strength in brittle thin films, *Surface and Coatings Technology*. 254 (2014) 1–10. doi:10.1016/j.surfcoat.2014.05.053.
- [427] T. Alan, P.M. Sarro, A Comparative Study of the Strength of Si, SiN and SiC used at Nanoscales, in: *Symposium DD – Microelectromechanical Systems–Materials and Devices*, 2007. doi:10.1557/PROC-1052-DD06-31.
- [428] Y. Zhu, F. Xu, Q. Qin, W.Y. Fung, W. Lu, Mechanical Properties of Vapor–Liquid–Solid Synthesized Silicon Nanowires, *Nano Lett.* 9 (2009) 3934–3939. doi:10.1021/nl902132w.
- [429] C.J. Wilson, A. Ormeggi, M. Narbutovskih, Fracture testing of silicon microcantilever beams, *Journal of Applied Physics*. 79 (1996) 2386–2393. doi:doi:10.1063/1.361102.

- [430] C.J. Wilson, P.A. Beck, Fracture testing of bulk silicon microcantilever beams subjected to a side load, *Journal of Microelectromechanical Systems*. 5 (1996) 142–150. doi:10.1109/84.536620.
- [431] V. Lehmann, *Electrochemistry of Silicon: Instrumentation, Science, Materials and Applications*, 1 edition, Wiley-VCH, Weinheim, 2002.
- [432] S. Imai, M. Takahashi, K. Matsuba, Asuha, Y. Ishikawa, H. Kobayashi, Formation and electrical characteristics of silicon dioxide layers by use of nitric acid oxidation method, *Acta Phys. Slovaca*. 55 (2005) 305–313.
- [433] H.K. Asuha, O. Maida, M. Takahashi, H. Iwasa, Nitric acid oxidation of Si to form ultrathin silicon dioxide layers with a low leakage current density, *Journal of Applied Physics*. 94 (2003) 7328–7335. doi:10.1063/1.1621720.
- [434] K. Mizuno, A. Nylund, I. Olefjord, Surface reactions during pickling of an aluminium-magnesium-silicon alloy in phosphoric acid, *Corrosion Science*. 43 (2001) 381–396. doi:10.1016/S0010-938X(00)00069-X.
- [435] A.N. Cleland, *Foundations of Nanomechanics*, Springer Berlin Heidelberg, Berlin, Heidelberg, 2003.
- [436] S. Wolf, R. Tauber, *Silicon Processing for the VLSI Era, Vol. 1: Process Technology*, 1st edition, Lattice Press, Sunset Beach, California, 1986.
- [437] K.R. Williams, R.S. Muller, Etch rates for micromachining processing, *Journal of Microelectromechanical Systems*. 5 (1996) 256–269. doi:10.1109/84.546406.
- [438] K.R. Williams, K. Gupta, M. Wasilik, Etch rates for micromachining processing-Part II, *Journal of Microelectromechanical Systems*. 12 (2003) 761–778. doi:10.1109/JMEMS.2003.820936.
- [439] ASTM B917/B917M-12 Standard Practice for Heat Treatment of Aluminum-Alloy Castings from All Processes, ASTM International, West Conshohocken, PA, 2012, https://doi.org/10.1520/B0917_B0917M-12, (n.d.).
- [440] M. Cerit, K. Genel, S. Eksi, Numerical investigation on stress concentration of corrosion pit, *Engineering Failure Analysis*. 16 (2009) 2467–2472. doi:10.1016/j.engfailanal.2009.04.004.
- [441] V. Pejchal, M. Fornabaio, G. Žagar, A. Mortensen, The local strength of microscopic particulate alumina reinforcements (Submitted), (2017).
- [442] E. Feilden, T. Giovannini, N. Ni, C. Ferraro, E. Saiz, L. Vandeperre, F. Giuliani, Micromechanical strength of individual Al₂O₃ platelets, *Scripta Materialia*. 131 (2017) 55–58. doi:10.1016/j.scriptamat.2017.01.008.
- [443] D.-M. Tang, C.-L. Ren, M.-S. Wang, X. Wei, N. Kawamoto, C. Liu, Y. Bando, M. Mitome, N. Fukata, D. Golberg, Mechanical Properties of Si Nanowires as Revealed by in Situ Transmission Electron Microscopy and Molecular Dynamics Simulations, *Nano Lett.* 12 (2012) 1898–1904. doi:10.1021/nl204282y.
- [444] G.T. Hahn, A.R. Rosenfield, Metallurgical factors affecting fracture toughness of aluminum alloys, *MTA*. 6 (1975) 653–668. doi:10.1007/BF02672285.
- [445] L. Lu, A.K. Dahle, Iron-rich intermetallic phases and their role in casting defect formation in hypoeutectic Al–Si alloys, *Metall and Mat Trans A*. 36 (2005) 819–835. doi:10.1007/s11661-005-1012-4.
- [446] Y.S. Choi, J.S. Lee, W.T. Kim, H.Y. Ra, Solidification behavior of Al–Si–Fe alloys and phase transformation of metastable intermetallic compound by heat treatment, *Journal of Materials Science*. 34 (1999) 2163–2168.
- [447] S. Terzi, J.A. Taylor, Y.H. Cho, L. Salvo, M. Suéry, E. Boller, A.K. Dahle, In situ study of nucleation and growth of the irregular α -Al/ β -Al₅FeSi eutectic by 3-D synchrotron X-ray

- microtomography, *Acta Materialia*. 58 (2010) 5370–5380. doi:10.1016/j.actamat.2010.06.012.
- [448] S.K. Tang, T. Sritharan, Morphology of β -AlFeSi intermetallic in Al-7Si alloy castings, *Mater. Sci. Technol.* 14 (1998) 738–742. doi:10.1179/mst.1998.14.8.738.
- [449] M. Timpel, N. Wanderka, B.S. Murty, J. Banhart, Three-dimensional visualization of the microstructure development of Sr-modified Al-15Si casting alloy using FIB-EsB tomography, *Acta Materialia*. 58 (2010) 6600–6608. doi:10.1016/j.actamat.2010.08.021.
- [450] Z. Li, X. Kuang, C. Liao, F. Yin, M. Zhao, Phase Equilibria of the Al-Fe-Si-Ti Quaternary System at 700 °C, *J. Phase Equilib. Diffus.* 37 (2015) 174–185. doi:10.1007/s11669-015-0443-x.
- [451] D.G. Mallapur, S.A. Kori, K.R. Udupa, Influence of Ti, B and Sr on the microstructure and mechanical properties of A356 alloy, *J Mater Sci.* 46 (2010) 1622–1627. doi:10.1007/s10853-010-4977-3.
- [452] S.A. Kori, B.S. Murty, M. Chakraborty, Development of an efficient grain refiner for Al-7Si alloy and its modification with strontium, *Materials Science and Engineering A*. 283 (2000) 94–104.
- [453] Z. Fan, Y. Wang, Y. Zhang, T. Qin, X.R. Zhou, G.E. Thompson, T. Pennycook, T. Hashimoto, Grain refining mechanism in the Al/Al-Ti-B system, *Acta Materialia*. 84 (2015) 292–304. doi:10.1016/j.actamat.2014.10.055.
- [454] S.K. Shaha, F. Czerwinski, W. Kasprzak, J. Friedman, D.L. Chen, Ageing characteristics and high-temperature tensile properties of Al-Si-Cu-Mg alloys with micro-additions of Cr, Ti, V and Zr, *Materials Science and Engineering: A*. 652 (2016) 353–364. doi:10.1016/j.msea.2015.11.049.
- [455] H. Jones, An Evaluation of Measurements of Solid/Liquid Interfacial Energies in Metallic Alloy Systems by the Groove Profile Method, *Metall and Mat Trans A*. 38 (2007) 1563–1569. doi:10.1007/s11661-007-9171-0.
- [456] M. Gündüz, J.D. Hunt, The measurement of solid-liquid surface energies in the Al-Cu, Al-Si and Pb-Sn systems, *Acta Metallurgica*. 33 (1985) 1651–1672. doi:10.1016/0001-6160(85)90161-0.
- [457] Z. Jian, X. Yang, F. Chang, W. Jie, Solid-Liquid Interface Energy between Silicon Crystal and Silicon-Aluminum Melt, *Metall and Mat Trans A*. 41 (2010) 1826–1835. doi:10.1007/s11661-010-0217-3.
- [458] J.M. Howe, *Interfaces in Materials: Atomic Structure, Thermodynamics and Kinetics of Solid-Vapor, Solid-Liquid and Solid-Solid Interfaces*, 1 edition, Wiley-Interscience, New York, 1997.
- [459] M.A. Tschopp, S.P. Coleman, D.L. McDowell, Symmetric and asymmetric tilt grain boundary structure and energy in Cu and Al (and transferability to other fcc metals), *Integrating Materials and Manufacturing Innovation*. 4 (2015) 11. doi:10.1186/s40192-015-0040-1.
- [460] U.A. Curle, H. Möller, J.D. Wilkins, Shape rheocasting of unmodified Al-Si binary eutectic, *Materials Letters*. 65 (2011) 1469–1472. doi:10.1016/j.matlet.2011.02.040.
- [461] A. Hekmat-Ardakan, F. Ajersch, Effect of conventional and rheocasting processes on microstructural characteristics of hypereutectic Al-Si-Cu-Mg alloy with variable Mg content, *Journal of Materials Processing Technology*. 210 (2010) 767–775. doi:10.1016/j.jmatprotec.2010.01.005.

Curriculum Vitae

Martin Guillermo Mueller

Chemin de Maillefer 3
1018 Lausanne – Switzerland
Phone number: +41 76 612 0034
e-mail: martin.mueller@epfl.ch
e-mail: cti.martin.mueller@gmail.com

Education

- | | |
|---------------------|--|
| Jun 2012 – Jul 2017 | PhD in Materials Science and Engineering
Ecole Polytechnique Fédérale de Lausanne (EPFL), Laboratory of Mechanical Metallurgy, Lausanne, Switzerland. |
| Sep 2007 – Jul 2011 | Materials Engineer (in Spanish “Ingeniero en Materiales”, a degree equivalent to a Master obtained after a total of 6 years of studies)
Prof. Jorge Sabato Institute, San Martin National University - National Atomic Energy Commission, San Martin, Argentina. |
| Mar 2003 – Dec 2006 | First years of Mechanical Engineering
Buenos Aires University, Engineering Faculty, Buenos Aires, Argentina. |
| 1991 – 2002 | Primary and secondary school
Deutsche Schule Bariloche (Instituto Primo Capraro), Bariloche, Argentina. |

Publications

M.G. Mueller, G. Žagar, A. Mortensen. In-situ strength of individual silicon particles within an aluminium casting alloy (*Submitted 2017*).

M.G. Mueller, G. Žagar, A. Mortensen. Stable room-temperature micron-scale crack growth in single-crystalline silicon (*Accepted in the Journal of Materials Research, 2017*). doi:10.1557/jmr2017.238

M.G. Mueller, M. Fornabaio, A. Mortensen, Silicon particle pinhole defects in aluminium–silicon alloys, *Journal of Materials Science*. 52 (2017) 858–868. doi:10.1007/s10853-016-0381-y.

M.G. Mueller, M. Fornabaio, G. Žagar, A. Mortensen, Microscopic strength of silicon particles in an aluminium–silicon alloy, *Acta Materialia*. 105 (2016) 165–175. doi:10.1016/j.actamat.2015.12.006.

G. Žagar, V. Pejchal, **M.G. Mueller**, L. Michelet, A. Mortensen, Fracture toughness measurement in fused quartz using triangular chevron-notched micro-cantilevers, *Scripta Materialia*. 112 (2016) 132–135. doi:10.1016/j.scriptamat.2015.09.032.

M.G. Mueller, V. Pejchal, G. Žagar, A. Singh, M. Cantoni, A. Mortensen, Fracture toughness testing of nanocrystalline alumina and fused quartz using chevron-notched microbeams, *Acta Materialia*. 86 (2015) 385–395. doi:10.1016/j.actamat.2014.12.016.

G. Žagar, V. Pejchal, **M.G. Mueller**, A. Rossoll, M. Cantoni, A. Mortensen, The local strength of microscopic alumina reinforcements, *Acta Materialia*. 100 (2015) 215–223. doi:10.1016/j.actamat.2015.08.026.

G. Žagar, A. Singh, V. Pejchal, **M.G. Mueller**, A. Mortensen, On measuring fracture toughness under load control in the presence of slow crack growth, *Journal of the European Ceramic Society*. 35 (2015) 3155–3166. doi:10.1016/j.jeurceramsoc.2015.04.004.

Z. Xie, M. Lugovy, N. Orlovskaya, T. Graule, J. Kuebler, **M. Mueller**, H. Gao, M. Radovic, D.A. Cullen, Hexagonal OsB₂: Sintering, microstructure and mechanical properties, *Journal of Alloys and Compounds*. 634 (2015) 168–178. doi:10.1016/j.jallcom.2015.01.291.

F. Gui, T. Ramgopal, **M.G. Muller**, Role of sour environments on the corrosion fatigue growth rate of x65 pipe steel, *Corrosion*. 68 (2012) 730–738. doi:10.5006/0590.

M. Kappes, G.S. Frankel, R. Thodla, **M. Mueller**, N. Sridhar, R.M. Carranza, Hydrogen permeation and corrosion fatigue crack growth rates of X65 pipeline steel exposed to acid brines containing thiosulfate or hydrogen sulfide, *Corrosion*. 68 (2012) 1015–1028. doi:10.5006/0636.

E. Chavez, **M. Mueller**, L. Mogni, A. Caneiro, Study of LnBaCo₂O_{6-δ} (Ln = Pr, Nd, Sm and Gd) double perovskites as new cathode material for IT-SOFC, *J. Phys.: Conf. Ser.* 167 (2009) 012043. doi:10.1088/1742-6596/167/1/012043.

Professional Experience

Jun 2012 – Jul 2017	PhD candidate at EPFL , Lausanne, Switzerland
Sep 2011 – Apr 2012	Engineering and Materials Consultant at the engineering consulting company CTI Solari y Asociados S.R.L. , Buenos Aires, Argentina
Jan – Jul 2011	R&D Internship in corrosion at Det Norske Veritas (DNV) GL Laboratory Columbus, Ohio, USA
Feb 2010	R&D Internship at the technology company Invap S.E. , Bariloche, Argentina
Feb 2009	Research Internship at the National Atomic Energy Commission facilities located in the city of Bariloche, Argentina.
Feb 2008	Research Internship at the National Atomic Energy Commission facilities located at the city of Bariloche, Argentina.

